THESIS ON NATURAL AND EXACT SCIENCES B232

Study of ZnO:In, Zn(O,S) and Sb_2S_3 Thin Films Deposited by Aerosol Methods

MERIKE KRIISA

TTÜ
PRESS

TALLINN UNIVERSITY OF TECHNOLOGY
School of Engineering
Department of Materials and Environmental Technology
Laboratory of Thin Film Chemical Technologies

This dissertation was accepted for the defence of the degree of Doctor of Philosophy in Natural and Exact Sciences on May 22nd, 2017.

Supervisors: Dr. Malle Krunks, Lead Research Scientist, Department of Materials and Environmental Technology, Tallinn University of Technology

Dr. Ilona Oja Acik, Senior Research Scientist, Department of Materials and Environmental Technology, Tallinn University of Technology

Opponents: Dr. Stephan Bücheler, Laboratory for Thin Films and Photovoltaics, Swiss Federal Laboratories for Materials Science and Technology (EMPA), Switzerland

Dr. Kaia Ernits, crystalsol OÜ, Estonia

Defence of the thesis: 28th of June, 2017 at 15:00
Lecture hall: U06A-201
Tallinn University of Technology, Ehitajate tee 5, Tallinn

Declaration:
Hereby I declare that this doctoral thesis, my original investigation and achievement, submitted for the doctoral degree at Tallinn University of Technology has not been submitted for any academic degree.

/Merike Kriisa/

European Union
European Social Fund

Investing in your future

ISSN 1406-4723
ISBN 978-9949-83-114-2 (publication)
ISBN 978-9949-83-115-9 (PDF)

LOODUS- JA TÄPPISTEADUSED B232

Aerosoolmeetoditel sadestatud ZnO:In, Zn(O,S) ja Sb_2S_3 õhukeste kilede uurimine

MERIKE KRIISA

TTÜ KIRJASTUS

TABLE OF CONTENTS

LIST OF PUBLICATIONS

The dissertation is based on the following publications that are referred in the text by Roman numerals **I-V**:

I. **Vent, M.;** Kärber, E.; Unt, T.; Mere, A.; Krunks, M. (2012). The effect of growth temperature and spraying rate on properties of ZnO:In films. physica status solidi (c), 9 (7), 1604−1606.

II. **Kriisa, M.;** Krunks, M.; Kärber, E.; Kukk, M.; Mikli, V.; Mere, A. (2013). Effect of Solution Spray Rate on the Properties of Chemically Sprayed ZnO:In Thin Films. Journal of Nanomaterials, 2013, Article ID 423632.

III. **Kriisa, M.;** Kärber, E.; Krunks, M.; Mikli, V.; Unt, T.; Kukk, M.; Mere, A. (2014). Growth and properties of ZnO films on polymeric substrate by spray pyrolysis method. Thin Solid Films, 555, 87−92.

IV. **Kriisa, M.;** Sáez-Araoz, R.; Fischer, C. -H.; Köhler, T.; Kärber, E.; Fu, Y.; Hergert, F.; Lux-Steiner, M. C.; Krunks, M. (2015). Study of Spray-CVD Deposited Zn(O,S) Films and their Application as Buffer Layers in Cu(In,Ga)(S,Se)$_2$ Solar Cells. Solar Energy, 115, 562−568.

V. **Kriisa, M.;** Krunks, M.; Oja Acik, I.; Kärber, E.; Mikli, V. (2015). The effect of tartaric acid in the deposition of Sb_2S_3 films by chemical spray pyrolysis. Materials Science in Semiconductor Processing, 40, 867−872.

Copies of these articles are included in Appendix A.

AUTHOR’S CONTRIBUTION

I. Deposition of the ZnO:In films by chemical spray pyrolysis (CSP), characterisation of film optical and structural properties (UV-VIS spectroscopy, XRD measurements), co-analysis of the results, and notable role in writing.

II. Deposition of the ZnO:In films by CSP, characterisation of film optical and structural properties (UV-VIS spectroscopy, XRD measurements), participation in the characterisation of film electrical properties, analysis of the results, and major role in writing.

III. Deposition of the ZnO:In films by CSP, characterisation of film optical and structural properties (UV-VIS spectroscopy, XRD measurements), participation in the characterisation of film electrical properties, analysis of the results, and major role in writing.

IV. Deposition of the Zn(O,S) films by aerosol assisted chemical vapour deposition (AA-CVD), analysis of the UV-VIS spectroscopy, XRD, SEM, EDX measurement results, characterisation and analysis of the solar cell performance (current-voltage and quantum efficiency), and major role in writing.

V. Deposition of the Sb_2S_3 films by CSP, characterisation of film optical and structural properties (UV-VIS spectroscopy, XRD and FTIR measurements), analysis of the results, and major role in writing.

LIST OF ABBREVIATIONS, TERMS AND SYMBOLS

AA-CVD	Aerosol assisted chemical vapour deposition
AFM	Atomic force microscopy
ALD	Atomic layer deposition
CBD	Chemical bath deposition
CIGSSe	$Cu(In,Ga)(S,Se)_2$
CSP	Chemical spray pyrolysis
CVD	Chemical vapour deposition
EBE	Electron beam evaporation
EDX	Energy dispersive X-ray spectroscopy
ETA	Extremely thin absorber
FF	Fill factor
FTIR	Fourier transmittance infrared spectroscopy
HZB	Helmholtz-Zentrum Berlin
ILGAR	Ion layer gas reaction
J_{SC}	Short-circuit current
PLD	Pulsed lased deposition
SEM	Scanning electron microscopy
TA	Tartaric acid
TCO	Transparent conductive oxide
TG/DTG/DTA	Thermogravimetric and differential thermal analysis
UV-VIS	Ultra violet visible light spectroscopy
V_{OC}	Open-circuit voltage
XRD	X-ray diffraction

INTRODUCTION

The population growth and the energy consumption increase simultaneously and the need for sustainable and environmentally friendly energy source is an inevitable reality. Utilising solar energy is logical as the research in the solar cell technology thrives for more efficient electricity production and for environmentally friendly materials that are abundant, thus cheaper. The solar cells or the photovoltaic devices are composed of different stacked layers that have certain roles in the device. For instance, the function of absorber layer is to absorb as much light as possible to generate the p-n junction between the n-type and the p-type semiconductor, thus generating the flow of electrons. In addition, the methods to prepare solar cells are of importance. Using cheap yet simple and effective deposition methods such as chemical spray pyrolysis (CSP) and aerosol assisted chemical vapour deposition (AA-CVD) are of interest as these methods are aerosol based deposition methods which do not need vacuum or complex apparatus. In those methods, the selection of precursors is wide as the precursors do not have to be volatile but soluble in the solvent and the films are grown at moderate temperatures (100°C–500°C).

The topics in this dissertation are directly related to the research topics and the corresponding research projects that are under study in the Laboratory of Thin Film Chemical Technologies.

The dissertation is based on five published articles and composes of three main parts. The first part is literature overview describing the aerosol methods and the properties of zinc oxide and antimony sulphide materials and films. Secondly, experimental description of used materials and characterisation methods is provided. The third part is a compendium of results that is divided into three sections.

In the first section, the growth and the characterisation of indium doped ZnO thin films grown by CSP on glass is introduced [**I**, **II**]. The more abundant materials and the cheaper production methods of ZnO:In thin film make it a potential candidate to substitute the currently used front contacts (indium doped tin oxide, ITO, and fluorine doped tin oxide, FTO) in the solar cell devices if prepared as transparent and conductive as possible. The effect of substrate temperature and the solution spray rate on the various thin film properties were studied. The optimal substrate temperature to grow the most conductive ZnO:In thin films was 400°C. Spray rate affects has a major effect on the properties of ZnO:In thin films. Spray rates below 3 mL/min are not suggested as ZnO:In films are not as conductive as films grown with spray rate above 3 mL/min [**II**]. In addition, the first results on the growth of ZnO:In films by CSP on polymer substrates are reported [**III**]. The morphology of ZnO:In layer is dependent on the morphology of ZnO layer that was used as a buffer layer. Homogeneous ZnO:In layer can be grown on a homogeneous buffer layer. Increasing the buffer layer thickness roughens the buffer layer morphology by increasing the size and the number of leaf-like grains that act as nucleation centres for large ZnO:In scrolled belts that exhibit high light scattering capability.

In the second section, the deposition of Zn(O,S) layers, alternate buffer layer in Cu(In,Ga)(S,Se)$_2$ absorber (CIGSSe) solar cell, by AA-CVD is reported [**IV**]. The growth of compact and smooth Zn(O,S) depends strongly on the carrier gas and the reactant gas flow rates. In addition, the compact Zn(O,S) layers were successfully applied in CIGSSe type solar cells as buffer layers. The best output parameters for Zn(O,S) buffered solar cell are Voc=573 mV, Jsc=39.2 mA/cm^2, FF=68.4% and η=15.4% which are comparable to reference solar cell (In_2S_3 or CdS buffered) output values.

The final section is dedicated to the deposition of Sb_2S_3 thin films by CSP [**V**]. Sb_2S_3 is a potential absorber material to be used in an extremely thin absorber (ETA) layer solar cell. While there are some reports on the growth of Sb_2S_3 by CSP, the main deposition method is chemical bath deposition (CBD). The study showed that the Sb_2S_3 spray solution recipe that is used in already published articles is based on the recipe used in CBD which is not applicable in CSP. The issues arising with the use of complexing agent in the deposition of Sb_2S_3 by CSP are discussed and possible solutions to grow organic residual free Sb_2S_3 films by CSP are proposed.

The work is financially supported by the Estonian Ministry of Education and Research under Projects SF0140092s08 (Thin film and nanostructured materials by chemical methods) and IUT19-4 (Thin films and nanomaterials by wet-chemical methods for next-generation photovoltaics), The European Regional Development Funds Projects TK114 (Centre of Excellence: Mesomaterials–Theory and Applications), TK141 (Centre of Excellence: Advanced materials and high-technology devices for sustainable energetics, sensorics and nanoelectronics) and AR12118 (Efficient plasmonic absorbers for solar cells), by Estonian Science Foundation grants ETF8509 (Development of ZnO nanorods by chemical spray) and ETF9081 (Absorber layers by chemical spray pyrolysis for nanostructured solar cells), Internationalisation Programme DoRa, graduate school of Functional materials and technologies.

1 LITERATURE OVERVIEW

1.1 Aerosol deposition methods

Aerosol is a colloidal system of fine solid or liquid particles in a gas. By definition, aerosol consists of particles with the size of 0.001 μm to 100 μm that are suspended generally in air or other gas [1]. Due to the fine particles and the possibility to guide the particle flow with the gas in the ambient condition, the aerosol is a good modus to carry precursor solution to substrates for the deposition of desired layers.

In the deposition of thin films by aerosol methods, usually two methods are used to generate aerosol: the nebulisation and the ultrasonic oscillation of precursor solution. Both aerosol generation techniques require that the used precursors are stable at room temperature, do not oxidise in air, are soluble in solvent, decompose at temperatures below 500°C and the forming unwanted by-products are volatile at used deposition temperature [2–5]. The fact that precursors do not have to be volatile widens the selection of suitable precursors for aerosol based deposition methods [6–9]. The selected solvent which acts solely as a transport medium and is not involved in chemical reaction [10] should not be readily inflammable and its viscosity should allow high aerosol flow rate [3, 8, 11, 12]. Generally, the use of alcoholic solvent results in more homogeneous films compared to an aqueous solvent due to smaller droplet sizes [12–14]. The aerosol is carried towards the substrate by carrier gas, either by N_2, Ar or He or by compressed air [3–5, 7, 8, 11, 12, 15–21]. As the aerosol approaches the heated substrate, the solvent evaporates either on the substrate or just above the substrate followed by the precipitation of solid particles on the substrate and the thermal decomposition of precursor into more stable film [22–24].

In this study, two aerosol based deposition methods were used to grow thin films: chemical spray pyrolysis and aerosol assisted chemical vapour deposition.

1.1.1 Chemical spray pyrolysis

In 1966, the pioneering article about the chemical spray pyrolysis (CSP) was published by Chamberlin and Skarman [25]. Since then, the number of reports on the deposition of various thin films by CSP has increased. The films grown by CSP have been harnessed in various applications, such as solar cells, sensors, microelectronics, antireflective coatings, optoelectronic devices, etc. [26–29]. The CSP is especially suitable for the growth of simple oxide layers, mixed oxides, binary, ternary and quaternary chalcogenides, etc. [2, 26].

The typical spraying system is presented in Figure 1.1. Chemical spray pyrolysis set-up consists of 1) precursor solution and spray solution container, 2) rotameter, 3) carrier gas flux tube, 4) air compressor or other carrier gas source, 5) spray nozzle, 6) substrate heater, 7) substrate and 8) temperature controller. In the spray pyrolysis method various processes occur simultaneously or sequentially. These processes are the generation and the transportation of the aerosol, the evaporation of the solvent, droplet impact and the precursor decomposition [24, 30]. The deposition parameter being involved in nearly all the mentioned processes is the substrate/deposition temperature. Thus, the deposition temperature is one the main parameter affecting the final thin film properties [2, 15, 26, 30–33]. For instance, an increase in the deposition temperature can alter the film morphology from a homogeneous adherent thin film to a cracked one, to a porous layer or to a structured layer [30, 32].

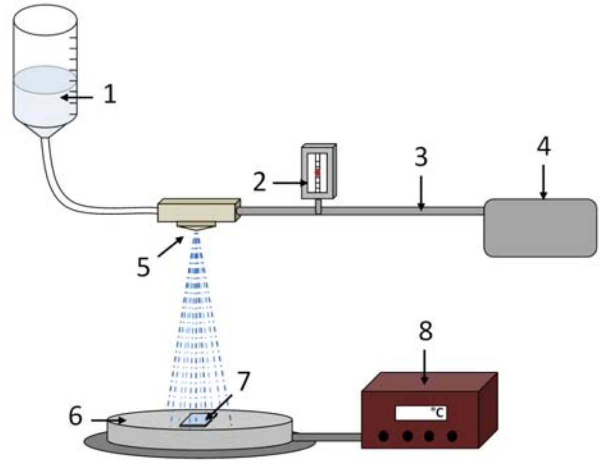

Figure 1.1. Schematic diagram of chemical spray pyrolysis set-up where 1) precursor solution and spray solution container, 2) rotameter, 3) carrier gas flux tube, 4) air compressor or other carrier gas source, 5) spray nozzle, 6) substrate heater, 7) substrate and 8) temperature controller.

Other parameters in the chemical spray pyrolysis that influence the deposition process and the final film are [12–18, 24, 26, 30, 32, 34]:

1. precursor solution and the properties of its constituents,
2. precursor solution concentration,
3. solvent and the solution volume,
4. solution spray rate,
5. carrier gas flow rate,
6. droplet size,
7. substrate type and properties,
8. substrate motion,
9. the nozzle-to-substrate distance,
10. ambient temperature and cooling rate after deposition.

The properties and the quality of the film depend on all the deposition parameters listed above [12–18, 26, 30, 32, 34]. For instance, the selected precursors and solvents affect the morphological and structural properties of deposited film [12, 13, 26, 34, 35]. The used substrate type influences the film formation (nucleation process and the crystal growth) that in turn controls the properties and the thickness of the desired material [32, 36, 37]. The thickness of the films also depends on the nozzle-to-substrate distance, substrate temperature, precursor solution and the volume of sprayed solution [15, 16, 18, 34, 36, 38]. The film formation on the substrate is related to substrate type and temperature, and the droplet size (its landing, reaction and the evaporation of the solvent) [15, 26, 36, 37]. Using ultrasonic generator in the CSP generates aerosol with narrower droplet size distribution and reduced droplet size compared to pneumatic spray pyrolysis [3]. This method is known as ultrasonic spray pyrolysis (USP) [39, 40]. According to Blandenet et al. [3], the narrow droplet size distribution assures as similar decomposition conditions as possible throughout all of the aerosol which will improve the uniformity and homogeneity of the coating. Similar observation has been made by Chen et al. [41], stating that the quality of the aerosol mist should be consistently good to obtain a uniform coverage on the substrate. The homogeneity of the aerosol and the aerosol droplet size is controlled by the frequency of the ultrasonic generator [3, 7, 8].

Chemical spray pyrolysis is a solution based deposition method that has many advantages. The simplicity of the apparatus, cost effective method and the possibility to cover large areas are considered to be the main advantages of CSP. In addition, CSP does not require vacuum, high amount of high-quality substrates nor chemicals. With CSP, it is relatively easy to modify and to control the composition and the microstructure of the final material due to the addition of the dopant directly into the precursor solution [12, 15, 42]. At moderate deposition temperatures (100°C–500°C), the film growth rates can be high (up to 100 nm/s [43]). CSP is a potential technique for mass production. Unlike some high-power methods (such as radiofrequency magnetron sputtering), the chemical spray pyrolysis causes no local overheating that damages the final desired layer [44–46]. In addition, using ultrasonic generator to produce precursor aerosol enhances the homogeneity of the film due to the generation of finer droplets [3].

As with every other deposition method, the chemical spray has its disadvantages as well. The CSP technique has many deposition variables (as listed above) which can be dependent on each other. Therefore, to study the effect of a particular deposition variable on the film formation and the final layer properties, the other remaining parameters have to be constant. During the deposition process in ambient air, the oxidation of sulphides and selenides could occur [22, 32]. The three-dimensional growth mechanism [38] and the direct control of the substrate temperature during the deposition process still remain a difficulty.

Despite the disadvantages of chemical spray pyrolysis, the advantages of CSP surpass the negative side of the method making CSP an attractive and a promising deposition technique compared to other methods used for thin film deposition.

1.1.2 Aerosol assisted chemical vapour deposition

The first reports about aerosol assisted chemical vapour deposition where the deposition temperature do not exceed 500°C were published in 1994 [9]. As the deposition temperatures in AA-CVD do not exceed 500°C [4, 5, 7, 9, 19, 21], the method name is imprecise since the precursors are not in gas phase as in CVD but decompose thermally. The AA-CVD originates from ion layer gas reaction (ILGAR), namely its sub-type spray-ILGAR as the methods have similar equipment [47]. In classical ILGAR, four steps occur in a cycle [47, 48]:

1. dipping the substrate in precursor solution for few seconds,
2. removing the substrate from precursor solution and drying the substrate with carrier gas,
3. purging of the reactant gas,
4. venting of the reaction chamber with carrier gas.

In spray-ILGAR, the dipping is substituted with spray process which leads to the deposition of more homogeneous films [21, 22, 48]. The aerosol in spray-ILGAR is generated with ultrasonic generator. However, in AA-CVD all the steps of spray-ILGAR occur simultaneously. Compactly, AA-CVD is a process where the carrier gas transports the dissolved precursors as an aerosol to the reaction chamber where the solvent evaporates leaving behind solid particles that react with the purging gas and then decompose on the preheated substrate. Various films, such as In_2O_3 [3, 49], SnO_2 [3, 50], SnS [6], TiO_2 [51], CdS [4], ZnS [4, 52], ZnO [19, 41, 53, 54], Sb_2S_3 [55], WO_3 [56], etc. have been grown by AA-CVD. The AA-CVD grown films have been found applications in gas sensors [3, 7, 11, 50, 56], as photocatalysts [3, 51, 53], photovoltaics [3, 20], etc.

A characteristic aerosol assisted chemical vapour deposition set-up is presented in Figure 1.2. The AA-CVD set-up consists of 1) carrier gas input, 2) precursor solution, 3) ultrasonic generator, 4) reactant gas input, 5) substrate, 6) substrate heater and 7) exhaust. Alternatively, the aerosol in AA-CVD technique can be produced by aerosol generators as pneumatic aerosol jet and electrostatic aerosol atomisation [8, 11].

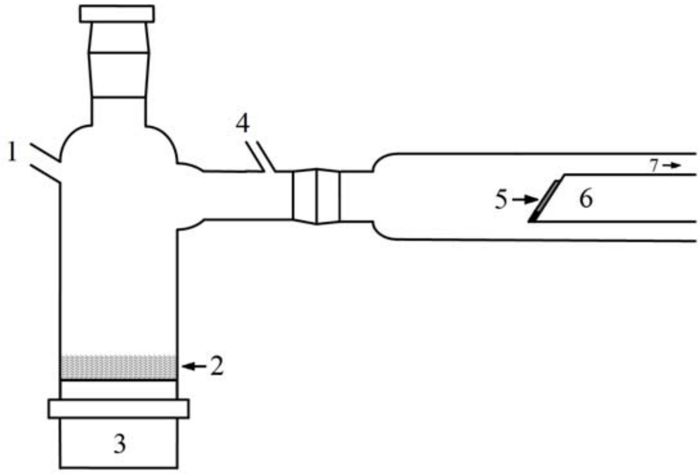

Figure 1.2. Characteristic aerosol assisted chemical vapour deposition set-up where 1) carrier gas input, 2) precursor solution, 3) ultrasonic generator, 4) reactant gas input, 5) substrate, 6) substrate heater and 7) exhaust.

As in CSP, the main deposition parameter in AA-CVD that controls the growth and the formation of a film is substrate temperature [3, 41]. With a slight variation in the substrate temperature, the layer thickness is considerably different [21, 57]. Other parameters in aerosol assisted chemical vapour deposition influencing the deposition process and the film formation are:

1. precursor solution and its constituent properties
2. precursor solution concentration
3. solvent type and volume
4. ultrasonic generator (frequency and power of ultrasonic generator),
5. droplet size in the aerosol,
6. aerosol flow rate,
7. carrier gas type and the flow rate,
8. reactant gas type and the flow rate,
9. substrate type.

Noor and Parkin [58] showed that the solvents have an extremely important and active role in the film growth affecting the film's functional properties. The typical solvents in the AA-CVD method are ethanol, butanol, methanol, acetylacetone, toluene [3, 4, 7, 19, 20, 41, 54–56, 59]. The selection of the carrier gas is determined by its suitability in the chemical reaction. When oxygen is needed in the chemical reaction, for instance for the deposition of an oxide layer, then air is used as a carrier gas [3, 8]. Otherwise, neutral gases are used [3–5, 7, 8, 11, 19–21, 59]. Together, the substrate type and the deposition temperature directly control the number and the size of the nuclei [41] and the final structural properties of the desired film [58].

The main advantages of AA-CVD are its ease of operation, low set-up and maintenance costs, safety, the good quality of coatings obtained originating from the narrow droplet size distribution and the high variety of precursors [3, 6, 59, 60]. In addition, no expensive targets, high vacuum and too much energy is needed in the AA-CVD method [7, 54]. The AA-CVD can be operated in several environments, such as low pressure, atmospheric pressure and even in an open environment [8]. The deposition rate (up to 100 nm/min [9]), composition, microstructure and the thickness of films grown by AA-CVD are easily controllable [8]. AA-CVD has a potential to be used as a mass production method when scaled-up to industrial size [8, 11, 59].

Similar to the chemical spray pyrolysis, the aerosol assisted chemical vapour deposition has many deposition variables which can be dependent on each other. Again, studying the effect of a particular deposition parameter on the film formation and the final layer properties requires the other remaining deposition parameters to be constant. Therefore, it is necessary to optimize the deposition conditions in detail to prevent film defects (e. g. pin holes, the deposition of large particles).

1.2 ZnO

1.2.1 General properties of zinc oxide

ZnO occurs naturally as a yellow to red coloured mineral zincite. Pure ZnO is a white powder due to its large band gap of 3.4 eV [61–64]. Crystalline ZnO is a thermochromic compound changing its colour from white to yellow when heated in air, during cooling the yellow colour of heated ZnO changes back to its initial state, white [65]. ZnO is practically insoluble in water but is soluble in most acids [66]. At the melting point, around 1975°C, ZnO decomposes into zinc (vapour) and oxygen; during carbothermic reaction, ZnO is converted into zinc vapour at lower temperature, around 950°C [62, 66]. The natural crystal structure of ZnO is hexagonal wurtzite structure [61, 67, 68] (Figure 1.3). At ambient conditions, it has the lattice constants a=b=0.33 nm and c=0.52 nm [67, 69]. ZnO exhibits a thermal expansion ($\alpha=4.3\cdot10^{-6}$ K^{-1} at standard conditions), meaning that the lattice parameters increase with the temperature [63, 70].

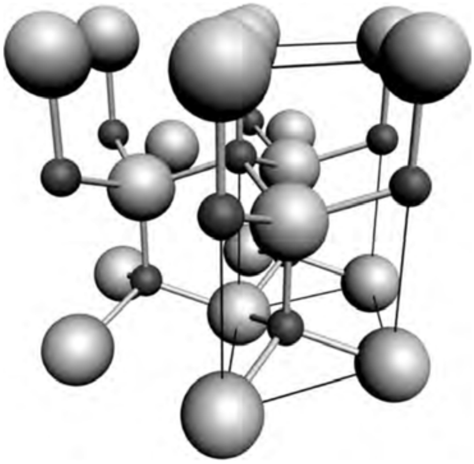

Figure 1.3. Illustration of natural crystal structure of ZnO is hexagonal wurtzite structure. Big light spheres represent zinc and small dark ones oxygen atoms [68].

Intrinsic ZnO (i-ZnO) is a semiconductor with relatively wide band gap (Eg=3.4 eV) at room temperature [61–64]. The transmittance of i-ZnO in the visible light region is ≤70% and the resistivity is ≥1 Ω·cm. The band gap, transmittance and the resistivity of ZnO can be tuned by altering the substrate temperature in deposition process and doping ZnO with suitable elements. Naturally, ZnO is a semiconductor with n-type conductivity (n-ZnO) due to the oxygen vacancies [63]. This means that the electron concentration is higher than the hole concentration in the material. To further increase the electron concentration in ZnO, the suitable substituents for Zn are group-III elements (Al, Ga and In) and for oxygen are group-VII elements (Cl and I) [61, 63, 67]. P-type doping occurs when hole concentration in the material is higher than the electron concentration. With ZnO, the sustainable p-type doping remains a challenge due to the low solubility of p-type dopants and the compensation of the p-type dopants by n-type impurities. However, the known p-type dopants are group-I elements (Li, Na, K) and Ag and Cu to substitute Zn, and group-V elements (N, P and As) for substituting oxygen [61, 63, 67].

1.2.2 ZnO thin films

In a solar cell structure, ZnO fits to several layers. ZnO can be a window or front contact if doped with suitable elements. In addition, ZnO is used as a buffer layer if pure [71] or another element (such as sulphur [72, 73]) is incorporated into the ZnO system.

ZnO thin films with different morphology (thin films or nanostructures) can be prepared by a number of physical and chemical methods. Physical method is classified as a process where no chemical reaction takes place and no by-products are formed when growing the desired layer. Some physical methods for the deposition of ZnO thin films are molecular beam epitaxy [74, 75], electron beam evaporation (EBE) [76, 77], sputtering [78–81], pulsed laser deposition [82, 83], ion beam deposition [84]. Chemical methods are processes where the desired layer is directly created from chemical reactions. Secondary products (in form of gases, liquids, or other solids) usually form along with the needed layer. Chemical methods can also be divided according to the phase of the source: gas phase methods (chemical vapour deposition (CVD) [85–88], atomic layer deposition (ALD) [80, 89, 90], etc.) or liquid source methods (chemical bath deposition (CBD) [91, 92], sol-gel [93, 94], chemical spray pyrolysis (CSP) [15, 38, 95], etc.).

As there are many methods to grow ZnO films, the properties of ZnO layers vary directly on the characteristics of deposition method. However, research groups working with solar cells and microelectronics where ZnO is a front electrode aim to obtain ZnO films with properties similar to transparent conductive oxide (TCO): as highly transparent and as conductive as possible. Compared to the most common TCO-s used currently (indium doped tin oxide, ITO, and fluorine doped tin oxide, FTO), high abundance, low toxicity, suitable band alignment and high chemical and thermal stabilities are a number of advantages characterising zinc oxide [24]. The optical transmittance and the resistivity of ZnO films grown with different deposition method are presented in Table 1.1. For comparison, currently used TCO-s have lowest resistivities of approximately $1–3\cdot10^{-4}$ Ω·cm [96–98].

Table 1.1. Examples of the optical transmittance and the resistivity of doped ZnO films grown on glass substrate with different deposition methods.

Deposition method	**Dopant**	**Optical transmittance**	**Resistivity**	**Reference**
EBE	Al	>85%	$2.5\cdot10^{-4}$ Ω·cm	[76]
Sputtering	Al	>90%	$1.5\cdot10^{-4}$ Ω·cm	[81]
CVD	Ga	90%	$3.6\cdot10^{-4}$ Ω·cm	[88]
ALD	Al	>80%	$4.4\cdot10^{-3}$ Ω·cm	[90]
CSP	In	>90%	10^{-3} Ω·cm	[38]

ZnO thin films are mainly grown on a soda-lime glass substrate. However, a future with bendable microelectronics and photovoltaics is intriguing and different types of flexible lightweight polymer substrates have emerged and are of interest [99–106]. Yet, depending on the used polymer, the polymer substrates have rougher surfaces and lower working temperature when compared to conventional glass substrates [105]. Some of the ZnO deposition methods onto a polymer substrate have been sputtering [99–101, 104–106], ion plating [102] and sol-gel [103]. During the recent years, the interest and the number of publications of ZnO films on flexible polymer substrates shows a rising trend. The growth of sputtered Al or Ga doped ZnO film on polymer substrate can be controlled if a buffer layer (e. g. Al, SiO_2 or ZnO) is used [104–106]. The lowest resistivity obtained for sputtered Al doped ZnO on polymer (polyethylene terephthalate, PET) substrate is $9\cdot10^{-4}$ Ω·cm [99].

The study of using ZnO as a buffer layer in a Cu(In,Ga)(S,Se)$_2$ (CIGSSe) absorber solar cell started already in 1996 [71]. Few years later, the ZnO buffer layer was substituted with ZnS in CIGSSe structure mainly due to its wider band gap of 3.8 eV [46, 107–109]. However, mixing ZnO and ZnS should create a buffer layer with more suitable band alignment for the CIGSSe solar cell than pure ZnO or ZnS alone [110, 111]. Zn(O,S) layers have been grown by CBD [112–115], ALD [72, 116–118] and sputtering [119–122].

1.2.3 ZnO thin films by CSP

The history of ZnO and doped ZnO thin films studies is long and immense. Furthermore, numbers of reports on ZnO and doped ZnO thin films grown on glass substrates by CSP have been published.

The sprayed ZnO thin film properties depend strongly on all the deposition parameters. One main parameter affecting the layer properties is the Zn source. Zinc acetate dihydrate, zinc acetylacetonate hydrate or zinc chloride is used as a Zn precursors to grow chemically sprayed ZnO thin films (APPENDIX B, Table 1). While the use of $ZnCl_2$ leads to structured ZnO morphology (such as the formation of hexagonal nanorods [32, 123]), the use of $Zn(C_2H_4O_2)_2{\cdot}2H_2O$ and $Zn(C_5H_7O_2)_2{\cdot}H_2O$ precursors lead to homogeneous film [15, 38]. Generally, the precursors are dissolved in either deionised water, alcohol or a mixture of them. With the use of zinc acetate dihydrate, acetic acid is added to the spray solution to inhibit the hydrolysis of Zn precursor. The substrate temperature varies from 350°C to 525°C, although there are reports with substrate temperature below 350°C [15, 124–127].

As it is relatively easy to create ZnO film with n-type conductivity, the main dopants are group-III elements (Al, Ga and In) to substitute Zn atoms and to create oxygen vacancies [35, 38, 42, 124, 126, 128–134]. Only a small number of studies report the substitution of O atoms with F, B, etc. [125, 127]. Dopant precursors are either chlorides, nitrates or other compounds that dissolve easily in the solvent and do not form persistent compounds with Zn precursor in the spray solution (APPENDIX B, Table 1). The dopant type determines the preferred growth orientation of crystallites. As the intrinsic ZnO crystallites grow along c-axis, the incorporation of In generally changes the preferred growth orientation to (101) plane parallel to the substrate [15, 38, 42, 128]. The incorporation of Al or Ga does not change the crystallite orientation growth preference of ZnO thin films [42, 125, 127, 132–134].

The transparency of spayed doped ZnO films is strongly affected by the substrate temperature and the dopant concentration. The dopant type is irrelevant as high transparencies are obtained with all dopants. The optimal temperature to spray doped ZnO with the highest transparency possible (85%–90% in the visible light region) is in the range of T=450°C to T=475°C [125, 127–131]. The dopant concentration also has an optimal region to spray doped ZnO films as transparent as possible. Increasing the dopant concentration in the spray solution up to an optimal value of 2–3 at.% decreases the characteristic haziness of intrinsic ZnO [14, 38]. Furthermore, the used solvent has an effect on the transparency of sprayed doped ZnO films. Films grown from mixed alcoholic solutions have slightly higher film transparency than films grown from aqueous solutions [128, 129]. This is due to the finer droplets of alcohol that lead to more homogeneous film.

The other characteristic property for TCO is conductivity (reciprocal value of resistivity). The deposition of doped ZnO films with as high conductivity or as low resistivity as possible is of interest in order to use doped ZnO as a front contact. Resistivities as low as $3\cdot10^{-3}$ $\Omega\cdot$cm are reported for sprayed ZnO films doped with In, Ga or B [127, 128, 132]. The resistivities for sprayed ZnO films doped with Al remain one order of magnitude higher possibly due to the fast oxidation of Al compared to other dopants [35, 42, 130]. The resistivities of doped ZnO films grown by CSP are slightly higher (inferior) than for films deposited with sputtering or other methods presented in Table 1.1.

Hence, the cheap and easy to operate spray pyrolysis is capable of depositing films that have nearly similar transmittance and conductivity as ZnO films deposited with more expensive and complicated processes or ITO and FTO that are currently used in solar cells as TCO-s.

As there are many deposition parameters affecting the transmittance and the resistivity of ZnO:In thin films, the substrate temperature is the primary one. In addition, one deposition parameter has been neglected. The effect of spray rate is an important deposition parameter affecting the final properties of ZnO:In thin film. Dedova et al. reported that the solution spray rate affects the morphological properties of ZnO thin films [135].

The research on using polymer substrates is a new trend in the scientific world which has found applications in many fields (such as thin film transistors, solar cells). However, there are no reports on the chemical spray pyrolysis deposition of ZnO and ZnO:In thin films on polymer substrates.

1.2.4 Zn(O,S) thin films

The ZnO film can also be used as a buffer layer in the solar cell structure if pure or another element is incorporated into ZnO lattice to substitute some O atoms. In Zn(O,S) layer, some of the oxygen atoms are substituted with sulphur ones. Zn(O,S) is used in the CIGSSe solar cell as a buffer layer due to its non-toxicity, effectiveness, and cost-efficiency and the abundance of materials compared to the conventional buffer layer of In_2S_3 or CdS. Using Zn(O,S) in CIGSSe type solar cell gives the possibility to omit the intrinsic ZnO window layer from the solar cell structure and therefore making the structure and the production of a final solar cell simpler and cheaper. In addition, using Zn(O,S) as a buffer layer should create more suitable interface between the absorber and the window layer in the CIGSSe solar cell [110, 111].

Furthermore, the solar cell efficiency can be increased when wider band gap buffer layer is used in the CIGSSe solar cell. The use of Zn(O,S) as a buffer layer allows to absorb more blue light compared to the conventional buffer layer of CdS [136, 137]. The optical band gap of ALD grown ZnO_x,S_{1-x} and CBD grown Zn(O,S) layer is 3.6 eV [118] of 3.8 eV [112], respectively. The slight variance in the band gap could be caused by the presence and the number of oxygen and hydroxides in the layer [112, 118]. It is reported that the S/(S+O) ratio influences the Zn(O,S) layers optical and structural properties [72, 118, 120, 121]. In addition, the optical band gap can be increased with the decrease in crystallite size [138]. For sputtered Zn(O,S) layer, the widest band gap of 3.6 eV is obtained when S/(S+O) ratio in the film is 1 [120, 121]. At the S/(S+O) ratio of 0.19 and 0.45 in the film, band gaps of 2.6 eV [120] and 2.8 eV [121] are characteristic for sputtered Zn(O,S) layers, respectively. These low band gap values are caused by the formation of $Zn(OH)_2$ that contaminates the Zn(O,S) layer [121]. In the $Zn(O_{1-x},S_x)$ film, an increase in the sulphur content from 0 to 1 follows the Vegard's law [139] resulting in the X-ray diffraction peaks distinctive to ZnS [120].

The production methods to grow Zn(O,S) layers are either time consuming or expensive (such as CBD [112–115], ALD [72, 116–118], sputtering [119–122, 140]). The highest efficiencies of CIGSSe solar cells with ALD deposited or sputtered Zn(O,S) buffer layer are similar, 18.5% and 18.3% respectively [117, 119]. The highest efficiency for CBD deposited Zn(O,S) buffered solar cell is 20.9% [141]. Here, a simple, cost-efficient and fast atmospheric pressure aerosol assisted chemical vapour deposition (AA-CVD) was used to grow Zn(O,S) layers. While the alternative buffers such as CdS [4, 142], ZnS [4, 142] and In_2S_3 [143] have been grown by AA-CVD, no studies on the AA-CVD grown Zn(O,S) layers have been published. The AA-CVD is a non-vacuum process where the deposition temperatures remain below 250°C [21] and the different solar cell layers can be grown in a continuous operation. If buffer layer in CIGSSe solar cell is grown by AA-CVD then it is possible to avoid breaking the vacuum for the scribing of P2 between sputtered intrinsic ZnO and n-ZnO. P2 is a second scribing step in monolithically integrated devices. Moreover, growing Zn(O,S) layers with AA-CVD gives great opportunity to grow intrinsic ZnO layer if needed. The deposition of i-ZnO layer with the AA-CVD technique begins simply by switching off the flow of H_2S after the deposition of Zn(O,S). Previous study conducted in Helmholtz-Zentrum Berlin (HZB), Germany, has shown that irrespective of the i-ZnO layers deposition method (sprayed or sputtered), the solar cell output parameters are similar [144].

1.3 Sb_2S_3

1.3.1 General properties of antimony(III)sulphide

The most common natural crystalline mineral for antimony trisulphide is stibnite [145]. The natural crystal structure of Sb_2S_3 is orthorhombic structure [146, 147] (Figure 1.4). At ambient conditions, the lattice constants for Sb_2S_3

are a=11.23 nm, b=11.31 nm and c=3.84 nm [69, 148]. The fresh Sb_2S_3 minerals occur as soft lead-grey needle-like crystals which during time turn black due to oxidation in ambient environment. The optical band gap of stoichiometric stibnite was determined in 1968 by Efstathiou and Levin to be 1.7 eV [149] which covers a high area of the solar spectrum in the visible and near infrared region. However, increasing the content of Sb in antimony trisulphide to the composition of $Sb_{2.28}S_3$ decreases the band gap to 1.6 eV [149]. The absorption coefficient of Sb_2S_3 is $\alpha=10^5$ cm^{-1} [150–152]. Sb_2S_3 is quick to oxidise, reacting actively with oxidising agents [153]. At the ambient environment and at the melting point of 546°C, the Sb_2S_3 forms oxysulphides [62, 154]. The boiling point for antimony trisulphide is approximately 1150°C [155]. Sb_2S_3 is insoluble in water but soluble in some acids, such as tartaric acid, oxalic acid, hydrochloric acid [62, 154, 156].

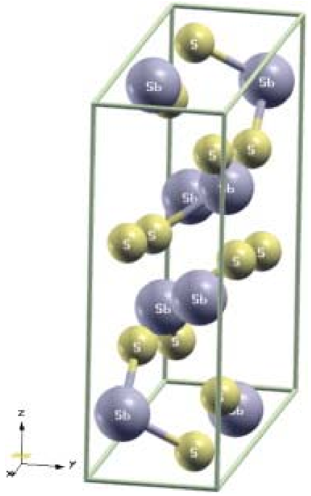

Figure 1.4. Illustration of natural crystal structure of antimony trisulphide is orthorhombic structure. Purple spheres represent antimony and yellow ones sulphur atoms [148].

Sb_2S_3 is a weak polar semiconducting ferroelectric but a good photoconductor [157, 158]. The electrical resistivity of antimony trisulphide is 10^4-10^7 $\Omega\cdot cm$ with n-type conductivity [147, 157]. The Sb_2S_3 semiconductor can be doped with appropriate elements to obtain n- or p-type conductivity. Studies where Ag, Sm, C, Sn have been used to dope Sb_2S_3 films have been published [159–162].

1.3.2 Sb_2S_3 thin films

In the extremely thin absorber (ETA) solar cell structure, Sb_2S_3 films can be used as an alternative absorber layer [151, 163–167]. The advantages of using Sb_2S_3 over $CuInS_2$ [168] as an absorber are the cost-effectiveness and the abundance of materials [151]. In addition, the optical band gap of 1.7 eV [149, 151, 169, 170] and high absorption coefficient of 10^5 cm^{-1} [150–152] suggest that this material could be suitable as an absorber. The ETA solar cell with CBD grown Sb_2S_3 as an absorber showed solar conversion efficiency of 3.37% [165] and adding an organic hole conductor to the solar cell increases the efficiency up to 8.5% [164, 167, 171]. For comparison, the ETA solar cell with sprayed $CuInS_2$ absorber layer has an efficiency of 3.0% [27]. In 2007, Manolache and Duta published an article where they stated that Sb_2S_3 can also be used as a buffer layer in 3D solar cell [163]. In 2010, Kieven et al. [172] concluded that theoretically Sb_2S_3 may be suitable buffer layer in CIGSSe solar call however the test devices showed poor photovoltaic performance attributed to the voltage dependent photocurrent collection. In this dissertation, Sb_2S_3 films grown by CSP are studied as a potential candidate for absorber layer in ETA solar cells. Sb_2S_3 films have been grown by various methods like CBD [165, 167, 169, 171, 173–175], successive ionic layer adsorption and reaction [147], electrodeposition [176], sputtering [151], vacuum thermal evaporation [152, 177–179], CSP [178, 180–184].

The most common method to grow Sb_2S_3 films is CBD. The as-deposited CBD grown Sb_2S_3 films require post-treatment for the growth of Sb_2S_3 crystals [169]. The optical transmittance of the post-treated Sb_2S_3 film (in N_2 at 300°C or 350°C) is approximately 35% in the visible light region and the band gap varies from 1.7 eV to 2.2 eV depending on the deposition temperature and time [165, 169, 174]. Desai and Lokhande [185] used $SbCl_3{:}9H_2O$ and tartrate complexed thioacetamide as antimony and sulphide source, respectively, and tartaric acid as complexing agent in chemical bath deposition solution. They obtained microcrystalline film with optical band gap of 1.87 eV [185].

Using sputtering as a deposition method results in amorphous as-deposited Sb_2S_3 films and crystalline Sb_2S_3 films were obtained after annealing in sulphur vapour at 400°C [151]. The absorption coefficients for amorphous and crystalline films are $1.8 \cdot 10^5$ cm^{-1} and $7.5 \cdot 10^4$ cm^{-1}, respectively [151]. The optical band gaps for the amorphous and crystalline Sb_2S_3 films are 2.2 eV and 1.7 eV, respectively [151].

With the vacuum thermal evaporation method, the original Sb_2S_3 material is thermally evaporated in vacuum [152, 177–179]. However, the layer on the substrates surface is amorphous and even after heat treatment crystalline film cannot be detected [152, 177]. According to Aousgi et al. [152], the thermally evaporated amorphous Sb_2S_3 layers with optical parameters (E_g=1.8–2.1 eV and absorption coefficient of 10^4 cm^{-1} to 10^5 cm^{-1}) are potential absorber materials in solar cells.

1.3.3 Sb_2S_3 thin films by CSP

The research of chemically sprayed Sb_2S_3 thin films started in the mid of 1990's with the first publication published by Bhosale et al. [183]. Bhosale et al. [183] used antimony trichloride and thioacetamide precursors with the Sb:S molar ratio of 2:3 in the spray solution. In addition, oxalic acid was added to the solution to retard the sulphide precipitation by forming a strong complex with antimony [183]. Based on this publication, other research groups started to grow Sb_2S_3 thin films on glass substrates by chemical spray pyrolysis. However, the reports on successfully CSP grown Sb_2S_3 layers are doubtable as the recipe for growing Sb_2S_3 thin films by CSP is taken from CBD recipe containing complexing agent [163, 183, 185, 186].

As the antimony precursor, antimony(III)acetate [163] or antimony trichloride [170, 178, 180–185, 187–191] have been used and the sulphur precursors have been thiourea [163, 170, 180, 181, 187–190], thioacetamide [178, 182–184] and sodium thiosulphate [191] (APPENDIX B, Table 2). The molar ratio of antimony to sulphur precursors in the spray solution is mainly kept at 2:3. If antimony precursor is dissolved in aqueous solvent then HCl or complexing agent is added to the solvent to inhibit the formation of precipitate in the solution [163, 184]. The presence of complexing agent is not necessary in the case of non-aqueous solvent (such as acetic acid) [170, 180, 182, 187]. In the case of growing Sb_2S_3 films from aqueous solutions by chemical spray pyrolysis, tartaric acid is often selected as a complexing agent [181, 182, 184]. The substrate temperature of chemically sprayed Sb_2S_3 thin films is in the region of 250°C–300°C.

A well-distinguished difference is observed for chemically sprayed Sb_2S_3 films when various solvents are being used. The use of glacial acetic acid leads to crystallite films while the use of aqueous solvents tends to lead amorphous thin films with some exceptions [181, 182]. According to Rajpure and Bhosale [182], annealing the sprayed Sb_2S_3 films in N_2 at 325°C does not make the films crystalline. The optical band gap of sprayed Sb_2S_3 thin film varies from 1.56 eV to 2.13 eV for crystalline films depending on the deposition parameters (APPENDIX B, Table 2) [163, 170, 180–182, 187, 191]. The optical band gap range for amorphous Sb_2S_3 thin films is 1.10 eV–2.70 eV [181–184]. The room temperature resistivity of Sb_2S_3 films is in the order of 10^6–10^8 $\Omega\cdot$cm. A resistivity of 10 $\Omega\cdot$cm is published by Bhosale et al. [183]. This is believed to be a typing error as in that publication on Figure 4 it can be read that resistivity is approximately in the order of 10^6 $\Omega\cdot$cm [183]. Only Gadakh et al. [181] reported the elemental composition of the Sb_2S_3 film, 38% of Sb and 62% of S.

1.4 Summary of the literature overview and the aim of study

The easy and low price deposition process decreases the cost of a final desired product. Thus, the use of cost-effective, efficient and simple deposition processes is of high importance. Chemical spray pyrolysis and aerosol-assisted chemical vapour deposition techniques are aerosol based deposition methods that are simple yet efficient processes. However, the deposition parameters have to be optimized according to the deposition process and the properties of the specified films that can be used in desired devices.

The studies reported and presented in the literature can be summarized as follows:

1. Adding III group dopants (such as In) into ZnO thin film increases the n-type conductivity and the transmittance of the ZnO layer. Amongst many possible applications of ZnO, the improved conductivity and transmittance make doped ZnO a potential candidate to substitute currently used front contacts (ITO and FTO) in the microelectronics and in the solar cell structure. While the lowest reported resistivity is obtain for sputtered doped ZnO, other deposition methods are suitable to grow doped ZnO thin films as well if deposition parameters are optimised.
2. The precursors, dopants and their concentration in the spray solution along with solvents and the substrate temperature are well studied in the field of chemically sprayed doped ZnO thin films. The substrate temperature is the most important deposition parameter influencing the final layer properties. Yet, the significance of spray rate has been neglected and practically no reports on the effect of this deposition parameter on the film properties have been published.
3. The future of microelectronics and photovoltaics thrives for lightweight and flexibility. Thus, the growth of ZnO and indium doped ZnO on polymer substrate is of interest. No studies on the growth of ZnO:In layers on polymer substrates by chemical spray pyrolysis have been published.
4. ZnO and ZnS have been used as an alternative buffer layer in chalcopyrite solar cell instead of commonly used In_2S_3 and CdS. Using Zn(O,S) that acts as a window and a buffer layer in solar cell enables to simplify the solar cell structure by omitting the window layer. In addition, Zn(O,S) can be used as a substitute buffer layer that should provide better band alignment with the CIGSSe absorber layer than ZnO or ZnS alone. Zn(O,S) has been successfully grown by ALD, CBD and sputtering, yet no publications on AA-CVD grown Zn(O,S) and its application in solar cell has been reported.
5. In the ETA solar cell structure, the cost-effective and abundant Sb_2S_3 can be used as an alternative absorber. Sb_2S_3 has a band gap of 1.7 eV and an absorption coefficient of 10^5 cm^{-1} being suitable for an absorber. CBD grown Sb_2S_3 has been tested in solar cell leading to efficiency of 8.5% compared to sprayed $CuInS_2$ absorber based solar cell with efficiency of 3.0%. The spray solution recipe to grow Sb_2S_3 films by CSP from aqueous solutions contains a complexing agent (taken from CBD). The growth of chemically sprayed Sb_2S_3 film and the effect of spray solution composition are sparsely studied. The study on the effect of deposition temperature is inconsistent and the Sb_2S_3 thin film elemental composition is practically unstudied.

Based on the summary of the literature overview, the aims of this thesis were:

1. to grow ZnO:In thin films by CSP on glass substrates and to study the structural, morphological, optical, electrical properties of sprayed films depending on substrate temperature and solution spray rate to determine optimal deposition conditions for the growth of conductive ZnO:In thin films;
2. to grow ZnO:In thin films by CSP on polymer substrates and to determine the deposition parameters that control the growth and the structural, morphological, optical, electrical properties of ZnO:In films;
3. to grow Zn(O,S) layers on Mo substrate by AA-CVD as a potential buffer layer in $Cu(In,Ga)(S,Se)_2$ solar cell and to study effects of reactive gas and carrier gas flow rate on the structural, morphological and optical properties of deposited layers; to use Zn(O,S) as a buffer layer in CIGSSe solar cell;
4. to grow Sb_2S_3 thin films by CSP as a potential absorber layer from antimony trichloride and thiourea as Sb and S sources, respectively, and to study the morphological, optical properties and the elemental and phase composition of sprayed films depending on the spray solution composition (aqueous solution with different concentration of tartaric acid as complexing agent and alcohol solution with no additive) and the substrate temperature.

2 EXPERIMENTAL

2.1 Deposition of ZnO:In films by CSP

Indium doped ZnO thin films were grown by pneumatic chemical spray pyrolysis (set-up depicted in Figure 1.1) on profoundly cleaned and preheated soda-lime glass (25x25x1 mm^3) [**I**, **II**] and polyimide substrates (1x25x0.15 mm^3) [**III**] in Tallinn University of Technology (TUT). The spray solution contained 0.2 M $Zn(CH_3COO)_2 \cdot 2H_2O$ (Merck, analytical, 99.5%) dissolved in deionised water and isopropyl alcohol mixture (2:3 by volume). To prevent the zinc precursor hydrolysis, few drops of CH_3COOH was added to spray solution. $InCl_3$ was used as a doping source and was added to spray solution with $[In^{3+}]/[Zn^{2+}]$ ratio of 3 at.%. The nebulised spray solution was transported to the substrates placed on molten tin bath by air with flow rate of 8 L/min. In the case of glass substrates, the substrate temperature and the solution spray rate varied from 350°C to 500°C and from 0.5 mL/min to 7.1 mL/min, respectively. To grow films on glass substrates with similar thicknesses at low solution spray rates (spray rate <1.5 mL/min), 150 mL of spray solution was used instead of 100 mL of spray solution.

The successful growth of ZnO:In films on polyimide substrate requires an adherent ZnO seed layer on top of the substrate [**III**]. ZnO seed layer was grown from 50 mL (designated as type A) or 30 mL of spray solution (designated as type B). ZnO:In layer was grown from 50 mL of spray solution. The substrate temperature for polyimide substrate was 380°C and the spray rate varied from 2 mL/min to 3 mL/min. It was verified that spray rate did not affect the substrate temperature on either substrate types (glass and polyimide).

2.2 Deposition of Zn(O,S) layers by AA-CVD

Aerosol assisted chemical vapour deposition (set-up depicted in Figure 1.2) was used to grow Zn(O,S) layers on properly cleaned and preheated Mo coated soda-lime glass substrates (25x25 mm^2) [**IV**] in Helmholtz-Zentrum Berlin (HZB), Germany. Zinc precursor solution consisted of 10 mM $Zn(C_5H_7O_2)_2 \cdot H_2O$ (Alfa Aesar, ≥98%) dissolved in ethanol (abs., ≥99.8%). Ultrasonic atomiser (at 1.7 MHz) nebulised the precursor solution into an aerosol and was carried towards preheated substrate by the laminar flow of N_2 at a precise angle of 45°. The N_2 flow rate was either 5 L/min or 7 L/min. Reactant gas H_2S (5% of H_2S in Ar), as a sulphur source, was introduced to the aerosol stream near the substrate. The reactant gas flow rate was varied from 0 mL/min to 20 mL/min. All the Zn(O,S) layers were grown at substrate temperature of 225°C for 30 minutes.

2.3 Deposition of Sb_2S_3 films by CSP

The chemically sprayed Sb_2S_3 films were grown on profoundly cleaned and preheated soda-lime glass substrates (25x25x1 mm^3) [**V**] in Tallinn University of Technology. The precursor solution contained 2 mM $SbCl_3$ (Sigma Aldrich,

≥99.0%, puriss) and 6 mM $CS(NH_2)_2$ (Merck, >98%, for synthesis) as antimony and sulphur precursors, respectively, dissolved in 50 mL of deionised H_2O [**V**]. To prevent the precipitation of antimony hydroxide, $C_4H_6O_6$ (tartaric acid (TA), VWR International, 99.7%) used as an complexing agent was added to the spray solution to obtain Sb:S:TA molar ratios of 1:3:10 [181, 184] and 1:3:1. The spray solution (spray rate ca. 1.5 mL/min) was nebulised to onto preheated soda-lime glass substrates place on molten tin bath. The substrate temperature was varied from 205°C to 355°C. Sb_2S_3 film grown with Sb:S:TA of 1:3:10 at 205°C was annealed at 400°C in air for 30 minutes.

2.4 Characterisation of ZnO:In films and Sb_2S_3 films, and Zn(O,S) layers

The methods and the apparatuses used to characterise ZnO:In and Sb_2S_3 thin films carried out in TUT, Estonia, are presented in Table 2.1. The methods and the apparatuses used to characterise Zn(O,S) layers in HZB, Germany, are presented in Table 2.2.

Table 2.1. Methods used to characterise ZnO:In and Sb_2S_3 thin films in TUT.

Properties	Characterisation method	Apparatus	Ref.
phase composition, crystallite orientation, crystallite size	XRD	Rigaku Ultima IV	[**I**], [**II**], [**III**], [**V**]
surface morphology + cross-sectional images, surface coverage, grain size (evaluation), surface roughness	SEM	Zeiss EVO-MA15 Zeiss HR FESEM Ultra 55	[**II**], [**III**] [**V**]
	AFM	NT-MDT Solver 47 Pro	[**II**]
elemental composition	EDX	Röntec EDX XFlash 3001 detector and an Oxford Instruments Inca Energy System	[**II**] [**V**]
optical transmittance, reflectance, absorbance, band gaps	UV-VIS spectroscopy	Jasco V-670	[**I**], [**II**], [**III**], [**V**]
resistivity, charge carrier mobility, charge carrier concentration	Van der Pauw and Hall measurements	MMR's Variable Temperature Hall System equipped with Hall/Van der Pauw Controller H-50	[**I**], [**II**], [**III**]
functional groups	FTIR	Perkin-Elmer GX1 spectrophotometer	[**V**]
thermal stability	TG/DTG/DTA	Set-Sys-Evolution	[**V**]

Table 2.2. Methods used to characterise Zn(O,S) layers in HZB.

Properties	Characterisation method	Apparatus	Ref.
surface morphology	SEM	Gemini LEO1530	[**IV**]
elemental composition	EDX		[**IV**]
phase composition	XRD	Bruker D8	[**IV**]
total transmittance, total reflectance	UV-VIS spectroscopy	Cary 500	[**IV**]

2.5 Preparation and characterisation of Zn(O,S) buffered solar cells

Zn(O,S) layers [**IV**] were grown by AA-CVD on glass/Mo/Cu(In,Ga),$(S,Se)_2$ substrates (2.5x2.5 cm^2) provided by BOSCH Solar CISTech GmbH (Germany) and cleaned by ethanol. Thereupon, r. f. sputtered intrinsic ZnO (i-ZnO) was grown on 50% of the prepared solar cells. Next, aluminium doped ZnO (AZO) was sputtered on all of the solar cells. Lastly, Ni/Al grid was deposited onto solar cells to enhance the collection. Thus, Zn(O,S) layers were implemented in two solar cell structures:

1. structure: glass/Mo/CIGSSe/Zn(O,S)/AZO/
2. structure: glass/Mo/CIGSSe/Zn(O,S)/i-ZnO/AZO/

CBD grown CdS and ILGAR sprayed In_2S_3 buffered solar cells were used as references.

The output parameters (Voc, Jsc, FF and η) of 8 solar cells per sample with total area of 0.5 cm^2 per cell were tested under standard test conditions (25°C, 100 mW/cm^2, AM1.5G) by home assembled class A sun simulator and external quantum efficiency apparatus.

3 RESULTS AND DISCUSSION

The following paragraphs contain the studies and characterisations of chemically sprayed ZnO:In and Sb_2S_3 thin films, and aerosol assisted chemical vapour deposition of Zn(O,S) layers and its application in solar cell. The results have been published in Articles [**I**], [**II**], [**III**], [**IV**] and [**V**].

3.1 ZnO:In thin films on glass substrate by CSP

This section is based on Articles [**I**] and [**II**] which focus on the deposition and the characterisation of ZnO:In thin films on glass and on polymer substrates. In addition, in Appendix A, Article [**I**], the presented temperatures are tin bath temperatures being 50°C higher than the substrate temperatures presented here.

3.1.1. Determination of substrate temperature to grow ZnO:In films

Irrespective of the substrate temperature, the ZnO:In thin films grown by chemical spray pyrolysis are of zincite (PDF no. 01-079-0208) [192], according to the XRD study (Figure 3.1). The preferred orientation of the crystallites of ZnO:In thin films grown at 350°C (not shown) and 400°C is (101) plane parallel to the substrate (Figure 3.1). The preferred orientation of ZnO:In crystallites is in accordance with the data presented in the literature [15, 38, 42, 128]. With an increase in substrate temperature to 450°C, the intensities of (100) and (110) reflections increase while the reflection of the peak (101) decreases and the ZnO:In crystallites are preferably orientated parallel to the (110) plane.

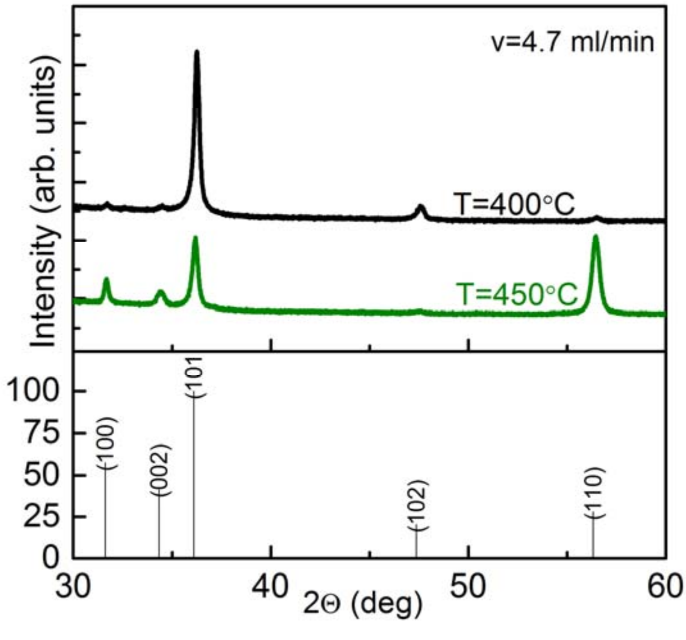

*Figure 3.1. XRD patterns of sprayed ZnO:In films deposited at 400°C and 450°C from 100 mL of solution with spray rate of 4.7 mL/min and ZnO powder diffractogram. [**I**]*

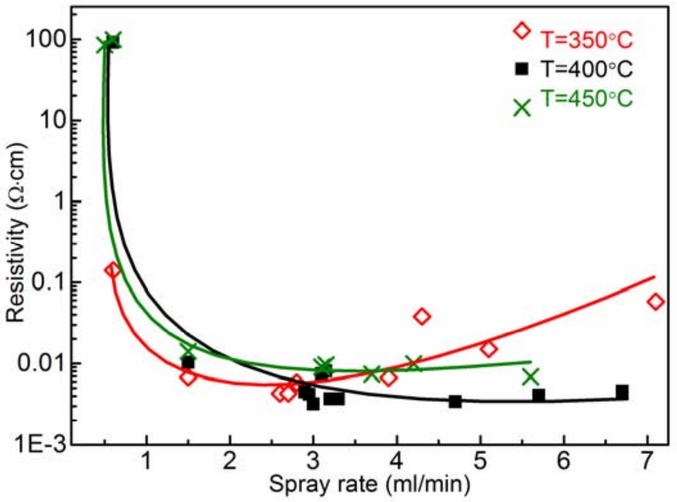

*Figure 3.2. The resistivities of ZnO:In films deposited at different temperatures from 100 mL of solution with various spray rates. [**I**]*

ZnO:In thin films were grown by CSP at substrate temperature of 350°C–450°C with solution spray rates of 0.5 mL/min to 7.1 mL/min (Figure 3.2). Independent of the substrate temperature, the highest resistivities (≥0.1 **Ω**·cm) are obtained for ZnO:In thin films with spray rates of 0.5 mL/min. An increase in spray rate from 0.5 mL/min to 3 mL/min decreases the resistivity to $3 \cdot 10^{-3}$ Ω·cm for film grown at 400°C (Figure 3.2). The resistivity of ZnO:In films grown at 350°C has a rising trend when increasing the spray rate from 3.0 mL/min to 7.1 mL/min. The tendencies between resistivities and spray rates are similar for films grown at 400°C and 450°C, although the films grown at higher temperature are less conductive (Figure 3.2). Thus, 400°C was chosen as a substrate temperature to grow ZnO:In thin films on glass substrates by chemical spray pyrolysis.

3.1.2. The effect of spray rate on the structural and morphological properties of ZnO:In films

The XRD study showed that all ZnO:In thin films were of zincite (PDF no. 01-079-0208) independent of the spray rate (figure presented in Appendix A, Article [**II**] as Figure 1) and the preferred crystallite orientation of ZnO:In thin films is (101) plane parallel to the substrate. However, the spray rate affects the crystallite size (Table 3.1). Crystallites with average size of 20 nm are obtained when spray rate is lower than 3 mL/min, respectively. Spray rate higher than 3 mL/min leads to crystallites with an average size of 35 nm.

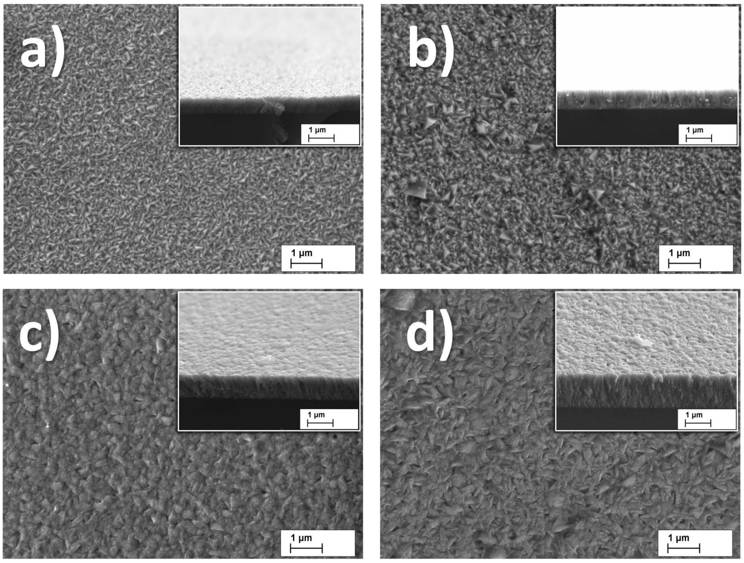

*Figure 3.3. SEM images of ZnO:In thin films grown at 400°C from 100 mL of spray solution at solution spray rates of (a) 0.5 mL/min, (b) 1.5 mL/min, (c) 3.3 mL/min and (d) 6.7 mL/min. The cross-sectional views are presented as insets on the surface images. [**II**]*

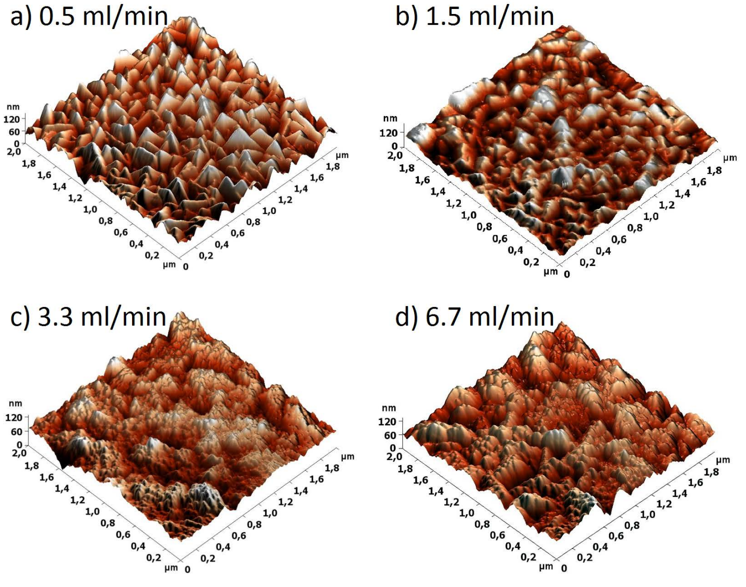

*Figure 3.4. AFM 3D images of ZnO:In films grown at 400°C from 100 mL of spray solution with solution flow rates of (a) 0.5 mL/min, (b) 1.5 mL/min, (c) 3.3 mL/min and (d) 6.7 mL/min. AFM images are of a 2x2 μm^2 area. [**II**]*

The microstructural study of ZnO:In thin films by SEM and AFM revealed that the ZnO:In films grown at 400°C have dense inner structure with a relatively smooth and homogeneous surface (Figure 3.3) with no pinholes and cracks. In addition, increasing the spray rate increases the average estimated grain size (Table 3.1). The well-shaped (with sharp edges and tip) prismatic or pyramidal grains in ZnO:In thin film grown with spray rate of 0.5 mL/min have equable size of ca. 100 nm (Figure 3.3a, Figure 3.4a). Increasing the spray rate to 1.5 mL/min causes the softening of grain edges and tip making the grains rounder (Figure 3.3b, Figure 3.4b). In addition, the grain size is irregular varying from 50 nm to 500 nm. Increase in spray rate up to 3.3 mL/min and above, leads to film with a network of interweaving grains resembling canvas or burlap (Figure 3.3c and d, Figure 3.4c and d). The grains with the average size of ca. 250 nm are covered with a fine-grain structure composed of small particles (diameter of ca. 40 nm) forming a double-layer surface. Interestingly, the root mean square (RMS) roughness is not affected by the spray rate being ca. 20 nm for all the films. The similar RMS roughness is also reported by Dedova et al. [135] for chemically sprayed ZnO:In films where the ZnO:In film also consisted of pyramidal grains.

3.1.3. The effect of spray rate on the electrical properties of ZnO:In films

The resistivity, carrier concentration and mobility of ZnO:In thin films is greatly influenced by solution spray rate and are presented in Figure 3.5. The highest resistivity of $6.3 \cdot 10^{-2}$ Ω·cm is achieved with spray rate of 0.5 mL/min. An increase in spray rate to 3.3 mL/min decreases the resistivity as low as $3.7 \cdot 10^{-3}$ Ω·cm. The carrier concentration and mobility increase from $2.3 \cdot 10^{19}$ $\mathrm{cm^{-3}}$ to $1.1 \cdot 10^{20}$ $\mathrm{cm^{-3}}$ and 4.4 $\mathrm{cm^2/V \cdot s}$ to 16 $\mathrm{cm^2/V \cdot s}$, respectively. The increase in carrier mobility can be attributed to the increasing grain size from 100 nm to 250 nm as indicated by AFM (Figure 3.4 and Table 3.1). This hypothesis is also supported by the positive correlation between carrier concentration and mobility (presented in Appendix A, Article [**II**] as Figure 5) observed in the ZnO:In films where the conduction mechanism is driven by grain boundary scattering. The analogous relation has been reported for ZnO:Al thin films grown by pulsed lased deposition (PLD) [193]. The use of spray rates above 3.3 mL/min has no significant effect on the ZnO:In films electrical properties. The carrier concentrations are around 10^{20} $\mathrm{cm^{-3}}$ and mobilities are in the range of 12–16 $\mathrm{cm^2/V \cdot s}$. Similar carrier concentration and mobility values have been also reported for ZnO:In thin films with 3 at.% of In in spray solution grown on glass at 370°C by ultrasonic spray [194].

The use of spray rates lower than 1.5 mL/min leads to ZnO:In thin films with carrier mobilities below 8 $\mathrm{cm^2/V \cdot s}$. The low mobility is commonly attributed to the thinner film and smaller crystallites and grains [126]. To minimise the thickness difference, ZnO:In thin films with spray rates of 0.5 mL/min and 1.5 mL/min were grown from 150 mL of spray solution. Films grown at 0.5 mL/min and 1.5 mL/min from 150 mL of spray solution had comparable thicknesses and grain sizes to films grown at spray rates higher than 3 mL/min from 100 mL of spray solution (Table 3.1). The correlation between spray solution amount and grain size is known [42, 195, 196]. The well-shaped prismatic grains in ZnO:In thin film grown with spray rate of 0.5 mL/min and the softened grain edges and tip for film grown with spray rate of 1.5 mL/min (Figure 3.3a, Figure 3.3b, respectively) are characteristic to ZnO:In thin films irrespective of the spray solution amount (SEM images of ZnO:In film grown from 150 mL of spray solution presented in Appendix A, Article [**II**] as Figure 6). The carrier mobilities increased from 4.4 cm^2/V·s and 7.7 cm^2/V·s to 9.2 cm^2/V·s and 11 cm^2/V·s for films grown at 0.5 mL/min and 1.5 mL/min, respectively. Although the carrier mobilities in films increased, these mobility values remain lower compared to the mobilities of ZnO:In films grown with spray rate of 3 mL/min and above regardless of the comparable thickness (Table 3.1). The lower carrier mobility of thicker films could be due to the wide grain size distribution (75–700 nm,) compared to the one for films grown at 3.3 mL/min (200–300 nm). Grain sizes were estimated from SEM images that are presented in Appendix A, Article [**II**] as Figure 6 and in Figure 3.3c, respectively.

*Table 3.1. The effect of the solution spray rate on the sprayed ZnO:In film thickness (t) according to SEM, crystallite size (d) according to XRD, grain size (D) according to AFM, electrical resistivity (ρ), main carrier mobility (μ) and concentration (n), and optical band gap (Eg). The films were grown at 400°C on soda-lime glass substrate except for layer designated with * where borosilicate glass was used.*

Spray rate, mL/min	V, ml	t, nm	d, nm	D, nm	ρ, Ω·cm	μ, cm^2/V·s	n, cm^{-3}	Eg, eV
0.5	100	700	22	115	$63\cdot10^{-3}$	4.4	$2.3\cdot10^{19}$	3.28
0.5	150	1400	26	250	$33\cdot10^{-3}$	9.2	$2.1\cdot10^{19}$	3.24
0.5*	150	1350	26	n. s.	$78\cdot10^{-3}$	3.9	$2.0\cdot10^{19}$	3.24
1.5	100	900	21	120	$12\cdot10^{-3}$	7.7	$6.9\cdot10^{19}$	3.31
1.5	150	1400	29	250	$7.3\cdot10^{-3}$	11	$7.6\cdot10^{19}$	3.27
3.3	100	1100	34	250	$3.7\cdot10^{-3}$	16	$1.1\cdot10^{20}$	3.34
4.7	100	1100	35	250	$3.2\cdot10^{-3}$	15	$1.4\cdot10^{20}$	3.36
6.7	100	1350	36	250	$4.6\cdot10^{-3}$	12	$1.2\cdot10^{20}$	3.32

n. s. – not studied

The carrier concentration is affected by the spray rate (Table 3.1). The carrier concentration in films grown with spray rate of 0.5 mL/min is ca. 10 times lower than in films grown with spray rates above 3.3 mL/min (ca. $2\cdot10^{19}$ cm^{-3} and $2\cdot10^{20}$ cm^{-3}, respectively). An extra experiment showed that lowering the spray rate from 0.5 mL/min to 0.35 mL/min decreased the carrier concentration to $6\cdot10^{18}$ cm^{-3} without diminishing the film thickness. Additional studies were performed to determine why the carrier concentration decreases with decreasing the spray rate.

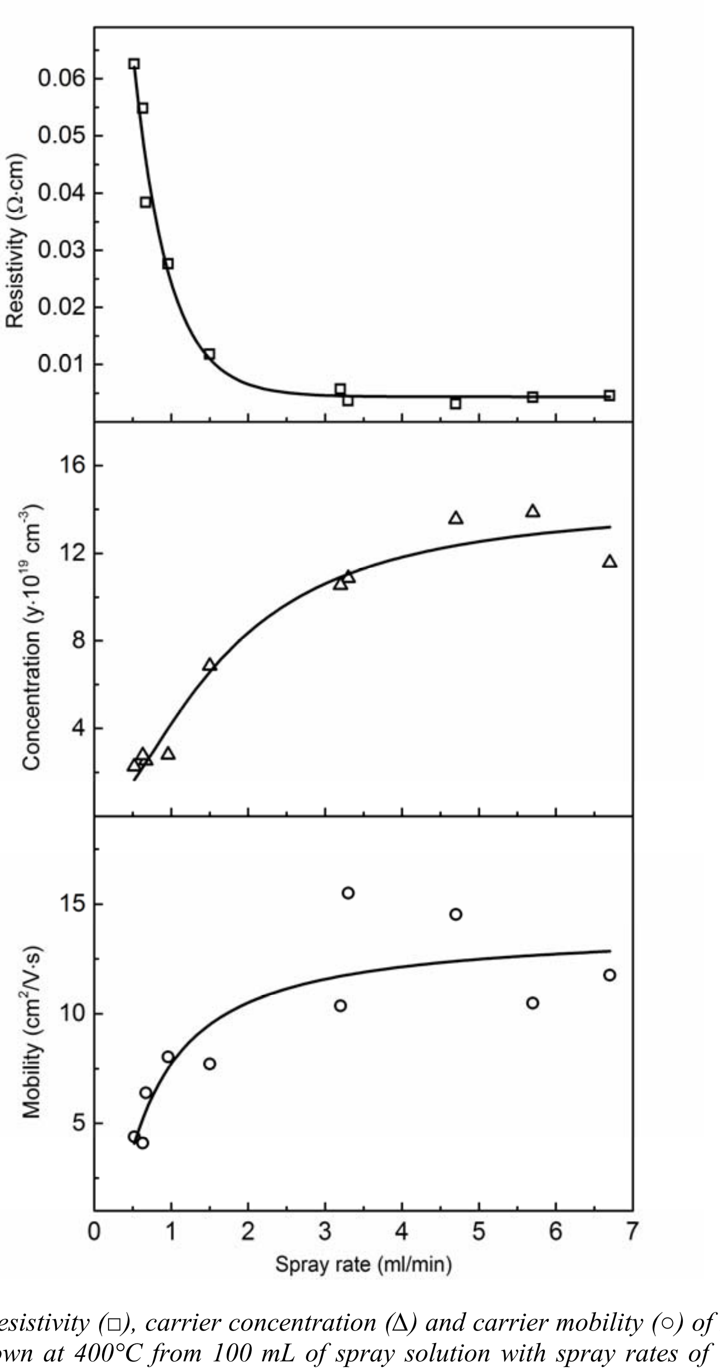

*Figure 3.5. Resistivity (□), carrier concentration (Δ) and carrier mobility (○) of ZnO:In thin films grown at 400°C from 100 mL of spray solution with spray rates of 0.5–6.7 mL/min. [**II**]*

Firstly, the relatively high vapour pressure of $InCl_3$ (ca. 1.0 k Pa at 400°C [197]) could be the reason for the poor integration of the additive. However, the EDX study confirmed that independent of the spray rate, there is no loss or the loss of the dopant source is similar in all the grown films (Table 3.2).

Table 3.2. Elemental composition (in at.%) of ZnO:In thin films grown at 400°C with solution spray rates of 0.5 mL/min and 3.2 mL/min according to EDX.

Spray rate, mL/min	Zn	O	In
0.5	43.4	54.4	2.2
3.2	43.3	54.7	2.0

Secondly, according to the literature, the diffusion of Na from soda-lime substrate to the ZnO film at 400°C during long spray deposition process [198] could be the reason for the low electron concentration. A ZnO:In film grown on borosilicate substrate with thickness of ca. 1350 nm had resistivity of $7.8 \cdot 10^{-2}$ $\Omega \cdot$cm, carrier mobility of 3.9 $cm^2/V \cdot s$ and concentration of $2 \cdot 10^{19}$ cm^{-3} (Table 3.1). As the carrier concentrations of the ZnO:In thin films are similar independent of the substrate, the lower carrier concentration in thin films grown at lower spray rates is not induced by the diffusion of sodium.

Lastly, the remaining reason for the lower carrier concentration in films grown at lower spray rates could be the oxidation of the dopant during spray process and therefore the failure to integrate In into the ZnO lattice.

3.1.4. The effect of spray rate on the optical properties of ZnO:In films

The specular transmittance of ZnO:In thin films grown at 400°C at various spray rates in the visible light region is above 75% (Figure 3.6). However, the transmittance of ZnO:In thin films in the near infrared (NIR) region is dependent on the spray rate: the lower the spray rate, the higher the transmittance in the NIR region. The decrease in transmittance in the NIR region corresponds to the increase in carrier concentration in thin films grown at higher spray rates (Table 3.1). The decrease in the NIR region transmittance of TCO films is caused by free carrier absorption [131, 199, 200]. This tendency is also reported for ILGAR [131] and PLD [199] grown conductive ZnO thin films with carrier concentrations of $3 \cdot 10^{20}$ cm^{-3} and $6 \cdot 10^{20}$ cm^{-3}, respectively.

The optical band gaps were determined form the transmittance spectra. Commonly used equation was used to determine the band gap values

$$\alpha h\upsilon = A \cdot (h\upsilon - Eg)^{\frac{1}{n}} \tag{1}$$

The members of the equation are explained in Appendix A, Article [**II**] as is shown the determination of band gap form the $(\alpha h\upsilon)^2$ versus $h\upsilon$ plot (in Article [**II**] as Figure 8). The obtained band gap values are given in Table 3.1. An increase in the spray rate from 0.5 mL/min to 4.7 mL/min increases the ZnO:In thin film band gap from 3.24 eV to 3.36 eV, respectively. The increased band gap is compatible with the carrier concentration increment and can be explained by the Burstein-Moss effect. The association between increasing band gap and the carrier concentration is also noted for PLD grown ZnO:Ga [200] and ultrasonically sprayed ZnO:In thin films [194].

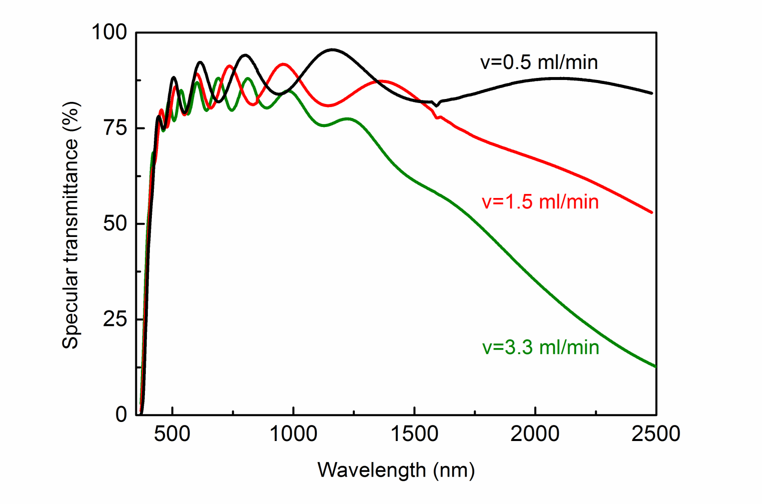

*Figure 3.6. Specular transmittance spectra of ZnO:In thin films deposited from 100 mL of spray solution at spray rates of 0.5 mL/min, 1.5 mL/min and 3.3 mL/min. [**II**]*

To summarise this section, the optimum substrate temperature to grow the most conductive ZnO:In thin films by chemical spray pyrolysis was determined to be 400°C. A commonly neglected deposition parameter spray rate affects the properties of ZnO:In thin films. With spray rate below 3 mL/min, the crystallites in the ZnO:In film are ca. 20 nm and the films are composed of sharp-edged prismatic grains. The use of spray rates higher than 3 mL/min leads to crystallite sizes of ca. 35 nm and to a network of interweaving grains with softened edges. Growing ZnO:In thin films at 400°C with spray rate of 3 mL/min and above leads to films with ρ of 3–4·10^{-3} Ω·cm, μ of ca. 15 $cm^2/V \cdot s$ and n of ca. 1.2·10^{20} cm^{-3}. At spray rates 3 mL/min and below, the sprayed ZnO:In films are of low conductivity (ρ of 10^{-1} Ω·cm and above). At the same time, the carrier mobility and concentration are below 10 $cm^2/V \cdot s$ and 3·10^{19} cm^{-3}, respectively. The low carrier mobility is probably caused by the oxidation of dopant. The optical transmittance of ca. 80% is characteristic of ZnO:In thin film. The optical band gap of a film increases with the conductivity of ZnO:In thin film reaching up to 3.36 eV.

3.2 ZnO:In films on polymer substrate by CSP

The search for lightweight and flexible substrates in various fields and also in the photovoltaics has led to the use of polymer substrates that fulfil those requirements. Due to the inferior temperature tolerance of polymer compared to glass substrates, substrate temperature of 380°C was used to grow ZnO and ZnO:In thin films on polymer substrate. This section, the study of CSP grown ZnO:In films on polymer substrate, is based on Article [**III**].

3.2.1 Structural properties of chemically sprayed ZnO:In layers

Independent of the solution volume and spray rate, the deposition of ZnO films on the polymer substrate leads to well adhered films which were smooth and crack free under visual examination. However, independent of the deposition parameters, ZnO:In thin films peeled off the substrate posterior to the deposition due to the cracking of the film.

A buffer layer of chemically sprayed ZnO was used for the successful growth the ZnO:In layer on the polymer substrate. The X-ray diffractograms of sprayed ZnO and ZnO/ZnO:In bilayers on polyimide and glass substrate grown at 380°C are presented in Appendix A, Article [**III**] as Figure 1 and Figure 2, respectively. Irrespective of the used substrate, the ZnO thin film is of zincite (PDF no. 01-079-0208), according to the XRD study [192]. On polymer, the $I_{(100)}/I_{(101)}$ intensity ratio of ZnO film is ca. 4.0 implying that the crystallites of the buffer layer are orientated in (100) plane parallel to the substrate (Appendix A, Article [**III**] as Figure 1). On glass substrate, the ZnO film is c-axis orientated (Appendix A, Article [**III**] as Figure 2) which correlates with the literature [15, 35, 38, 125, 127, 135, 201]. However, the $I_{(100)}/I_{(101)}$ intensity ratio for the ZnO powder reference is 0.56 [192]. The $I_{(100)}/I_{(101)}$ intensity ratio for ZnO:In layer is ca. 2.6 being slightly lower than the respective ratio in the buffer layer. On the glass substrate, the intensities of (100) and (101) plane reflections, the most intense powder reference reflections, increase with the growth of ZnO:In layer (Appendix A, Article [**III**] as Figure 2). Thus, independent of the used substrate and the crystallite orientation in the ZnO buffer layer, the ZnO:In crystallites have no preferential growth orientation compared to the powder reference. This does not coincide with the literature where the preferred crystallite orientation of ZnO:In grown on glass is (101) plane parallel to the substrate [15, 38, 42, 128]. The reason of different growth orientation of ZnO:In crystallites on glass and on ZnO buffer will be discussed in section 3.2.2.

3.2.2 Morphological and optical properties of chemically sprayed ZnO:In layers

The ZnO buffer layer grown on polyimide from 50 mL of spray solution (type A) exhibit leaf-like grains with size of ca. 2 µm on a relatively smooth surface (Figure 3.7a). A decrease in spray solution volume to 30 mL (type B) decreases the size and the number of leaf-like grains (Figure 3.7c). The formation and the morphology of ZnO/ZnO:In bilayer is strongly affected by the morphology of the buffer layer according to SEM images. The flat area of the bilayer resembles canvas. The leaf-like grains in ZnO buffer layer act as growth centres to grow large grains in the bilayer. The large ZnO:In grains have a diameter of ca. 3 µm and resemble scrolled belts (Figure 3.7b). The density of the grains in the

ZnO:In layer (scrolled belts) follows the grain density in the buffer layer. The formation of these scrolled belts could explain why ZnO:In layer has no preferential crystallite orientation as shown by XRD in section 3.2.1. With type A buffer layer, a decrease in spray rate to 2 mL/min increases the size number and the size of the leaf-like grains in the buffer layer and leads to the formation of ZnO:In scrolled belts with size of ca. 6 μm.

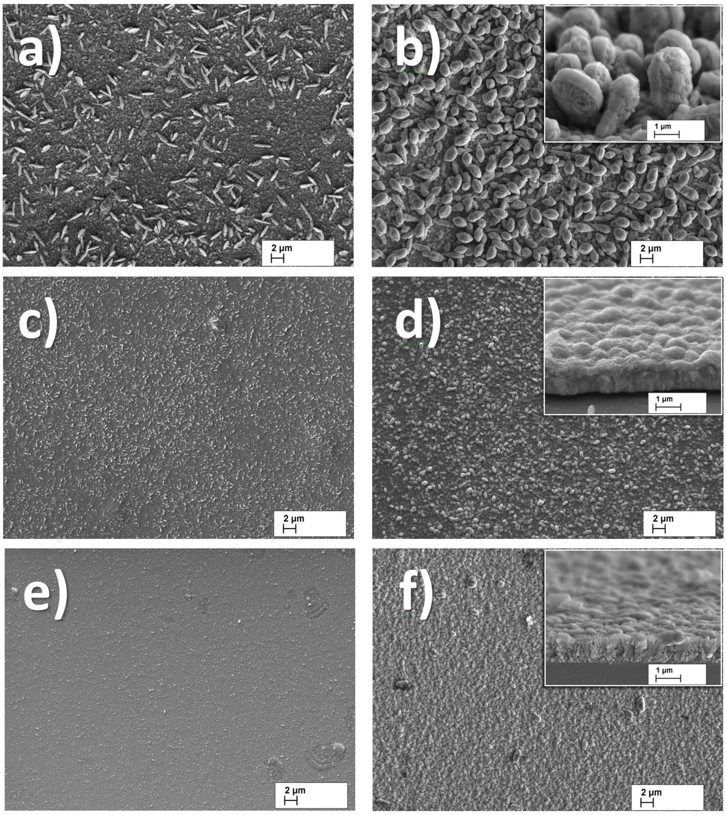

*Figure 3.7. SEM image of (a) type A ZnO buffer layer and (b) the corresponding ZnO/ZnO:In bilayer grown on PI substrate. SEM images of (c) ZnO buffer layer of type B and (d) ZnO/ZnO:In bilayer grown on PI substrate; and of (e) ZnO buffer layer type B and (f) ZnO/ZnO:In bilayer grown on glass. The films were grown at 380°C with spray rate of 3 mL/min. The corresponding SEM cross-sectional images of bilayers are presented as insets. [**III**]*

The formation of the scrolled belts is discussed in Article [**III**] in chapter 3.2 (Appendix A). The mechanism suggested by Li et al. [202] does not describe the formation of scrolled belts. However Z. L. Wang proposed a theory on the polarity of ZnO:In layer surface which could be a possible reason for the formation of scrolled belts during chemical spray pyrolysis. According to Wang [203], the polar dominated belt acts as a capacitor where two parallel charged plates tend to roll over to form an enclosed ring and therefore reduce the electrostatic energy.

Interestingly, the ZnO/ZnO:In bilayer grown on glass surface is also composed of canvas resembling scrolled belts (Figure 3.7f), although the morphology of ZnO/ZnO:In bilayer on glass substrate is smoother than that on a polyimide substrate (Figure 3.7e). The existence of the scrolled belt on the bilayer surface implies that independent of the substrate the scrolled belts are of ZnO:In. The morphology of ZnO/ZnO:In bilayer on glass substrate is smoother than that on a polyimide substrate.

The total reflectance of spectra of ZnO/ZnO:In bilayers on polyimide substrate are similar in the spectral region of 400–1500 nm, irrespective of the buffer layer type, showing reflectance of 8%–19% (Appendix A, Article [**III**] as Figure 5a and b). However, the average reflectance of ZnO/ZnO:In bilayer and ZnO:In single layer grown on glass decrease from ca. 15% to ca. 10% at 400 nm to 1500 nm, respectively (Appendix A, Article [**III**] as Figure 5c and d, respectively). The interference visible in the ZnO:In single layer and implicit in all the bilayers spectra is explained by higher granular structure of bilayers.

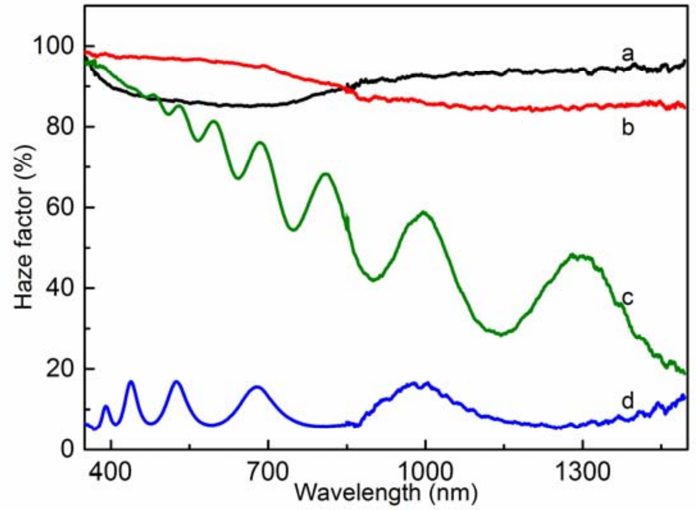

Figure 3.8. Haze factor spectra of (a) ZnO/ZnO:In bilayers on PI using type A and (b) type B buffer layer, (c) bilayer on glass substrate using buffer layer of type B and (d) ZnO:In film on glass substrate. All the layers were grown at 380 °C, ZnO:In layer from 50 mL of spray solution. SEM images of bilayers with total reflectance spectra a, b and c are shown in Figure 3.7b, d and f, respectively; SEM image of ZnO:In layer on glass with haze spectrum d is presented in [135]. ***[III]***

The interferences presence in the haze factor spectra indicates the relative smoothness and uniform thickness of the films grown on glass substrates (Figure 3.8, curves c and d). This interference is originated from the total reflectance's specular component. Haze factor is a measure of light scattering within the material calculated by the ratio of diffuse and total transmittance or reflectance, in this study, by reflectance:

$$Haze = 100\% \cdot \frac{R_{dif}}{R_{total}} \qquad (2)$$

The bilayers grown on polyimide however lack the interference in the haze factor spectra (Figure 3.8, curves a and b) referring to the granular structure and high surface roughness of the layers as was visible in corresponding SEM images (Figure 3.7 curves b and d). The type A buffered ZnO/ZnO:In bilayer grown on polyimide substrate scatter light ca. 85% and 95% in the visible spectrum part and in the wavelength range of 800–1500 nm, respectively, as can be seen in Figure 3.8a. The highest light scattering occurs when the incident wavelength resembles the grains dimension where the light reflects [204]. Therefore, the higher haze factor in the wavelength range of 800–1500 nm could be due to the higher number of grains with size of 800–1500 nm. On contrast, the type B buffered bilayer shows haze factor of 95% and 85% in the visible part of spectrum and in the wavelength range of 800–1500 nm, respectively, as can be seen in Figure 3.8b. Hence, more light is scattered from grains with size of 300–700 nm.

The light scattering of type B buffered ZnO/ZnO:In bilayer grown on glass decreases rapidly from 95% at 350 nm to 20% at 1500 nm (Figure 3.8). This indicates the high number of fine-scale grains which scatter light. Relatively low haze factor is registered for the single ZnO:In film on glass substrate – ca. 10% in the spectral region of 350–1500 nm (Figure 3.8d). The reported haze factor of sputtered ZnO:Al thin films at the visible part of the spectrum is 5% [205].

3.2.3 Electrical properties of chemically sprayed ZnO:In layers

Growing type B buffered bilayers on polyimide substrate leads to resistivity of $4.4 \cdot 10^{-2}$ Ω·cm (presented in Table 3.3) being similar to that reported for r. f. sputtered ZnO:Al on polymer substrate [206]. Interestingly, the bilayers grown on glass substrate have resistivity of $6.7 \cdot 10^{-3}$ Ω·cm. Independent of the substrate type, the carrier concentration in the ZnO/ZnO:In bilayers are comparable at $7 \cdot 10^{19}$ to $9 \cdot 10^{19}$ cm^{-3}. The carrier mobility in the layer grown on polyimide and glass is 1.5 cm^2/V·s and 13 cm^2/V·s, respectively. This variation in mobility could be explained by thicker homogeneous ZnO:In film grown on glass compared to that grown on polyimide substrate (Table 3.3). This assumption correlates with the results published by Fortunato et al. [105] for sputtered ZnO:Ga where the carrier mobility increases with layer thickness. In addition, the low mobility in ZnO:In film grown on polyimide could be also due to the heterogeneous surface of the ZnO:In film on polymer substrate as the canvas-like structure is more apparent on polymer substrate than on glass (Figure 3.7).

The thickness of single ZnO:In layer grown on glass is 1400 nm being 2.3 times thicker than the bilayer grown on the polyimide substrate (Table 3.3). The resistivity of the single ZnO:In layer grown on glass is $3.2 \cdot 10^{-3}$ Ω·cm being ca. 10 times lower than that of a bilayer grown on polyimide due to the 10 times higher carrier mobility of 15 $cm^2/V \cdot s$. Thus, much thicker ZnO:In layers with lower surface roughness should be grown to obtain conductive chemically sprayed ZnO:In films on polyimide substrate.

Table 3.3. Electrical properties and thicknesses of the sprayed ZnO:In layers grown onto ZnO buffer layer B at 380°C. The corresponding SEM images of bilayers grown on polyimide (PI/ZnO/ZnO:In) and soda-lime glass (SLG/ZnO/ZnO:In) are presented on Figure 3.7. For reference, ZnO:In single layer (SLG/ZnO:In) on glass is presented.

Structure	ZnO:In film thickness, nm	ρ, Ωcm	n, cm^{-3}	μ, $cm^2/V \cdot s$
PI/ZnO/ZnO:In	300	$4.4 \cdot 10^{-2}$	$9.3 \cdot 10^{19}$	1.5
SLG/ZnO/ZnO:In	600	$6.7 \cdot 10^{-3}$	$7.0 \cdot 10^{19}$	13
SLG/ZnO:In	1400	$3.2 \cdot 10^{-3}$	$1.4 \cdot 10^{20}$	15

In summary, the successful growth of ZnO:In thin films on polymer substrate by chemical spray pyrolysis requires the use of a ZnO buffer layer on top of the polymer. The morphology of the buffer layer dictates the morphology of the ZnO:In layer. A smooth buffer layer surface leads to relatively smooth ZnO:In layer. Higher amount of spray solution roughens the surface of buffer layer and leads to the formation of ZnO:In scrolled belts. The bilayers with scrolled belts have high light scattering capability, ca. 90% of the light in the spectral region of 350–1500 nm is scattered. For smooth bilayers, the light scattering decreases from 95% to 20% in spectral region from 350 nm to 1500 nm, respectively. Resistivity of $4.4 \cdot 10^{-2}$ $\Omega \cdot$cm, carrier mobility of 1.5 $cm^2/V \cdot s$ and carrier concentration ca. 10^{20} cm^{-3} are characteristic to smooth ZnO/ZnO:In bilayer on polymer substrate. The bilayer grown on glass substrate has lower resistivity of $6.7 \cdot 10^{-3}$ $\Omega \cdot$cm mainly due to higher carrier mobility of 13 $cm^2/V \cdot s$. The lower carrier mobility of bilayer grown on polymer substrate may be due to the thinner and more heterogeneous ZnO:In layer.

3.3 Zn(O,S) layers by aerosol assisted chemical vapour deposition and their application in CIGSSe solar cell

The study of aerosol assisted chemical vapour deposition of Zn(O,S) layers and its application in ETA solar cell was carried out in Helmholtz-Zentrum Berlin, Germany. This section, AA-CVD grown Zn(O,S) and its application in solar cell, is based on Article [**IV**].

3.3.1 Characterisation of Zn(O,S) layer

The Zn(O,S) layer surface morphology is affected by the flow rate and the concentration of H_2S, purging gas. An increase in the purging gas flow rate from 2 mL/min to 10 mL/min increases the size and number of particles (with maximum diameter of ca. 1 µm) on compact Zn(O,S) layer (Figure 3.9a and c, respectively). The particles on top of Zn(O,S) layer could be ZnS as the increasing number and size of the particles on the Zn(O,S) surface increases with the purging gas flow rate. The film thickness for film grown with the H_2S

flow rate of 2 mL/min and 3 mL/min is 55 nm and 45 nm, respectively. Based on the SEM images, relatively compact Zn(O,S) layers can be grown when following deposition parameters are used: M_{Zn}=10 mM, T=225°C, deposition time=30 minutes, $N_{2,\ flow\ rate}$=5 L/min and $H_2S_{flow\ rate}$=2 mL/min (**recipe 1**) (Figure 3.9a).

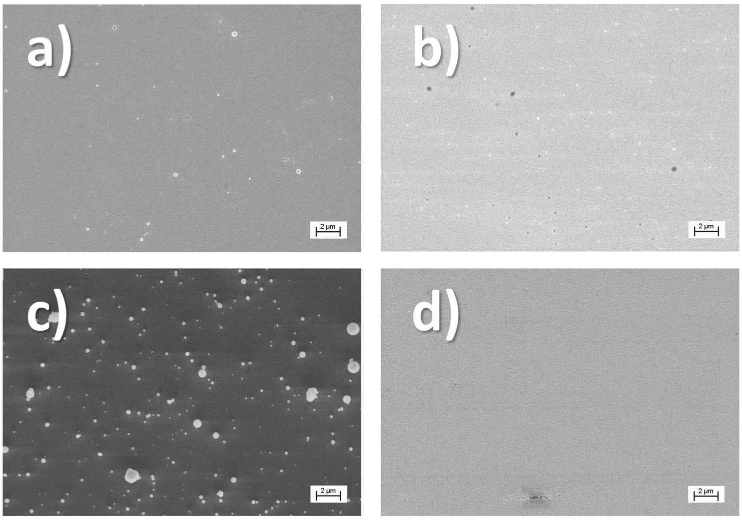

Figure 3.9. SEM images of Zn(O,S) layers on gl/Mo substrates deposited at 225°C according to ***recipe 1*** *(N_2 flow rate is 5 L/min) with varied H_2S flow rate of 2 (a) mL/min, (b) 3 mL/min and (c) 5 mL/min and (d) Zn(O,S) layer grown at 225°C according to* ***recipe 2*** *with N_2 and H_2S flow rate of 7 L/min and 5 mL/min, respectively. [**IV**]*

The EDX study (measured from 9 different regions) showed that the O/(S+O) ratio in the Zn(O,S) layer is ca. 16%. According to XRD, all Zn(O,S) layers were crystalline and the peaks in the Zn(O,S) layer resemble hexagonal ZnS (PDF no. 01-075-1534) rather than hexagonal ZnO (PDF no. 01-079-0208) (Appendix A, Article [**IV**] as Figure 3) [192]. The XRD study results conform to the results obtained by EDX.

The optical properties of the Zn(O,S) layers were studied for Zn(O,S) layer grown on quartz substrate. In the visible region of the spectrum, the optical transmittance, reflectance and absorbance of Zn(O,S) layers are ca. 70%, ca. 20% and ca. 10%, respectively (figure presented in Appendix A, Article [**IV**] as Figure 4a). The direct band gap of 3.6 eV (determined from the Tauc plot presented in Appendix A, Article [**IV**] as Figure 4b) is slightly higher than that reported for ALD grown Zn(O,S). The ALD grown Zn(O,S) band gap varies from 2.9 eV to 3.58 eV when sulphur content in the layer is increased [72, 118].

Fischer et al. [21] proved that an increase in the carrier gas flow rate decreases the aerosols residence time over the substrate. Therefore, an increase in N_2 flow rate from 5 L/min to 7 L/min is compensated with the increase in

H_2S flow rate from 2 mL/min to 5 mL/min (**recipe 2**) to grow compact Zn(O,S) layers while other deposition parameters were unaltered. The surface morphologies of Zn(O,S) layers grown according to **recipe 1** and **recipe 2** are similar (Figure 3.9a and d, respectively). However, the use of **recipe 2** leads to a slightly thicker film (60 nm) which is caused by the extra aerosol transferred to the heated substrate compared to **recipe 1** (55 nm and less).

3.3.2 Zn(O,S) based solar cell characteristics

Two Zn(O,S) buffered solar cell structures were tested:

1. **Structure 1**: glass/Mo/CIGSSe/Zn(O,S)/AZO
2. **Structure 2**: glass/Mo/CIGSSe/Zn(O,S)/i-ZnO/AZO

The Zn(O,S) layer was grown according to **recipe 1**. It is visible from the solar cell output parameters (Voc, Jsc, FF and η) presented in Figure 3.10 that the use of r. f. sputtered i-ZnO in the solar cell structure leads to lower deviation from the mean value (**structure 2**). The high deviation for **structure 1** is probably caused by the higher risk of shunts if the less conductive layer, intrinsic ZnO, is excluded from the structure. According to Grabitz et al. [207] the i-ZnO inhibits the areas with low-performance from dominating the devices open circuit voltage.

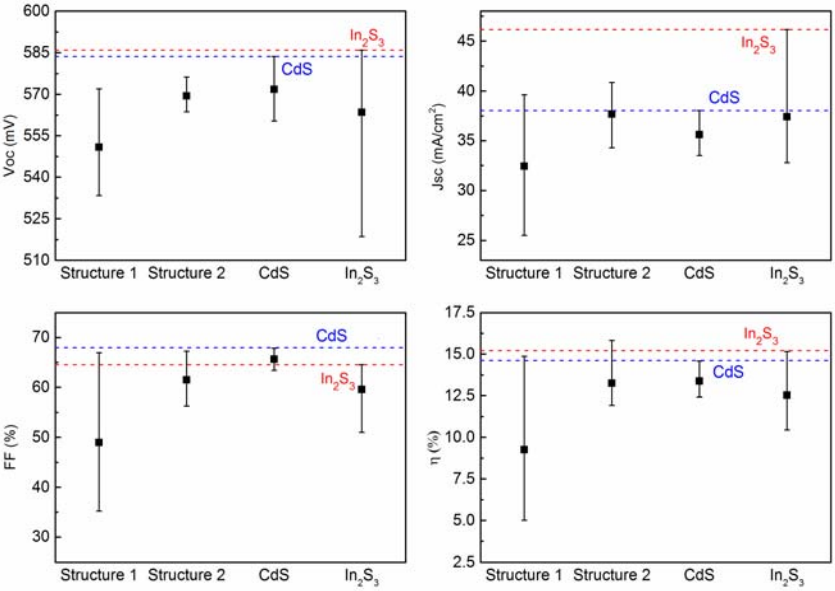

Figure 3.10. Zn(O,S) buffered solar cell output parameter variances (16 solar cells, area of 0.5 cm^2 per cell) and CdS or In_2S_3 buffered solar cells (16 reference cells). ***Structure 1*** *is glass/Mo/CIGSSe/AA-CVD-Zn(O,S)/AZO/Ni/Al and* ***structure 2*** *is glass/Mo/CIGSSe/AA-CVD-Zn(O,S)/i-ZnO/AZO/Ni/Al. The Zn(O,S) buffer layer was deposited according to* ***recipe 1*** *for 30 min. For comparison, the output parameter variances of CdS and In_2S_3 buffered cells are given. [**IV**]*

However, the best solar cell output parameters for **structure 1** and **structure 2** are comparable to each other and to the CdS and In_2S_3 buffered solar cells (Figure 3.10 and Table 3.4). The buffer layer thicknesses in the solar cell are ca. 60 nm for Zn(O,S), ca. 40 nm for CdS and ca. 20 nm for In_2S_3. The best output parameters for Zn(O,S) buffered solar cell are: Voc=573 mV, Jsc=39.2 mA/cm^2, FF=68.4% and η=15.4% (Figure 3.10 and Table 3.4). The output parameters for ALD grown Zn(O,S) buffered solar cell are: Voc=684 mV, Jsc=32 mA/cm^2, FF=73% and η=16% [116]. The higher output parameters for ALD grown Zn(O,S) buffered solar cells are possibly due to higher homogeneity of Zn(O,S) layer.

Decreasing the Zn(O,S) layer deposition time from 30 minutes to 20 minutes increases the Voc and FF slightly, therefore increasing the efficiency of a solar cell (Table 3.4). Yet, Voc is ca. 10 mV lower than that of a reference cell (Table 3.4). The efficiencies of solar cells with Zn(O,S) buffer grown for 20 minutes are comparable with the efficiencies of reference (CdS and In_2S_3 buffered) solar cells, 15.4%, 14.6% and 15.2%, respectively (Table 3.4).

*Table 3.4. The best output parameters for Zn(O,S) buffered solar cells (**structure 1**) with Zn(O,S) grown according to **recipe 1** and **recipe 2** with deposition times of 20 minutes and 30 minutes. The best output parameters of CdS and In_2S_3 buffered cells are given for comparison.*

	Deposition time, min	Voc, mV	Jsc, mA/cm^2	FF, %	η, %
Recipe 1 (N_2 of 5 L/min, H_2S of 2 mL/min)	20	573	39.2	68.4	15.4
	30	572	38.8	66.9	14.9
Recipe 2 (N_2 of 7 L/min, H_2S of 5 mL/min)	20	562	36.9	52.3	10.9
	30	577	38.3	56.8	12.5
In_2S_3 reference	n. a.	582	40.4	64.5	15.2
CdS reference	n. a.	584	36.8	67.9	14.6

n. a. – not available

For **recipe 2** grown Zn(O,S) layer, all the solar cell output values are inferior compared to the values of **recipe 1** grown and buffered solar cell (Table 3.4). The main cause for the different output parameters of Zn(O,S) buffered solar cell originates from the fill factor. Concluding from the data presented in Table 3.4, the best Zn(O,S) buffered solar cell efficiency is obtained according to **recipe 1** at decreased process time and therefore cost.

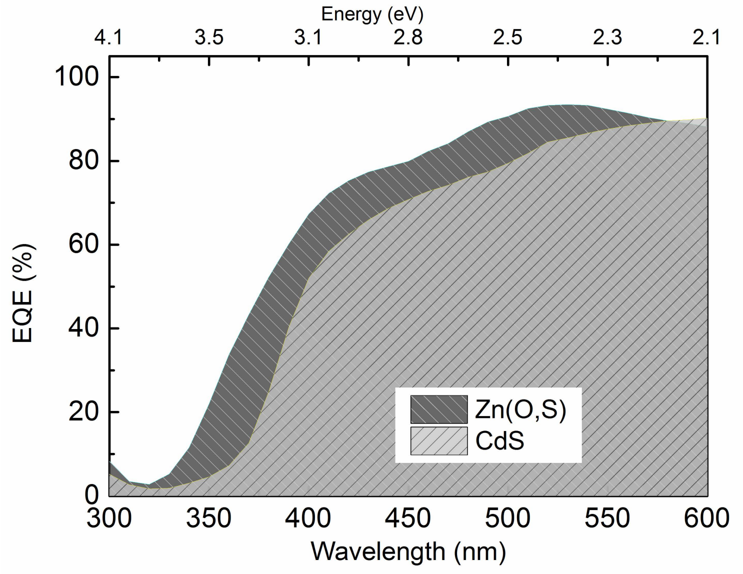

Figure 3.11. EQE spectra of CIGSSe/Zn(O,S)/AZO and CIGSSe/CdS/i-ZnO/AZO solar cell structures. The Zn(O,S) was deposited according to ***recipe 1*** *for 30 minutes. [**IV**]*

The spectra of external quantum efficiency of Zn(O,S) (**structure 1**, Zn(O,S) layer grown for 30 minutes according to **recipe 1**) and CdS buffered cells are shown in Figure 3.11. The thicknesses of CdS and Zn(O,S) buffer layers in the corresponding solar cells are ca. 40 nm and ca. 60 nm, respectively. The corresponding band gaps are 2.4 eV and 3.6 eV, respectively. It is visible that for Zn(O,S) buffered solar cell, 20% of EQE is already obtained at 345 nm while CdS buffered solar cell reaches 20% at 375 nm. Thus, the use of higher band gap Zn(O,S) layer instead of CdS as a buffer in solar cell results in higher integral quantum efficiency.

To summarise, compact and smooth Zn(O,S) layers can be grown on Mo substrates by aerosol assisted chemical vapour deposition method at 225°C if carrier gas and reactant gas flow rates are 5 L/min and 2mL/min, respectively. An increase in reactant gas flow rate results in powdery Zn(O,S) films. According to XRD, the Zn(O,S) film resembles more ZnS than ZnO. This is confirmed by EDX, as the O/(O+S) ratio in the Zn(O,S) layers is ca. 16%. In the visible range of the spectrum the transmittance of Zn(O,S) layer is ca. 70% and the band gap is ca. 3.6 eV. The best output parameters of Zn(O,S) buffered solar cell are Voc=573 mV, Jsc=39.2 mA/cm^2, FF=68.4% and η=15.4% being comparable to the CdS and In_2S_3 buffered reference solar cells.

3.4 Sb_2S_3 thin films by chemical spray

3.4.1 The growth of Sb_2S_3 films at various substrate temperatures from aqueous solutions containing tartaric acid

Based on the literature overview, the aqueous spray solution consisting of trichloride, thiourea and complexing agent such as tartaric acid (Sb:S:TA) with molar ratios of 1:3:10 is chosen to chemically spray Sb_2S_3 films [181, 184].

The Sb_2S_3 film grown at substrate temperature of 205°C is almost amorphous while the peaks on the diffractogram of Sb_2S_3 film grown at 230°C belong to the orthorhombic stibnite (Sb_2S_3) (PDF no. 01-075-4013) [192] (figure presented in Appendix A, Article [**V**] as Figure 1) with crystallite size of 20 nm (calculated from (201) peak). Annealing the Sb_2S_3 film grown at 205°C in air at 400°C for 30 minutes (designated as annealed film) increases the crystallinity of the as-deposited amorphous film (crystallite size of 13 nm). Rajpure et al. [180] reported that annealing the sprayed Sb_2S_3 films in N_2 environment at 200°C increases the films crystallinity and the grain size. However, an unidentified peak occurs at 2Θ of 23.5° in the annealed film (Appendix A, Article [**V**] as Figure 1). The new phase could be oxidized antimony as the annealing takes place in the air. The presence of Sb_2O_3 has been proven also in CBD grown Sb_2S_3 film which was annealed in the N_2 environment at 300°C and cooled in air [165].

The optical band gap of 2.2 eV is characteristic to Sb_2S_3 film sprayed at 205°C with Sb:S:TA molar ratio of 1:3:10 (Table 3.5). An increase in substrate temperature to 230°C decreased the optical band gap to 2.1 eV. The similar Sb_2S_3 film band gap of 2.1 eV was obtained by Gadakh and Bhosale [181]. In addition, Gadakh and Bhosale reported that a decrease in complexing agent concentration in the spray solution from 1 M to 0.4 M decreased the optical band gap of Sb_2S_3 films to 1.9 eV [181].

Table 3.5. Mean film thickness (t), mean crystallite size of Sb_2S_3 (D), elemental composition and Eg of sprayed films with Sb:S:TA molar ratios of 1:3:10 grown at substrate temperature (T) of 205°C and 1:3:1 grown at T of 205°C, 255°C, 305°C and 355°C, according to SEM, XRD, EDX and band gap obtained from optical measurements, respectively.

Sb:S:TA	T, °C	t, nm	D, nm	Elemental composition, at.%							Eg, eV
				Sb	S	C	O	Cl	Na	Si	
1:3:10	205	1430	52	5	5	52	32	<1	2	4	2.2
1:3:1	205	510	25	12	15	15	36	<1	4	17	2.3
	255	470	24	6	6	11	48	<1	6	22	2.1
	305	340	22	7	7	19	44	<1	6	17	2.2
	355	390	15	10	4	18	53	<1	3	11	2.5

According to EDX study, none of the sprayed films have the stoichiometry corresponding to Sb_2S_3 (Table 3.5). Curiously, Gadakh and Bhosale [181] presented a study where the elemental composition of sprayed Sb_2S_3 films was 38 at.% of Sb and 62 at.% of S for films grown from similar spray solution at 260°C. Here however, unclean Sb_2S_3 films were grown as all the deposited Sb_2S_3 films, including the annealed film, contained extremely high amount of organic residues. The typical Sb_2S_3 film elemental composition with Sb:S:TA=1:3:10 in the spray solution is given in Table 3.5. The high amount of organic residues in the Sb_2S_3 film is mainly probably originated from organic complexing compound, tartaric acid. As the spray solution also contains thiourea, the organic residuals in Sb_2S_3 films grown at 205°C could also originate from that [208–210]. It is possible that the poor crystallisation of Sb_2S_3 films is caused by the high amount of organic residuals in the film. The origin of secondary phases is discussed in section 3.4.2.

Due to the high amount of organic residuals in the Sb_2S_3 film grown with Sb:S:TA molar ratio of 1:3:10, a lower concentration of tartaric acid was used to grow Sb_2S_3 thin film. The minimum amount of TA required in the spray solution to inhibit the Sb precursor hydrolysis, determined experimentally by observation, was Sb:S:TA ratio of 1:3:1 in spray solution.

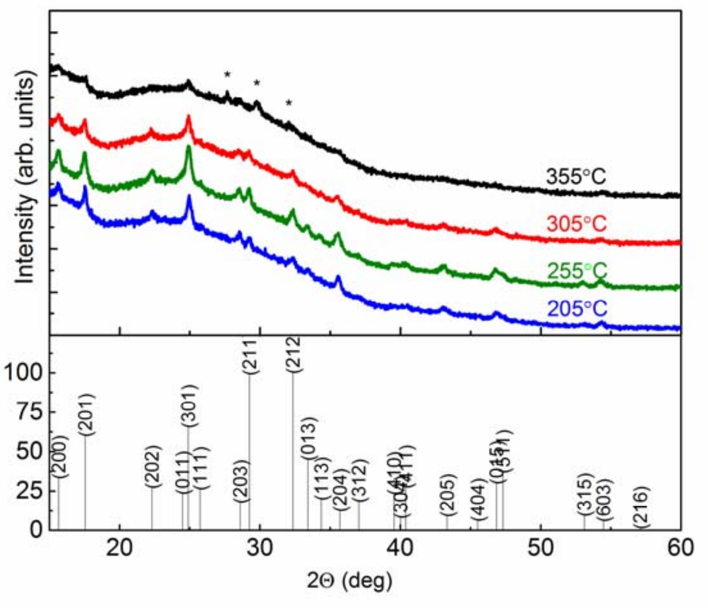

*Figure 3.12. XRD patterns of Sb_2S_3 films with Sb:S:TA molar ratio of 1:3:1 in spray solution grown at 205°C, 255°C, 305°C and 355°C. Unknown phase peaks are marked with *. [**V**]*

Irrespective of the deposition temperature (205°C–355°C), all the sprayed Sb_2S_3 films with Sb:S:TA ratio of 1:3:1 in spray solution were crystalline and the peaks presented in Figure 3.12 belong to the orthorhombic Sb_2S_3. The film grown at 355°C contains an unidentified secondary phase with peaks at 27.7°, 29.8° and 32.1° that was in later studies confirmed as Sb_2O_3 by Raman [211].

The crystallite size decreases from 25 nm to 15 nm with the increase in temperature from 205°C to 355°C (Table 3.5). However, for sprayed films the crystallite size generally increases with increasing the substrate temperature. Here, the reversed tendency (decreasing crystallite size with increasing the substrate temperature) can be explained by the presence of secondary phase of Sb_2O_3 retarding the crystallite growth. The same tendency was observed for SnS films where the crystallite size decreased from 25 nm to 6 nm with increasing the substrate temperature from 200°C to 320°C [212].

From SEM images, the estimated Sb_2S_3 film thicknesses for all the films with Sb:S:TA=1:3:10 is above 1 µm independent of the substrate temperature or annealing (Figure 3.13a and b). The Sb_2S_3 film grown at 205°C consists of two layers: the lower part of the film that is in contact with the substrate is granular while the upper part of the film in nearly granular free yet homogeneous (Figure 3.13a). Increasing the substrate temperature from 205°C to 230°C leads to not well adhered films with pores in it (Appendix A, Article [**V**] as Figure 2b). The holes in that film could be the reason the film is not well adhered to the substrate. Due to this, films grown with higher complexing agent concentration at temperatures higher than 230°C were not studied. Interestingly, studies on the growth of sprayed Sb_2S_3 films at temperatures higher than 230°C are published [180–183, 191]. The morphology of annealed film is homogeneous and similar to film grown at 205°C with the exception of the presence of unknown clusters throughout the film (Figure 3.13b).

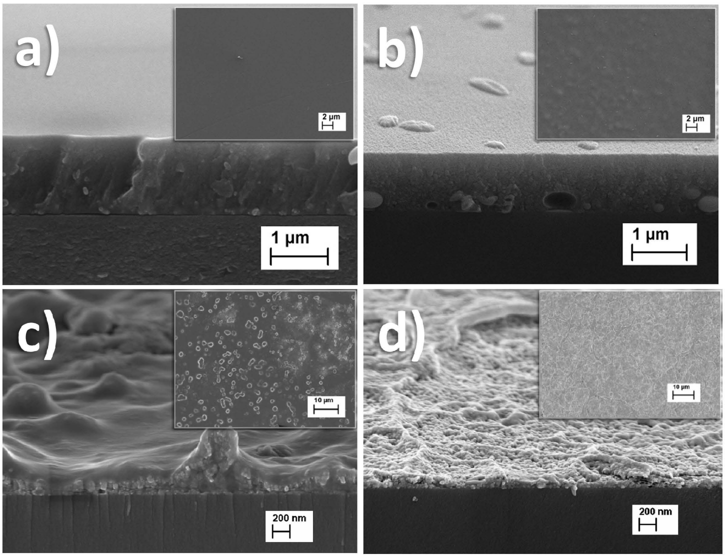

*Figure 3.13. Cross-sectional SEM images of Sb_2S_3 films with Sb:S:TA molar ratio of 1:3:10 in spray solution grown at temperatures of (a) 205°C, (b) 205°C followed by annealing in air at 400°C, and Sb_2S_3 films with Sb:S:TA molar ratio of 1:3:1 grown at temperatures of (c) 205°C and (d) 355°C. Corresponding film plane views are presented as insets. [**V**]*

The SEM image of Sb_2S_3 film grown at 205°C with Sb:S:TA ratio of 1:3:1 indicates that the granular part of the film is covered with amorphous substance (Figure 3.13c) and the film thickness is 510 nm. Increasing the temperature from 205°C to 355°C decreases the amount of amorphous substance on the surface (Figure 3.13d) and reduces the film thickness to 390 nm. The amorphous substance on the surface of Sb_2S_3 films is probably an organic residue. The presence of organic traces in the film was also confirmed by FTIR studies (Appendix A, Article [**V**] as Figure 5). According to EDX, the amount of organic residuals in the Sb_2S_3 thin films grown at 355°C is still high (Table 3.5). As the organic residuals in the films grown at temperatures above 300°C do not originate from thiourea [208, 210, 213, 214], it should be considered that the complexing agent, tartaric acid, is the main source for the high amount of organic residuals in the sprayed Sb_2S_3 thin films.

3.4.2 Residuals in the sprayed Sb_2S_3 films grown from spray solution containing tartaric acid as complexing agent

According to TG/DTG/DTA, the tartaric acids thermal decomposition takes place in three steps starting from 160°C and ending at 495°C with total mass loss of 100% (Figure 3.14). The first step in the thermal decomposition of tartaric acid begins at 160°C and the mass loss at the end of the first step (220°C) is ca. 25%. The second step of the mass loss is in the temperature region of 220°C to 280°C with the main mass loss of ca. 70%. The final decomposition step ends at 495°C with mass loss of ca. 5% indicating the complete decomposition of tartaric acid. The main mass loss in the thermal decomposition of tartaric acid takes place in the second step (220°C to 280°C) which explains the high amount of organic residues in the sprayed Sb_2S_3 thin film with the surface morphology and the microstructure of the Sb_2S_3 thin film.

Based on the thermal analysis results, all the films sprayed at moderate temperatures (substrate temperatures of 100°C–500°C being characteristic to spray pyrolysis) with tartaric acid in the spray solution are expected to contain tartaric acid residuals. From the results obtained with EDX, FTIR and the thermal analysis of tartaric acid it can be concluded that using tartaric acid as complexing agent in the deposition of Sb_2S_3 thin film by chemical spray pyrolysis is not justified.

The quality of Sb_2S_3 film can be improved by eliminating the use of complexing agent. Aqueous spray solution should be substituted with methanol or 2-propanol solutions, thus, eliminating the need for complexing agent.

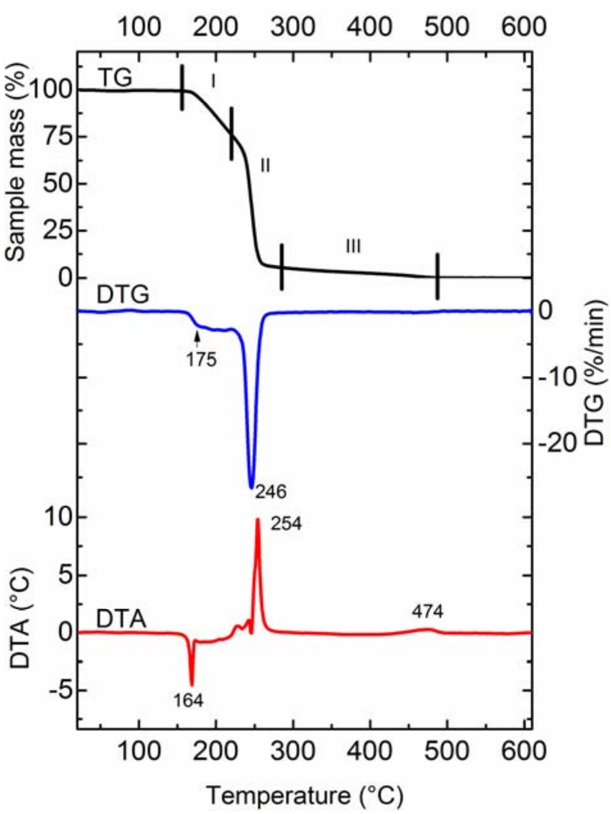

*Figure 3.14. Simultaneous TG, DTG and DTA curves of tartaric acid. Measurement conditions: Flowing 80% Ar + 20% O_2: 60 mL/min; heating rate: 5°C/min; initial sample mass: 2.5 mg. [**V**]*

3.4.3 Sb_2S_3 films grown methanol and 2-propanol solutions

The selected substrate temperature was 225°C and as in previous experiments, the Sb:S molar ratio in the spray solution was kept at 1:3.

The X-ray diffraction patters of Sb_2S_3 films grown from alcohol solvents reveal that all films are crystalline with orthorhombic phase (Figure 3.15). Again, a secondary phase at 2Θ of 27.7°, 32.1°, 35.0° and 46.1°, attributed to Sb_2O_3 according to PDF no.01-071-0365 [192], was present in Sb_2S_3 films irrespective of the used alcohol solvent. The 2Θ values of secondary phase Sb_2O_3 in Figure 3.12 and Figure 3.15 coincided. The Sb_2O_3 in the Sb_2S_3 film could have formed from partially hydrolysed $SbCl_3$ that decomposed into oxide at the deposition temperature. It is reported for sprayed In_2S_3 [209, 215], $CuInS_2$ [208] and SnS [212] thin films that the oxide phase formation could be inhibited with the use of excess thiourea.

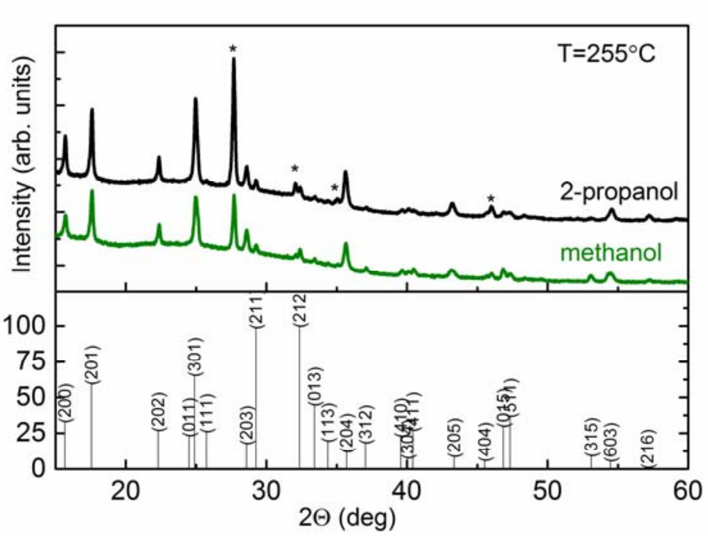

*Figure 3.15. XRD patterns of Sb_2S_3 films grown at 255°C using methanol and 2-propanol solvents. Sb_2O_3 phase peaks are marked with *. [V]*

The optical band gap of Sb_2S_3 film grown from alcohol solution is lower than that of an aqueous spray solution grown film, 1.7 eV and 2.1 eV, respectively (Table 3.6). Boughalmi et al. [191] have reported equivalent band gap of 1.72 eV for sprayed Sb_2S_3 layers grown from acetone-aqua mixed solution (CBD recipe). The ratio of S/Sb in the Sb_2S_3 film grown from 2-propanol solution was similar to that of a film grown at comparable conditions from aqueous solution with low tartaric acid concentration, S/Sb=1.0 (Table 3.5 and Table 3.6). The S/Sb ratio in Sb_2S_3 film grown at similar conditions from methanol solution was 1.4 (Table 3.6). Although the film grown from methanol solution contained a secondary phase of Sb_2O_3, this S/Sb ratio in the film is rather close to the Sb_2S_3 stoichiometry of 1.5.

Table 3.6. S/Sb ratio in the sprayed films according to EDX and Eg of the films (data acquired from Tauc plots) deposited from aqueous, methanol and 2-propanol solutions at 255°C. Independent of the solvent, the Sb:S molar ratio in the spray solutions is 1:3, a complexing agent (tartaric acid with the molar ratio of Sb:S:TA=1:3:1) is added to aqueous solvent to prevent the hydrolysis of the Sb precursor.

	Aqueous solvent, Sb:S:TA=1:3:1	Methanol solvent, Sb:S=1:3	2-propanol solvent, Sb:S=1:3
S/Sb	1.0	1.4	1.0
Eg, eV	2.1	1.7	1.7

This present research on sprayed Sb_2S_3 thin films was the base study for the preparation of ultrasonically sprayed Sb_2S_3 that was used in hybrid solar cell (structure glass/ITO/TiO_2/Sb_2S_3/P3HT/Au) [211] and in ETA solar cell (structure glass/O/ZnO_{NW}/TiO_2/Sb_2S_3/P3HT/Au) [216]. In [211], the presence of secondary phase was avoided at deposition temperature of 250°C with increasing the amount of sulphur source (thiourea) in the spray solution (Sb:S molar ratio in spray solution 1:6 or more). The hybrid solar cells had following output parameters at AM1.5: Voc=630 mV, Jsc=5 mA/cm^2, FF=42%, η=1.3% [211]. In [216], ZnO nanowires were integrated into the solar cell structure to enhance the light trapping phenomena and charge-carrier management. The best output parameters of solar cell were: Voc=656 mV, Jsc=7.5 mA/cm^2, FF=47%, η=2.3% [216].

In summary, Sb_2S_3 thin films can be grown by CSP but the aqueous recipe is taken from CBD and contains complexing agent to avoid the hydrolysis of $SbCl_3$. The Sb_2S_3 films are contaminated with organic residuals according to EDX and FTIR, irrespective of the complexing agent's concentration in the spray solution. The organic residuals originate from tartaric acid which was used as a complexing agent as the used substrate temperatures (205°C–355°C) were insufficient. The tartaric acid is completely decomposed at ca. 475°C, according to TG/DTG/DTA. Increasing the substrate temperature from 205°C to 355°C or annealing the film grown at 205°C decreases the crystallite size from 25 nm to 15 nm. The decrease in crystallite size is caused by the formation of Sb_2O_3 at higher temperatures or annealing in air at 400°C. The presence of Sb_2O_3 in the Sb_2S_3 films was in latter studies confirmed by Raman. With the increase in substrate temperature from 205°C to 355°C, the optical band gap increases from 2.3 eV to 2.5 eV. Using alcohol solutions to grow Sb_2S_3 films has the advantage of not needing a complexing agent which contaminates the film. Irrespective of the used alcohol solvent, the Sb_2S_3 films grown by CSP were crystalline and the optical band gap is 1.7 eV. However, the Sb_2S_3 films grown from alcohol solutions contained Sb_2O_3 as a secondary phase which can be prevented if the sulphur amount in the spray solution is increased. This study of Sb_2S_3 films by CSP was a base study to ultrasonically grow Sb_2S_3 films that were successfully used in ETA and hybrid solar cell structures.

CONCLUSIONS

Concluding from the studies carried out in this dissertation, the main outcomes are:

1. The optimum substrate temperature to grow the most conductive ZnO:In thin films by CSP is ca. 400°C (resistivity of $3\cdot10^{-3}$ Ω·cm). Substrate temperatures of 350°C and 450°C result in ZnO:In film with higher resistivity (ρ) of $9\cdot10^{-3}$ Ω·cm and above.
2. The commonly neglected deposition parameter spray rate affects the properties of a ZnO:In thin film. The crystallite size in the ZnO:In film grown with spray rate below 3 mL/min is ca. 20 nm and the films are composed of sharp-edged prismatic grains. Using spray rates higher than 3 mL/min lead to crystallite sizes of ca. 35 nm and to a network of interweaving grains with softened edges. Growing ZnO:In thin films at 400°C with spray rate of 3 mL/min and above leads to films with ρ of $3\text{-}4\cdot10^{-3}$ Ω·cm, carrier mobility of ca. 15 $cm^2/V\cdot s$ and concentration of ca. $1.2\cdot10^{20}$ cm^{-3}. Using spray rates below 3 mL/min leads to films with low conductivity (ρ of 10^{-1} Ω·cm and higher). Concurrently, the carrier mobility and concentration are below 10 $cm^2/V\cdot s$ and $3\cdot10^{19}$ cm^{-3}, respectively. The low carrier mobility is caused by low film thickness (700 nm) and grain size (100 nm). The lower carrier concentration is probably caused by the oxidation of dopant. Growing ZnO:In thin films at 400°C with spray rate of 3 mL/min and above leads to films with thickness of ca. 1350 nm and grain size of 250 nm. The optical transmittance of a conductive ZnO:In thin film in the visible light region is ca. 80% and the optical band gap is ca. 3.35 eV.
3. ZnO:In thin films were grown on polymer substrates at 380°C by CSP if a ZnO buffer layer was first deposited onto polymer. The morphology of a ZnO:In film depends strongly on the ZnO buffer layer morphology. A relatively smooth ZnO:In film with canvas-resembling structure can be grown on smooth ZnO buffer layer. Increasing the buffer layer thickness roughens the buffer layer morphology by increasing the size and the number of leaf-like grains that act as nucleation centres for large ZnO:In scrolled belts.
4. The ZnO/ZnO:In bilayers grown on polymer substrates and composing of scrolled belts exhibited high light scattering capability (Haze factor of ca. 90% in spectral region of 350 nm–1500 nm). In the same region, the Haze factor for smoother bilayers decreases from 95% to 20%. Resistivity of $4.4\cdot10^{-2}$ Ω·cm, carrier mobility of 1.5 $cm^2/V\cdot s$ and carrier concentration ca. 10^{20} cm^{-3} are characteristic to smooth ZnO/ZnO:In bilayer on polymer substrate. The lower resistivity ($6.7\cdot10^{-3}$ Ω·cm) of bilayer grown on glass substrate is mainly due to higher carrier mobility (13 $cm^2/V\cdot s$). The higher carrier mobility of bilayer grown on glass

substrate may be due to the thicker and more homogeneous ZnO:In layer.

5. Compact and smooth Zn(O,S) layers were grown by AA-CVD on Mo substrates at 225°C with carrier gas flow rate of 5 L/min and reactant gas flow rate of 2 mL/min. An increase in the reactant gas flow rate leads to powdery layers. XRD study showed that the Zn(O,S) films resemble more ZnS than ZnO and according to EDX, the compact Zn(O,S) layers contain more sulphur than oxygen as the O/(O+S) ratio is ca. 16%. The optical transmittance in the visible range of the spectrum is ca. 70% and the band gap of Zn(O,S) is ca. 3.6 eV. The best output parameters of Zn(O,S) buffered solar cell (Voc=573 mV, Jsc=39.2 mA/cm^2, FF=68.4% and η=15.4%) are comparable to the CdS and In_2S_3 buffered reference solar cells.
6. The aqueous spray solution recipe to grow Sb_2S_3 thin films by CSP from antimony trichloride and thiourea as Sb and S sources, respectively, and contains tartaric acid as complexing agent to avoid the hydrolysis of $SbCl_3$. Irrespective of the complexing agent concentration in the spray solution, all the films were contaminated with organic residuals according to EDX and FTIR. The organic residuals originated from tartaric acid and the used substrate temperatures (from 205°C up to 355°C) are insufficient to get rid of the organic residuals as tartaric acid is completely decomposed at ca. 475°C, as shown by TG/DTG/DTA study. Increasing the substrate temperature from 205°C up to 355°C decreases the Sb_2S_3 crystallite size (from 25 nm to 15 nm) which is caused by the formation of Sb_2O_3 (confirmed in latter studies by Raman). The optical band gap of Sb_2S_3 thin films is ca. 2.4 eV.
7. Sb_2S_3 thin films can be grown by CSP from alcohol solutions having the advantage of not needing a complexing agent that would contaminate the thin film. Irrespective of the used alcohol solvent, 2-propanol or methanol, the sprayed Sb_2S_3 films from solutions containing $SbCl_3$ and $SC(NH_2)_2$ at molar ratio of 1:3 at 255°C in air are of orthorhombic stibnite phase but contain Sb_2O_3 as a secondary phase. The optical band gap of Sb_2S_3 film grown by CSP from alcohol solutions is 1.7 eV.

ACKNOWLEDGEMENTS

I sincerely appreciate and venerate the guidance, support and the positive attitude of my supervisors Dr. Malle Krunks, Lead Research Scientist, and Dr. Ilona Oja Acik, Senior Research Scientist. I value the advice you gave and the fruitful discussions we had.

I am thankful to Dr. Arvo Mere and Dr. Erki Kärber for the assistance on the electrical characterisation of the films, to Dr. Valdek Mikli for the SEM, EDX and AFM measurements, and to Dr. Kaia Tõnsuaadu for carrying out the TG/DTG/DTA experiment. In addition, I thank all the former and present members of Laboratory of Thin Film Chemical Technologies for their outgoing attitude, nice lab atmosphere and co-operation.

I appreciate that prof. Christian-Herbert Fischer invited me to carry out part of my studies in HZB. The discussions with Dr. Rodrigo Sáez-Araoz and Tristan Köhler are valued. I still remind HZB and all the members of Institute for Heterogeneous Material Systems warmly as they took me as one of the group members from the very beginning.

I thank prof. Andres Öpik, the Head of doctoral studies curriculum in Faculty of Chemical and Materials Technology in Tallinn University of Technology, for the opportunity to participate in the doctoral studies and in the graduate school. In addition, I would like to thank prof. Enn Mellikov and Dr. Marit Kauk-Kuusik, the Heads of the Department of Materials Science, for the opportunity to carry out the research in Tallinn University of Technology.

The work is financially supported by the Estonian Ministry of Education and Research under Projects IUT19-4 (Thin films and nanomaterials by wet-chemical methods for next-generation photovoltaics) and SF0140092s08 (Thin film and nanostructured materials by chemical methods), The European Regional Development Funds Projects TK114 (Centre of Excellence: Mesomaterials–Theory and Applications), TK141 (Centre of Excellence: Advanced materials and high-technology devices for sustainable energetics, sensorics and nanoelectronics) and AR12118 (Efficient plasmonic absorbers for solar cells), by Estonian Science Foundation grants ETF8509 (Development of ZnO nanorods by chemical spray) and ETF9081 (Absorber layers by chemical spray pyrolysis for nanostructured solar cells), Internationalisation Programme DoRa, European Social Fund's project (1.2.0401.09-0079) graduate school "Functional materials and technologies" and European Regional Fund's project (2014-2020.4.01.16-0032) Graduate School of Functional Materials and Technologies.

My deepest gratitude belongs to my loved ones.

ABSTRACT

The increasing electricity consumption demands an alternative, environmentally friendly and sustainable energy source. It would be reasonable to harvest solar energy and to convert it to electricity with solar cells. To make the solar cells commercially more available, the solar cell production costs must be lowered. Therefore, the solar cells must be prepared from abundant, cheap and environmentally friendly materials with effective and low-cost methods. Two aerosol based deposition methods, chemical spray pyrolysis (CSP) and aerosol assisted chemical vapour deposition (AA-CVD), are used in this dissertation. The advantages of CSP and AA-CVD are the simplicity of apparatus, fast deposition process and possibility to cover large areas.

This dissertation "Study of ZnO:In, Zn(O,S) and Sb_2S_3 thin films deposited by aerosol methods" is directly related to the research projects carried out by the Laboratory of Thin Film Chemical Technologies, TUT, Estonia.

The aim of this dissertation was to grow electrically conductive indium doped ZnO (ZnO:In) films by CSP on glass and polymer substrates and to study the effect of substrate temperature and solution spray rate on the film properties. Secondly, to grow a non-toxic cost-efficient Zn(O,S) layers by AA-CVD method, to study the effect of technology variables such as reactive gas and carrier gas flow rate on the properties of Zn(O,S) layers and to utilised them in solar cell. Thirdly, to grow potential absorber material Sb_2S_3 thin films by CSP and to study effect of substrate temperature and spray solution composition on Sb_2S_3 films.

The dissertation is based on five publications. The thesis composes of literature overview describing the aerosol methods and the properties of zinc oxide and antimony sulphide materials and films; of experimental description of used materials and characterisation methods; and of compendium of results that is divided into three sections.

The first section introduces the deposition and the characterisation of ZnO:In thin films grown on glass and polymer substrates by CSP from water-alcohol mixed solution containing zinc acetate and indium(III)chloride (with [In]/[Zn]=3 at.%). If ZnO:In is grown electrically conductive and optically transparent, it can be a potential front contact in microelectronics and in solar cell structure. Mainly, the effect of substrate temperature (350°C–500°C) and the solution spray rate (0.5 mL/min–7.1 mL/min) on the structural, morphological, electrical and optical properties of ZnO:In thin films was studied. The most conductive ZnO:In thin films (resistivity of $3 \cdot 10^{-3}$ $\Omega \cdot$cm) were grown at substrate temperature of 400°C. We concluded that solution spray affects the properties of ZnO:In thin films majorly. The ZnO:In films grown at spray rates of 0.5 and 3.3 mL/min are composed of sharp-edged pyramidal grains and canvas-resembling surfaces, respectively. Increasing the

spray rate from 0.5 mL/min to 6.7 mL/min increases film thickness and grain size (from 1400 nm to 700 nm and 250 nm to 100 nm, respectively). The electrical resistivity of sprayed ZnO:In films decreases with the spray rate from $6.3 \cdot 10^{-2}$ Ω·cm to $3.7 \cdot 10^{-3}$ Ω·cm from 0.5 mL/min to 3.3 mL/min, respectively. Concurrently, the carrier concentration increases from $2 \cdot 10^{19}$ cm^{-3} to $1 \cdot 10^{20}$ cm^{-3}. Lower carrier concentration in slowly sprayed films is likely due to the indium oxidation. The carrier mobilities 10 $cm^2/V \cdot s$ and lower are characteristic to films with spray rate below 3 mL/min. The optical transmittance of ZnO:In films is ca. 80% in the visible light. Increasing the spray rate from 0.5 mL/min to 3.3 mL/min decreases the transmittance in the NIR region and increases the band gap along with carrier concentration.

The upward trend for flexible lightweight microelectronics and solar cells has led to the use of polymer substrates. The first results on growing ZnO:In films by CSP on polymer substrates is reported and the effect of spray rate on the structural, morphological, optical and electrical properties of sprayed films was studied. The adherent ZnO film was used as a buffer layer to grow ZnO:In thin films on polymer substrate. We concluded that the morphology of a ZnO:In layer depends strongly on the morphology of a ZnO buffer layer. Relatively smooth ZnO:In layers resembling canvas-like structure were grown on smooth buffer layer. Increasing the buffer layer thickness roughens the buffer layer morphology by increasing the size and the number of leaf-like grains that act as nucleation centres for large ZnO:In scrolled belts that exhibit high light scattering capability (Haze of ca. 90%). The resistivity ($4.4 \cdot 10^{-2}$ Ω·cm) and carrier mobility (1.5 $cm^2/V \cdot s$) of a smooth bilayer on polymer substrate are more inferior compared to those on glass substrate (resistivity of $6.7 \cdot 10^{-3}$ Ω·cm, carrier mobility of 13 $cm^2/V \cdot s$) due to more heterogeneous microstructure. Irrespective of the substrate, the carrier concentrations of ZnO:In layer are comparable at ca. 10^{20} cm^{-3}. The conductivity of a ZnO:In layer on polymer can be increased if the microstructure of the ZnO layer is as homogeneous as possible.

The second part of the dissertation is dedicated to the deposition of Zn(O,S) layer by AA-CVD. Zn(O,S) can be used as an alternative buffer layer in the CIGSSe solar cell structure instead of toxic CdS or expensive In_2S_3. In addition, using Zn(O,S) should make the structure and the production of a final solar cell simpler and cheaper as it gives the possibility to omit intrinsic ZnO window layer from the solar cell structure. Optimal carrier gas and reactant gas flow rates are determined experimentally and the structural, morphological and optical properties, and the elemental composition of grown compact Zn(O,S) layers are studied. The optical transmittance in the visible light of Zn(O,S) layer is ca. 70% and the band gap is ca. 3.6 eV. The AA-CVD grown Zn(O,S) films contain more sulphur than oxide, according to EDX. Zn(O,S) was successfully used as a buffer layer in a CIGSSe solar cell. The best output parameters for Zn(O,S) buffered CIGSSe solar cell are: Voc=573 mV, Jsc=39.2 mA/cm^2, FF=68.4% and η=15.4%. These results were comparable to the In_2S_3 and CdS buffered solar cell reference output values.

The last section introduces the deposition of potential absorber Sb_2S_3 thin films by CSP. Films were sprayed from aqueous solution containing $SbCl_3$ and $SC(NH_2)_2$ at molar ratio of 1:3 and tartaric acid (TA) as complexing agent to avoid the hydrolysis of $SbCl_3$. The effect of spray solution composition and of substrate temperature on the phase composition, morphology and optical properties and the elemental composition of the Sb_2S_3 thin films are studied. Our study showed that the Sb_2S_3 films grown from spray solution with high tartaric acid concentrations (Sb:S:TA molar ratio of 1:3:10) were amorphous at substrate temperatures of 205°C and 230°C. In addition, these films contained high amount of organic residues that originated from tartaric acid. Decreasing the tartaric acid concentration to Sb:S:TA=1:3:1 results in stable spray solution yet the polycrystalline Sb_2S_3 films grown at 355°C contains traces of organic residues. According to TG/DTG/DTA, tartaric acid is completely decomposed at ca. 475°C. Thus, growing Sb_2S_3 thin films from spray solution containing tartaric acid as complexing agent is not suitable for CSP. Additionally, an alternative route using alcohol solutions that need no complexing agent is suggested to chemically spray organic residual free crystalline Sb_2S_3 thin films with Eg of 1.7 eV.

KOKKUVÕTE

Elektrienergia tarbimise kasvuga on tekkinud nõudlus alternatiivsete, loodusesõbralike ja jätkusuutlike energiaallikate järele. Mõistlik variant oleks koguda päikeenergiat ja muuta see elektriks päikesepatareidega. Päikesepatareide laialdasemaks kasutamiseks on vaja vähendada patareide tootmiskulusid. Päikesepatareid peavad olema valmistatud odavatest, keskkonnasõbralikest ja külluslikult leiduvatest materjalidest efektiivsete ning ökonoomsete tehnoloogiatega. Käesolevas doktoritöös kasutatakse õhukeste kilede valmistamiseks kahte aerosooli sadestamisel põhinevat meetodit - keemiline pihustuspürolüüs (*chemical spray* pyrolysis, CSP) ja keemiline sadestamine aurufaasist aerosooli kaasabil (*aerosol assisted chemical vapour deposition*, AA-CVD). CSP ja AA-CVD meetodite eeliseks on kasutatava aparatuuri lihtsus, tehnoloogilise protsessi kiirus ja võimalus katta suuri pindu.

Antud doktoritöö „Aerosoolmeetoditel sadestatud ZnO:In, Zn(O,S) ja Sb_2S_3 õhukeste kilede uurimine“ on otseselt seotud TTÜ Materjali- ja keskkonnatehnoloogia instituudi Keemiliste kiletehnoloogiate teaduslaboratooriumi uurimistemaatikaga.

Antud töö eesmärgiks oli sadestada elektrit juhtivad ZnO:In kiled klaas ja polümeersetele alustele CSP meetodil ja uurida aluse temperatuuri ja lahuse pihustuskiiruse mõju kilede füüsikalistele omadustele. Teiseks, kasvatada Zn(O,S) puhverkihid AA-CVD meetodil ja uurida tehnoloogiliste muutujate nagu reaktiivgaasi ja kandegaasi voolukiirus mõju Zn(O,S) kihtide omadustele. Lisaks, rakendada valmistatud puhverkihte $Cu(In,Ga)(S,Se)_2$ tüüpi absorberiga päikesepatareides. Kolmandaks, sadestada Sb_2S_3 absorber kiled CSP meetodiga ning uurida aluse temperatuuri ja pihustuslahuse koostise mõju Sb_2S_3 kilede omadustele.

Doktoritöö põhineb viiel publitseeritud teadusartiklil. Töö koosneb kirjanduse ülevaatest, mis kirjeldab aerosoolmeetodeid ning ZnO ja Sb_2S_3 materjalide ja kilede omadusi; eksperimentaalsest osast, mis kirjeldab kasutatud materjale, katsemetoodikat ja uurimismeetodid; ja eksperimentaalseid tulemusi kokkuvõtvast osast, mis omakorda on jagatud kolmeks allosaks.

Esimene osa tutvustab ZnO:In kilede sadestamist CSP meetodiga, kus tsinkatsetaati ja indium(III)kloriidi sisaldav lahus ([In]/[Zn]=3 at.%) pihustatakse eelkuumutatud klaas- ja polümeeralustele, ning kilede karakteriseerimist. Kui ZnO:In kile valmistatakse võimalikult elektrit juhtivana ja optiliselt läbipaistvana, saab seda kasutada nii mikroelektroonikas kui ka päikesepatareides valgust läbilaskva elektroodina. Uuriti aluse temperatuuri (350°C–500°C) ja lahuse pihustuskiiruse (0.5 mL/min–7.1 mL/min) mõju ZnO:In kilede struktuursetele, morfoloogilistele, elektrilistele ja optilistele omadustele. Kõige juhtivamad ZnO:In kiled (eritakistus $3\cdot10^{-3}$ $\Omega\cdot$cm) saadi aluse temperatuuril 400°C. Ilmnes, et lahuse pihustuskiiruse mõju ZnO:In

kilede omadustele on märkimisväärne. Kiled, mis kasvatati pihustuskiirusega 0.5 mL/min ja 3 mL/min, koosnevad vastavalt terava-tipulistest püramiidsetest teradest ning ümardunud teradest, mis moodustavad kanvaa-laadse pinna. Pihustuskiiruse kasvades 0.5 mL/min kuni 6.7 mL/min-i väheneb kile paksus ja ZnO:In terade suurus (vastavalt 1400 nm-st 700 nm-ni ja 250 nm-st 100 nm-ni). ZnO:In kilede eritakistus väheneb $6.3 \cdot 10^{-2}$ $\Omega \cdot$cm-lt $3.7 \cdot 10^{-3}$ $\Omega \cdot$cm-le kui pihustuskiirust tõsta 0.5 mL/min-st 3.3 mL/min-ni. Samaaegselt, suureneb ka laengukandjate kontsentratsioon $2 \cdot 10^{19}$ cm^{-3}-lt kuni $1 \cdot 10^{20}$ cm^{-3}-le. Madalamatel pihustuskiirustel saadud madalad kontsentratsioonid on tõenäoliselt tingitud legeeriva elemendi oksüdatsioonist. Laengukandjate liikuvused alla 10 $cm^2/V \cdot s$ on omased kiledele, mille kasvatamisel olid pihustuskiirused väiksemad kui 3 mL/min. ZnO:In kilede optiline läbilaskvus nähtavas spektri osas on ligikaudu 80%. Pihustuskiiruse suurenedes 0.5 mL/min-s 3.3 mL/min-s väheneb kilede läbilaskvus NIR regioonis ning suureneb kilede keelutsooni laius proportsionaalselt laengukandjate kontsentratsiooni kasvuga.

Kergekaaluliste ja painduvate mikroelektroonika ja päikesepatareide kasvav trend on viinud polümeersete aluste kasutamiseni. Uurimistöö tulemusena avaldati esimesed tulemused ZnO:In kiled kasvatamisest polümeersetele alustele CSP meetodiga. ZnO:In kile kasvatamiseks polümeerile kasutasime alusega hästihaakuvat ZnO kilet puhverkihina. Ilmnes, et puhverkihi morfoloogia määrab ZnO:In kile morfoloogia. Ühtlasemale puhverkihile kasvas suhteliselt ühtlase kanvaa-laadse struktuuriga ZnO:In kile. Puhverkihi paksuse suurenedes muutus puhverkihi pind ebaühtlasemaks. Paksemas ZnO puhverkihis moodustusid lehe-sarnased terad, mis olid kasvuidudeks kuni 6 µm-se diameeteriga valgust hajutatavatele (Haze ca. 90%) ZnO:In rullistele (*scrolled* belts). Lisaks, ühtlasem ZnO puhverkihi pinna morfoloogia tagab kõrgema ZnO:In kilede juhtivuse. Polümeerile kasvatatud ühtlase ZnO/ZnO:In kaksikkihi eritakistus on $4.4 \cdot 10^{-2}$ $\Omega \cdot$cm ja laengukandjate liikuvus 1.5 $cm^2/V \cdot s$. Samas, klaasile kasvatatud ZnO/ZnO:In kaksikkihi eritakistus on $6.7 \cdot 10^{-3}$ $\Omega \cdot$cm ja laengukandjate liikuvus on 13 $cm^2/V \cdot s$ tänu ühtlasemale mikrostruktuurile võrreldes polümeerile kasvatatud kaksikkihiga. ZnO:In kihi laengukandjate kontsentratsioon polümeer- ja klaasalustel on samaväärne, ligikaudu 10^{20} cm^{-3}.

Doktoritöö teine osa on pühendatud Zn(O,S) kihtide sadestamisele AA-CVD meetodiga. CIGSSe absorberiga päikesepatareides saab Zn(O,S) kasutada alternatiivse puhverkihina CdS või In_2S_3 asemel. Lisaks sellele võimaldab Zn(O,S) kasutamine jätta päikesepatarei struktuurist välja ZnO aknakihi, muutes päikesepatarei struktuuri ja valmistamise lihtsamaks ja soodsamaks. Ühtlase Zn(O,S) kihi saamiseks määrati eksperimentaalselt kandegaasi ja reaktiivaine gaasi optimaalsed voolukiirused ning uuriti kasvatatud Zn(O,S) kihtide struktuurilisi, morfoloogilisi ja optilisi omadusi ning elementkoostist. Zn(O,S) kihtide optiline läbilaskvus nähtavas spektri osas on ligikaudu 70% ja keelutsoon ca. 3.6 eV. EDX uuring näitas, et Zn(O,S) kihid sisaldavad rohkem väävlit kui hapnikku. Zn(O,S) rakendati edukalt puhverkihina CIGSSe tüüpi päikesepatareis. Zn(O,S) puhverkihiga CIGSSe päikesepatarei parimad väljundparameetrid on: Voc=573 mV, Jsc=39.2 mA/cm^2, FF=68.4% ja η=15.4%. Saadud tulemused on võrreldavad CIGSSe päikesepatareide väljundparameetritega, kus puhverkihtidena kasutati In_2S_3 ja CdS kihti.

Viimane allosa tutvustab Sb_2S_3 kui potentsiaalse absorbermaterjali kilede sadestamist CSP meetodiga. Kiled sadestati vesilahusest, kus lähteainetena kasutati $SbCl_3$ ja $SC(NH_2)_2$ molaarsuhtega 1:3 ja $SbCl_3$ hüdrolüüsi vältimiseks viinhapet (TA) kompleksimoodustajana. Uuriti pihustuslahuse koostise ning kasvutemperatuuri mõju Sb_2S_3 kilede faasikoostisele, morfoloogiale ja optilistele omadustele ning elementkoostisele. Uuringud näitasid, et kõrge viinhappe sisaldusega (Sb:S:TA molaarsuhe 1:3:10) lahuse pihustamisel saadakse nii 205°C ja 230°C amorfsed kiled, mis sisaldavad suurel hulgal viinhappe termilise lagunemise produkte. Viinhappe kontsentratsiooni kümnekordne vähendamine võimaldab valmistada stabiilse pihustuslahuse, kuid 355°C juures kasvatatud polükristallilised Sb_2S_3 kiled sisaldavad ikkagi viinhappe jääke. Termilise analüüsi (TG/DTG/DTA) tulemuste põhjal laguneb viinhape täielikult alles 475°C juures. Seega, Sb_2S_3 kilede kasvatamiseks CSP meetodiga ei saa kasutada pihustuslahuseid, mis sisaldavad viinhapet kompleksimoodustajana. Näitasime, et alkoholipõhiste lahuste kasutamine võimaldab vältida kompleksimoodustaja kasutamist pihustuslahuses ja CSP meetodiga on võimalik kasvatada kristallilised orgaanika jääkidest vabad Sb_2S_3 kiled, mille keelutsooni laius on 1.7 eV.

REFERENCES

1. Colbeck, I., Lazaridis, M.: Aerosol Science: Technology and Applications. Wiley (2014).
2. Mooney, J.B., Radding, S.B.: Spray pyrolysis processing. Annu. Rev. Mater. Sci. 12, 81–101 (1982).
3. Blandenet, G., Court, M., Lagarde, Y.: Thin layers deposited by the pyrosol process. Thin Solid Films. 77, 81–90 (1981).
4. Nyman, M., Hampden-Smith, M.J., Duesler, E.N.: Low temperature, aerosol-assisted chemical vapor deposition (AACVD) of CdS, ZnS, and $Cd_{1-x}Zn_xS$ using monomeric single-source precursors: $M(SOCCH_3)_2$ TMEDA. Chem. Vap. Depos. 2, 171–174 (1996).
5. Bakar, S.A., Hussain, S.T., Trimizi, S.A., Tahir, M.N.: Crack free and spherical shape copper–zinc composite oxide thin films fabrications by AACVD. Polyhedron. 49, 138–144 (2013).
6. Kevin, P., Lewis, D.J., Raftery, J., Azad Malik, M., O'Brien, P.: Thin films of tin(II) sulphide (SnS) by aerosol-assisted chemical vapour deposition (AACVD) using tin(II) dithiocarbamates as single-source precursors. J. Cryst. Growth. 415, 93–99 (2015).
7. Hussain, S.T., Bakar, S.A., Saima, B., Muhammad, B.: Low temperature deposition of silver sulfide thin films by AACVD for gas sensor application. Appl. Surf. Sci. 258, 9610–9616 (2012).
8. Hou, X., Choy, K.-L.: Processing and Applications of Aerosol-Assisted Chemical Vapor Deposition. Chem. Vap. Depos. 12, 583–596 (2006).
9. Roger, C., Corbitt, T.S., Hampden-Smith, M.J., Kodas, T.T.: Aerosol-assisted chemical vapor deposition of copper: A liquid delivery approach to metal thin films. Appl. Phys. Lett. 65, 1021 (1994).
10. Hubert-Pfalzgraf, L.G., Guillon, H.: Trends in precursor design for conventional and aerosol-assisted CVD of high-Tc superconductors. Appl. Organomet. Chem. 12, 221–236 (1998).
11. Annanouch, F.E., Vallejos, S., Stoycheva, T., Blackman, C., Llobet, E.: Aerosol assisted chemical vapour deposition of gas-sensitive nanomaterials. Thin Solid Films. 548, 703–709 (2013).
12. Arca, E., Fleischer, K., Shvets, I. V.: Influence of the precursors and chemical composition of the solution on the properties of ZnO thin films grown by spray pyrolysis. J. Phys. Chem. C. 113, 21074–21081 (2009).
13. Jiang, C., Koh, W.L., Leung, M.Y., Hong, W., Li, Y., Zhang, J.: Influences of alcoholic solvents on spray pyrolysis deposition of TiO_2 blocking layer films for solid-state dye-sensitized solar cells. J. Solid State Chem. 198, 197–202 (2013).
14. Guillemoles, J.F., Lincot, D., Cowache, P., Vedel, J.: Solvent Effect on ZnO thin films prepared by spray pyrolysis. In: Luque, A., Sala, G., Palz, W., Santos, G., and Helm, P. (eds.) Tenth E.C. Photovoltaic Solar Energy Conference. Springer Netherlands, Dordrecht (1991).

15. Krunks, M., Mellikov, E.: Zinc oxide thin films by the spray pyrolysis method. Thin Solid Films. 270, 33–36 (1995).

16. Jongthammanurak, S., Witana, M., Cheawkul, T., Thanachayanont, C.: The effects of carrier gas and substrate temperature on ZnO films prepared by ultrasonic spray pyrolysis. Mater. Sci. Semicond. Process. 16, 625–632 (2013).

17. Oja, I., Mere, A., Krunks, M., Nisumaa, R., Solterbeck, C.H.H., Es-Souni, M.: Structural and electrical characterization of TiO_2 films grown by spray pyrolysis. Thin Solid Films. 515, 674–677 (2006).

18. Caglar, Y., Zor, M., Caglar, M., Ilican, S.: Influence of the indium incorporation on the structural and electrical properties of zinc oxide films. J. Optoelectron. Adv. Mater. 8, 1867–1873 (2006).

19. Hamid, M., Tahir, A.A., Mazhar, M., Ahmad, F., Molloy, K.C., Kociok-Kohn, G.: Deposition and characterization of ZnO thin films from a novel hexanuclear zinc precursor. Inorganica Chim. Acta. 361, 188–194 (2008).

20. Hepp, A.F., McNatt, J.S., Dickman, J.E., Jin, M.H.-C., Banger, K.K., Kelly, C. V., Gonzalez, A.R.A., Rockett, A.A.: Aerosol-Assisted Chemical Vapor Deposited Thin Films for Space Photovoltaics. In: Fourth International Energy Conversion Engineering Conference and Exhibit (IECEC) (2006).

21. Fischer, C.H., Allsop, N., Gledhill, S., Köhler, T., Krüger, M., Sáez-Araoz, R., Fu, Y., Schwieger, R., Richter, J., Wohlfart, P., Bartsch, P., Lichtenberg, N., Lux-Steiner, M.C.: The spray-ILGAR® (ion layer gas reaction) method for the deposition of thin semiconductor layers: Process and applications for thin film solar cells. Sol. Energy Mater. Sol. Cells. 95, 1518–1526 (2011).

22. Fu, Y.: Ph.D. Thesis. Spray-ILGAR® deposition of controllable ZnS nanodots and application as passivation/point contact at the In_2S_3/$Cu(In,Ga)(S,Se)_2$ junction in thin film solar cells, (2012).

23. Viguié, J.C., Spitz, J.: Chemical Vapor Deposition at Low Temperatures. J. Electrochem. Soc. 122, 585–588 (1975).

24. Miles, R.W., Zoppi, G., Reddy, K.T.R., Forbes, I.: Thin Film Solar Cells Based on the Use of Polycrystalline Thin Film Materials. In: Zhang, S. (ed.) Organic Nanostructured Thin Film Devices and Coatings for Clean Energy. pp. 1–56. Taylor and Francis Group, LLC (2010).

25. Chamberlin, R.R., Skarman, J.S.: Chemical Spray Deposition Process for Inorganic Films. J. Electrochem. Soc. 113, 86–89 (1966).

26. Patil, P.S.: Versatility of chemical spray pyrolysis technique. Mater. Chem. Phys. 59, 185–198 (1999).

27. Kärber, E., Abass, A., Khelifi, S., Burgelman, M., Katerski, A., Krunks, M.: Electrical characterization of all-layers-sprayed solar cell based on ZnO nanorods and extremely thin CIS absorber. Sol. Energy. 91, 48–58 (2013).

28. Albin, D.S., Risbud, S.H.: Spray pyrolysis processing of optoelectronic materials. Adv. Ceram. Mater. 2, 243–252 (1987).

29. Tomar, M.S., Garcia, F.J.: Spray pyrolysis in solar cells and gas sensors. Prog. Cryst. Growth Charact. 4, 221–248 (1981).

30. Perednis, D., Gauckler, L.J.: Thin film deposition using spray pyrolysis. J. Electroceramics. 14, 103–111 (2005).

31. Nakaruk, A., Sorrell, C.C.: Conceptual model for spray pyrolysis mechanism: fabrication and annealing of titania thin films. J. Coatings Technol. Res. 7, 665–676 (2010).

32. Dedova, T.: Ph.D. Thesis. Chemical Spray Pyrolysis Deposition of Zinc Sulfide Thin Films and Zinc Oxide Nanostructured Layers, (2007).

33. Ma, Y.Y., Bube, R.H.: Properties of CdS Films Prepared by Spray Pyrolysis. J. Electrochem. Soc. 124, 1430 (1977).

34. El Hichou, A., Addou, M., Ebothé, J., Troyon, M.: Influence of deposition temperature (Ts), air flow rate (f) and precursors on cathodoluminescence properties of ZnO thin films prepared by spray pyrolysis. J. Lumin. 113, 183–190 (2005).

35. Romero, R., Leinen, D., Dalchiele, E.A., Ramos-Barrado, J.R., Martín, F.: The effects of zinc acetate and zinc chloride precursors on the preferred crystalline orientation of ZnO and Al-doped ZnO thin films obtained by spray pyrolysis. Thin Solid Films. 515, 1942–1949 (2006).

36. Thahab, S.M., Omran Alkhayat, A.H., Saleh, S.M.: Influence of substrate type on the structural, optical and electrical properties of $Cd_xZn_{1-x}S$ MSM thin films prepared by Spray Pyrolysis method. Mater. Sci. Semicond. Process. 26, 49–54 (2014).

37. Bhatia, S., Bedi, R.K.: Morphological, electrical and optical properties of zinc oxide films grown on different substrates by spray pyrolysis technique. Nanostructured Thin Film. III. 7766, 776610-776610–10 (2010).

38. Krunks, M., Bijakina, O., Mikli, V., Varema, T., Mellikov, E.: Zinc Oxide Thin Films by Spray Pyrolysis Method. Phys. Scr. T79, 209–212 (1999).

39. Daranfed, W., Aida, M.S., Hafdallah, A., Lekiket, H.: Substrate temperature influence on ZnS thin films prepared by ultrasonic spray. Thin Solid Films. 518, 1082–1084 (2009).

40. Babu, B.J., Maldonado, A., Velumani, S., Asomoza, R.: Electrical and optical properties of ultrasonically sprayed Al-doped zinc oxide thin films. Mater. Sci. Eng. B Solid-State Mater. Adv. Technol. 174, 31–37 (2010).

41. Chen, S., Wilson, R.M., Binions, R.: Synthesis of highly surface-textured ZnO thin films by aerosol assisted chemical vapour deposition. J. Mater. Chem. A. 3, 5794–5797 (2015).

42. de la L. Olvera, M., Gomez, H., Maldonado, A.: Doping, vacuum

annealing, and thickness effect on the physical properties of zinc oxide films deposited by spray pyrolysis. Sol. Energy Mater. Sol. Cells. 91, 1449–1453 (2007).

43. Sun, H., Wang, C., Pang, S., Li, X., Tao, Y., Tang, H., Liu, M.: Photocatalytic TiO_2 films prepared by chemical vapor deposition at atmosphere pressure. J. Non. Cryst. Solids. 354, 1440–1443 (2008).

44. Kushiya, K., Ohshita, M., Hara, I., Tanaka, Y., Sang, B., Nagoya, Y., Tachiyuki, M., Yamase, O.: Yield issues on the fabrication of 30cm×30cm-sized Cu(In,Ga)Se-based thin-film modules. Sol. Energy Mater. Sol. Cells. 75, 171–178 (2003).

45. Kushiya, K., Sang, B., Okumura, D., Yamase, O.: Application of Stacked ZnO Films as a Window Layer to $Cu(InGa)Se_2$ Based Thin-Film Modules. Jpn. J. Appl. Phys. 38, 3997–4001 (1999).

46. Nakada, T., Furumi, K., Kunioka, A.: High-efficiency cadmium-free $Cu(In,Ga)Se_2$ thin-film solar cells with chemically deposited ZnS buffer layers. IEEE Trans. Electron Devices. 46, 2093–2097 (1999).

47. Allsop, N.A., Camus, C., Hänsel, A., Gledhill, S.E., Lauermann, I., Lux-Steiner, M.C., Fischer, C.-H.: Indium sulfide buffer/CIGSSe interface engineering: Improved cell performance by the addition of zinc sulfide. Thin Solid Films. 515, 6068–6072 (2007).

48. Möller, J., Fischer, C.-H., Muffler, H.-J., Könenkamp, R., Kaiser, I., Kelch, C., Lux-Steiner, M..: A novel deposition technique for compound semiconductors on highly porous substrates: ILGAR. Thin Solid Films. 361–362, 113–117 (2000).

49. Girtan, M., Folcher, G.: Structural and optical properties of indium oxide thin films prepared by an ultrasonic spray CVD process. Surf. Coatings Technol. 172, 242–250 (2003).

50. Stoycheva, T.T., Vallejos, S., Pavelko, R.G., Popov, V.S., Sevastyanov, V.G., Correig, X.: Aerosol-Assisted CVD of SnO_2 Thin Films for Gas-Sensor Applications. Chem. Vap. Depos. 17, 247–252 (2011).

51. Edusi, C., Hyett, G., Sankar, G., Parkin, I.P.: Aerosol-Assisted CVD of Titanium Dioxide Thin Films from Methanolic Solutions of Titanium Tetraisopropoxide; Substrate and Aerosol-Selective Deposition of Rutile or Anatase. Chem. Vap. Depos. 17, 30–36 (2011).

52. Hou, X., Choy, K.-L.: Crystal Growth of ZnS Films by a Charged Aerosol-Assisted Vapor Deposition Process. Chem. Vap. Depos. 12, 631–636 (2006).

53. Waugh, M.R., Hyett, G., Parkin, I.P.: Zinc Oxide Thin Films Grown by Aerosol Assisted CVD. Chem. Vap. Depos. 14, 366–372 (2008).

54. Qin, X.J., Zhao, L., Shao, G.J., Wang, N.: Influence of solvents on deposition mechanism of Al-doped ZnO films synthesized by cold wall aerosol-assisted chemical vapor deposition. Thin Solid Films. 542, 144–149 (2013).

55. Rodriguez-Castro, J., Dale, P., Mahon, M.F., Molloy, K.C., Peter, L.M.: Deposition of antimony sulfide thin films from single-source antimony thiolate precursors. Chem. Mater. 19, 3219–3226 (2007).
56. Di Maggio, F., Ling, M., Tsang, A., Covington, J., Saffell, J., Blackman, C.: Aerosol-assisted CVD synthesis, characterisation and gas-sensing application of gold-functionalised tungsten oxide. J. Sens. Sens. Syst. 3, 325–330 (2014).
57. Ramos-Cano, J., Hurtado-Macías, A., Antúnez-Flores, W., Fuentes-Cobas, L., González-Hernández, J., Amézaga-Madrid, P., Miki-Yoshida, M.: Synthesis by aerosol assisted chemical vapor deposition and microstructural characterization of $PbTiO_3$ thin films. Thin Solid Films. 531, 179–184 (2013).
58. Noor, N., Parkin, I.P.: Enhanced transparent-conducting fluorine-doped tin oxide films formed by Aerosol-Assisted Chemical Vapour Deposition. J. Mater. Chem. C. 1, 984–996 (2013).
59. Liu, L., Wang, L., Qin, X., Cui, L., Shao, G.: Effects of intermittent atomization on the properties of Al-doped ZnO thin films deposited by aerosol-assisted chemical vapor deposition. Thin Solid Films. 605, 163–168 (2016).
60. Weiss, F., Schmatz, U., Pisch, A., Felten, F., Pignard, S., Sénateur, J.P., Abrutis, A., Fröhlich, K., Selbmann, D., Klippe, L.: HTS thin films by innovative MOCVD processes. J. Alloys Compd. 251, 264–269 (1997).
61. Klingshirn, C.: ZnO: Material, Physics and Applications. In: Fundamental properties of ZnO nanostructures. pp. 782–803. John Wiley & Sons Ltd (2007).
62. U.S. Department of Health & Human Services: National Center for Biotechnology Information. PubChem Compound Database, https://pubchem.ncbi.nlm.nih.gov.
63. Ellmer, K., Klein, A., Rech, B.: Transparent conductive zinc oxide - Basics and Applications in Thin Films Solar Cells. (2008).
64. Kołodziejczak-Radzimska, A., Jesionowski, T.: Zinc Oxide—From Synthesis to Application: A Review. Materials (Basel). 7, 2833–2881 (2014).
65. Wiberg, E., Holleman, A.F.: Inorganic Chemistry. Elsevier (2001).
66. Greenwood, N., Earnshaw, A.: Chapter 29 – Zinc, Cadmium and Mercury. In: Chemistry of the Elements (2nd Edition). pp. 1201–1226. Butterworth-Heinemann (1997).
67. Klingshirn, C., Meyer, B., Waag, A., Hoffmann, A., Geurts, J.: Zinc Oxide - From fundamental properties towards novel applications. Springer (2010).
68. Jagadish, C., Pearton, S.: Zinc Oxide Bulk, Thin Films and Nanostructures – Processing, Properties and Application. Elsevier (2006).

69. Haynes, W.M.: CRC Handbook of Chemistry and Physics. CRC Press/Taylor & Francis.

70. Hanada, T.: Basic Properties of ZnO, GaN, and Related Materials. In: Yao, T. and Hong, S.K. (eds.) Advances in Materials Research: Oxide and Nitride Semiconductors. pp. 1–19. Springer (2009).

71. Olsen, L.C., Aguilar, H., Addis, F.W., Wenhua Lei, Jun Li: CIS solar cells with ZnO buffer layers. In: Conference Record of the Twenty Fifth IEEE Photovoltaic Specialists Conference - 1996. pp. 997–1000. IEEE (1996).

72. Platzer-Björkman, C., Törndahl, T., Abou-Ras, D., Malmström, J., Kessler, J., Stolt, L.: Zn(O,S) buffer layers by atomic layer deposition in $Cu(In,Ga)Se_2$ based thin film solar cells: Band alignment and sulfur gradient. J. Appl. Phys. 100, 44506 (2006).

73. Rusu, M., Eisele, W., Würz, R., Ennaoui, A., Lux-Steiner, M.C., Niesen, T.P., Karg, F.: Current transport in $ZnO/ZnS/Cu(In,Ga)(S,Se)_2$ solar cell. J. Phys. Chem. Solids. 64, 2037 (2003).

74. Lu, C.Y.J., Chang, L., Ploog, K.H., Chou, M.M.C.: Epitaxial growth of nonpolar ZnO on MgO (100) substrate by molecular beam epitaxy. J. Cryst. Growth. 378, 172–176 (2013).

75. Wang, X.D., Zhou, H., Wang, H.Q., Ren, F., Chen, X.H., Zhan, H.H., Zhou, Y.H., Kang, J.Y.: Cubic ZnO films obtained at low pressure by molecular beam epitaxy. Chinese Phys. B. 24, 97106 (2015).

76. Sahu, D.R., Lin, S.Y., Huang, J.L.: Improved properties of Al-doped ZnO film by electron beam evaporation technique. Microelectronics J. 38, 245–250 (2007).

77. Shen, H., Xu, L., Zheng, G., Su, J., Zhu, R.: Structural and optical properties of ZnO thin films deposited by electron beam evaporation with different annealing temperatures. J. Optoelectron. Adv. Mater. 15, 244–248 (2013).

78. Rahmane, S., Aida, M.S., Djouadi, M.A., Barreau, N.: Effects of thickness variation on properties of ZnO:Al thin films grown by RF magnetron sputtering deposition. Superlattices Microstruct. 79, 148–155 (2015).

79. Pat, S., Şenay, V., Özen, S., Korkmaz, Ş., Geçici, B.: Influence of RF Power on Optical and Surface Properties of the ZnO Thin Films Deposited by Magnetron Sputtering. J. Nanoelectron. Optoelectron. 10, 183–186 (2015).

80. Lim, S.J., Kwon, S., Kim, H.: ZnO thin films prepared by atomic layer deposition and rf sputtering as an active layer for thin film transistor. Thin Solid Films. 516, 1523–1528 (2008).

81. Minami, T., Nanto, H., Takata, S.: Highly conductive and transparent ZnO thin films prepared by r.f. magnetron sputtering in an applied external d.c. magnetic field. Thin Solid Films. 124, 43–47 (1985).

82. Wei, X.Q., Huang, J.Z., Zhang, M.Y., Du, Y., Man, B.Y.: Effects of substrate parameters on structure and optical properties of ZnO thin films fabricated by pulsed laser deposition. Mater. Sci. Eng. B. 166, 141–146 (2010).
83. Drmosh, Q.A., Rao, S.G., Yamani, Z.H., Gondal, M.A.: Crystalline nanostructured Cu doped ZnO thin films grown at room temperature by pulsed laser deposition technique and their characterization. Appl. Surf. Sci. 270, 104–108 (2013).
84. Xie, J., Lu, Q., Chen, Q.: Influence of post-annealing time on properties of ZnO:(Li, N) thin films prepared by ion beam enhanced deposition method. J. Mater. Sci. Mater. Electron. 26, 2669–2673 (2015).
85. Faÿ, S., Kroll, U., Bucher, C., Vallat-Sauvain, E., Shah, A.: Low pressure chemical vapour deposition of ZnO layers for thin-film solar cells: temperature-induced morphological changes. Sol. Energy Mater. Sol. Cells. 86, 385–397 (2005).
86. Mohanta, A., Simmons, J.G., Everitt, H.O., Shen, G., Margaret Kim, S., Kung, P.: Effect of pressure and Al doping on structural and optical properties of ZnO nanowires synthesized by chemical vapor deposition. J. Lumin. 146, 470–474 (2014).
87. Tang, K., Gu, S., Liu, J., Ye, J., Zhu, S., Zheng, Y.: Effects of indium doping on the crystallographic, morphological, electrical, and optical properties of highly crystalline ZnO films. J. Alloys Compd. 653, 643–648 (2015).
88. Zhao, J.L., Sun, X.W., Ryu, H., Moon, Y.B.: Thermally stable transparent conducting and highly infrared reflective Ga-doped ZnO thin films by metal organic chemical vapor deposition. Opt. Mater. (Amst). 33, 768–772 (2011).
89. Yamada, A., Sang, B., Konagai, M.: Atomic layer deposition of ZnO transparent conducting oxides. Appl. Surf. Sci. 112, 216–222 (1997).
90. Banerjee, P., Lee, W.J., Bae, K.R., Lee, S.B., Rubloff, G.W.: Structural, electrical, and optical properties of atomic layer deposition Al-doped ZnO films. J. Appl. Phys. 108, 43504 (2010).
91. Ouerfelli, J., Regragui, M., Morsli, M., Djeteli, G., Jondo, K., Amory, C., Tchangbedji, G., Napo, K., Bernède, J.C.: Properties of ZnO thin films deposited by chemical bath deposition and post annealed. J. Phys. D. Appl. Phys. 39, 1954–1959 (2006).
92. Shanmuganathan, G., Banu, I.B.S., Krishnan, S., Ranganathan, B.: Influence of K-doping on the optical properties of ZnO thin films grown by chemical bath deposition method. J. Alloys Compd. 562, 187–193 (2013).
93. Ohyama, M., Kouzuka, H., Yoko, T.: Sol-gel preparation of ZnO films with extremely preferred orientation along (002) plane from zinc acetate solution. Thin Solid Films. 306, 78–85 (1997).
94. Duan, L., Zhao, X., Zhang, Y., Shen, H., Liu, R.: Fabrication of flexible

Al-doped ZnO films via sol–gel method. Mater. Lett. 162, 199–202 (2016).

95. Wienke, J., van der Zanden, B., Tijssen, M., Zeman, M.: Performance of spray-deposited ZnO:In layers as front electrodes in thin-film silicon solar cells. Sol. Energy Mater. Sol. Cells. 92, 884–890 (2008).

96. Fortunato, E., Ginley, D., Hosono, H., Paine, D.C.: Transparent Conducting Oxides for Photovoltaics. MRS Bull. 32, 242–247 (2007).

97. Ishibashi, S.: Low resistivity indium–tin oxide transparent conductive films. II. Effect of sputtering voltage on electrical property of films. J. Vac. Sci. Technol. A Vacuum, Surfaces, Film. 8, 1403 (1990).

98. Kwak, D.J., Moon, B.H., Lee, D.K., Park, C.S., Sung, Y.M.: Comparison of transparent conductive indium tin oxide, titanium-doped indium oxide, and fluorine-doped tin oxide films for dye-sensitized solar cell application. J. Electr. Eng. Technol. 6, 684–687 (2011).

99. Kwak, D.J., Kim, J.H., Park, B.W., Sung, Y.M., Park, M.W., Choo, Y.B.: Growth of ZnO:Al transparent conducting layer on polymer substrate for flexible film typed dye-sensitized solar cell. Curr. Appl. Phys. 10, S282–S285 (2010).

100. Wang, X.J., Li, D.J., Tao, H.Q., Wang, J.: Effects of Deposition Temperatures on ZnO:Al Films Deposited on Polymer Substrates by RF Magnetron Sputtering. Adv. Mater. Res. 415–417, 1871–1874 (2011).

101. Agarwal, M., Modi, P., Dusane, R.O.: Study of Electrical, Optical and Structural Properties of Al-Doped ZnO Thin Films on PEN Substrates. J. NANO- Electron. Phys. 5, 2027-2027–4 (2013).

102. Nagamoto, K., Kato, K., Naganawa, S., Kondo, T., Sato, Y., Makino, H., Yamamoto, N., Yamamoto, T.: Structural, electrical and bending properties of transparent conductive Ga-doped ZnO films on polymer substrates. Thin Solid Films. 520, 1411–1415 (2011).

103. Yu, X., Hu, Z.Y., Huang, Z.H., Yu, X.M., Zhang, J.J., Zhao, G.S., Zhao, Y.: Effects of annealing rate and morphology of sol-gel derived ZnO on the performance of inverted polymer solar cells. Chinese Phys. B. 22, 118801 (2013).

104. Gong, L., Lu, J., Ye, Z.: Room-temperature growth and optoelectronic properties of GZO/ZnO bilayer films on polycarbonate substrates by magnetron sputtering. Sol. Energy Mater. Sol. Cells. 94, 1282–1285 (2010).

105. Fortunato, E., Gonçalves, A., Assunção, V., Marques, A., Águas, H., Pereira, L., Ferreira, I., Martins, R.: Growth of ZnO:Ga thin films at room temperature on polymeric substrates: Thickness dependence. Thin Solid Films. 442, 121–126 (2003).

106. Kao, J.Y., Hsu, C.Y., Chen, G.C., Wen, D.C.: The characteristics of transparent conducting Al-doped zinc oxide thin films deposited on polymer substrates. J. Mater. Sci. Mater. Electron. 23, 1352–1360 (2012).

107. Huang, H.-W., Chen, S.-H., Lee, C.-C.: Research of ZnS as a buffer layer for CIGS solar cells. Thin Film Sol. Technol. II. 7771, 77710Q–77710Q–8 (2010).

108. Ohtake, Y., Kushiya, K., Ichikawa, M., Yamada, A., Konagai, M.: Polycrystalline Cu(InGa)Se_2 thin-film solar cells with ZnSe buffer layers. Japanese J. Appl. Physics, Part 1 Regul. Pap. Short Notes Rev. Pap. 34, 5949–5955 (1995).

109. Nakada, T., Mizutani, M.: 18% efficiency Cd-free Cu(In, Ga)Se_2 thin-film solar cells fabricated using chemical bath deposition (CBD)-ZnS buffer layers. Japanese J. Appl. Physics, Part 2 Lett. (2002).

110. Platzer-Björkman, C., Hultqvist, A., Pettersson, J., Törndahl, T.: Band gap engineering of ZnO for high efficiency CIGS based solar cells. Oxide-based Mater. Devices. 7603, 76030F–76030F–9 (2010).

111. Siebentritt, S.: Alternative buffers for chalcopyrite solar cells. Sol. Energy. 77, 767–775 (2004).

112. Buffière, M., Harel, S., Arzel, L., Deudon, C., Barreau, N., Kessler, J.: Fast chemical bath deposition of Zn(O,S) buffer layers for Cu(In,Ga)Se_2 solar cells. Thin Solid Films. 519, 7575–7578 (2011).

113. Kushiya, K.: Development of Cu(InGa)Se-based thin-film PV modules with a Zn(O,S,OH) buffer layer. Sol. Energy. 77, 717–724 (2004).

114. Sáez-Araoz, R., Ennaoui, A., Kropp, T., Veryaeva, E., Niesen, T.P., Lux-Steiner, M.C.: Use of different Zn precursors for the deposition of Zn(S,O) buffer layers by chemical bath for chalcopyrite based Cd-free thin-film solar cells. Phys. Status Solidi. 205, 2330–2334 (2008).

115. Witte, W., Abou-Ras, D., Hariskos, D.: Chemical bath deposition of Zn(O,S) and CdS buffers: Influence of Cu(In,Ga)Se_2 grain orientation. Appl. Phys. Lett. 102, 51607 (2013).

116. Platzer-Björkman, C., Kessler, J., Stolt, L., Platzer-Bjorkman, C., Kessler, J., Stolt, L.: Atomic layer deposition of Zn(O,S) buffer layers for high efficiency Cu(In,Ga)Se_2 solar cells. In: 3rd World Conference on Photovoltaic Energy Conversion. pp. 461–464 (2003).

117. Zimmermann, U., Ruth, M., Edoff, M.: Cadmium-free CIGS min-modules with ALD-grown Zn(O,S)-based buffer layers. 21st Eur. Photovolt. Sol. Energy Conf. 1831–1834 (2006).

118. Sanders, B.W., Kitai, A.: Zinc oxysulfide thin films grown by atomic layer deposition. Chem. Mater. 4, 1005–1011 (1992).

119. Klenk, R., Steigert, A., Rissom, T., Greiner, D., Kaufmann, C.A., Unold, T., Lux-Steiner, M.C.: Junction formation by Zn(O,S) sputtering yields CIGSe-based cells with efficiencies exceeding 18%. Prog. Photovoltaics Res. Appl. 22, 161–165 (2013).

120. Grimm, A., Kieven, D., Klenk, R., Lauermann, I., Neisser, A., Niesen, T., Palm, J.: Junction formation in chalcopyrite solar cells by sputtered wide gap compound semiconductors. Thin Solid Films. 520, 1330–1333

(2011).

121. Kobayashi, T., Kumazawa, T., Jehl Li Kao, Z., Nakada, T.: Cu(In,Ga)Se_2 thin film solar cells with a combined ALD-Zn(O,S) buffer and MOCVD-ZnO:B window layers. Sol. Energy Mater. Sol. Cells. 119, 129–133 (2013).
122. Nakamura, M., Kouji, Y., Chiba, Y., Hakuma, H., Kobayashi, T., Nakada, T.: Achievement of 19.7% efficiency with small-sized Cu(InGa)$(SeS)_2$ solar cells prepared by sulfurization after selenization process with Zn-based buffer. In: 2013 IEEE 39TH PHOTOVOLTAIC SPECIALISTS CONFERENCE (PVSC). pp. 849–852 (2013).
123. Dedova, T., Volobujeva, O., Klauson, J., Mere, A., Krunks, M.: ZnO Nanorods via Spray Deposition of Solutions Containing Zinc Chloride and Thiocarbamide. Nanoscale Res. Lett. 2, 391 (2007).
124. Romero, R., López-Ibáñez, R., Dalchiele, E.A., Ramos-Barrado, J.R., Martín, F., Leinen, D.: Compositional and physico-optical characterization of 0–5% Al-doped zinc oxide films prepared by chemical spray pyrolysis. J. Phys. D. Appl. Phys. 43, 95303 (2010).
125. Pawar, B.N., Jadkar, S.R., Takwale, M.G.: Deposition and characterization of transparent and conductive sprayed ZnO:B thin films. J. Phys. Chem. Solids. 66, 1779–1782 (2005).
126. Benouis, C.E., Benhaliliba, M., Sanchez-Juarez, A., Aida, M.S., Chami, F., Yakuphanoglu, F.: The effect of indium doping on structural, electrical conductivity, photoconductivity and density of states properties of ZnO films. J. Alloys Compd. 490, 62–67 (2010).
127. Sanchez-Juarez, A., Tiburcio-Silver, A., Ortiz, A., Zironi, E.P., Rickards, J.: Electrical and optical properties of fluorine-doped ZnO thin films prepared by spray pyrolysis. Thin Solid Films. 333, 196–202 (1998).
128. Maldonado, A.: Indium-doped zinc oxide thin films deposited by chemical spray starting from zinc acetylacetonate: effect of the alcohol and substrate temperature. Sol. Energy Mater. Sol. Cells. 82, 75–84 (2004).
129. Maldonado, A., de la L. Olvera, M., Asomoza, R., Tirado-Guerra, S., Maldonado, A., Reyes, A.: Highly conductive and transparent In-doped zinc ocide thin films deposited by chemical spray using $Zn(C_5H_7O_2)_2$. J. Mater. Sci. Mater. Electron. 508, 623–627 (2001).
130. Mondragón-Suárez, H., Maldonado, A., de la L. Olvera, M., Reyes, A., Castanedo-Pérez, R., Torres-Delgado, G., Asomoza, R.: ZnO:Al thin films obtained by chemical spray: Effect of the Al concentration. Appl. Surf. Sci. 193, 52–59 (2002).
131. Gledhill, S., Grimm, A., Greiner, D., Bohne, W., Lux-Steiner, M.C., Fischer, C.H.: Doping induced structural and compositional changes in ZnO spray pyrolysed films and the effects on optical and electrical properties. Thin Solid Films. 519, 4293–4298 (2011).

132. Babar, A.R., Deshamukh, P.R., Deokate, R.J., Haranath, D., Bhosale, C.H., Rajpure, K.Y.: Gallium doping in transparent conductive ZnO thin films prepared by chemical spray pyrolysis. J. Phys. D. Appl. Phys. 41, 135404 (2008).

133. Prasada Rao, T., Santhosh Kumar, M.C.: Physical properties of Ga-doped ZnO thin films by spray pyrolysis. J. Alloys Compd. 506, 788–793 (2010).

134. Gomez, H., Maldonado, A., de la L. Olvera, M., Acosta, D.R.: Gallium-doped ZnO thin films deposited by chemical spray. Sol. Energy Mater. Sol. Cells. 87, 107–116 (2005).

135. Dedova, T., Klauson, J., Badre, C., Pauporté, T., Nisumaa, R., Mere, A., Volobujeva, O., Krunks, M.: Chemical spray deposition of zinc oxide nanostructured layers from zinc acetate solutions. Phys. Status Solidi Appl. Mater. Sci. 205, 2355–2359 (2008).

136. Maticiuc, N., Hiie, J., Mikli, V., Potlog, T., Valdna, V.: Structural and optical properties of cadmium sulfide thin films modified by hydrogen annealing. Mater. Sci. Semicond. Process. 26, 169–174 (2014).

137. Maticiuc, N., Hiie, J.: Annealing effect on CdS films: transition from glass to ITO. IOP Conf. Ser. Mater. Sci. Eng. 49, 12061 (2013).

138. Hodes, G.: Chemical Solution Deposition of Semiconductor Films. Marcel Dekker, Inc., New York, NY (2003).

139. Vegard, L.: Die Konstitution der Mischkristalle und die Raumfüllung der Atome. Zeitschrift für Phys. 5, 17–26 (1921).

140. Grimm, A., Just, J., Kieven, D., Lauermann, I., Palm, J., Neisser, A., Rissom, T., Klenk, R.: Sputtered Zn(O,S) for junction formation in chalcopyrite-based thin film solar cells. Phys. status solidi - Rapid Res. Lett. 4, 109–111 (2010).

141. Kushiya, K.: Solar Frontier Sets Thin-Film PV World Record with 20.9% CIS Cell. Press release., http://www.solar-frontier.com/eng/news/2014/C031367.html.

142. Hamid, M., Wattoo, S., Syed, ·, Tirmizi, A., Quddos, A., Bilal, M., Feroza, K. ·, Wattoo, H., Wadood, A., Ghangro, A.B., Wattoo, M.H.S., Tirmizi, S.A., Quddos, A., Khan, M.B., Wattoo, F.H., Wadood, A., Ghangro, A.B.: Aerosol-Assisted Chemical Vapor Deposition of Thin Films of Cadmium Sulfide and Zinc Sulfide Prepared from Bis(dibutyldithiocarbamato)Metal Complexes. Arab J Sci Eng. 36, (2011).

143. Ehsan, M.A., Peiris, T.A.N., Wijayantha, K.G.U., Olmstead, M.M., Arifin, Z., Mazhar, M., Lo, K.M., McKee, V., Lux-Steiner, M.C., Fischer, C.-H.: Development of molecular precursors for deposition of indium sulphide thin film electrodes for photoelectrochemical applications. Dalt. Trans. 42, 10919 (2013).

144. Gledhill, S., Grimm, A., Allsop, N., Köhler, T., Camus, C., Lux-Steiner, M.C., Fischer, C.H.: A spray pyrolysis route to the undoped ZnO layer

of $Cu(In,Ga)(S,Se)_2$ solar cells. Thin Solid Films. 517, 2309–2311 (2009).

145. Sun, H.: Biological Chemistry of Arsenic, Antimony and Bismuth. John Wiley & Sons Ltd (2010).

146. Barthelmy, D.: Mineralogy Database, http://www.webmineral.com/data/Stibnite.shtml#.V9-exvB96Ht.

147. Pathan, H.M., Lokhande, C.D.: Deposition of metal chalcogenide thin films by successive ionic layer adsorption and reaction (SILAR) method. Bull. Mater. Sci. 27, 85–111 (2004).

148. Ben Nasr, T., Maghraoui-Meherzi, H., Ben Abdallah, H., Bennaceur, R.: Electronic structure and optical properties of Sb_2S_3 crystal. Phys. B. 406, 287–292 (2011).

149. Efstathiou, A., Levin, E.R.: Optical Properties of As_2Se_3, $(As_xSb_{1-x})_2Se_3$, and Sb_xS_3. J. Opt. Soc. Am. 58, 373 (1968).

150. Lim, C.S., Im, S.H., Kim, H.J., Chang, J.A., Lee, Y.H., Seok, S. Il: Enhancing the device performance of Sb_2S_3-sensitized heterojunction solar cells by embedding Au nanoparticles in the hole-conducting polymer layer. Phys. Chem. Chem. Phys. 14, 3622 (2012).

151. Versavel, M.Y., Haber, J.A.: Structural and optical properties of amorphous and crystalline antimony sulfide thin-films. Thin Solid Films. 515, 7171–7176 (2007).

152. Aousgi, F., Kanzari, M.: Structural and optical properties of amorphous Sb_2S_3 thin films deposited by vacuum thermal evaporation method. Curr. Appl. Phys. 13, 262–266 (2013).

153. Greenwood, N.N., Earnshaw, A.: Chapter 13 - Arsenic, Antimony and Bismuth. In: Chemistry of the Elements (2nd Edition). p. 1600. Elsevier (2012).

154. McKetta Jr., J.J.: Encyclopedia of Chemical Processing and Design: Volume 3 - Aluminum to Asphalt: Design. CRC Press (1977).

155. Perry, D.L.: Handbook of Inorganic Compounds. CRC Press (1995).

156. Rich, R.: Inorganic Reactions in Water. Springer (2007).

157. Madelung, O., Rössler, U., Schulz, M. eds: Non-Tetrahedrally Bonded Elements and Binary Compounds I. In: Landolt-Börnstein - Group III Condensed Matter. Springer Berlin Heidelberg (1998).

158. Rodriguez-Castro, J., Mahon, M.F., Molloy, K.C.: Aerosol-Assisted CVD of Antimony Sulfide from Antimony Dithiocarbamates. Chem. Vap. Depos. 12, 601–607 (2006).

159. Lee, H.Y., Kim, J.K., Chung, H.B.: On Ag-doping in amorphous Sb_2S_3 thin film by HeNe and HeCd laser exposures and its optical characteristics. J. Non. Cryst. Solids. 279, 209–214 (2001).

160. Frumarov, B., Bilkova, M., Frumar, M., Repka, M., Jedelsky, J.: Thin films of Sb_2S_3 doped by Sm^{3+} ions. J. Non. Cryst. Solids. 326&327, 348–352 (2003).

161. Cardenas, E., Arato, A., Perez-Tijerina, E., Roy, T.K. Das, Castillo, G.A., B. Krishnan: Carbon-doped Sb2S3 thin films: Structural, optical and electrical properties. Sol. Energy Mater. Sol. Cells. 93, 33–36 (2009).
162. Aousgi, F., Kanzari, M.: Study of the Optical Properties of Sn-doped Sb_2S_3 Thin Films. Energy Procedia. 10, 313–322 (2011).
163. Manolache, S.A., Duta, A.: The development of crystalline Sb_2S_3 thin films as buffer layer or as absorber material for three-dimensional (3D) solar cells. In: Proceedings of the International Semiconductor Conference, CAS. pp. 373–376 (2007).
164. Moon, S.J., Itzhaik, Y., Yum, J.H., Zakeeruddin, S.M., Hodes, G., Grätzel, M.: Sb_2S_3 -Based Mesoscopic Solar Cell using an Organic Hole Conductor. J. Phys. Chem. Lett. 1, 1524–1527 (2010).
165. Itzhaik, Y., Niitsoo, O., Page, M., Hodes, G.: Sb_2S_3-Sensitized Nanoporous TiO_2 Solar Cells. J. Phys. Chem. C. 113, 4254–4256 (2009).
166. Messina, S., Nair, M.T.S., Nair, P.K.: Solar cells with Sb_2S_3 absorber films. Thin Solid Films. 517, 2503–2507 (2009).
167. Boix, P.P., Larramona, G., Jacob, A., Delatouche, B., Mora-Seró, I., Bisquert, J.: Hole Transport and Recombination in All-Solid Sb_2S_3 -Sensitized TiO_2 Solar Cells Using CuSCN As Hole Transporter. J. Phys. Chem. C. 116, 1579–1587 (2012).
168. Krunks, M., Kärber, E., Katerski, A., Otto, K., Oja Acik, I., Dedova, T., Mere, A.: Extremely thin absorber layer solar cells on zinc oxide nanorods by chemical spray. Sol. Energy Mater. Sol. Cells. 94, 1191–1195 (2010).
169. Messina, S., Nair, M.T.S., Nair, P.K.: Antimony sulfide thin films in chemically deposited thin film photovoltaic cells. Thin Solid Films. 515, 5777–5782 (2007).
170. Killedar, V.V., Lokhande, C.D., Bhosale, C.H.: Preparation and characterization of spray deposited Sb2S3 thin films from non-aqueous medium. Mater. Chem. Phys. 47, 104–107 (1997).
171. Nezu, S., Larramona, G., Choné, C., Jacob, A., Delatouche, B., Péré, D., Moisan, C.: Light Soaking and Gas Effect on Nanocrystalline TiO_2/Sb_2S_3/CuSCN Photovoltaic Cells following Extremely Thin Absorber Concept. J. Phys. Chem. C. 114, 6854–6859 (2010).
172. Kieven, D., Grimm, A., Lauermann, I., Rissom, T., Klenk, R.: Band alignment at Sb_2S_3/Cu(In,Ga)Se_2 heterojunctions and electronic characteristics of solar cell devices based on them. Appl. Phys. Lett. 96, 262101 (2010).
173. Maghraoui-Meherzi, H., Ben Nasr, T., Kamoun, N., Dachraoui, M.: Structural, morphology and optical properties of chemically deposited Sb_2S_3 thin films. Phys. B Condens. Matter. 405, 3101–3105 (2010).
174. Salem, A.M., Selim, M.S.: Structure and optical properties of chemically

deposited Sb_2S_3 thin films. J. Phys. D. Appl. Phys. 34, 12–17 (2001).

175. Ito, S., Tsujimoto, K., Nguyen, D.-C., Manabe, K., Nishino, H.: Doping effects in Sb_2S_3 absorber for full-inorganic printed solar cells with 5.7% conversion efficiency. Int. J. Hydrogen Energy. 38, 16749–16754 (2013).

176. Yesugade, N.S., Lokhande, C.D., Bhosale, C.H.: Structural and optical properties of electrodeposited Bi_2S_3, Sb_2S_3 and As_2S_3 thin films. Thin Solid Films. 263, 145–149 (1995).

177. Mady, K.A., El-Nahas, M.M., Farid, A.M., Soliman, H.S.: Electrical resistivity of amorphous antimony trisulphide films. J. Mater. Sci. 23, 3636–3639 (1988).

178. Srikanth, S., Suriyanarayanan, N., Prabahar, S., Balasubramanian, V., Kathirvel, D.: Photoluminescence studies on Sb_2S_3 thin films prepared by vacuum evaporation and spray pyrolysis technique. Optoelectron. Adv. Mater. – Rapid Commun. 4, 2057–2058 (2010).

179. Abd-El-Rahman, K.F., Darwish, A.A.A.: Fabrication and electrical characterization of p-Sb_2S_3/n-Si heterojunctions for solar cells application. Curr. Appl. Phys. 11, 1265–1268 (2011).

180. Rajpure, K.Y., Bhosale, C.H.: Effect of composition on the structural, optical and electrical properties of sprayed Sb_2S_3 thin films prepared from non-aqueous medium. J. Phys. Chem. Solids. 61, 561–568 (2000).

181. Gadakh, S.R., Bhosale, C.H.: Effect of concentration of complexing agent (tartaric acid) on the properties of spray deposited Sb_2S_3 thin films. Mater. Chem. Phys. 78, 367–371 (2002).

182. Rajpure, K.Y., Bhosale, C.H.: Preparation and characterization of spray deposited photoactive Sb_2S_3 and Sb_2Se_3 thin films using aqueous and non-aqueous media. Mater. Chem. Phys. 73, 6–12 (2002).

183. Bhosale, C.H., Uplane, M.D., Patil, P.S., Lokhande, C.D.: Preparation and properties of sprayed antimony trisulphide films. Thin Solid Films. 248, 137–139 (1994).

184. Rajpure, K.Y., Lokhande, C.D., Bhosale, C.H.: A comparative study of concentration effect of complexing agent on the properties of spray deposited Sb_2S_3 thin films and precipitated powders. Mater. Chem. Phys. 51, 252–257 (1997).

185. Desai, J.D., Lokhande, C.D.: Solution growth of microcrystalline Sb_2S_3 thin films from thioacetamide bath. J. Non. Cryst. Solids. 181, 70–76 (1995).

186. Rajpure, K.Y., Dhebe, A.L., Lokhande, C.D., Bhosale, C.H.: Effect of relative amount of complexing agents on the properties of Sb_2S_3 precipitated powders. Mater. Chem. Phys. 56, 177–183 (1998).

187. Killedar, V.V., Rajpure, K.Y., Patil, P.S., Bhosale, C.H.: Transient photoconductivity measurements of spray deposited Sb_2S_3 and Bi_2S_3 thin films from non-aqueous medium. Mater. Chem. Phys. 59, 237–241

(1999).

188. Rajpure, K.Y., Bhosale, C.H.: Sb_2S_3 semiconductor-septum rechargeable storage cell. Mater. Chem. Phys. 64, 70–74 (2000).

189. Rajpure, K.Y., Bhosale, C.H.: A study of substrate variation effects on the properties of n-Sb_2S_3 thin film/polyiodide/C photoelectrochemical solar cells. Mater. Chem. Phys. 64, 14–19 (2000).

190. Rajpure, K.Y., Bhosale, C.H.: (Photo) electrochemical investigations on spray deposited Sb_2S_3 thin film/polysulphide/c photoelectrochemical solar cell. Appl. Sol. Energy. 46, 194–201 (2010).

191. Boughalmi, R., Boukhachem, A., Kahlaoui, M., Maghraoui, H., Amlouk, M.: Physical investigations on Sb_2S_3 sprayed thin film for optoelectronic applications. Mater. Sci. Semicond. Process. 26, 593–602 (2014).

192. International Centre for Diffraction Data (ICDD). (2008).

193. Minami, T.: Transparent conducting oxide semiconductors for transparent electrodes. Semicond. Sci. Technol. 20, S35–S44 (2005).

194. Wienke, J., Booij, A.S.: ZnO:In deposition by spray pyrolysis - Influence of the growth conditions on the electrical and optical properties. Thin Solid Films. 516, 4508–4512 (2008).

195. Keller, R.M., Baker, S.P., Arzt, E.: Quantitative analysis of strengthening mechanisms in thin Cu films: Effects of film thickness, grain size, and passivation. J. Mater. Res. 13, 1307–1317 (1998).

196. Venkatraman, R., Bravman, J.C.: Separation of film thickness and grain boundary strengthening effects in Al thin films on Si. J. Mater. Res. 7, 2040–2048 (1992).

197. Brunetti, B., Piacente, V., Scardala, P.: A torsion Study on the Sublimation Process of $InCl_3$. Mater. Chem. Phys. 43, 101–104 (1998).

198. Katerski, A., Mere, A., Kazlauskiene, V., Miskinis, J., Saar, A., Matisen, L., Kikas, A., Krunks, M.: Surface analysis of spray deposited copper indium disulfide films. Thin Solid Films. 516, 7110–7115 (2008).

199. Gong, L., Ye, Z., Lu, J., Zhu, L., Huang, J., Gu, X., Zhao, B.: Highly transparent conductive and near-infrared reflective ZnO:Al thin films. Vacuum. 84, 947–952 (2010).

200. Bhosle, V., Tiwari, A., Narayan, J.: Electrical properties of transparent and conducting Ga doped ZnO. J. Appl. Phys. 100, (2006).

201. Hafdallah, A., Yanineb, F., Aida, M.S., Attaf, N.: In doped ZnO thin films. J. Alloys Compd. 509, 7267–7270 (2011).

202. Li, D.P., Zheng, Z., Lei, Y., Yang, F.L., Ge, S.X., Zhang, Y.D., Huang, B.J., Gao, Y.H., Wong, K.W., Lau, W.M.: From nanoplates to microtubes and microrods: A surfactant-free rolling mechanism for facile fabrication and morphology evolution of Ag_2S films. Chem. - A Eur. J. 17, 7694–7700 (2011).

203. Wang, Z.L.: ZnO nanowire and nanobelt platform for nanotechnology. Mater. Sci. Eng. R Reports. 64, 33–71 (2009).

204. Söderström, T., Haug, F.J., Niquille, X., Terrazzoni, V., Ballif, C.: Asymmetric intermediate reflector for tandem micromorph thin film silicon solar cells. Appl. Phys. Lett. 94, 1–4 (2009).

205. Guillén, C., Herrero, J.: Optical, electrical and structural characteristics of Al:ZnO thin films with various thicknesses deposited by DC sputtering at room temperature and annealed in air or vacuum. Vacuum. 84, 924–929 (2010).

206. Fortunato, E., Nunes, P., Costa, D., Brida, D., Ferreira, I., Martins, R.: Characterization of aluminium doped zinc oxide thin films deposited on polymeric substrates. Vacuum. 64, 233–236 (2002).

207. Grabitz, P.O., Rau, U., Werner, J.H.: A multi-diode model for spatially inhomogeneous solar cells. Thin Solid Films. 487, 14–18 (2005).

208. Oja Acik, I., Otto, K., Krunks, M., Tõnsuaadu, K., Mere, A.: Thermal behaviour of precursors for $CuInS_2$ thin films deposited by spray pyrolysis. J. Therm. Anal. Calorim. 113, 1455–1465 (2013).

209. Otto, K., Bombicz, P., Madarász, J., Oja Acik, I., Krunks, M., Pokol, G.: Structure and evolved gas analyses (TG/DTA-MS and TG-FTIR) of mer-trichlorotris(thiourea)-indium(III), a precursor for indium sulfide thin films. J. Therm. Anal. Calorim. 105, 83–91 (2011).

210. Madarász, J., Pokol, G.: Comparative evolved gas analyses on thermal degradation of thiourea by coupled TG-FTIR and TG/DTA-MS instruments. J. Therm. Anal. Calorim. 88, 329–336 (2007).

211. Kärber, E., Katerski, A., Acik, I.O., Mere, A., Mikli, V., Krunks, M.: Sb_2S_3 grown by ultrasonic spray pyrolysis and its application in a hybrid solar cell. Beilstein J. Nanotechnol. 7, 1662–1673 (2016).

212. Polivtseva, S., Acik, I.O., Katerski, A., Mere, A., Mikli, V., Krunks, M.: Spray Pyrolysis Deposition of Sn_xS_y Thin Films. Energy Procedia. 60, 156–165 (2014).

213. Krunks, M., Kijatkina, O., Rebane, H., Oja, I., Mikli, V., Mere, A., Rebane, H., Oja, I., Krunks, M., Kijatkina, O., Mikli, V.: Composition of $CuInS_2$ thin films prepared by spray pyrolysis. Thin Solid Films. 403–404, 71–75 (2002).

214. Krunks, M., Mere, A., Katerski, A., Mikli, V., Krustok, J.: Characterization of sprayed $CuInS_2$ films annealed in hydrogen sulfide atmosphere. Thin Solid Films. 511–512, 434–438 (2006).

215. Otto, K., Katerski, A., Mere, A., Volobujeva, O., Krunks, M.: Spray pyrolysis deposition of indium sulphide thin films. Thin Solid Films. 519, 3055–3060 (2011).

216. Parize, R., Katerski, A., Gromyko, I., Rapenne, L., Roussel, H., Kärber, E., Appert, E., Krunks, M., Consonni, V.: $ZnO/TiO_2/Sb_2S_3$Core–Shell Nanowire Heterostructure for Extremely Thin Absorber Solar Cells. J. Phys. Chem. C. in press, acs.jpcc.7b00178 (2017).

APPENDIX A

Article **I**

Vent, M.; Kärber, E.; Unt, T.; Mere, A.; Krunks, M. (2012). The effect of growth temperature and spraying rate on properties of ZnO:In films. physica status solidi (c), 9 (7), 1604−1606.

Phys. Status Solidi C **9**, No. 7, 1604–1606 (2012) / **DOI** 10.1002/pssc.201200008

physica status solidi pss c
www.pss-c.com
current topics in solid state physics

The effect of growth temperature and spraying rate on the properties of ZnO:In films

Merike Vent, Erki Kärber, Tarmo Unt, Arvo Mere, and Malle Krunks[*]

Department of Materials Science, Tallinn University of Technology, Ehitajate tee 5, 19086 Tallinn, Estonia

Received 14 February 2012, accepted 16 February 2012

Keywords zinc oxide, spray pyrolysis, spraying rate, electrical resistivity

---

[*] Corresponding author: e-mail malle.krunks@ttu.ee, Phone: +372 620 33 63, Fax: +372 620 33 67

ZnO:In thin films were deposited by chemical spray pyrolysis from zinc acetate solutions containing 3 at.% of $InCl_3$. The films were grown in the temperature region of 400-500 °C using solution spraying rates 0.6-7.1 ml/min. ZnO:In films were characterized by XRD, Hall and van der Pauw methods. The dependence of the film resistivity vs growth temperature is parabolic. ZnO:In films with resistivity minimum of $3\mathrm{x}10^{-3}$ Ωcm can be deposited at 450 °C. The solution spraying rate has strong effect on the film resistivity, deposition rates below 3 ml/min result in high resistivities.

1 Introduction Zinc oxide (ZnO) is a widely used semiconductor material for applications such as gas sensors, reflecting coatings and transparent conductive layers in photovoltaic devices [1–7]. ZnO thin films could be deposited by several methods, such as magnetron sputtering, metal-organic chemical vapour deposition, and pulsed laser deposition. Chemical spray pyrolysis, used in this study, is a simple and fast method to obtain electrically conductive and highly transparent ZnO thin films at low cost. Electrically conductive ZnO thin films can be obtained by doping with suitable elements (e.g. Al, Ga, In) [1, 6, 7]. The effect of dopant concentration in spray solution has been vastly studied [2–6]. It is reported that 3 at.% of dopant in the spray solution is optimal to grow electrically conductive ZnO films [1, 5, 6]. The effect of the growth temperature to the electrical and optical properties of ZnO films has been studied [5, 6], the film growth temperatures close to 400 °C are reported to be optimal. The influence of spraying rate has been less studied, it is found that the spraying rate affects the film morphology [8]. The aim of this study is to investigate the effect of growth temperature and spraying rate to structural and electrical properties of ZnO:In thin films.

2 Experimental ZnO films were deposited by pneumatic spray of precursor solution onto preheated glass substrate (thickness 1 mm). $Zn(CH_3COO)_2 \cdot 2H_2O$ (Merck, 99.5%) was used as the precursor dissolved in a mixture of deionized water and isopropyl alcohol (2:3 by volume). The precursor concentration in solution was fixed to 0.2 mol/l, few drops of acetic acid were added to avoid precipitation of zinc hydroxide. Indium(III)chloride ($InCl_3$) was used as doping agent added to the spray solution. Indium to zinc concentration was kept constant at 3 at.%. Glass substrates were placed onto a hot plate with a temperature (T_S) ranging from 400 °C to 550 °C. The growth temperature of thin films is about 50 °C lower than the T_s depending slightly on the spraying rate. Spray solution volumes of 50 ml and 100 ml were used for deposition and the spraying rate (v) varied from 0.5 to 7.1 ml/min. The structure of the films was characterized by X-ray diffraction (XRD) using a Rigaku Ultima IV diffractometer with monochromatic Cu Kα radiation. Crystallite size was calculated using the Debye-Scherrer method. Electrical properties (resistivity, Hall mobility and carrier concentration) of the thin films were measured by Van der Pauw and Hall method at room temperature.

3 Results and discussions

3.1 Effect of solution volume and growth temperature on the film electrical properties

The resistivity of the sprayed ZnO:In films has a parabolic dependency on the growth temperature (Fig. 1). As the temperature (T_S) increases from 400 °C to 450 °C, the resistivity (ρ) of thin films decreases from 1.5×10^{-2} to 4×10^{-3} Ωcm as both mobility (μ) and carrier concentration (n) are increasing. Mobility increased from 10 to 15 $cm^2V^{-1}s^{-1}$ due to larger crystallite sizes of films deposited at 450 °C (32 nm) compared to that at 400 °C (25 nm), and n increased from 3×10^{19} to 2×10^{20} cm^{-3}. Further increase in T_S from 450 to 550 °C increases the ρ from 4×10^{-3} to 1.8×10^{-2} Ωcm as μ and n decrease. The decrease in μ could be explained by decreased film thickness (from 700 to 500 nm) and crystallite size (from 33 to 25 nm). Dependence of μ on the film thickness and crystallite size is well-known [10, 11].

Followingly, to eliminate the limitations caused by the film thickness, 100 ml of solution was sprayed instead of 50 ml. The films with thicknesses of 1100-1500 nm were obtained. The film resistivity had a parabolic dependency vs T_S with an optimum temperature of 450°C which corresponds to a minimum of the resistivity (3×10^{-3} Ωcm) (not shown). Similarly to the films from 50 ml of solution, n decreases (from 2×10^{20} to 5×10^{19} cm^{-3}) while increasing the T_S. Decrease in n while increasing film growth temperaure is similar to that reported for ZnO:Al [6]. Likely, the lowered carrier concentration could be explained by the oxidation of the dopant at elevated temperatures. As higher solution amount results in thicker films with $\mu>10$ $cm^2V^{-1}s^{-1}$ then our next experiments on the effect of the solution v at different T_S were performed using solution volume of 100 ml.

3.2 Effect of growth temperature and spraying rate on the film structure and thickness Figure 2 depicts the effect of the T_S and v on the structure of sprayed ZnO:In films. The crystallites in ZnO:In films deposited at T_S of 450 °C (Fig. 2a) are preferably orientated (101) plane parallel to the substrate, which is in good accordance with that reported for sprayed ZnO:In films [3, 12], the spraying rate has insignificant effect. XRD patterns of ZnO:In films grown at T_S 500 °C with v<3.0 ml/min are similar to the films grown at 450 °C. Using v>3 ml/min, the relative intensities of (100) and (110) reflections increase (Fig. 2a) and the crystallites in ZnO:In film are preferably orientated parallel to the (110) plane. XRD patterns of the films grown at T_S of 400 °C with v<1.5 ml/min (Fig. 2b) are similar to the films grown at 450 °C. Increasing the v up to 3.9 ml/min increases the intensities of (002), (102) and (103) reflections. Further rise in v increases the intensities of (100) and (110) reflections. XRD study shows that spraying rate has strong effect on the crystallite orientation when deposited at 400 or 500 °C. Table 1 presents the film thicknesses (measured from the SEM cross-sections) and crystallite sizes depending on the T_S and v. At slower spraying rates the films are thinner and crystallite sizes are smaller. Crystallites in the films grown at T_S=500 °C are smaller than in the films grown at lower T_S. Similar tendency was observed by El Hichou et al. [13].

3.3 Effect of spraying rate on the film electrical properties Spraying rate has critical effect on the resistivity of ZnO:In films (Fig. 3). Using the slowest solution spraying rate of 0.6 ml/min the film resistivities are the highest independent of T_S. Increasing the v decreases the resistivities drastically and the lowest values are obtained for the films deposited with the v≥3 ml/min. It is interesting to notice that at T_S=400 °C, the ρ starts to in-

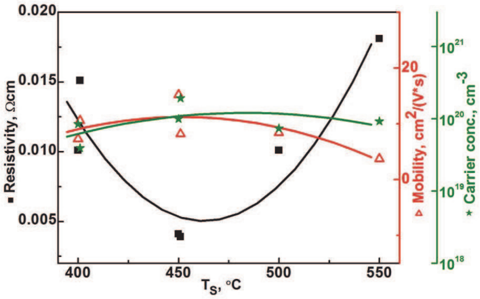

Figure 1 The resistivity (■), mobility (Δ) and carrier concentration (✱) of ZnO:In films grown at different temperatures from 50 ml of solution with spraying rate of 3.8 ml/min.

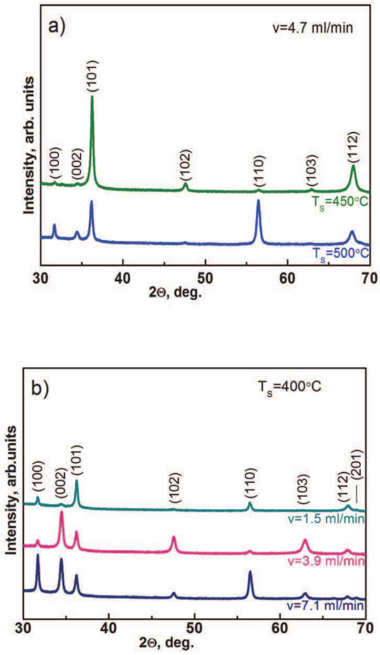

Figure 2 XRD patterns of sprayed ZnO:In films deposited at a) T_S of 450 °C and 500 °C, v= 4.7 ml/min; b) T_S of 400 °C with v=1.5, 3.9 and 7.1 ml/min.

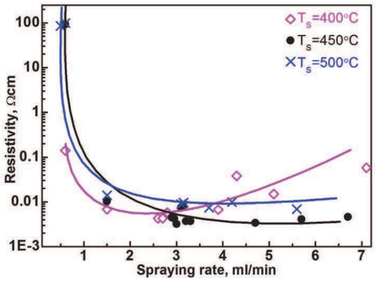

Figure 3 The resistivities of ZnO:In films deposited at different temperatures with various spraying rates.

crease using v>4 ml/min. The films deposited at 450 °C and 500 °C show similar tendency with respect to spraying rate (Fig. 3), however, films grown at 500 °C remain less conductive. This could be explained by a smaller average crystallite size in films deposited at 500 °C (Table 1), leading to a decreased carrier mobility. In addition, a slightly lower carrier concentration is characteristic of the films deposited at T_S of 500 °C. The film resistivity of $1.8x10^2$ Ωcm obtained with the slowest spraying rate of 0.6 ml/min is mainly caused by low n in the order of 10^{16} cm^{-3}. In addition, a relatively low mobility of 5 $cm^2V^{-1}s^{-1}$ at lower spraying rates is observed, which can be explained by lower film thickness and smaller crystallite size (Table 1 and Fig. 4), compared to films deposited at higher spraying rates. Increasing spraying rate v up to 1.5 ml/min increases both, n and μ. Using spraying rates between 2.9 and 6.7 ml/min, n~10^{20} cm^{-3} and μ remains above 10 $cm^2V^{-1}s^{-1}$ for the whole set of samples deposited at T_S=450 °C. The highest obtained μ was 14 $cm^2V^{-1}s^{-1}$ and highest n was $2x10^{20}$ cm^{-3}. These results are close to that reported for ZnO:In films deposited by ultrasonic [9] or pneumatic spray [2, 3].

4 Conclusions The effect of the temperature on the film resistivity was clearly parabolic, measurements indicated resistivity minimum of ca $3x10^{-3}$ Ωcm if grown at 450 °C. Low spraying rates result in high film resistivity as both carrier concentration and mobility are low. The results of this study show that chemical spray pyrolysis is a promising method for deposition of electrically conductive ZnO films.

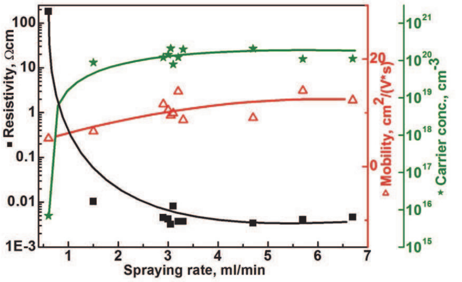

Figure 4 The resistivity (■), mobility (Δ) and carrier concentration (✱) of ZnO:In films grown from 100 ml of solution with various spraying rates at T_S=450 °C.

Acknowledgements Financing by Estonian Ministry of Education and Research (SF0140092s08), Estonian Science Foundation (ETF8509, ETF9081) is gratefully acknowledged.

References

[1] M. de la L. Olvera, H. Gomez, and A. Maldonado, Sol. Energy Mater. Sol. Cells **91**, 1449 (2007).

[2] T. Prasada Rao and M. C. Santhosh Kumar, J. Alloys Compd. **506**, 788 (2010).

[3] S. S. Shinde, P. S. Shinde, C. H. Bhosale, and K. Y. Rajpure, J. Phys. D: Appl. Phys. **41**, 105 (2008).

[4] C. M. Muiva, T. S. Sathiarah, and K. Maabong, Ceram. Int. **37**, 555 (2011).

[5] A. Maldonado, M. de la L. Olvera, S. Tirado Guerra, and R. Asomoza, Sol. Energy Mater. Sol. Cells **82**, 75 (2004).

[6] B. J. Babu, A. Maldonado, S. Velumani, and R. Asomoza, Mater. Sci. Eng. B **174**, 31 (2008).

[7] P. Nunes, E. Fortunato, and R. Martins, Thin Solid Films **383**, 277 (2001).

[8] T. Dedova, J. Klauson, C. Badre, Th. Pauporte, R. Nisumaa, A. Mere, O. Volobujeva, and M. Krunks, Phys Status Solidi A **10**, 2355 (2008).

[9] J. Wienke and A. S. Booij, Thin Solid Films **516**, 4508 (2008).

[10] T. Minami, Semicond. Sci. Technol. **20**, S35 (2005).

[11] C. Guillén and J. Herrero, Vacuum **84**, 924 (2010).

[12] P. Nunes, A. Malik, B. Fernandes, E. Fortunato, P.Vilarinho, and R. Martins, Vacuum **52**, 45 (1999).

[13] A. El Hichou, M Addou, J. Ebothé, and M. Tyron, J. Lumin. **113**, 183 (2005).

Table 1 Film thickness and crystallite size for ZnO:In films deposited from 100 ml of solution at different temperatures (T_S) and spraying rates (v).

Spraying rate (v), ml/min	Film thickness, nm			Crystallite size, nm		
	T_S=400 °C	T_S=450 °C	T_S=500 °C	T_S=400 °C	T_S=450 °C	T_S=500 °C
0.6	835	720	840	31	22	20
1.5	750	940	1180	38	21	22
3.0	1100	1300	1520	39	29	30
3.9	1310	1440	1220	32	35	29
5.6	-	1170	1520	-	35	24

Article **II**

Kriisa, M.; Krunks, M.; Kärber, E.; Kukk, M.; Mikli, V.; Mere, A. (2013). Effect of Solution Spray Rate on the Properties of Chemically Sprayed ZnO:In Thin Films. Journal of Nanomaterials, 2013, Article ID 423632.

Hindawi Publishing Corporation
Journal of Nanomaterials
Volume 2013, Article ID 423632, 9 pages
http://dx.doi.org/10.1155/2013/423632

Research Article

Effect of Solution Spray Rate on the Properties of Chemically Sprayed ZnO:In Thin Films

Merike Kriisa,[1] Malle Krunks,[1] Erki Kärber,[1] Mart Kukk,[1] Valdek Mikli,[2] and Arvo Mere[1]

[1] Department of Materials Science, Tallinn University of Technology, Ehitajate Tee 5, 19086 Tallinn, Estonia
[2] Centre for Materials Research, Tallinn University of Technology, Ehitajate Tee 5, 19086 Tallinn, Estonia

Correspondence should be addressed to Malle Krunks; malle.krunks@ttu.ee

Received 14 December 2012; Accepted 1 March 2013

Academic Editor: Jie-Fang Zhu

ZnO:In thin films were grown from 100 mL of spray solution on glass substrates by chemical spray at $T_s = 400^\circ$C using solution spray rates of 0.5–6.7 mL/min. Zinc acetate and indium(III)chloride were used as Zn and In sources, respectively, with [In]/[Zn] = 3 at.%. Independent of solution spray rate, the crystallites in ZnO:In films grow preferentially in the (101) plane parallel to the substrate. The solution spray rate influences the surface morphology, grain size, film thickness, and electrical and optical properties. According to SEM and AFM studies, sharp-edged pyramidal grains and canvas-resembling surfaces are characteristic of films grown at spray rates of 0.5 and 3.3 mL/min, respectively. To obtain films with comparable film thickness and grain size, more spray solution should be used at low spray rates. The electrical resistivity of sprayed ZnO:In films is controlled by the solution spray rate. The carrier concentration increases from $2 \cdot 10^{19}$ cm^{-3} to $1 \cdot 10^{20}$ cm^{-3} when spray rate is increased from 0.5 mL/min to 3.3 mL/min independent of the film thickness; the carrier mobilities are always lower in slowly grown films. Sprayed ZnO:In films transmit 75–80% of the visible light while the increase in solution spray rate from 0.5 mL/min to 3.3 mL/min decreases the transmittance in the NIR region and increases the band gap in accordance with the increase in carrier concentration. Lower carrier concentration in slowly sprayed films is likely due to the indium oxidation.

1. Introduction

The wide band gap zinc oxide can be used in many applications, for example, in piezoelectric transducers, as transparent conductive layers (TCO-s), and as window layers in photovoltaic devices [1]. Various methods such as atomic layer deposition (ALD) [2], pulsed laser deposition (PLD) [3], chemical bath deposition (CBD) [4], RF magnetron sputtering [5], and chemical spray pyrolysis (CSP) [3, 6–16] have been used to deposit ZnO thin films. Among these methods, the spray pyrolysis is a versatile and cost-effective method for the rapid production of large-area metal oxide thin films.

Up to date, the effect of several technological parameters (zinc source and concentration, dopant type and concentration, solvent, growth temperature, etc.) on the properties of sprayed ZnO films have been studied [6–16] to determine the optimal deposition conditions to obtain as high electrical conductivity and optical transparency as possible. Earlier studies have shown that the preferred crystallite orientation of intrinsic ZnO and gallium- and aluminium-doped ZnO is along *c*-axis [8, 9, 15] while the preferred crystallite orientation of indium-doped ZnO film is (101) plane parallel to the substrate [7–9, 12, 15]. The use of Ga or Al as the dopant leads to smaller grains than the use of In as a dopant [6, 7, 9]. Additionally, the density and the optical transmittance of sprayed ZnO film is controlled by the dopant type and concentration [7]. It has been reported that an optimal growth temperature for sprayed ZnO films is in the range of 350–500°C. Independent of dopant, the optical transmittance is ca. 85% [7, 9, 17–19] while the lowest resistivities of sprayed indium-doped and gallium-doped ZnO thin films are in the order of 10^{-4}–10^{-3} Ωcm [17, 18] and in the order of 10^{-3}–10^{-2} Ωcm for aluminium-doped ZnO [19].

Sprayed ZnO:In thin films have been used successfully as front electrodes in thin film silicon solar cells [20] and as window layer in Cu(In,Ga)(S,Se) solar cells [21]. Our long-term goal is to study the feasibility of ITO substitution with

ZnO:In, for use as the front electrode in the CSP-prepared extremely thin inorganic absorber (ETA) solar cell [22].

Among mentioned technological parameters, the solution spray rate (or solution flow rate) and its effect on ZnO thin films have received little attention. Ebothé et al. [16] studied the effect of the solution flow rate on the growth of undoped ZnO films prepared from $ZnCl_2$ solution and reported that the solution flow rate influences the surface topology. Dedova et al. [10] concluded that the solution spray rate affects the surface morphology and roughness of undoped ZnO thin films produced by spraying Zn acetate solutions.

Recently, we showed that the electrical resistivity of chemically sprayed In-doped ZnO thin films grown at 400°C can be altered within an interval of 10^{2}–10^{-3} Ωcm by varying the solution spray rate [12]. In this study we will not focus on obtaining the highest electrical conductivity or optical transmittance; we study the effect of the solution spray rate on the structural, morphological, optical, and electrical properties of ZnO:In thin films deposited by chemical spray. The aim is to find the optimal solution spray rate to deposit transparent and conductive ZnO:In thin films.

2. Experimental

ZnO thin films were grown from 100 mL of spray solution that was pneumatically sprayed onto preheated soda-lime glass substrate ($25 \times 25 \times 1\,\mathrm{mm}^3$). The chemical spray pyrolysis (CSP) setup is described elsewhere [23]. The spray solution consisted of $Zn(CH_3COO)_2 \cdot 2H_2O$ (Merck, analytical grade, 99.5%), dissolved in a mixture of deionised water and isopropyl alcohol (2 : 3 by volume) with $Zn(CH_3COO)_2$ concentration of 0.2 mol/L. To avoid the precipitation of zinc hydroxide, a few drops of acetic acid were added to the spray solution. As a doping agent, indium(III)chloride ($InCl_3$) was added to the spray solution with an indium to zinc atomic ratio of 3 ($[In^{3+}]/[Zn^{2+}] = 3$ at.%). Compressed air (flow rate 8 L/min) was used as the carrier gas. The glass substrate was washed with soapy water, rinsed with deionised water, and cleaned ultrasonically in ethanol. After cleaning, the substrate was dried using compressed air and placed onto a hot plate. According to the results of our previous study [12], a film growth temperature of 400°C was chosen as optimal and kept constant within ±5°C throughout the experiments using a feedback control system for the heater. The solution spray rate was varied from 0.5 mL/min to 6.7 mL/min. We verified that the solution spray rate has no effect on the growth temperature.

For a comparison, films with spray rates of 0.35 mL/min, 0.5 mL/min, and 1.5 mL/min were grown from 150 mL of spray solution on a soda-lime glass substrate to obtain films with comparable thicknesses throughout the solution spray rate range.

The structure of the films was characterised by X-ray diffraction (XRD) using a Rigaku Ultima IV diffractometer with monochromatic Cu Kα radiation ($\lambda = 1.5406$ Å), a tube voltage of 40 kV, and a current of 40 mA using a D/teX Ultra silicon strip detector. The crystallite size was calculated by the Debye-Scherrer method from the FWHM (full width at half maximum) of the (101) reflection of ZnO. The surface morphology of the films was characterised by scanning electron microscopy (SEM) and atomic force microscopy (AFM). SEM was performed with a Zeiss EVO-MA15 microscope at magnifications of 25000x and 50000x. AFM was performed on NT-MDT Solver 47 Pro system in tapping mode. The samples were studied over a $2 \times 2\,\mu\mathrm{m}^2$ area. The grain sizes estimated from the SEM images were comparable to those measured with the AFM. The surface roughness analysis was performed according to the ISO 4287/1 standard. The root mean square (RMS) roughness was calculated over a $3 \times 3\,\mu\mathrm{m}^2$ scanned surface area with an accuracy of ±0.5 nm. Image analysis (IA) was achieved using the Media Cybernetics Image-Pro 7 analysing system. The specular UV-VIS-NIR transmittance was recorded in the wavelength range of 350–2500 nm with Jasco V-670 spectrophotometer. The film thickness was calculated using the Spectra Manager software (version 2.02.00) by analysing the interference in the transmittance spectra. The film thickness calculated from the optical spectra is in good agreement (less than ±10% variance) with that obtained from the SEM images. The elemental composition of the thin films was evaluated from four different $20 \times 20\,\mu\mathrm{m}^2$ areas on the film using energy dispersive X-ray (EDX) analysis with an Oxford Instruments INCA at an accelerating voltage of 7 kV. The electrical properties of the thin films (resistivity, charge carrier concentration, and mobility) were measured at room temperature using MMR's Variable Temperature Hall System supplied with Hall, Van der Pauw Controller H-50. The contact material used for the Van der Pauw and Hall measurements was graphite.

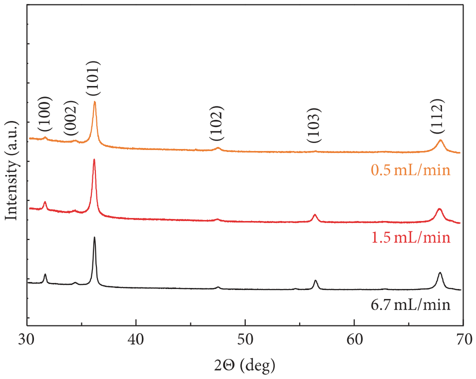

Figure 1: X-ray diffraction patterns of ZnO:In thin films deposited from 100 mL of spray solution at solution spray rates of 0.5 mL/min, 1.5 mL/min, and 6.7 mL/min.

3. Results and Discussion

3.1. Structural Properties. The X-ray diffraction patterns of ZnO:In thin films deposited at various solution spray rates at 400°C are presented in Figure 1. All of the determined

Table 1: The effect of the solution spray rate on the sprayed ZnO:In film thickness (t), crystallite size (d), average grain size (D), electrical resistivity (ρ), main carrier mobility (μ), carrier concentration (n), and optical band gap (E_g). Soda-lime and borosilicate glasses are designated as Na-gl and B-gl, respectively.

Spray rate, mL/min	V, mL	Substrate	t, nm	d, nm	D, nm	ρ, Ωcm	μ, cm^2/Vs	n, cm^{-3}	E_g, eV
0.5	100	Na-gl	700	22	~100	$6.3 \cdot 10^{-2}$	4.4	$2.3{\cdot}10^{19}$	3.28
0.5	150	Na-gl	1400	26	~250	$3.3 \cdot 10^{-2}$	9.2	$2.1{\cdot}10^{19}$	3.24
0.5	150	B-gl	1350	26	*n.m.	$7.8 \cdot 10^{-2}$	3.9	$2.0{\cdot}10^{19}$	3.24
1.5	100	Na-gl	900	21	~120	$1.2 \cdot 10^{-2}$	7.7	$6.9{\cdot}10^{19}$	3.31
1.5	150	Na-gl	1400	29	~250	$7.3 \cdot 10^{-3}$	11	$7.6{\cdot}10^{19}$	3.27
3.3	100	Na-gl	1100	34	~250	$3.7 \cdot 10^{-3}$	16	$1.1{\cdot}10^{20}$	3.34
4.7	100	Na-gl	1100	35	~250	$3.2 \cdot 10^{-3}$	15	$1.4{\cdot}10^{20}$	3.36
6.7	100	Na-gl	1350	36	~250	$4.6 \cdot 10^{-3}$	12	$1.2{\cdot}10^{20}$	3.32

*n.m.: not measured.

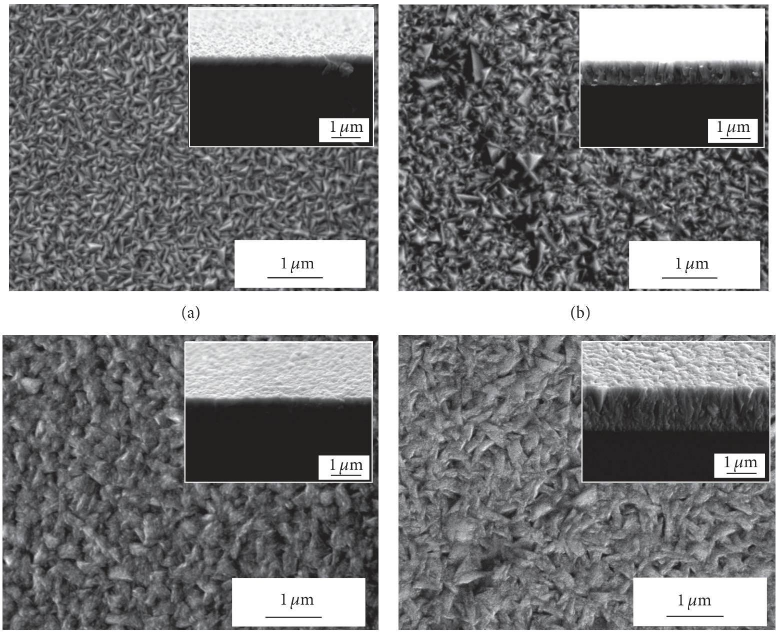

(a) (b) (c) (d)

Figure 2: SEM images of ZnO:In thin films deposited from 100 mL of spray solution at solution spray rates of (a) 0.5 mL/min, (b) 1.5 mL/min, (c) 3.3 mL/min, and (d) 6.7 mL/min. The cross-sectional views are presented as insets on the surface images.

peaks belong to zincite (PDF card number 01-079-0208) [24]. According to Figure 1, ZnO:In film is preferably orientated in the (101) plane parallel to the substrate irrespective of the solution spray rate. Solution spray rates below 3 mL/min lead to smaller crystallites (average size of 20 nm), whereas solution spray rates above 3 mL/min result in crystallite sizes of ca. 35 nm (Table 1).

The microstructure of ZnO:In films was studied using SEM and AFM. According to the SEM study, sprayed ZnO:In films exhibit a dense inner structure and relatively smooth surface with no cracks or pinholes. The SEM surface and cross-sectional images of ZnO:In films obtained at various solution spray rates are presented in Figure 2. The surface of the film deposited at the solution spray rate of 0.5 mL/min has well-shaped prismatic grains with similar sizes of ca. 100 nm (Figure 2(a)). The surface of the film grown with the solution flow rate of 1.5 mL/min consists of grains that vary in size from 50 nm to 500 nm (Figure 2(b)). The surface

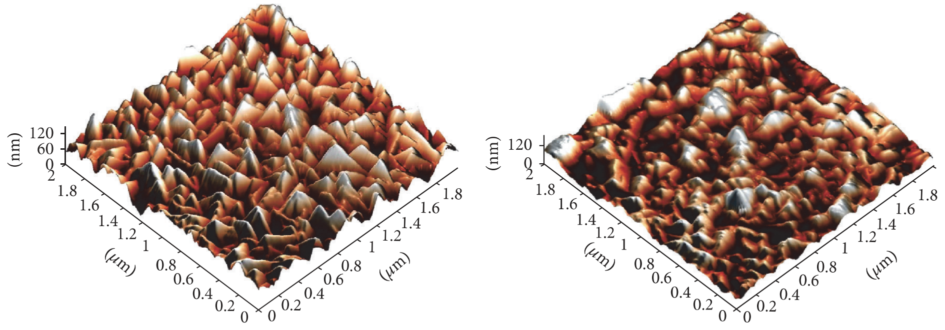

(a) 0.5 mL/min (b) 1.5 mL/min

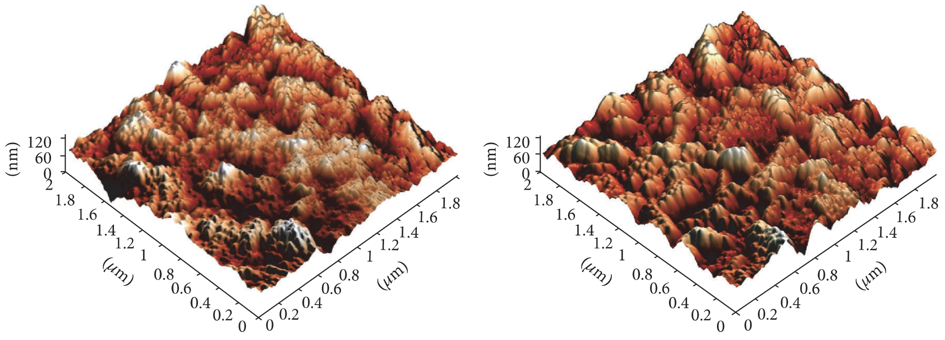

(c) 3.3 mL/min (d) 6.7 mL/min

FIGURE 3: AFM 3D images of ZnO:In films deposited from 100 mL of spray solution with solution flow rates of (a) 0.5 mL/min, (b) 1.5 mL/min, (c) 3.3 mL/min, and 6.7 mL/min (d). AFM images are of a $2 \times 2\,\mu\text{m}^2$ area.

structure of the film deposited with the solution spray rate of 3.3 mL/min is a network of interweaving grains (size of ca. 250 nm) resembling canvas or burlap (see Figure 2(c)). Further increase in the solution spray rate to 6.7 mL/min has a minor effect on the surface of ZnO:In thin film (Figure 2(d)).

The surface morphology of the ZnO:In films deposited at different solution spray rates was also characterised by AFM using images acquired over a $2 \times 2\,\mu\text{m}^2$ area (Figure 3). The AFM images reveal that the solution spray rate has a strong effect on the surface morphology. The surface of the ZnO:In film obtained at a solution spray rate of 0.5 mL/min (Figure 3(a)) consists of well-shaped pyramidal grains with sharp edges and tip. The mean grain size is ca. 100 nm and the grain aspect ratio (the ratio of the major axis length to the minor axis length of an equiareal ellipse) is ca. 2.0. For the ZnO:In film with solution spray rate of 1.5 mL/min, the peaks and edges of the grains are rounded (Figure 3(b)), and the grain size varied from 70 nm to 200 nm (Figure 3(b)). According to the SEM image (Figure 2(b)), some of the grains had a diameter of ca. 500 nm. According to the AFM study, the mean grain size is ca. 120 nm and the aspect ratio of the grains is ca. 1.7. In contrast, the ZnO:In films prepared at solution spray rates of 3.3 mL/min and above have more complex surface structure (Figures 3(c) and 3(d)). Using the solution spray rate of 3.3 mL/min, the film surface (Figure 3(c)) shows a fine-grain structure on top of grains with the size of ca. 200–250 nm and an aspect ratio of ca. 1.6, forming a double-layer surface. The fine-grain layer is composed of particles with an average diameter of ca. 40 nm. The surface structure of the film deposited at a solution spray rate of 6.7 mL/min (Figure 3(d)) is similar to that prepared at 3.3 mL/min (Figure 3(c)). The ca. 200–300 nm sized grains are covered by individually distinct particles with an average diameter of ca. 50 nm (Figure 3(d)).

Interestingly, the RMS roughness was ca. 20 nm for all sprayed ZnO:In films independent of solution spray rate and surface morphology. This RMS is similar to that reported by Dedova et al. [10] for sprayed ZnO:In films.

AFM study showed that the grain size increases with increasing solution spray rate. It is generally recognised that large grains are formed due to the recrystallisation of smaller grains. An extra phase on the grain boundaries may inhibit the growth of grains. This problem will be discussed in more detail in Section 3.2.

3.2. Electrical Properties. The resistivity, carrier concentration, and mobility of ZnO:In thin films dependent on the solution spray rate are presented in Figure 4. The films

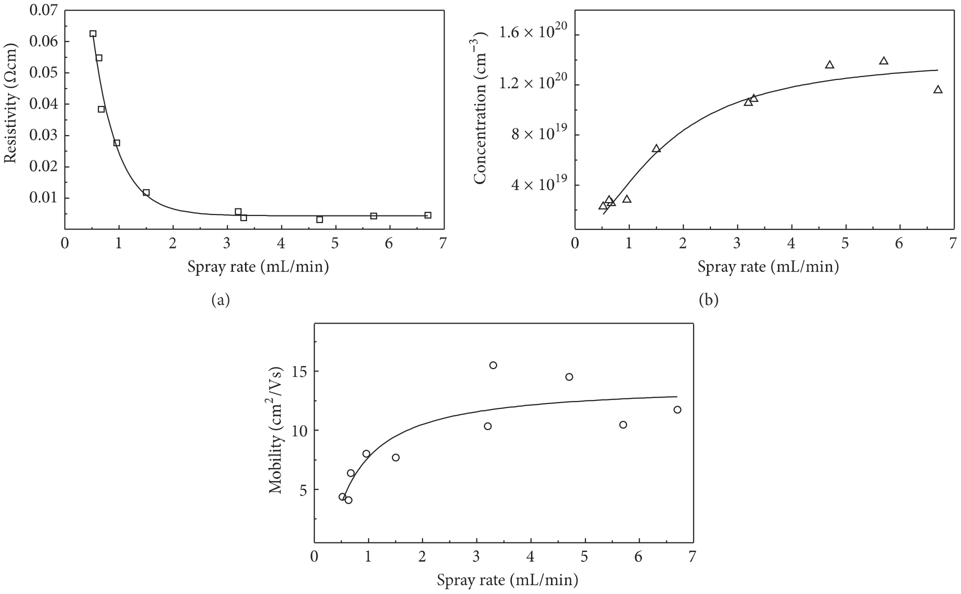

(a)

(b)

(c)

Figure 4: Resistivity (□), carrier concentration (Δ), and carrier mobility (○) of ZnO:In thin films deposited from 100 mL of spray solution at solution spray rates of 0.5–6.7 mL/min.

presented in Figure 4 are sprayed from 100 mL of spray solution. The resistivity of the sprayed ZnO:In films decreases from ca. $6.3 \cdot 10^{-2}$ Ωcm to $3.7 \cdot 10^{-3}$ Ωcm while increasing the solution spray rate from 0.5 mL/min to 3.3 mL/min, respectively (Figure 4 and Table 1). Increasing the solution spray rate from 0.5 mL/min to 3.3 mL/min increases the carrier concentration from $2.3 \cdot 10^{19}$ cm^{-3} to $1.1 \cdot 10^{20}$ cm^{-3} and mobility from 4.4 cm^2/Vs to 16 cm^2/Vs, respectively. The increase in the carrier mobility with increasing solution spray rate can be ascribed to the increased grain size from 100 to 250 nm as shown by AFM (Figure 3 and Table 1). This hypothesis is further supported by the following. The positive correlation between the carrier concentration and carrier mobility observed in our films is presented in Figure 5. A similar relation has been noted for ZnO:Al films grown by PLD [25], indicating that the conduction mechanism is driven by grain boundary scattering. Further increase in spray rate from 3.3 mL/min to 6.7 mL/min has minor effect on the electrical properties of ZnO:In thin films. The films prepared with spray rates above 3 mL/min show carrier concentrations around $1 \cdot 10^{20}$ cm^{-3} and carrier mobilities in the range of 12–16 cm^2/Vs. A minor rise in resistivity (to $4.6 \cdot 10^{-3}$ Ωcm) in the film deposited at spray rate of 6.7 mL/min is attributed to lower carrier mobility of 12 cm^2/Vs. Wienke and Booij [15] reported similar carrier mobility of ca. 14 cm^2/Vs and concentration of $1.4 \cdot 10^{20}$ cm^{-3} for ultrasonically sprayed ZnO:In film.

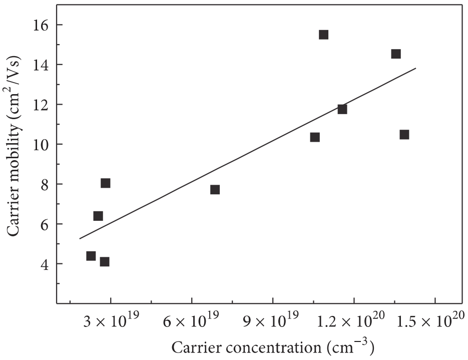

Figure 5: Carrier mobility versus carrier concentration of ZnO:In thin films deposited from 100 mL of spray solution at solution spray rates of 0.5–6.7 mL/min.

The films grown with the spray rates of 0.5–1.5 mL/min show carrier mobilities of 4.4–7.7 cm^2/Vs that is up to three times lower than recorded for the films grown with the spray rates above 3 mL/min (Figure 4, Table 1). It is known that the carrier mobility in the film is thickness and grain size dependent [26]. To prepare films with comparable thicknesses, the ZnO:In films with spray rates of 0.5 mL/min and 1.5 mL/min were deposited from 150 mL of spray solution and as a result,

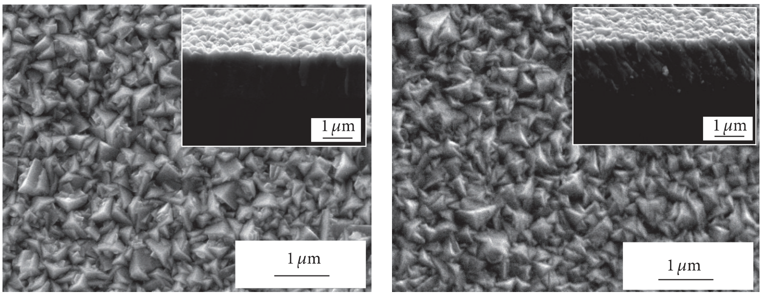

(a) (b)

Figure 6: SEM images of ZnO:In thin films deposited from 150 mL of spray solution at solution spray rates of (a) 0.5 mL/min, and (b) 1.5 mL/min. The cross-sectional views are presented as insets on the surface images.

films with thicknesses of ca. 1400 nm were grown (Table 1). According to SEM images in Figure 6, the shape of the grains in the thicker films is similar to that reported for the thinner films with spray rates of 0.5 mL/min and 1.5 mL/min in Section 3.1 (Figures 2(a) and 2(b)). The grain sizes of the thicker films with spray rates of 0.5–1.5 mL/min were estimated from SEM images (Figure 6). The grain size of the thicker films is ca. 2 times higher when compared to the thinner films (Figures 2(a) and 2(b)). Thus, larger grains (size of ca. 250 nm) were obtained in thicker films and that is in accordance with the literature [9, 27, 28]. The carrier mobilities increased with the film thickness from 4.4 cm^2/Vs to 9.2 cm^2/Vs and from 7.7 cm^2/Vs to 11 cm^2/Vs for films deposited at 0.5 mL/min and 1.5 mL/min, respectively. Still, the mobilities in the films deposited at spray rates of 0.5–1.5 mL/min are slightly lower than in the films grown with solution spray rates above 3 mL/min regardless of comparable thicknesses (Table 1). The decrease could be due to the larger grain size distribution (75–700 nm) in the film with spray rate of 0.5 mL/min (Figure 6(a)) compared to the film with spray rate of 3.3 mL/min (200–300 nm) (Figure 2(c)).

It can be seen from Table 1 that carrier concentration depends on the solution spray rate independent of the film thickness. The carrier concentration of ca. $2 \cdot 10^{19}$ cm^{-3} in film grown at 0.5 mL/min is ca. 10 times lower than in films with solution spray rate above 3 mL/min (ca. $1 \cdot 10^{20}$ cm^{-3}). Moreover, a ZnO:In film with thickness of 1400 nm was grown with solution spray rate of 0.35 mL/min and the carrier concentration of the mentioned film was $6 \cdot 10^{18}$ cm^{-3}. As the carrier concentration depends on the doping level [6, 8, 15] then it is possible that part of the indium was not incorporated into the ZnO lattice at lower solution spray rates.

It could be speculated that part of the dopant source might have left the system at slow spray rates due to relatively high $InCl_3$ vapour pressure of ca. 1.0 kPa at 400°C [29]. For this reason, the elemental composition of the films obtained with different spray rates was studied. According to EDX, the films deposited at different solution spray rates have similar elemental compositions (Table 2). Thus, the [In]/[Zn] ratio in the film is constant at varied spray rates. As the EDX measurements were performed using factory-defined standards only, the atomic percentages of the elements are not absolute values. However, EDX confirms that there is no loss of the dopant source or that the loss is similar at all solution spray rates used.

Table 2: Elemental composition (in at.%) of ZnO:In thin films deposited at solution spray rates of 0.5 mL/min and 3.2 mL/min according to EDX.

Solution spray rate, mL/min	Zn	O	In
0.5	43.4	54.4	2.2
3.2	43.3	54.7	2.0

Another cause for lower electron concentration while using low solution spray rates can be the diffusion of Na to the ZnO film from the soda-lime glass substrate at 400°C during long spray process [30]. In that case, Na could create defects that reduce the concentration of free electrons. Unfortunately, EDX cannot be used to detect Na due to the overlapping peaks of Zn and Na. To overcome this problem, a thicker ZnO:In film (from 150 mL) with thickness comparable to that on a soda-lime glass was deposited onto a borosilicate substrate at 0.5 mL/min. Film with thickness of ca. 1350 nm has a resistivity of $7.8 \cdot 10^{-2}$ Ωcm, carrier mobility of 3.9 cm^2/Vs, and concentration of $2.0 \cdot 10^{19}$ cm^{-3} (see Table 1). The carrier concentrations of ZnO:In films on soda-lime and borosilicate glass substrate are comparable and thus the diffusion of Na is not responsible for the lower concentration of electrons in the films with low spray rates.

As there is no difference in the dopant concentration in the films deposited at different solution spray rates and the diffusion of sodium is not the case, the lower carrier concentration in the films with lower solution spray rates could be due to the failing of In incorporation into the ZnO lattice due to the oxidation of indium source. The study of ZnO:In films structural properties supports this hypothesis, as an extra phase on the grain boundaries inhibited the grain growth at low solution spray rates (see Section 3.1).

3.3. Optical Properties.

3.3. Optical Properties. The optical transmittance spectra of the ZnO:In films grown from 100 mL of spray solution using

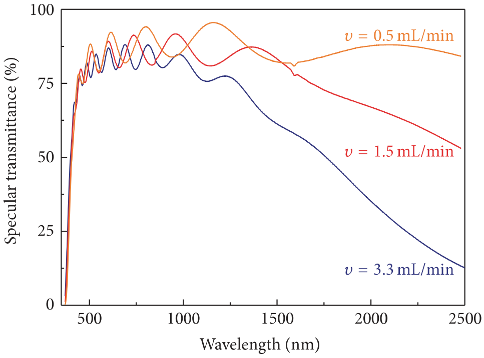

FIGURE 7: Specular transmittance of ZnO:In thin films deposited from 100 mL of spray solution at solution spray rates of 0.5 mL/min, 1.5 mL/min, and 3.3 mL/min.

various solution spray rates are presented in Figure 7. In the visible light region, the ZnO:In thin films show specular transmittance above 75% irrespective of the solution spray rate.

For the film prepared at 0.5 mL/min or lower, the transmittance in the near infrared region (NIR) is comparable to that in UV-VIS region. The increase in solution spray rate decreases film transmittance in the NIR region and the lowest transmittance is recorded for the film with solution spray rate of 3.3 mL/min. The decrease in the optical transmittance in the NIR spectral region corresponds to the increased concentration of carriers in the films sprayed at higher solution spray rates (Table 1). According to the literature, the decrease in the transmittance of TCO films in NIR spectral region is caused by the free carrier absorption [31–33]. This has been recorded for conductive ZnO films with electron concentrations of $3 \cdot 10^{20}$ cm^{-3} and $6 \cdot 10^{20}$ cm^{-3} deposited by ion-layer gas reaction spray [31] and PLD [32], respectively.

The optical band gap of the films is determined from the transmittance spectra. The optical band gap values were determined from the commonly used equation

$$\alpha h\nu = A \cdot (h\nu - E_g)^{1/n}, \quad (1)$$

where A is the parameter that does not depend on the photon energy, h is the Planck constant, E_g is the band gap energy, $h\nu$ is the incident photon energy, and $1/n$ is an exponent that depends on the nature of the optical transition ($n = 0.5$ for direct transition). The determination of E_g from $(\alpha h\nu)^2$ versus the $h\nu$ plot is shown in Figure 8 and the E_g values of ZnO:In films depending on the solution spray rate are given in Table 1. The ZnO:In film band gap increases from 3.24 eV to 3.36 eV as the solution spray rate increases from 0.5 mL/min to 4.7 mL/min, respectively. The increase in the band gap is in accordance with the increase in the carrier concentration (Table 1) and can be explained by the Burstein-Moss effect [33]. Thus, we have achieved a good agreement with the results of similar studies on ZnO [11, 13, 15, 25, 33].

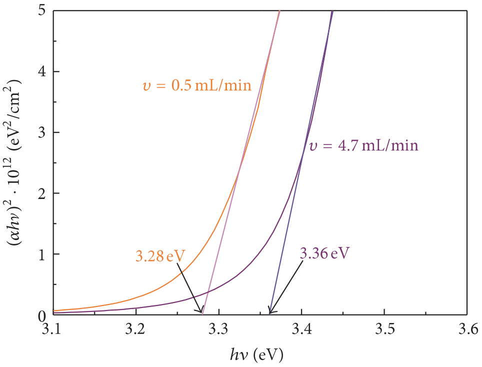

FIGURE 8: Graphical determination of direct optical band gap of ZnO:In thin films deposited from 100 mL of spray solution with solution spray rates of 0.5 mL/min and 4.7 mL/min.

4. Conclusions

At constant spray solution volume, an increase in the solution spray rate results in thicker ZnO:In films with larger crystallites and grains; also the surface morphology and electrical conductivity are affected. The grains in the film with spray rate of 1.5 mL/min are roundish when compared to the sharp-edged grains in the film with spray rate of 0.5 mL/min. The surface of the films with spray rate above 3 mL/min is composed of canvas-resembling grains (size ca. 250 nm) covered with particles with the size of ca. 40–50 nm. Increasing the spray rate from 0.5 mL/min to 3.3 mL/min decreases the electrical resistivity from $6.3 \cdot 10^{-2}$ Ωcm to $3.7 \cdot 10^{-3}$ Ωcm as the carrier concentration increases from $2.3 \cdot 10^{19}$ cm^{-3} to $1.1 \cdot 10^{20}$ cm^{-3} and mobility from 4.4 cm^2/Vs to 16 cm^2/Vs, respectively.

To obtain films with comparable thicknesses throughout the solution spray rate range, more spray solution has to be used for films deposited at 1.5 mL/min and below. An increase in film thickness from 700 nm to 1400 nm and in grain size from 100 nm to ca. 250 nm increases the carrier mobility from 4.4 cm^2/Vs to 9.2 cm^2/Vs and from 7.7 cm^2/Vs to 11 cm^2/Vs for films deposited at 0.5 mL/min and 1.5 mL/min, respectively. Independent of the similar film thicknesses and the mean grain sizes, the mobilities in the slowly grown films are lower than in films with spray rate above 3 mL/min. Higher spray rates lead to higher carrier concentrations: spray rates of 0.5, 1.5, and 3.3 mL/min result in carrier concentrations of ca. $2 \cdot 10^{19}$, $7 \cdot 10^{19}$, and $1 \cdot 10^{20}$ cm^{-3}, respectively. The decreased carrier concentrations characteristic of the films with lower spray rates could be due to the oxidation of indium source that prevents indium from acting as the dopant in ZnO. Sprayed ZnO:In films with thickness of 1.1–1.4 μm transmit 75–80% of visible light. A decrease of the transmittance in NIR spectral region and an increase in band gap is characteristic of films with higher spray rate and corresponds to the increased carrier concentration in these films.

This study shows that the solution spray rate is an important technological parameter controlling the film thickness, morphology, grain size, optical properties, and electrical conductivity of the sprayed ZnO:In films. Still, the optimal spray rate should be determined for every setup to obtain films with properties required for a transparent and conductive material.

Conflict of Interests

The authors declare that they have no conflict of interests in the submitted paper.

Acknowledgments

Financing by the Estonian Ministry of Education and Research under Project SF0140092s08, the Estonian Science Foundation (ETF9081), and the European Regional Development Fund (Centre of Excellence "Mesosystems: Theory and Applications" TK114 and Project 3.2.1101.12-0023) is gratefully acknowledged. This work has been partially supported by the graduate school "Functional materials and technologies" receiving funding from the European Social Fund under Project 1.2.0401.09-0079 in Estonia.

References

[1] N. H. Nickel and E. Terukov, *Zinc Oxide—A Material For Micro- and Optoelectronic Applications*, Springer, Dordrecht, The Netherlands, 2005.

[2] L. Niinistö, J. Päiväsaari, J. Niinistö, M. Putkonen, and M. Nieminen, "Advanced electronic and optoelectronic materials by Atomic Layer Deposition: an overview with special emphasis on recent progress in processing of high-*k* dielectrics and other oxide materials," *Physica Status Solidi A*, vol. 201, pp. 1443–1452, 2004.

[3] X. M. Li, J. L. Zhao, J. M. Bian, W. D. Yu, and C. Y. Zhang, "Comparison of structural and photoluminescence properties of ZnO thin films grown by pulsed laser deposition and ultrasonic spray pyrolysis," *Thin Solid Films*, vol. 515, no. 4, pp. 1763–1766, 2006.

[4] A. Drici, G. Djeteli, G. Tchangbedji et al., "Structured ZnO thin films grown by chemical bath deposition for photovoltaic applications," *Physica Status Solidi A*, vol. 201, no. 7, pp. 1528–1536, 2004.

[5] M. K. Jayaraj, A. Antony, and M. Ramachandran, "Transparent conducting zinc oxide thin film prepared by off-axis rf magnetron sputtering," *Bulletin of Materials Science*, vol. 25, no. 3, pp. 227–230, 2002.

[6] A. Hafdallah, F. Yanineb, M. S. Aida, and N. Attaf, "In doped ZnO thin films," *Journal of Alloys and Compounds*, vol. 509, no. 26, pp. 7267–7270, 2011.

[7] A. R. Babar, P. R. Deshamukh, R. J. Deokate, D. Haranath, C. H. Bhosale, and K. Y. Rajpure, "Gallium doping in transparent conductive ZnO thin films prepared by chemical spray pyrolysis," *Journal of Physics D*, vol. 41, no. 13, Article ID 135404, 2008.

[8] M. Krunks, O. Bijakina, V. Mikli, T. Varema, and E. Mellikov, "Zinc oxide thin films by spray pyrolysis method," *Physica Scripta*, vol. 79, pp. 209–212, 1999.

[9] M. L. Olvera, H. Gómez, and A. Maldonado, "Doping, vacuum annealing, and thickness effect on the physical properties of zinc oxide films deposited by spray pyrolysis," *Solar Energy Materials and Solar Cells*, vol. 91, no. 15-16, pp. 1449–1453, 2007.

[10] T. Dedova, J. Klauson, C. Badre et al., "Chemical spray deposition of zinc oxide nanostructured layers from zinc acetate solutions," *Physica Status Solidi A*, vol. 205, no. 10, pp. 2355–2359, 2008.

[11] T. V. Vimalkumar, N. Poornima, C. Sudha Kartha, and K. P. Vijayakumar, "On tuning the orientation of grains of spray pyrolysed ZnO thin films," *Applied Surface Science*, vol. 256, no. 20, pp. 6025–6028, 2010.

[12] M. Vent, E. Kärber, T. Unt, A. Mere, and M. Krunks, "The effect of growth temperature and spraying rate on the properties of ZnO:In films," *Physica Status Solidi C*, vol. 9, pp. 1604–1606, 2012.

[13] A. Maldonado, J. Rodríguez-Baez, and M. L. Olvera, "Physical properties of indium and fluorine codoped zinc oxide thin films deposited by chemical spray," *Materials Chemistry and Physics*, vol. 129, no. 1-2, pp. 109–115, 2011.

[14] R. Biswal, L. Castañeda, R. Moctezuma, J. Vega-Pérez, M. L. Olvera, and A. Maldonado, "Formation of indium-doped zinc oxide thin films using ultrasonic spray pyrolysis: the importance of the water content in the aerosol solution and the substrate temperature for enhancing electrical transport," *Materials*, vol. 5, pp. 432–442, 2012.

[15] J. Wienke and A. S. Booij, "ZnO:In deposition by spray pyrolysis—influence of the growth conditions on the electrical and optical properties," *Thin Solid Films*, vol. 516, no. 14, pp. 4508–4512, 2008.

[16] J. Ebothé, A. El Hichou, P. Vautrot, and M. Addou, "Flow rate and interface roughness of zinc oxide thin films deposited by spray pyrolysis technique," *Journal of Applied Physics*, vol. 93, no. 1, pp. 632–640, 2003.

[17] S. Major, A. Banerjee, and K. L. Chopra, "Highly transparent and conducting indium-doped zinc oxide films by spray pyrolysis," *Thin Solid Films*, vol. 108, no. 3, pp. 333–340, 1983.

[18] K. T. R. Reddy, T. B. S. Reddy, I. Forbes, and R. W. Miles, "Highly oriented and conducting ZnO:Ga layers grown by chemical spray pyrolysis," *Surface and Coatings Technology*, vol. 151-152, pp. 110–113, 2002.

[19] M. L. Olvera, A. Maldonado, R. Asomoza, R. Castanedo-Pérez, G. Torres-Delgado, and J. Cañetas-Ortega, "Conductive and transparent ZnO:Al thin films obtained by chemical spray," *Journal of Materials Science*, vol. 11, no. 5, pp. 383–387, 2000.

[20] J. Wienke, B. van der Zanden, M. Tijssen, and M. Zeman, "Performance of spray-deposited ZnO:In layers as front electrodes in thin-film silicon solar cells," *Solar Energy Materials and Solar Cells*, vol. 92, no. 8, pp. 884–890, 2008.

[21] C. H. Fischer, N. A. Allsop, S. E. Gledhill et al., "The spray-ILGAR (ion layer gas reaction) method for the deposition of thin semiconductor layers: process and applications for thin film solar cells," *Solar Energy Materials and Solar Cells*, vol. 95, no. 6, pp. 1518–1526, 2011.

[22] M. Krunks, E. Kärber, A. Katerski et al., "Extremely thin absorber layer solar cells on zinc oxide nanorods by chemical spray," *Solar Energy Materials and Solar Cells*, vol. 94, no. 7, pp. 1191–1195, 2010.

[23] K. Otto, A. Katerski, A. Mere, O. Volobujeva, and M. Krunks, "Spray pyrolysis deposition of indium sulphide thin films," *Thin Solid Films*, vol. 519, no. 10, pp. 3055–3060, 2011.

[24] "International Centre for Diffraction Data (ICDD)," PDF-2 Release 2008.

[25] T. Minami, "Transparent conducting oxide semiconductors for transparent electrodes," *Semiconductor Science and Technology*, vol. 20, no. 4, pp. S35–S44, 2005.

[26] C. E. Benouis, M. Benhaliliba, A. Sanchez Juarez, M. S. Aida, F. Chami, and F. Yakuphanoglu, "The effect of indium doping on structural, electrical conductivity, photoconductivity and density of states properties of ZnO films," *Journal of Alloys and Compounds*, vol. 490, no. 1-2, pp. 62–67, 2010.

[27] R. Venkatraman and J. C. Bravman, "Separation of film thickness and grain boundary strengthening effects in Al thin films on Si," *Journal of Materials Research*, vol. 7, no. 8, pp. 2040–2048, 1992.

[28] R. M. Keller, S. P. Baker, and E. Arzt, "Quantitative analysis of strengthening mechanisms in thin Cu films: effects of film thickness, grain size, and passivation," *Journal of Materials Research*, vol. 13, no. 5, pp. 1307–1317, 1998.

[29] B. Brunetti, V. Piacente, and P. Scardala, "Torsion study on the sublimation process of $InCl_3$," *Journal of Chemical and Engineering Data*, vol. 43, no. 1, pp. 101–104, 1998.

[30] A. Katerski, A. Mere, V. Kazlauskiene et al., "Surface analysis of spray deposited copper indium disulfide films," *Thin Solid Films*, vol. 516, no. 20, pp. 7110–7115, 2008.

[31] S. Gledhill, A. Grimm, D. Greiner, W. Bohne, M. Lux-Steiner, and C. H. Fischer, "Doping induced structural and compositional changes in ZnO spray pyrolysed films and the effects on optical and electrical properties," *Thin Solid Films*, vol. 519, no. 13, pp. 4293–4298, 2011.

[32] L. Gong, Z. Ye, J. Lu et al., "Highly transparent conductive and near-infrared reflective ZnO:Al thin films," *Vacuum*, vol. 84, no. 7, pp. 947–952, 2010.

[33] V. Bhosle, A. Tiwari, and J. Narayan, "Electrical properties of transparent and conducting Ga doped ZnO," *Journal of Applied Physics*, vol. 100, no. 3, Article ID 033713, 6 pages, 2006.

Article **III**

Kriisa, M.; Kärber, E.; Krunks, M.; Mikli, V.; Unt, T.; Kukk, M.; Mere, A. (2014). Growth and properties of ZnO films on polymeric substrate by spray pyrolysis method. Thin Solid Films, 555, 87−92.

Thin Solid Films 555 (2014) 87–92

Contents lists available at ScienceDirect

Thin Solid Films

journal homepage: www.elsevier.com/locate/tsf

Growth and properties of ZnO films on polymeric substrate by spray pyrolysis method

Merike Kriisa [a], Erki Kärber [a], Malle Krunks [a,*], Valdek Mikli [b], Tarmo Unt [a], Mart Kukk [a], Arvo Mere [a]

[a] Department of Materials Science, Tallinn University of Technology, Ehitajate tee 5, 19086 Tallinn, Estonia
[b] Centre for Materials Research, Tallinn University of Technology, Ehitajate tee 5, 19086 Tallinn, Estonia

ARTICLE INFO

Available online 14 June 2013

Keywords:
ZnO
ZnO:In
Chemical spray pyrolysis
Polymeric substrate
Scrolled belts

ABSTRACT

The growth of ZnO layers deposited by spray pyrolysis on polymeric substrate was studied. Zinc acetate precursor solution was sprayed onto preheated polyimide (PI) and glass reference substrates at 380 °C. The structural, morphological, optical and electrical properties of the layers were measured by X-ray diffraction, scanning electron microscopy, optical spectroscopy and van der Pauw and Hall method. ZnO:In layers could be grown on PI when deposited onto undoped ZnO layer acting as a buffer layer on PI. Independent of the substrate type, the ZnO/ZnO:In bilayer showed a mixed morphology from smooth canvas-like surface to large scrolled belt grains dependent on buffer layer morphology. Due to the formation of scrolled belts, the ZnO:In layer shows no preferential orientation, yet the preferred orientation of the ZnO buffer crystallites is (100) plane parallel to the substrate. The bilayers deposited on PI exhibit high light scattering capability (haze factor of 85–95% in the spectral region of 350–1500 nm). The resistivity of the ZnO:In film in bilayer on PI is 4.4×10^{-2} Ω cm mainly due to low carrier mobility of 1.5 cm^2/Vs, the carrier concentration is 10^{20} cm^{-3}.

1. Introduction

Polymers are substituting glass substrates in the deposition of TCO-s (transparent conductive oxide) due to its low weight, excellent mechanical toughness, and ductility. Up to date, TCO-s such as indium oxide [1], indium tin oxide [2], tin oxide [1] and zinc oxide have been grown on polymer substrates (polyester [3], polyimide [4], polyethylene terephthalate [5,6] etc.). Methods like sputtering [3,4,7,8], pulsed laser deposition [9], atomic layer deposition (ALD) [10] and ion-plating [11] have been used to grow TCO thin films on polymers.

It has been reported that the undoped ZnO thin film has c-axis orientation independent of deposition method and polymer substrate [3,6,11–13]. Furthermore, the c-axis orientation of ZnO film on polymer remains when doping with Ga or Al independent of the deposition method [3,5,7,8,12,14,15]. The electrical resistivity of the r.f. magnetron sputtered ZnO:Ga film on polymer is slightly higher when compared to films deposited on glass substrates, 7×10^{-4} Ω cm and 6×10^{-4} Ω cm, respectively [11]. The carrier concentration and mobility for ZnO:Ga films on polymer are ca. 6×10^{20} cm^{-3} and 14 cm^2/Vs, respectively [8,15] while the corresponding values for ZnO:Ga film on glass are ca. 7×10^{20} cm^{-3} and 16.5 cm^2/Vs [11]. The lower resistivity and higher mobility of charge carriers in ZnO:Ga films on glass are due to the increased grain sizes of ZnO:Ga thin film on glass compared to the films on polymer [11]. The lowest resistivity reported for ZnO:Al film grown on polymer by r.f. magnetron sputtering is in the order of 10^{-4} Ω cm [4,5] while the highest carrier concentration and mobility are $2–3 \times 10^{21}$ cm^{-3} and 16 cm^2/Vs, respectively [4]. Some studies report using a thin buffer layer such as Al, SiO_2 or ZnO (layer thickness varies from 3 nm to 100 nm) between polymer and doped ZnO film to optimise the interface of film and polymer substrate, to smoothen the surface of polymer and to reduce the diffusion of oxygen into the polymer [7,10,14,15]. It was observed that the use of thin buffer layer decreased the resistivity as mobility increased due to increased crystallinity and crystallite size [7,15].

Among the deposition methods used nowadays to grow TCO thin films, Chemical Spray Pyrolysis (CSP) is an attractive method due to its simplicity and low cost. ZnO thin films prepared by CSP have been used as components in optoelectronic and microelectronic devices, e.g. in solar cells [16,17] or thin-film transistors [18], respectively. The electrical resistivities of 7.6×10^{-4} Ω cm and 3×10^{-3} Ω cm are characteristic to sprayed ZnO:Ga [19] and ZnO:Al [20] thin films on glass substrates. The electrical resistivity of sprayed ZnO:In thin film deposited on glass in our laboratory is 3×10^{-3} Ω cm [21] which is a little higher than the lowest resistivity of $8–9 \times 10^{-4}$ Ω cm reported for sprayed ZnO:In films [22].

Up to date, no studies on the growth of chemically sprayed ZnO thin films on polymeric substrates have been reported. Yet, the chemically sprayed ZnO and doped ZnO thin films on polymers can be of great interest in the flexible electronic devices and solar cells due to simple and low cost deposition. The aim of the paper was to study the growth of ZnO and ZnO:In film on flexible polyimide substrates. Since the spray

---

* Corresponding author. Tel.: +372 620 3363; fax: +372 620 2020.
E-mail address: malle.krunks@ttu.ee (M. Krunks).

0040-6090/$ – see front matter © 2013 Elsevier B.V. All rights reserved.
http://dx.doi.org/10.1016/j.tsf.2013.05.150

deposition requires substrate temperatures of 300–450 °C [21,23], the polyimide film (Kapton® with a thickness of 150 μm supplied by Katco Ltd.) was selected as polymer substrate due to its stability up to 400 °C [24]. The growth of sprayed ZnO and ZnO:In thin films on polymeric substrates is studied, the film structural, morphological, optical and electrical properties of sprayed ZnO and ZnO:In films on polymeric substrate are presented and discussed and compared to the films grown on glass substrates.

2. Experimental details

The chemical spray pyrolysis (CSP) set-up used in this study is described elsewhere [25] and the deposition conditions were selected based on our previous studies on growth of ZnO:In films on glass substrate [21]. ZnO layers and ZnO/ZnO:In bilayers were deposited onto polyimide (PI) substrates that were placed on melted tin bath at 400 °C. The corresponding film growth temperature was ca. 20 °C lower due to cooling by air (flow rate of 8 l/min) used as a carrier gas; hence the film growth temperature (T_S) was kept at ca. 380 °C. For reference, the ZnO, ZnO:In films and ZnO/ZnO:In bilayers were grown on soda-lime glass substrates (SLG) at growth temperature of ca. 380 °C. For the deposition of ZnO and ZnO:In layers, zinc acetate was dissolved in a mixture of deionized water and 2-propanol (volume ratio 2/3). The zinc acetate concentration was 0.2 mol/l. A few drops of acetic acid was added to the spray solution to prevent the precipitation of $Zn(OH)_2$. As a dopant source, $InCl_3$ was introduced into the spray solution with the atomic ratio of indium to zinc, $[In^{3+}]/[Zn^{2+}] = 3$ at.%. ZnO buffer layers were grown from 50 ml (marked as buffer layer type A) and 30 ml (marked as buffer layer type B) of spray solution. ZnO:In film was deposited from 50 ml of solution. The spray rate was varied from 2 to 3 ml/min. We verified that the solution spray rate did not affect the film growth temperature.

X-ray diffraction (XRD) patterns of sprayed ZnO thin films and bilayers (ZnO/ZnO:In) on PI and glass substrates were recorded using a Rigaku Ultima IV diffractometer with monochromatic Cu Kα radiation ($\lambda = 1.5406$ Å, 40 kV at 40 mA). Data were gathered in the 2θ range of 30°–80° with scan speed of 4°/min and scan step 0.01° using the silicon strip detector D/teX Ultra. The X-ray diffractograms were analyzed using the software on the Rigaku system (PDXL 1.4.0.3). The morphology was characterized and the thickness of the layers was determined with scanning electron microscopy (SEM) using EVO MA 15 Zeiss apparatus at operating voltage of 7 kV. The optical diffuse and total reflectance spectra were recorded in the wavelength range of 350–1500 nm on Jasco V-670 spectrophotometer using an integrating sphere. Electrical resistivity, charge carrier mobility and charge carrier concentration were measured using standard 4-probe method at room temperature using Hall, van der Pauw Controller H-50. The contacts for van der Pauw and Hall measurements were made from graphite.

3. Results and discussions

3.1. Structural properties

Zinc oxide thin films grown on PI at 380 °C were visually smooth, crack-free and showed good adhesion independent of solution volume sprayed and spray rate. However, ZnO:In thin films cracked and peeled off from the PI within a few minutes after deposition independent of the deposition conditions. XRD pattern of a ZnO film deposited onto PI substrate presented in Fig. 1 shows that the crystallites in the ZnO film grow preferably (100) plane parallel to the substrate because the (100) reflection to (101) reflection intensity ratio ($I_{(100)}/I_{(101)}$) varies between 2.0 and 4.0 depending on the procedure variables while $I_{(100)}/I_{(101)}$ of the powder reference is 0.56 [26]. This result is different from that recorded for sprayed ZnO film grown onto a glass substrate at similar conditions (Fig. 2). According to Fig. 2, ZnO films grown on glass substrate are c-axis orientated. This result is in good correlation with the results published for ZnO films deposited by chemical spray method onto glass substrate [27,28].

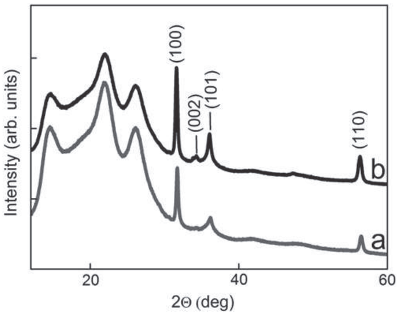

Fig. 1. XRD patterns of sprayed ZnO buffer layer of type A (a) and ZnO/ZnO:In bilayer (b) grown on PI substrate at 380 °C.

A buffer layer of ZnO, SiO_2, Al_2O_3, Al, etc. has often been used to obtain controllable growth of metal oxide thin films on polymers by ALD [10] and by r.f. magnetron sputtering [7,14,15]. To be able to grow adhesive ZnO:In film by spray on PI, an undoped ZnO film showing good adherence to PI was sprayed and used as a buffer layer. XRD patterns of the sprayed crack-free ZnO/ZnO:In bilayers on the PI and glass substrates are presented in Figs. 1 and 2, respectively. In the case of PI substrate, the $I_{(100)}/I_{(101)}$ intensity ratio for bilayers varies between 2.0 and 3.0, being slightly lower when compared to the respective ratio of the buffer layers. Thus, no relevant change in the preferential orientation of crystallites in bilayer compared to that in ZnO buffer layer has been observed. In the case of glass substrate, the deposition of ZnO:In layer onto the buffer layer increases the intensities of the reflections of (100) and (101) planes (Fig. 2), the most intense reflections of powder reference [26]. According to XRD, independent of the substrate and orientation of crystallites in the ZnO buffer layer, the crystallites of ZnO:In film in bilayer do not show preferential orientation compared to powder reference. This result does not conform to that characteristic of sprayed ZnO:In films on glass substrates where crystallites are preferentially grown the (101) plane parallel to the substrate [21,23,29]. The cause of different growth of ZnO:In layer on glass and on ZnO buffer layer will be discussed.

3.2. Morphological properties

The undoped ZnO films deposited from 50 ml of spray solution on PI exhibit leaf-like grains on relatively smooth surface (Fig. 3a, c). The sizes and density of grains depend on the solution spray rate and solution volume. Grains with the size of ca. 2–4 μm are formed at spray

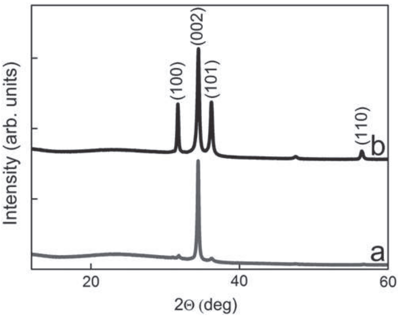

Fig. 2. XRD patterns of ZnO buffer layer of type A (a) and ZnO/ZnO:In bilayer (b) grown on glass substrate at 380 °C.

rate of 2 ml/min (Fig. 3a), while the higher number of smaller grains (with a length of ca. 2 μm) is formed at spray rate of 3 ml/min (Fig. 3c). According to SEM images presented in Fig. 3b and d, the morphology of a bilayer is controlled by the buffer layer. In the bilayer, a canvas-like ZnO:In layer is formed on the flat area of the buffer layer (Fig. 3b, d). It can be clearly seen that leaf-like grains in the buffer layer act as growth centres for large grains in the bilayer. Large grains on the surface of bilayer resemble a ball of yarn or scrolled belts with a diameter of ca. 5–6 μm and 3 μm (see insets in Fig. 3b, d) when grown using spray rates of 2 and 3 ml/min, respectively. The density of large grains (scrolled belts) in a bilayer follows the density of grains in the buffer layer. The formation of ZnO:In scrolled belts explains why the ZnO:In layer acts as a powder, according to XRD analysis (see Figs. 1 and 2). The formation of ZnO grains as scrolled belts by chemical spray pyrolysis method is not introduced up to now.

It is known that tubular structures can be formed from layered materials by a surfactant or additive assisted rolling mechanism [30]. According to this approach, the formation of wolfram disulfide and vanadium oxide nanotubes has been explained [30]. The thermal stress has been proposed as a driving force for surfactant-free rolling mechanism used to explain the transformation of Ag_2S from lamellar to tubular structures [30]. Both rolling mechanisms describe the formation of nanotubes but not of scrolled belts. We propose that the formation of ZnO scrolled belt grains during the chemical spray process could be explained by the ZnO:In polar surfaces induced growth mechanism presented by Z.L. Wang [31]. According to the mechanism introduced, a polar surface dominated belt acts as a capacitor with two parallel charged plates tending to roll over into an enclosed ring to reduce the electrostatic energy [31].

As we obtained the buffer layers with smaller features (grains) using the spray rate of 3 ml/min compared to 2 ml/min, then from here forward the spray rate of 3 ml/min was used to grow ZnO buffer and ZnO/ZnO:In bilayers on PI and reference samples on glass. It has been found that the film thickness is a critical factor controlling the ZnO buffer layer morphology. A buffer layer of type B on PI grown from 30 ml solution is ca. 350 nm thick, the surface morphology of this film is evaluated from Fig. 4a. The length of leaf-like grains on the surface is less than 1 μm, while a buffer of type A on PI grown at similar conditions from 50 ml of solution is ca. 650 nm thick with leaf-like grains with the length of ca. 2 μm on the surface (Fig. 3c). Thus, leaf-like grains are smaller in thinner films. The comparison of the SEM cross-sectional images (not presented) shows that thinner films (type B) have smoother surface. Smoother buffer layer leads to a smoother bilayer (Fig. 3b). The variation of ZnO buffer layer thickness from 350 nm to 650 nm did not induce cracking in ZnO/ZnO:In bilayer. The density of grains in the bilayer follows the density of grains in the buffer layer similarly to the films grown onto type A buffer layers (Fig. 3), yet the size of the grains is ca. 5–8 times smaller (Fig. 4b).

Interestingly, as shown by the SEM surface view (Fig. 4d), the bilayer grown on glass is also composed of scrolled grains forming a canvas-like surface in spite of the fact that morphology of the ZnO buffer layer on glass (see Fig. 4c) is different from that observed for buffer layers on PI. According to SEM image in Fig. 4c, there are nanoneedles on the surface of ZnO buffer layer on glass, this observation is in accordance with the results published in [28]. The existence of scrolled belts also in the bilayer on glass substrate, where morphology of a buffer layer as well as the orientation of crystallites are different from that observed on PI substrates, implies that the formation of scrolled belts is caused by ZnO:In, and is not due to the substrate type or orientation of crystallites in a buffer layer. At the same time the surface of a bilayer on glass seems to be smoother (Fig. 4d, inset) when compared to a bilayer on PI (Fig. 4b, inset).

3.3. Optical properties

Fig. 5 compares the total reflectance spectra of ZnO/ZnO:In bilayers grown onto PI using buffer layers type A and type B (spectra a and b, respectively) and glass using buffer layer type A (spectrum c), and a ZnO:In single layer on glass (spectrum d). The total reflectance spectra of bilayers on PI (a and b) are similar and show reflectance of 10–17%

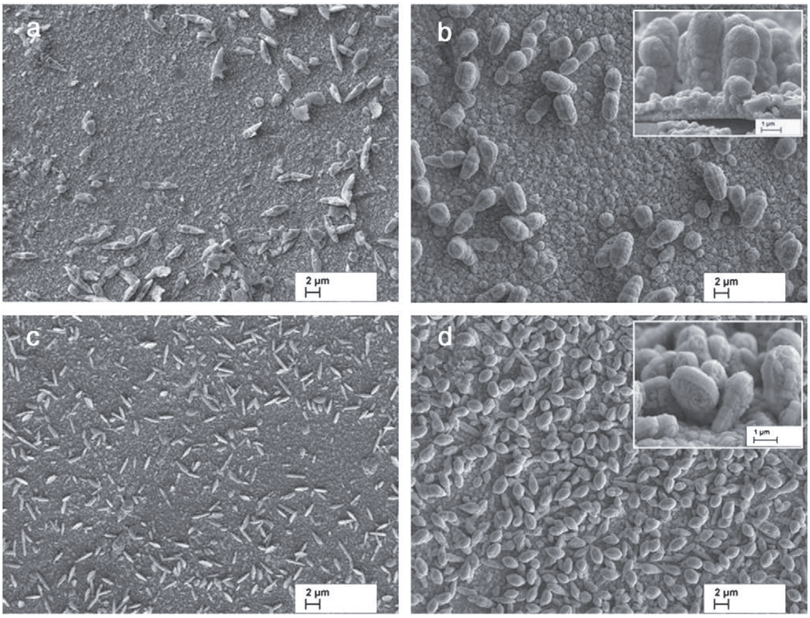

Fig. 3. SEM images of ZnO buffer layers of type A (a, c) and the corresponding ZnO/ZnO:In bilayers (b, d) grown at $T_S = 380$ °C on PI substrate. Solution spray rate(s) of 2 ml/min (a, b) and 3 ml/min (c, d) were used, respectively. The SEM cross-sectional images of bilayers are presented as insets.

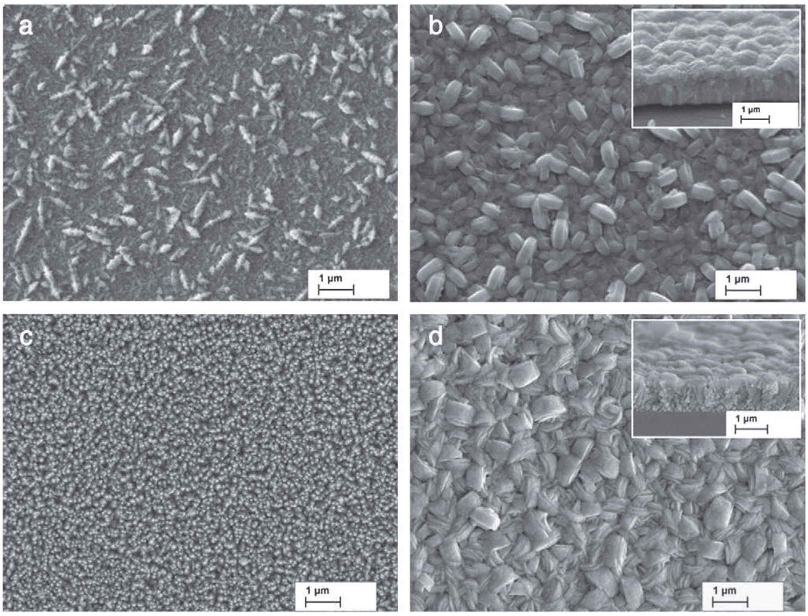

Fig. 4. SEM images of ZnO buffer layer of type B (a) and ZnO/ZnO:In bilayer (b) grown on PI substrate; and of ZnO buffer layer type B (c) and ZnO/ZnO:In bilayer (d) grown on glass. The films were grown at $T_S = 380$ °C. The SEM cross-sectional images of bilayers are presented as insets.

in the spectral region of 400–1500 nm. At the same time, the average total reflectance of both, the bilayer and the ZnO:In single layer on glass (spectra c and d, respectively) slightly decreases, from ca. 15% at 400 nm to ca. 10% at 1500 nm. The interference is less pronounced in the spectrum of the bilayer (spectrum c) compared to a single ZnO:In layer on glass (spectrum d), and could be explained by more granular structure of the bilayer (see SEM image of bilayer in Fig. 4d and SEM image of ZnO:In in [28]).

Fig. 6 shows wavelength-dependent haze factor spectra for same thin films in the same order as in the total reflectance spectra. Haze factor is defined as the ratio of diffused reflectance with respect to the total reflectance ($H = R_{diff}/R_{total}$). The haze factor expresses the ZnO films capability to scatter light.

The presence of interference in the haze spectra of layers grown on glass (see Fig. 6c and d) originates from the specular component of the total reflectance (see Fig. 5c and d) and indicates that the layers are relatively smooth and uniform in thickness, compared to bilayers grown on PI (see Fig. 6a and b). The lack of any interference in the haze spectra of the bilayers grown on PI refers to high surface roughness. This observation is in accordance with the SEM when comparing Fig. 3d with Fig. 4d that correspond to bilayers grown on PI and glass, respectively.

Haze factor of the bilayer on PI (see corresponding SEM image in Fig. 3d) is about 85% and 95% in the visible part of the spectrum and in the wavelength region of 800–1500 nm, respectively (see Fig. 6a). In contrast, ZnO:Al films grown on glass by DC magnetron sputtering show haze factor of 5% at visible spectral range [32]. The light scattering

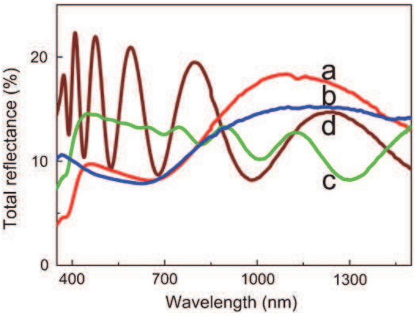

Fig. 5. Total reflectance spectra of ZnO/ZnO:In bilayer on PI using buffer layer of type A (a), bilayer on PI using buffer layer of type B (b), bilayer on glass substrate using buffer layer of type A (c) and ZnO:In film on glass substrate (d). All the layers were grown at 380 °C, ZnO:In layer from 50 ml of spray solution. SEM images of bilayers with total reflectance spectra a, b and c are shown in Figs. 3d, 4b and d, respectively; SEM image of ZnO:In layer on glass with haze spectrum d is presented in [28].

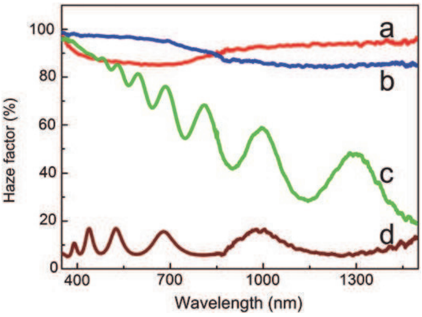

Fig. 6. Haze factor spectra of ZnO/ZnO:In bilayer on PI using buffer layer of type A (a), bilayer on PI using buffer layer of type B (b), bilayer on glass substrate using buffer layer of type A (c) and ZnO:In on glass substrate (d). All the layers were grown at 380 °C, ZnO:In layer from 50 ml of spray solution.

is highest when the incident light wavelength is similar to the feature dimension where the light is reflected [33]. Thus, it could be proposed that higher haze factor in the spectral region of 800–1500 nm is due to the higher share of features with sizes of 800–1500 nm. On the contrary, the bilayer on PI with a characteristic SEM image shown in Fig. 4b demonstrates haze factor of ca. 95% in the visible part of the spectrum (Fig. 6b) while the haze factor is ca. 85% at wavelengths between 900 nm and 1500 nm. In this case, the light scattering is slightly higher from features with the size of 350–700 nm.

For bilayer on glass (see SEM image on Fig. 4d) the haze factor decreases rapidly from 95% down to 20% at wavelengths 350 nm up to 1500 nm, respectively, indicating the increased light scattering from the fine-scale features. The single ZnO:In layer on glass shows relatively low haze factor of ca. 10% over the spectral region 350–1500 nm.

3.4. Electrical properties

Electrical properties of the sprayed bilayer on PI and on glass substrate are presented in Table 1. Electrical resistivities of 4.4×10^{-2} Ω cm and 6.7×10^{-3} Ω cm are measured for a ZnO:In layer in bilayers on PI and on glass substrates, respectively. The resistivity of 4.4×10^{-2} Ω cm of sprayed ZnO:In film on PI is comparable to that obtained for r.f. sputtered ZnO:Al films on polymer [3]. Regardless of the substrate type used, at similar deposition conditions comparable carrier concentrations in ZnO/ZnO:In films are present. Carrier concentrations of 9.3×10^{19} cm^{-3} and 7.0×10^{19} cm^{-3} are characteristic for ZnO:In films in bilayer structure deposited onto buffer layer type B at 380 °C on PI and glass, respectively, (see Table 1). However, the carrier mobility is 13 cm^2/Vs in the layer on glass and 1.5 cm^2/Vs in the layer on PI. As the mobility of carriers is controlled by the film thickness and grain size [7] then such a distinctive variation could be explained by a higher ZnO:In film thickness and larger grain size in the ZnO:In film in bilayer on glass compared to that on PI (Table 1, Fig. 4a and b). For comparison, the electrical properties of a single layer ZnO:In film are presented in Table 1. ZnO:In film as a single layer on glass shows about 10 times lower resistivity compared to ZnO:In film in bilayer on PI, mainly caused by 10 times higher carrier mobility. Thus, to obtain conductive ZnO:In films on PI substrate, much thicker ZnO:In films with lower roughness should be grown.

4. Conclusions

It has been shown that ZnO films can be grown by CSP method on polyimide substrate at 380 °C. The crystallites in undoped ZnO film on the polyimide substrate show preferential growth of the (100) plane parallel to the substrate while the crystallites in ZnO film on a glass substrate are c-axis orientated. It appears that ZnO:In films cracked and peeled off when deposited directly onto polyimide. The ZnO:In films where grown onto an undoped ZnO layer acting as a buffer layer on top of polyimide. The ZnO:In layer shows mixed morphology from smooth canvas-like surface to large grains dependent on buffer layer local morphology — a flat buffer area tends to support the growth of smooth ZnO:In layer while distinctive grains in the buffer layer act as growth centres for large grains. According to SEM, the large grains with diameters from 1 μm up to 6 μm are bundles of scrolled belts.

It appears that a bilayer grown on a glass substrate is also composed of grains resembling scrolled belts. The formation of the ZnO:In layer in form of scrolled belts could explain why the crystallites in ZnO:In layer, when grown onto ZnO buffer layer, do not show preferential orientation. We speculate that the formation of ZnO:In scrolled belt grains could occur according to the ZnO:In polar surfaces induced growth mechanism [31].

When grown on the polyimide substrate, the bilayers exhibit haze factor of 85–95% in the spectral region of 350–1500 nm indicating high light scattering capability. The resistivity of the ZnO:In film in bilayer on polyimide is 4.4×10^{-2} Ω cm. This relatively high resistivity, when compared to that obtained on a glass substrate, is mainly due to the low carrier mobility of 1.5 cm^2/Vs, the carrier concentration of ca. 10^{20} cm^{-3} is comparable to that obtained in a ZnO:In single layer film on glass. To achieve lower resistivity, the ZnO:In films should be grown significantly thicker, additionally, the buffer layer properties should be optimised to grow a smoother ZnO:In film in a bilayer enabling better carriers transport conditions.

Table 1
Electrical properties and thicknesses of the sprayed ZnO:In layers grown onto ZnO buffer layer B at 380 °C. SEM images of bilayers grown on polyimide (PI/ZnO/ZnO:In) and soda-lime glass (SLG/ZnO/ZnO:In) are presented on Fig. 4b and d, respectively. For reference, ZnO:In single layer (SLG/ZnO:In) on glass is presented.

Structure	ZnO:In film thickness, nm	ρ, Ω cm	n, cm^{-3}	μ, cm^2/Vs
PI/ZnO/ZnO:In	300	4.4×10^{-2}	9.3×10^{19}	1.5
SLG/ZnO/ZnO:In	600	6.7×10^{-3}	7.0×10^{19}	13
SLG/ZnO:In	1400	3.2×10^{-3}	1.4×10^{20}	15

Acknowledgements

Financing by the Estonian Ministry of Education and Research under the project SF0140092s08, Estonian Science Foundation (ETF9081) and European Regional Development Fund (Centre of Excellence “Mesosystems: Theory and Applications” TK114 and project 3.21101.12-0023) is gratefully acknowledged. This work has been partially supported by graduate school “Functional materials and technologies” receiving funding from the European Social Fund under project 1.2.0401.09-0079 in Estonia.

References

[1] M. Čada, O. Churpita, Z. Hubička, H. Šíchová, L. Jastrabík, Surf. Coat. Technol. 177–178 (2004) 699.
[2] J.W. Park, G. Kim, S.H. Lee, E.H. Kim, G.H. Lee, Surf. Coat. Technol. 205 (2010) 915.
[3] E. Fortunato, P. Nunes, D. Costa, D. Brida, I. Ferreira, R. Martins, Vacuum 64 (2002) 233.
[4] J.H. Lee, J. Electroceram. 23 (2009) 512.
[5] S. Fernández, F.B. Naranjo, Sol. Energy Mater. Sol. Cells 94 (2010) 157.
[6] A.N. Banerjee, C.K. Ghosh, K.K. Chattopadhyay, H. Minoura, A.K. Sarkar, A. Akiba, A. Kamiya, T. Endo, Thin Solid Films 496 (2006) 112.
[7] E. Fortunato, A. Gonçalves, V. Assunção, A. Marques, H. Águas, L. Pereira, I. Ferreira, R. Martins, Thin Solid Films 442 (2003) 121.
[8] L. Gong, J. Lu, Z. Ye, Sol. Energy Mater. Sol. Cells 94 (2010) 937.
[9] C. Koidis, S. Logothetidis, D. Georgiou, A. Laskarakis, S. Lousinian, I. Tsiaoussis, N. Frangis, Phys. Status Solidi A 205 (2008) 1988.
[10] A.W. Ott, R.P.H. Chang, Mater. Chem. Phys. 58 (1999) 132.
[11] A. Miyake, T. Yamada, H. Makino, N. Yamamoto, T. Yamamoto, Thin Solid Films 517 (2009) 3130.
[12] S.H. Chen, Y.C. Chen, IEEE Trans. Electron Devices 59 (2012) 1709.
[13] P. Prepelita, R. Medianu, B. Sbarcea, F. Garoi, M. Filipescu, Appl. Surf. Sci. 256 (2010) 1807.
[14] J.Y. Kao, C.Y. Hsu, G.C. Chen, D.C. Wen, J. Mater. Sci. Mater. Electron. 23 (2012) 1352.
[15] L. Gong, J. Lu, Z. Ye, Sol. Energy Mater. Sol. Cells 94 (2010) 1282.
[16] M. Krunks, E. Kärber, A. Katerski, K. Otto, I. Oja Açik, T. Dedova, A. Mere, Sol. Energy Mater. Sol. Cells 94 (2010) 1191.
[17] S. Gledhill, A. Grimm, N. Allsop, T. Koehler, C. Camus, M. Lux-Steiner, C.H. Fisher, Thin Solid Films 517 (2009) 2309.
[18] G. Adamopoulos, S. Thomas, P.H. Wöbkenberg, D.D.C. Bradley, M.A. McLachlan, T.D. Anthopoulos, Adv. Mater. 23 (2011) 1894.
[19] K.T.R. Reddy, T.B.S. Reddy, I. Forbes, R.W. Miles, Surf. Coat. Technol. 151–152 (2002) 110.
[20] A. Crossay, S. Buecheler, L. Kranz, J. Perrenoud, C.M. Fella, Y.E. Romanyuk, A.N. Tiwari, Sol. Energy Mater. Sol. Cells 101 (2012) 283.
[21] M. Vent, E. Kärber, T. Unt, A. Mere, M. Krunks, Phys. Status Solidi C 9 (2012) 1604.
[22] S. Major, A. Banerjee, K.L. Chopra, Thin Solid Films 108 (1983) 333.
[23] M. Krunks, E. Mellikov, Thin Solid Films 270 (1995) 33.
[24] Technical Information on Kapton-H Polyimide Film, Dupont, Bulletin K-15345-1 04/11 (2011).
[25] K. Otto, A. Katerski, A. Mere, O. Volobujeva, M. Krunks, Thin Solid Films 519 (2011) 3055.
[26] International Centre for Diffraction Data (ICDD), PDF-2 Release, 2008.
[27] A. Hafdallah, F. Yanineb, M.S. Aida, N. Attaf, J. Alloys Compd. 509 (2011) 7267.

[28] T. Dedova, J. Klauson, C. Badre, Th. Pauporté, R. Nisumaa, A. Mere, O. Volobujeva, M. Krunks, Phys. Status Solidi A 205 (2008) 2355.
[29] M.D.L.L. Olvera, H. Gómez, A. Maldonado, Sol. Energy Mater. Sol. Cells 91 (2007) 1449.
[30] D.P. Li, Z. Zheng, Y. Lei, F.L. Yang, S.X. Ge, Y.D. Zhang, B.J. Huang, Y.H. Gao, K.W. Wong, W.M. Lau, Chem. Eur. J. 17 (2011) 7694.
[31] Z.L. Wang, Mater. Sci. Eng. R 64 (2009) 33.
[32] C. Guillén, J. Montero, J. Herrero, Appl. Surf. Sci. 264 (2013) 448.
[33] T. Söderström, F.J. Haug, X. Niquille, V. Terrazzoni, C. Ballif, Appl. Phys. Lett. 94 (2009) 063501.

Article **IV**

Kriisa, M.; Sáez-Araoz, R.; Fischer, C. -H.; Köhler, T.; Kärber, E.; Fu, Y.; Hergert, F.; Lux-Steiner, M. C.; Krunks, M. (2015). Study of Spray-CVD Deposited Zn(O,S) Films and their Application as Buffer Layers in Cu(In,Ga)(S,Se)$_2$ Solar Cells. Solar Energy, 115, 562−568.

Available online at www.sciencedirect.com

ScienceDirect

Solar Energy 115 (2015) 562–568

SOLAR ENERGY

www.elsevier.com/locate/solener

Study of Zn(O,S) films grown by aerosol assisted chemical vapour deposition and their application as buffer layers in $Cu(In,Ga)(S,Se)_2$ solar cells

Merike Kriisa [a,b,*], Rodrigo Sáez-Araoz [a], Christian-Herbert Fischer [a,c], Tristan Köhler [a], Erki Kärber [b], Yanpeng Fu [a], Frank Hergert [d], Martha Christina Lux-Steiner [a,e], Malle Krunks [b]

[a] Institute for Heterogeneous Material Systems, Helmholtz Centre Berlin for Materials and Energy, Hahn-Meitner-Platz 1, 14109 Berlin, Germany
[b] Laboratory of Thin Film Chemical Technologies, Department of Materials Science, Tallinn University of Technology, Ehitajate tee 5, 19086 Tallinn, Estonia
[c] Freie Universität Berlin, Institut für Chemie, Fabeckstr. 34-36, 14195 Berlin, Germany
[d] Bosch Solar CISTech GmbH, Muenstersche Str. 24, 14772 Brandenburg an der Havel, Germany
[e] Fachbereich Physik, Freie Universität Berlin, Arnimallee 14, 14195 Berlin, Germany

Received 10 December 2014; received in revised form 20 January 2015; accepted 17 February 2015
Available online 30 March 2015

Communicated by: Associate Editor Igor Tyukhov

Abstract

Manufacturing chalcopyrite thin film solar cells from cost-efficient and environmentally friendly materials is of high priority. Therefore, the materials used in buffer layer production nowadays (such as indium and cadmium) need to be substituted. Zn(O,S) is considered to be a potential buffer layer material when deposited with a fast and inexpensive method. Zn(O,S) layers have been prepared by aerosol assisted chemical vapour deposition (AACVD) technique. AACVD technique is a simple non-vacuum process where the thin film deposition temperatures do not exceed 250 °C. 10 mM spray solution was made by dissolving zinc(II)acetylacetonate monohydrate in ethanol. The films were grown on Mo substrate at 225 °C (film growth temperature). The effect of deposition parameters (spray solution concentration, N_2 flow rate, H_2S flow rate) on Zn(O,S) thin film properties were studied with SEM and XRD. Thereupon optimising the deposition parameters, homogeneous and compact Zn(O,S) thin films were obtained and the films were employed in the chalcopyrite thin film solar cell structure by growing films on $Cu(In,Ga)(S,Se)_2$ substrates industrially produced by BOSCH Solar CISTech GmbH. The resulting cells were studied using current–voltage and quantum efficiency analysis and compared with solar cell references that include In_2S_3 and CdS as buffer layer deposited by ion layer gas reaction and chemical bath deposition, respectively. The best output of the solar cell containing Zn(O,S) as buffer layer and without intrinsic ZnO under standard test conditions (AM 1.5G, 100 mW/cm^2, 25 °C) is: Voc = 573 mV, Jsc = 39.2 mA/cm^2, FF = 68.4% and efficiency of 15.4% being slightly better than the In_2S_3 or CdS containing solar cell references.

Keywords: Chalcopyrite thin film solar cells; Zn(O,S); Cd-free buffer layer; Aerosol assisted chemical vapour deposition (AACVD)

1. Introduction

Manufacturing solar cells that have high efficiency while consisting of cost-effective and environmentally friendly

---

* Corresponding author at: Laboratory of Thin Film Chemical Technologies, Department of Materials Science, Tallinn University of Technology, Ehitajate tee 5, 19086 Tallinn, Estonia. Tel.: +372 6203369; fax: +372 6202020.
E-mail address: merike.kriisa@ttu.ee (M. Kriisa).

http://dx.doi.org/10.1016/j.solener.2015.02.046

materials is of great interest. Therefore, the amount of In and Cd in the chalcopyrite-based solar cell structures needs to be reduced. Due to their abundance and harmlessness Zn compounds can be potential candidates to be used as buffer layers in solar cell structures (Bhattacharya and Ramanathan, 2004; Ennaoui et al., 2003; Kushiya, 2014, 2004; Merdes et al., 2009). For the last decade, Zn(O,S) has been used as an effective, non-toxic, cost-efficient buffer layer in solar cell structures (Buffière et al., 2011; Ennaoui, 2006; Grimm et al., 2010; Hultqvist et al., 2009; Klenk et al., 2013; Platzer-Björkman et al., 2006; Ramanathan et al., 2012; Sáez-Araoz et al., 2008; Witte et al., 2013). Using Zn(O,S) in solar cell as buffer layer gives also the opportunity to omit the intrinsic ZnO window layer in the solar cell structure and therefore making the solar cell structure and production simpler and cheaper.

So far, Zn(O,S) layers have been prepared by methods that are either slow, not in-line suitable or vacuum techniques, such as chemical bath deposition (CBD) (Buffière et al., 2011; Kushiya, 2004; Sáez-Araoz et al., 2008; Witte et al., 2013), atomic layer deposition (ALD) (Platzer-Bjorkman et al., 2003; Platzer-Björkman et al., 2006; Sanders and Kitai, 1992; Zimmermann et al., 2006) and sputtering (Grimm et al., 2011, 2010; Klenk et al., 2013; Kobayashi et al., 2013; Nakamura et al., 2013). The best efficiencies for solar cells with sputtered or ALD deposited Zn(O,S) buffer layer are similar, 18.3% and 18.5% respectively (Klenk et al., 2013; Zimmermann et al., 2006). At the moment, the highest reported CBD deposited Zn(O,S) buffered solar cell efficiency is 20.9% (Kushiya, 2014). In this study, a simple, fast and cost-efficient atmospheric pressure aerosol assisted chemical vapour deposition (AACVD) was used. The AACVD is a simple non-vacuum process where the deposition temperatures do not exceed 250 °C (Fischer et al., 2011) and the deposition of the solar cell component is a continuous operation; AACVD can be carried out in an in-line process where the yield is a function of the travelling speed and the line length. With the AACVD method, breaking of the vacuum for the P2 scribing (second scribing step in monolithically integrated devices) between intrinsic ZnO (i-ZnO) and n-type (n-ZnO), that is necessary for the regular solar cell structure where P2 is applied after the i-ZnO deposition, is avoided.

Due to a higher band gap, the Zn(O,S) buffers have the advantage of absorbing less blue light from the sun spectrum than the state of the art CdS buffer layers, therefore reducing the losses in that wavelength region. The reported band gap of ALD and CBD deposited Zn(O,S) layers are 3.6 eV (Sanders and Kitai, 1992) and 3.7 eV (Buffière et al., 2011), respectively. The band gap of sputtered Zn(O,S) has a parabolic dependency with the S/(S + O) ratio varying from 2.6 eV to 3.6 eV (Grimm et al., 2011; Kobayashi et al., 2013). Naturally, the S/(S + O) ratio influences the structural and optical properties of Zn(O,S) layers (Grimm et al., 2011; Kobayashi et al., 2013; Platzer-Björkman et al., 2006). An increase in the sulphur content from 0 to 1 in the $Zn(O_{1-x},S_x)$ film follows the Vegard's law (Vegard, 1921) and results in X-ray diffraction peaks characteristic to ZnS.

This is the first publication of AACVD grown Zn(O,S) layers and the aim is to study the effect of reactive gas concentration and carrier gas flow rate on the morphological, structural and optical properties of Zn(O,S) layers deposited by AACVD on Mo substrates. Furthermore, the solar cell characteristics of $Cu(In,Ga)(S,Se)_2$ devices with AACVD grown Zn(O,S) as buffer layer are discussed.

2. Experimental

2.1. Zn(O,S) layer deposition

Zn(O,S) layers were deposited by AACVD onto preheated molybdenum coated soda lime glass substrates (2.5×2.5 cm^2). Prior to each deposition, the glass/molybdenum (gl/Mo) substrates were cleaned by rinsing with technical ethanol. 10 mmol/L zinc(II)acetylacetonate solution ($C_{10}H_{14}O_4Zn \cdot H_2O$, Alfa Aesar, $\geqslant$98%, dissolved in ethanol, abs., $\geqslant$99.8%) was used as the zinc precursor solution. This solution is nebulised by an ultrasonic atomiser and the aerosol is blown towards the preheated substrate by a laminar flow of the carrier gas N_2 at a constant angle of 45°. The N_2 flow rate was 5 L/min or 7 L/min. To grow Zn(O,S) layers, the deposition time and temperature (T) are kept constant at 30 min and at 225 °C using a feedback control system for the heater supply, respectively. 5% H_2S in Ar (flow rate varied from 0 mL/min up to 20 mL/min) is introduced as the reactant gas into the aerosol stream towards the heated substrate. Above the heated substrate the solvent droplets vaporise and the desired film is formed on the substrate. The scheme of the aerosol assisted chemical vapour deposition set-up used in this study is presented in Fig. 1.

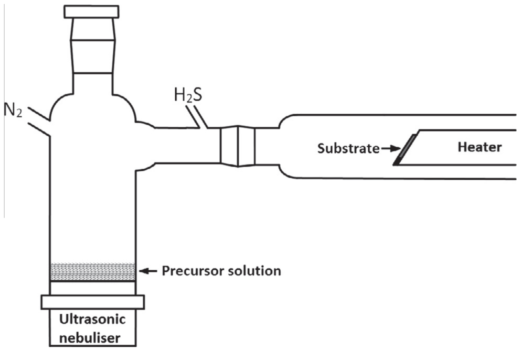

Fig. 1. The scheme of atmospheric pressure aerosol assisted chemical vapour deposition (AACVD) set-up.

2.2. Zn(O,S) layer characterisation

The surface morphology of Zn(O,S) layers on glass/Mo substrate was characterised by scanning electron microscopy (SEM). In addition, the film thickness was obtained from the SEM cross-sectional images. The elemental composition of the layers was evaluated from different areas on the film using energy dispersive X-ray (EDX) analysis. SEM and EDX analysis was performed using a Gemini LEO1530. For the EDX analysis, the Zn(O,S) layer was deposited onto cleaned steel substrate to avoid the overlapping of S and Mo signals. X-ray diffractions of Zn(O,S) layers on gl/Mo substrate were recorded with grazing incidence using a Bruker D8 diffractometer with a Cu Kα-source ($\lambda = 1.5406$ Å). To study the optical properties, the Zn(O,S) layers were deposited onto quartz substrate and measured using a *Cary 500* Spectrophotometer equipped with an integrating sphere. The Zn(O,S) band gap was determined from absorption and reflection measurements by the Tauc-Plot.

2.3. Solar cell preparation

In order to obtain solar cells, Zn(O,S) layers were deposited by AACVD on glass/Mo/Cu(In,Ga)(S,Se)$_2$ (CIGSSe) substrates obtained from BOSCH Solar CISTech GmbH, Germany (2.5×2.5 cm^2) and cleaned by rinsing with ethanol. Thereupon, Al-doped ZnO (AZO) was directly sputtered on half of the number of solar cells while the other half had radio frequency (rf) deposited intrinsic ZnO (i-ZnO) in addition to AZO layers on top of the AACVD Zn(O,S) buffer layer. Finally, Ni/Al grid contacts were deposited on the solar cells to improve the collection. Hence, two solar cell structures were formed: glass/Mo/CIGSSe/AACVD-Zn(O,S)/AZO/ and glass/Mo/CIGSSe/AACVD-Zn(O,S)/i-ZnO/AZO/, designated as **structure 1** and **structure 2**, respectively. For references, solar cells with CdS and In$_2$S$_3$ buffer layers were deposited by CBD and ion layer gas reaction (ILGAR), respectively.

2.4. Solar cell characterisation

The solar cell performance (scribed total area of 0.5 cm^2, 8 cells per sample) was tested with a class A sun simulator under standard test conditions (25 °C, 100 mW/cm^2, AM1.5G) and an external quantum efficiency apparatus.

3. Results and discussions

3.1. Properties of Zn(O,S) layers

SEM was used to study the morphology of Zn(O,S) layers deposited on gl/Mo substrates with different H$_2$S flow rates while other deposition parameters were constant ($M_{Zn} = 10$ mmol/L, $T = 225$ °C, N$_2$ flow rate of 5 L/min, deposition time 30 min). The surface morphology of Zn(O,S) layers depends strongly on the flow rate and therefore on the concentration of the purging gas (H$_2$S): higher reactive gas concentrations lead to powdery films. It can be seen that increasing the flow rate of the reactive gas from 2 mL/min (Fig. 2a) to 3 mL/min (Fig. 2b) has a small effect yet slightly increases the number and the size of particles on

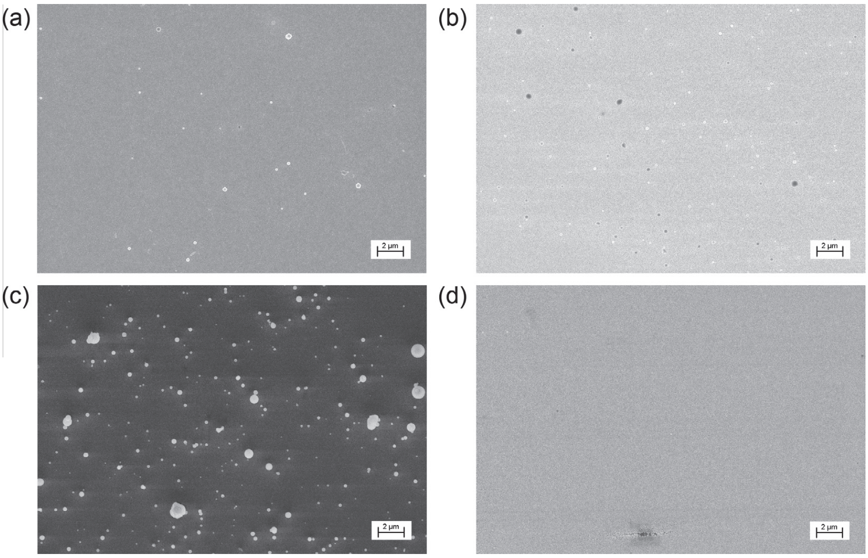

Fig. 2. SEM images of Zn(O,S) layers on gl/Mo substrates deposited according to **recipe 1** (N$_2$ flow rate is 5 L/min) with varied H$_2$S flow rate of 2 mL/min (a), 3 mL/min (b) and 10 mL/min (c) and Zn(O,S) layer grown according to **recipe 2** (d) with N$_2$ and H$_2$S flow rate of 7 L/min and 5 mL/min, respectively.

top of a compact Zn(O,S) surface. With further increase of H_2S flow rate to 10 mL/min the number of particles on the surface increases; their size reaches a maximum diameter of ca. 1 μm (Fig. 2c). The film thickness decreases from 55 nm to 45 nm with the increase of H_2S flow rate from 2 mL/min to 3 mL/min, respectively. Therefore, using the following deposition parameters leads to relatively compact Zn(O,S) layer: $M_{Zn} = 10$ mmol/L, $T = 225$ °C, N_2 flow rate of 5 L/min, deposition time 30 min and the flow rate of purging gas is 2 mL/min (**recipe 1**).

The formation of the powdery particles on top of the Zn(O,S) layer can be caused by the formation and precipitation of ZnS already either in the droplet or from the gas phase. This is supported by the increasing number of particles on the surface with increasing the H_2S flow rate, as can be seen in Fig. 2a–c.

From our previous study (Fischer et al., 2011) we know that increasing the carrier gas flow rate shortens the residence time of the aerosol over the substrate. Therefore, we increased the N_2 flow rate from 5 L/min to 7 L/min and used the H_2S flow rate of 5 mL/min (**recipe 2**) while other deposition parameters were as mentioned in the beginning of this section. These deposition conditions led to a compact and homogeneous Zn(O,S) with very little particles on the film surface (Fig. 2d) and to film thickness of 60 nm. These films are thicker due to the higher amount of aerosol transported to the heated sample. According to EDX, the O/(S + O) ratio in the compact layer is ca. 16% (measured from 9 different areas).

Crystalline films were obtained independently of the used recipe. The X-ray diffraction patterns of AACVD deposited Zn(O,S) layers on gl/Mo substrate according to **recipe 2** and the ZnO and ZnS powder references (International Centre for Diffraction Data, 2008) are shown in Fig. 3. It can be seen that the XRD peaks of the deposited Zn(O,S) are more similar to hexagonal ZnS (PDF card No. 01-075-1534) rather than to hexagonal ZnO (PDF card No. 01-079-0208). The XRD study supports the results obtained with EDX.

The optical transmittance, reflectance and the absorbance of Zn(O,S) deposited according to **recipe 2** on quartz substrate in the visible range of the spectrum is ca. 70%, ca. 20% and ca. 10%, respectively (Fig. 4a). The direct band gap of Zn(O,S) layer is approximately 3.6 eV (Fig. 4b) being slightly higher than the Eg value presented by Sanders and Kitai (1992) for ALD deposited Zn(O,S) films with sulphur to zinc ratio of 0.9.

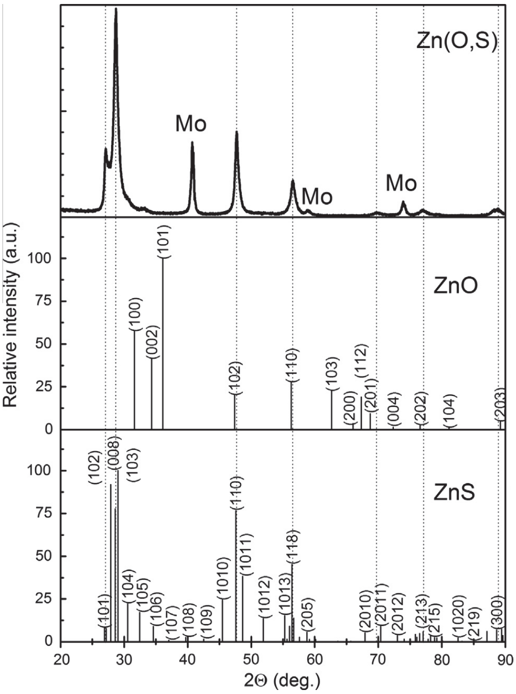

Fig. 3. X-ray diffractogram of Zn(O,S) deposited according to **recipe 2** (N_2 and H_2S flow rate of 7 L/min and 5 mL/min, respectively), ZnO and ZnS powder diffractograms.

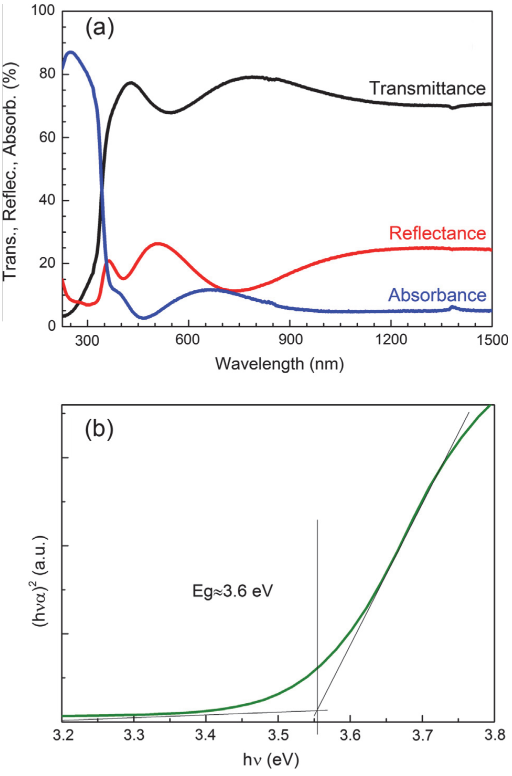

Fig. 4. Optical properties (transmittance, reflectance and absorbance) (a) and Tauc plot of Zn(O,S) film on quartz substrate (b) deposited according to **recipe 2**: N_2 and H_2S flow rate of 7 L/min and 5 mL/min, respectively.

3.2. Characteristics of solar cells with Zn(O,S)

The Zn(O,S) buffered solar cells (deposited according to **recipe 1**) were tested in two solar cell structures: **structure 1** (glass/Mo/CIGSSe/AACVD-Zn(O,S)/AZO) and **structure 2** (glass/Mo/CIGSSe/AACVD-Zn(O,S)/i-ZnO/AZO). The variance in solar cell parameters (Voc, Jsc, FF and η), analysed for 16 solar cells for all solar cell structures, are presented in Fig. 5. It is visible that using rf intrinsic ZnO in the solar cell structure results in output parameters that have lower deviation from the mean value (Fig. 5 **structure 2**) compared to solar cells without rf-deposited i-ZnO (Fig. 5 **structure 1**). The high deviation from the mean value for **structure 1** is due to the higher risk of shunts when less conductive i-ZnO is excluded from the solar cell structure. This has been studied and explained by (Grabitz et al., 2005). Still, there is no significant difference in the best cell parameters between **structure 1** and **structure 2** (Fig. 5). Omitting the rf-deposited i-ZnO window layer from the solar cell structure allows us to simplify the solar cell structure. Therefore, the deposition process would become simpler, cheaper and faster leading to decreased solar cell production cost being attractive in a solar module production, where for the P2 scribe line application in between sputtered i-ZnO and n-ZnO the vacuum has to be broken. Moreover, if the i-ZnO layer should be used it can be also deposited just by switching off the H_2S after the Zn(O,S) deposition. Such sprayed i-ZnO gave similar solar cell results as with sputtered i-ZnO (Gledhill et al., 2009).

The variance of output parameters of 16 solar cells for the references, CdS and In_2S_3 buffered, are presented in Fig. 5. The thicknesses of buffer layers in the solar cell are as follows: Zn(O,S) ca. 60 nm, CdS ca. 40 nm and In_2S_3 ca. 20 nm. Independent of the solar cell structure with Zn(O,S) as buffer layer, the best solar cell output parameters are comparable with In_2S_3 and CdS buffered solar cells although the deviation from the mean value is high. The best solar cell output parameters with Zn(O,S) as the buffer layer are Voc = 573 mV, Jsc = 39.2 mA/cm^2, FF = 68.4% and $\eta = 15.4\%$ (Fig. 5 and Table 1). In 2003, (Platzer-Bjorkman et al., 2003) presented the study of solar cells (area < 1 cm^2) with ALD deposited Zn(O,S) buffer layers where the Voc is 684 mV, Jsc = 32 mA/cm^2, FF = 73% and $\eta = 16\%$. The higher solar cell output parameter values with ALD grown Zn(O,S) buffer layer are possibly due to more homogeneous Zn(O,S) layer.

A decrease in layer deposition time from 30 min to 20 min to grow Zn(O,S) films according to **structure 1** and **recipe 1**, increases slightly the Voc and FF and therefore also the efficiency of a solar cell (see Fig. 5 and Table 1). For **recipe 2**, all the solar cell output parameter values decrease slightly when the deposition time is decreased to 20 min. The main loss in the Zn(O,S) buffered solar cell efficiency between **recipe 1** and **recipe 2** is originated from the fill factor, up to 16% lower fill factor is characteristic to solar cells with Zn(O,S) buffer layer grown according to **recipe 2** compared to **recipe 1**.

Independent of the deposition time, the efficiency of Zn(O,S) buffered solar cell grown according to **recipe 1**

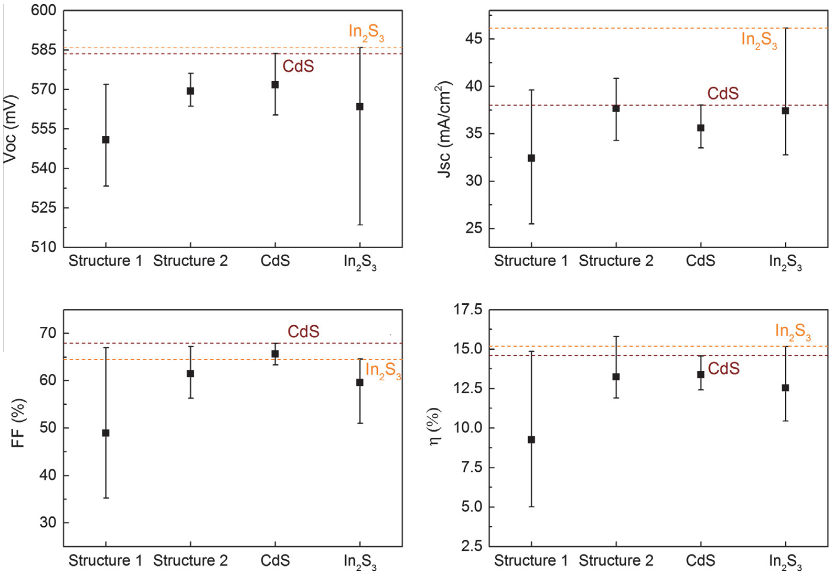

Fig. 5. Variance of output parameters of 16 solar cells (cell area of 0.5 cm^2) with Zn(O,S) as buffer layer and of 16 reference solar cells with CdS or In_2S_3 as buffer layer. **Structure 1** is glass/Mo/CIGSSe/AACVD-Zn(O,S)/AZO/Ni/Al and **structure 2** is glass/Mo/CIGSSe/AACVD-Zn(O,S)/i-ZnO/AZO/Ni/Al. Zn(O,S) as the buffer layer was deposited according to **recipe 1** for 30 min. The output parameter variance of CdS and In_2S_3 buffered cells is given for comparison.

Table 1
The best output parameters for Zn(O,S) buffered solar cells (**structure 1**) with Zn(O,S) grown according to **recipe 1** and **recipe 2** with deposition times of 20 min and 30 min. The best output parameters of CdS and In_2S_3 buffered cells are given for comparison.

	Deposition time (min)	Voc (mV)	Jsc(mA/cm^2)	FF(%)	η(%)
Recipe 1 (N_2 of 5 L/min, H_2S of 2 mL/min)	20	573	39.2	68.4	15.4
	30	572	38.8	66.9	14.9
Recipe 2 (N_2 of 7 L/min, H_2S of 5 mL/min)	20	562	36.9	52.3	10.9
	30	577	38.3	56.8	12.5
In_2S_3 reference	n.a.	582	40.4	64.5	15.2
CdS reference	n.a.	584	36.8	67.9	14.6

n.a. – not available.

is comparable with reference solar cells (14.9% for solar cell with Zn(O,S) grown for 30 min, 15.4% for solar cell with Zn(O,S) grown for 20 min and 15.2% for In_2S_3 or 14.6% for CdS buffered solar cells) (Table 1). While the Jsc and FF are comparable to the reference solar cells parameters, the main difference is in the Voc. Independent of the deposition time, the Voc of the Zn(O,S) buffered solar cell is 5–20 mV lower than for the In_2S_3 or CdS or buffered solar cells (582 mV and 584 mV and, respectively). The output parameters of solar cells with Zn(O,S) buffer layers grown according to **recipe 2**, are lower than the reference values for CdS or In_2S_3 buffered solar cells, independent of the Zn(O,S) layer deposition time (Table 1). Interestingly, to lower the process cost and time to prepare solar cell, the Zn(O,S) buffer layer could be grown for 20 min instead of 30 min only according to **recipe 1**.

The external quantum efficiency spectra of AACVD-Zn(O,S) (**structure 1**, grown according to **recipe 1** for 30 min) and CBD-CdS buffered solar cells are presented in Fig. 6. The Zn(O,S) and CdS buffer layer thicknesses in the corresponding solar cells are ca. 60 nm and ca. 40 nm, respectively. The advantage of the use of Zn(O,S) versus the use of CdS as the buffer layer is evident from the EQE of the respective cells (Fig. 6). The CdS, with a band gap of 2.4 eV, absorbs light in the wavelength region of 380–550 nm resulting in lower quantum efficiency. However, the presence of the Zn(O,S) with a band gap of 3.6 eV, that will transmit light down to its absorbing edge at around 350 nm, does not lead to absorption losses in this wavelength region. It can be speculated that the decline in EQE at around 2.5 eV for Zn(O,S) buffered solar cell can be due to the interference pattern.

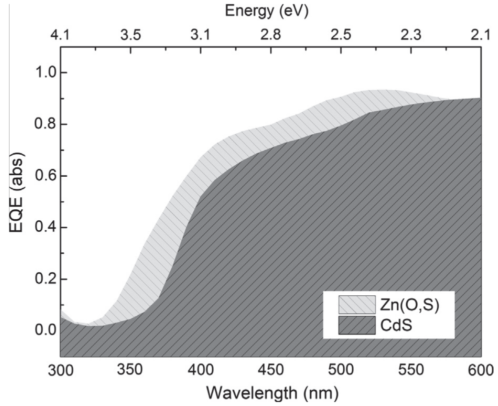

Fig. 6. EQE spectra of thin film solar cells with CIGSSe/Zn(O,S)/AZO and CIGSSe/CdS/i-ZnO/AZO structures. The Zn(O,S) was deposited according to **recipe 1** for 30 min. The corresponding Jsc values for Zn(O,S) and CdS buffered solar cells are 38.8 mA/cm^2 and 36.8 mA/cm^2, respectively.

4. Conclusions

The Zn(O,S) layers were grown by a simple, cost-efficient and continuous aerosol assisted chemical vapour deposition (AACVD). The surface morphology of AACVD deposited Zn(O,S) is dependent on the flow rate and therefore the concentration of the H_2S: flow rates higher than 2 mL/min lead to non-homogeneous and non-compact layers. To obtain compact Zn(O,S) layers, the deposition parameters should be 2 mL/min of 5% H_2S in Ar and carrier gas flow rate of 5 L/min (**recipe 1**) or 5 mL/min of reactive gas and 7 L/min of carrier gas (**recipe 2**) corresponding to a solution concentration of 10 mmol/L. Values greater than the mentioned parametric numbers lead to powdery and not compact films. XRD patterns show the presence of crystalline matter being similar rather to ZnS than to ZnO. The XRD study supports the results obtained by EDX showing that the Zn(O,S) layer is formed with an excess of sulphur. The transmittance of the Zn(O,S) film in the visible spectrum range is ca. 70% and the Eg ≈ 3.6 eV.

The solar cells with Zn(O,S) as the buffer layer were grown on industrial glass/Mo/Cu(In,Ga)$(S,Se)_2$ substrates. The solar cells with Zn(O,S) buffer layer have comparative solar cell output characteristics with CdS and In_2S_3 references. The use of Zn(O,S) as a buffer layer in solar cell makes the cell structure and production simpler and cheaper by allowing to omit the intrinsic ZnO from the solar cell structure. Hence, the use of AACVD deposited Zn(O,S) allows to avoid the breaking of vacuum for the P2 scribing (second scribing step in monolithically integrated devices) between i-ZnO and n-ZnO that is necessary for the regular solar module structure (if P2 is applied after the i-ZnO deposition). Decreasing the deposition time from

30 to 20 min for the deposition of Zn(O,S) layer according to **recipe 1**, the solar cell output characteristics increase slightly being comparable with the reference CdS and In_2S_3 buffered solar cell output parameters. Yet, at the moment the variation in deposition time has not been optimised for the lab scale depositions but the preliminary results are promising. Nevertheless, effective, non-toxic and cost-efficient Zn(O,S) grown by AACVD can be used as a buffer layer in solar cells without the loss in efficiency. Using AACVD for the deposition of Zn(O,S), especially with an in-line process, decreases the solar cell production time and cost when compared to the use of ALD or CBD methods to grow In and Cd containing buffer layers in modern solar cells.

Acknowledgements

We are grateful to Carola Ferber and Michael Kirsch for completing the solar cells. This research was supported by European Social Fund's Doctoral Studies and Internationalisation Programme DoRa, which is carried out by Foundation Archimedes. This work has been partially supported by graduate school "Functional materials and technologies" receiving funding from the European Social Fund under project 1.2.0401.09-0079. Financing by the Estonian Ministry of Education and Research under project IUT 19-4 is gratefully acknowledged.

References

Bhattacharya, R.N., Ramanathan, K., 2004. Cu(In, Ga)Se_2 thin film solar cells with buffer layer alternative to CdS. Sol. Energy 77, 679–683. http://dx.doi.org/10.1016/j.solener.2004.05.009.

Buffière, M., Harel, S., Arzel, L., Deudon, C., Barreau, N., Kessler, J., 2011. Fast chemical bath deposition of Zn(O, S) buffer layers for Cu(In, Ga)Se_2 solar cells. Thin Solid Films 519, 7575–7578. http://dx.doi.org/10.1016/j.tsf.2011.01.104.

Ennaoui, A., 2006. Highly-efficient Cd-free $CuInS_2$ thin-film solar cells and mini-modules with Zn(S, O) buffer layers prepared by an alternative chemical bath process. Prog. Photovoltaics 14, 499–511. http://dx.doi.org/10.1002/pip.682.

Ennaoui, A., Eisele, W., Lux-Steiner, M., Niesen, T.P., Karg, F., 2003. Highly efficient Cu(Ga, In)(S, $Se)_2$ thin film solar cells with zinc-compound buffer layers. Thin Solid Films 431–432, 335–339.

Fischer, C.-H., Allsop, N.A., Gledhill, S.E., Köhler, T., Krüger, M., Sáez-Araoz, R., Fu, Y., Schwieger, R., Richter, J., Wohlfart, P., Bartsch, P., Lichtenberg, N., Lux-Steiner, M.C., 2011. The spray-ILGAR® (ion layer gas reaction) method for the deposition of thin semiconductor layers: process and applications for thin film solar cells. Sol. Energy Mater. Sol. Cells 95, 1518–1526. http://dx.doi.org/10.1016/j.solmat.2010.12.019.

Gledhill, S., Grimm, A., Allsop, N., Koehler, T., Camus, C., Lux-Steiner, M., Fischer, C.-H., 2009. A spray pyrolysis route to the undoped ZnO layer of Cu(In, Ga)(S, $Se)_2$ solar cells. Thin Solid Films 517, 2309–2311. http://dx.doi.org/10.1016/j.tsf.2008.10.110.

Grabitz, P.O., Rau, U., Werner, J.H., 2005. A multi-diode model for spatially inhomogeneous solar cells. Thin Solid Films 487, 14–18. http://dx.doi.org/10.1016/j.tsf.2005.01.027.

Grimm, A., Just, J., Kieven, D., Lauermann, I., Palm, J., Neisser, A., Rissom, T., Klenk, R., 2010. Sputtered Zn(O, S) for junction formation in chalcopyrite-based thin film solar cells. Phys. Status Solidi – Rapid Res. Lett. 4, 109–111. http://dx.doi.org/10.1002/pssr.201004083.

Grimm, A., Kieven, D., Klenk, R., Lauermann, I., Neisser, A., Niesen, T., Palm, J., 2011. Junction formation in chalcopyrite solar cells by sputtered wide gap compound semiconductors. Thin Solid Films 520, 1330–1333. http://dx.doi.org/10.1016/j.tsf.2011.04.150.

Hultqvist, A., Platzer-Björkman, C., Pettersson, J., Törndahl, T., Edoff, M., 2009. $CuGaSe_2$ solar cells using atomic layer deposited Zn(O, S) and (Zn, Mg)O buffer layers. Thin Solid Films 517, 2305–2308. http://dx.doi.org/10.1016/j.tsf.2008.10.109.

International Centre for Diffraction Data (ICDD), 2008. PDF-2 Release.

Klenk, R., Steigert, A., Rissom, T., Greiner, D., Kaufmann, C.A., Unold, T., Lux-Steiner, M.C., 2013. Junction formation by Zn(O, S) sputtering yields CIGSe-based cells with efficiencies exceeding 18%. Prog. Photovoltaics Res. Appl. 22, 161–165. http://dx.doi.org/10.1002/pip.2445.

Kobayashi, T., Kumazawa, T., Jehl Li Kao, Z., Nakada, T., 2013. Cu(In, Ga)Se_2 thin film solar cells with a combined ALD-Zn(O, S) buffer and MOCVD-ZnO: B window layers. Sol. Energy Mater. Sol. Cells 119, 129–133. http://dx.doi.org/10.1016/j.solmat.2013.05.052.

Kushiya, K., 2004. Development of Cu(InGa)Se-based thin-film PV modules with a Zn(O, S, OH) buffer layer. Sol. Energy 77, 717–724. http://dx.doi.org/10.1016/j.solener.2004.08.027.

Kushiya, 2014. Solar Frontier. Press Release 2014.

Merdes, S., Sáez-Araoz, R., Ennaoui, A., Klaer, J., Lux-Steiner, M.C., Klenk, R., 2009. Recombination mechanisms in highly efficient thin film Zn(S, O)/Cu(In, Ga)S_2 based solar cells. Appl. Phys. Lett. 95, 213502. http://dx.doi.org/10.1063/1.3266829.

Nakamura, M., Kouji, Y., Chiba, Y., Hakuma, H., Kobayashi, T., Nakada, T., 2013. Achievement of 19.7% efficiency with small-sized Cu(InGa)$(SeS)_2$ solar cells prepared by sulfurization after selenization process with Zn-based buffer. In: Proc. 39th IEEE Photovolt. Spec. Conf., pp. 849–852.

Platzer-Bjorkman, B., Kessler, J., Stolt, L., 2003. Atomic layer deposition of Zn(O,S) buffer layers for high efficiency Cu(In,Ga)Se_2 solar cells. In: 3rd World Conf. Photovolt. Energy Convers., pp.461–464.

Platzer-Björkman, C., Törndahl, T., Abou-Ras, D., Malmström, J., Kessler, J., Stolt, L., 2006. Zn(O, S) buffer layers by atomic layer deposition in Cu(In, Ga)Se_2 based thin film solar cells: band alignment and sulfur gradient. J. Appl. Phys. 100, 044506. http://dx.doi.org/10.1063/1.2222067.

Ramanathan, K., Mann, J., Glynn, S., Christensen, S., Pankow, J., Li, J., Scharf, J., Mansfield, L., Contreras, M., Noufi, R., 2012. A comparative study of Zn(O, S) buffer layers and CIGS solar cells fabricated by CBD, ALD, and sputtering. In: Photovoltaic Specialists Conference (PVSC), 2012 38th IEEE. IEEE, pp. 001677–001681. http://dx.doi.org/10.1109/PVSC.2012.6317918.

Sáez-Araoz, R., Ennaoui, A., Kropp, T., Veryaeva, E., Niesen, T.P., Lux-Steiner, M.C., 2008. Use of different Zn precursors for the deposition of Zn(S, O) buffer layers by chemical bath for chalcopyrite based Cd-free thin-film solar cells. Phys. Status Solidi 205, 2330–2334. http://dx.doi.org/10.1002/pssa.200779421.

Sanders, B.W., Kitai, A., 1992. Zinc oxysulfide thin films grown by atomic layer deposition. Chem. Mater. 4, 1005–1011. http://dx.doi.org/10.1021/cm00023a015.

Vegard, L., 1921. Die Konstitution der Mischkristalle und die Raumfüllung der Atome. Z. Phys. 5, 17–26. http://dx.doi.org/10.1007/BF01349680.

Witte, W., Abou-Ras, D., Hariskos, D., 2013. Chemical bath deposition of Zn(O, S) and CdS buffers: influence of Cu(In, Ga)Se_2 grain orientation. Appl. Phys. Lett. 102, 051607. http://dx.doi.org/10.1063/1.4788717.

Zimmermann, U., Ruth, M., Edoff, M., 2006. Cadmium-free CIGS min-modules with ALD-grown Zn(O, S)-based buffer layers. In: 21st Eur. Photovolt. Sol. Energy Conf., pp. 1831–1834.

Article **V**

Kriisa, M.; Krunks, M.; Oja Acik, I.; Kärber, E.; Mikli, V. (2015). The effect of tartaric acid in the deposition of Sb_2S_3 films by chemical spray pyrolysis. Materials Science in Semiconductor Processing, 40, 867−872.

Materials Science in Semiconductor Processing 40 (2015) 867–872

Contents lists available at ScienceDirect

Materials Science in Semiconductor Processing

journal homepage: www.elsevier.com/locate/mssp

The effect of tartaric acid in the deposition of Sb_2S_3 films by chemical spray pyrolysis

Merike Kriisa [a,*], Malle Krunks [a], Ilona Oja Acik [a], Erki Kärber [a], Valdek Mikli [b]

[a] Laboratory of Thin Film Chemical Technologies, Department of Materials Science, Tallinn University of Technology, Ehitajate tee 5, Tallinn 19086, Estonia
[b] Chair of Semiconductor Materials Technology, Department of Materials Science, Tallinn University of Technology, Ehitajate tee 5, Tallinn 19086, Estonia

ARTICLE INFO

Article history:
Received 12 March 2015
Received in revised form
22 June 2015
Accepted 18 July 2015
Available online 7 August 2015

Keywords:
Sb_2S_3
Thin film
Chemical spray pyrolysis
Tartaric acid
Thermal analysis

ABSTRACT

Sb_2S_3 films grown by chemical bath deposition have been used as an absorber in extremely thin inorganic absorber solar cells. In the present work, Sb_2S_3 thin films were deposited by chemical spray pyrolysis. The aqueous spray solution consisted of $SbCl_3$ (Sb=2 mmol/L), thiourea (S) and tartaric acid (TA) in molar ratios of Sb:S:TA=1:3:10 or 1:3:1, and the solution was nebulized onto preheated soda-lime glass substrates. The deposition temperature ranged from 205 °C to 230 °C and 205 °C to 355 °C for Sb:S:TA=1:3:10 and 1:3:1, respectively. The effect of the tartaric acid concentration in spray solution, deposition temperature and the annealing temperature on the film properties was studied with X-ray diffraction (XRD), scanning electron microscopy (SEM), energy-dispersive X-ray spectroscopy and Fourier transform infrared spectroscopy (FTIR), thermogravimetric and differential thermal analysis (TG/DTA) of tartaric acid was carried out.

The films deposited from solutions with Sb:S:TA ratio of 1:3:10 at 205 °C are ca. 1 μm thick, contain orthorhombic stibnite (Sb_2S_3) phase and high amount of carbon and oxygen residues. The reduced TA concentration (1:3:1) in the spray solution leads to orthorhombic Sb_2S_3 films with decreased content of carbon and oxygen in the films compared to solutions with Sb:S:TA=1:3:10. An increase in the deposition temperature from 205 °C to 355 °C decreases the mean crystallite size from 25 nm to 15 nm and a decrease in sulfur and an increase in oxygen content was detected. SEM images indicate that the morphology and the thickness of the films grown with Sb:S:TA ratio of 1:3:1 are not homogeneous and an increase in deposition temperature results in thinner films. FTIR spectra of Sb_2S_3 film substance confirm that the TA has not completely decomposed at the used deposition temperatures. According to the thermal analysis study, TA decomposition takes place in three steps where 95% of mass is lost by 254 °C and the TA is completely decomposed only at 495 °C. Additionally, we report the first results on growing Sb_2S_3 films with band gap of 1.7 eV by chemical spray pyrolysis using alcohol solutions.

1. Introduction

For the low cost production and industrialization of photovoltaic devices, new selections of abundant and inexpensive materials are needed to fill the global energy needs. For this, Sb_2S_3 has a potential to be used in extremely thin absorber (ETA) solar cells as an alternative absorber layer [1–6]. Mainly chemical bath deposition (CBD) has been used to grow Sb_2S_3 layers for the application in solar cells [1,3–6] and currently the highest ETA solar cell efficiency reported is 5.7% [6]. In its crystalline stibnite form, the Sb_2S_3 has suitable optical properties for the application as an absorber: a direct band gap of 1.7–1.8 eV and a high absorption coefficient of $1.8 \cdot 10^5$ cm^{-1} at 450 nm [2,5,7].

Methods like CBD [1–6,8,9], successive ionic layer adsorption and reaction [10], radio frequency sputtering [7], thermal treatment of Sb layer in S atmosphere [11], electrodeposition [12], vacuum evaporation [13], chemical spray pyrolysis [14–19] have been used to grow Sb_2S_3 films. Among these methods, the chemical spray pyrolysis is a fast, low cost and relatively easy to use technique. $SbCl_3$ and C_2H_5NS, $CS(NH_2)_2$ or $Na_2S_2O_3$ have been used as antimony (Sb) and sulfur (S) precursors, respectively [14–19]. With the chemical spray pyrolysis method, crystalline Sb_2S_3 films are formed when glacial acetic acid [14,16] or acetone-water mixture [19] is used as solvent. For chemically sprayed films from non-aqueous solution, the Sb:S ratio influences the grain size having the reported maxima of 350 Å at Sb:S of 4:6 [14]. With the use of non-aqueous solution, the direct band gap of sprayed Sb_2S_3 ranges from 1.72 eV [19] to 2.26 eV [14]. The use of aqueous solvents requires the presence of an additional compound in the spray solution that acts as a complexing agent and prevents the

---

[*] Corresponding author. Fax: +372 6202020.
E-mail address: merike.kriisa@ttu.ee (M. Kriisa).

http://dx.doi.org/10.1016/j.mssp.2015.07.049
1369-8001/

hydrolysis of Sb precursor [15–18,20]. Oxalic acid ($C_2H_2O_4$) [17] or more commonly tartaric acid ($C_4H_6O_6$) have been used as complexing agent [15,16,18]. Independent of the complexing agent used, the deposited films are mainly amorphous [16–18]. Still, not many articles have been published regarding the deposition parameters and the properties of sprayed Sb_2S_3 films from aqueous solutions where tartaric acid (TA) was used as complexing agent. The effect of the TA concentration on the structural, optical and electrical properties of the chemically sprayed films from aqueous solutions has been of interest [15,18]. However, the reported results of Sb_2S_3 films from aqueous solutions are discrepant. For example, the increase in TA increases the crystallinity of the Sb_2S_3 [15]. According to Ref. [15], the film surface was uneven, devoid of any irregular grain growth and the elemental composition of the films was nearly stoichiometric: 38% of Sb and 62% of S. The reported direct band gap of the Sb_2S_3 films grown from $SbCl_3$, thiourea and tartaric acid dissolved in deionized water varies from 1.1 eV to 2.7 eV [15,16,18].

In the articles of chemical spray pyrolysis grown Sb_2S_3 films, no consistent study has been done on the effect of deposition temperature on the sprayed films deposited from aqueous solutions with tartaric acid as a complexing agent. In addition, the elemental composition of the Sb_2S_3 films is practically unstudied while the films phase composition has been investigated with XRD. The aim of this paper is to study the effect of tartaric acid concentration in the spray solution and the effect of deposition temperature on elemental and phase composition, morphological and optical properties of the film.

2. Experimental

The chemical spray pyrolysis set-up used in this study is described elsewhere [21]. The antimony and sulfur precursors of $SbCl_3$ (Sb) and $CS(NH_2)_2$ (S), respectively, were dissolved in 50 ml of deionized H_2O to molarities of 2 mM and 6 mM. To prevent the hydrolysis of Sb precursor, $C_4H_6O_6$, tartaric acid (TA), was used as complexing agent with molar ratios of 1:3:10 (Sb:S:TA), being similar to literature [15,18], and 1:3:1 (Sb:S:TA) in the spray solution. The solution with spray rate of ca. 1.5 mL/min was nebulized onto preheated glass substrates that were placed onto molten tin bath. Compressed air with flow rate of 8 L/min was used as the carrier gas. The films with the Sb:S:TA molar ratio of 1:3:10 and 1:3:1 were deposited at substrate temperatures (T_s) of 205 °C, 230 °C and in the range of 205–355 °C with the step of 50 °C, respectively. The film grown with high TA concentration of 1:3:10 in the spray solution at 205 °C was annealed in air at 400 °C.

X-ray diffraction (XRD) patterns of the films on glass substrates were recorded using a Rigaku Ultima IV diffractometer with monochromatic Cu Kα radiation ($\lambda = 1.5406$ Å, 40 kV at 40 mA). Data were gathered in the 2Θ range of 15–60° with scan speed of 4°/min and scan step of 0.02° using the silicon strip detector D/teX Ultra. The X-ray diffractograms were analyzed using the software on the Rigaku System (PDXL 1.4.0.3). The crystallite size was calculated using the Scherrer method. The surface morphology of the films was characterized and the film thickness was determined with scanning electron microscopy (SEM) using Zeiss HR FESEM Ultra 55 apparatus at operating voltage of 4 kV. The elemental composition of films was evaluated by energy dispersive X-ray (EDX) analysis using Röntec EDX XFlash 3001 detector and the Oxford Instruments INCA Energy system. Optical measurements were carried out in the wavelength range of 250–2500 nm on Jasco V-670 spectrophotometer using an integrating sphere and the direct band gap of the films was acquired from Tauc plots. FTIR transmission spectra of the substance of sprayed films were measured in the range of 4000–400 cm^{-1} on Perkin-Elmer GX1 spectrophotometer using the KBr pellet technique. Thermogravimetric and differential thermal analysis (TG/DTA) measuremenTartaric acid were carried out on a Set-Sys-Evolution instrument. The analyses were carried out in a dynamic 80% Ar+20% O_2 (artificial air) atmosphere in the temperature range of 30–600 °C using a heating rate of 5 °C/min, the gas flow rate of 60 mL/min and open Al_2O_3 crucibles.

3. Results and discussion

3.1. Sb_2S_3 films with Sb:S:TA ratio of 1:3:10 in the aqueous spray solution

The molar ratio of 1:3:10 for Sb:S:TA was chosen according to literature [15,18]. The as deposited films grown at T_s of 205 °C in this study are of low crystallinity, all the peaks in the XRD pattern presented in Fig. 1 correspond to orthorhombic stibnite (Sb_2S_3) phase (PDF no. 01-075-4015) [22]. All the peaks for film grown at T_s of 230 °C also belong to orthorhombic Sb_2S_3 (Fig. 1) and the crystallite size is 20 nm. The crystallite sizes calculated from the (201) peak (Fig. 1) according to Scherrer method for films grown at T_s of 205 °C and grown at T_s of 205 °C and annealed at 400 °C (205 °C+400 °C) are 52 nm and 13 nm, respectively. Here, the annealing the film was carried out in air environment that led to decreased crystallinity of Sb_2S_3 films. In contrast, annealing in N_2 environment has been reported to increase the crystallinity of the Sb_2S_3 films [14]. In Fig. 1, new unidentified peak is present at 2Θ of 23.5° for the film 205 °C+400 °C. This new phase might be oxidized antimony that occurs due to annealing the films in air at 400 °C. Itzhaik et al. [1] showed the presence of Sb_2O_3 when CBD grown Sb_2S_3 layer was annealed in N_2 at 300 °C and cooled in air.

Irrespective of the deposition temperature and annealing, the thickness of all the Sb_2S_3 films with Sb:S:TA ratio of 1:3:10 is above 1 μm, according to the SEM images in Fig. 2. The SEM images show that the film grown at T_s of 205 °C is morphologically homogeneous containing two distinct layers: grains at the lower part of the film (on top of the substrate) and the upper part of the layer having nearly no grains in it (Fig. 2a). An increase in the deposition temperature from 205 °C to 230 °C results in films that are peeling from the substrate and the films surface has a number of holes in it (Fig. 2b). The high number of holes in the film grown at T_s of 230 °C could be the reason for the peeling of the film. Hence, deposition temperatures higher than 230 °C were not studied though according to literature, deposition temperatures

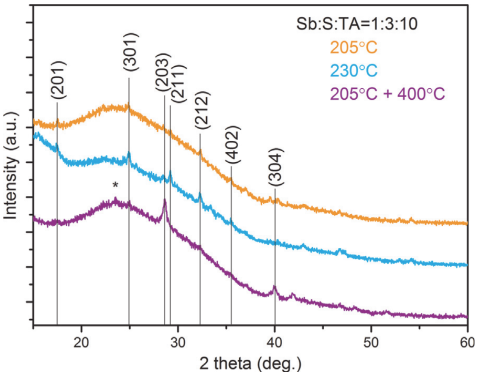

Fig. 1. XRD patters of Sb_2S_3 films with Sb:S:TA molar ratio of 1:3:10 in spray solution deposited at 205 °C, 230 °C, and 205 °C followed by annealing at 400 °C (designated as 205 °C+400 °C). Unknown phase peak is marked with *.

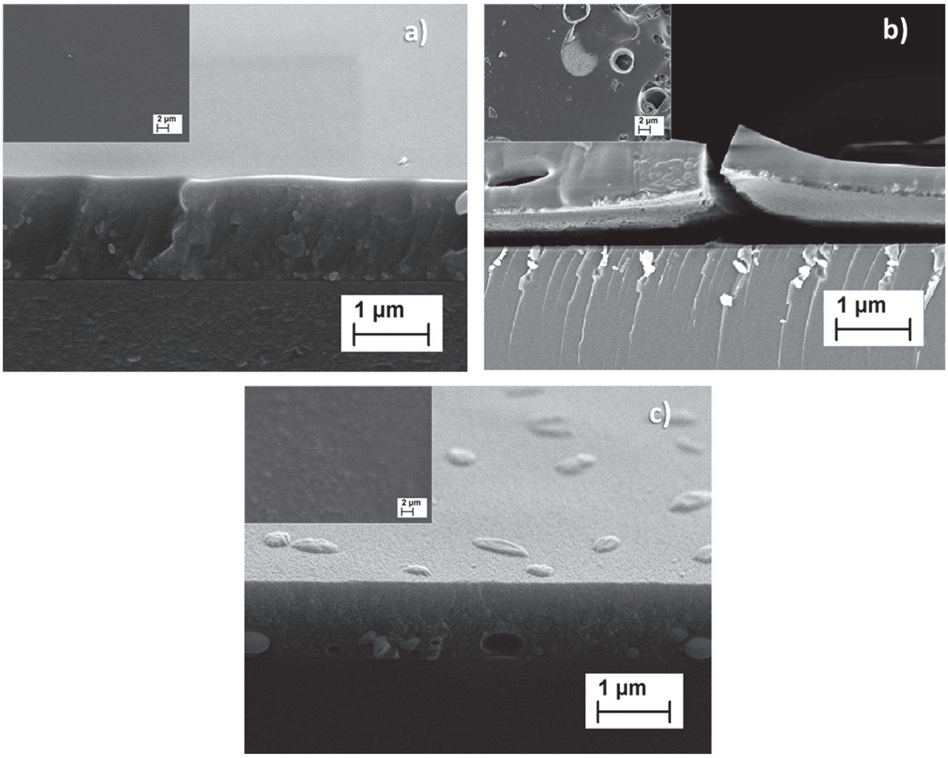

Fig. 2. Cross-sectional SEM images of Sb_2S_3 films with Sb:S:TA molar ratio of 1:3:10 in spray solution deposited at (a) 205 °C, (b) 230 °C and 205 °C followed by annealing at (c) 400 °C (designated as 205 °C+400 °C). Plane views of the films are presented as insets on the cross-sectional images.

higher than 230 °C were used to spray Sb_2S_3 films [14–17,19].

The film grown at T_s of 205 °C and annealed at 400 °C has homogeneous morphology similar to the as deposited film but with unknown roundish agglomerates throughout the film (Fig. 2c).

EDX study showed that none of the films had the Sb to S ratio corresponding to the Sb_2S_3 stoichiometry. Interestingly, Gadakh et al. [15] deposited films where the elemental composition of the film was 38 at% and 62 at% for Sb and S, respectively. In addition, irrespective of the deposition temperature and annealing, all the sprayed Sb_2S_3 films contained high amount of carbon and oxygen and this occurrence has been neglected so far in all the published articles. Hence, the films were not clean. The typical elemental composition of the Sb_2S_3 film grown with Sb:S:TA=1:3:10 is presented in Table 1. The carbon and the oxygen in the film could be a residue from tartaric acid independent of the deposition and annealing temperature. For the films grown at T_s of 205 °C the organic residues can originate from thiourea [23–25] but only in small amounts [26]. It is probable that due to the high amount of the secondary phases in the film, the Sb_2S_3 films are poorly crystallized. The origin of the organic residues is discussed in Section 3.3.

The optical band gap of Sb_2S_3 film grown at T_s of 205 °C is 2.2 eV (Table 1). The optical band gap decreased slightly to 2.1 eV when the deposition temperature was increased to 230 °C.

3.2. *The effect of deposition temperature on films grown from aqueous solutions with Sb:S:TA molar ratio of 1:3:1*

Hereon, a lower tartaric acid concentration was chosen due to the high carbon contamination in the Sb_2S_3 films grown with Sb:S:TA molar ratio of 1:3:10. The Sb:S:TA molar ratio of 1:3:1 in the spray solution was selected experimentally that is the minimum amount of TA necessary to inhibit the hydrolysis of Sb precursor.

Table 1
Mean film thickness (t), mean crystallite size of Sb_2S_3 (D), elemental composition and Eg of sprayed films with Sb:S:TA molar ratios of 1:3:10 deposited at temperature (T_S) of 205 °C and 1:3:1 deposited at T_S of 205 °C, 255 °C, 305 °C and 355 °C, according to SEM, XRD, EDX and band gap obtained from optical measurements, respectively.

				Elemental composition (at%)							
Sb:S:TA	**T_S (°C)**	**t (nm)**	**D (nm)**	**Sb**	**S**	**C**	**O**	**Cl**	**Na**	**Si**	**Eg (eV)**
1:3:10	205	1430	52	5	5	52	32	< 1	2	4	2.2
1:3:1	205	510	25	12	15	15	36	< 1	4	17	2.3
	255	470	24	6	6	11	48	< 1	6	22	2.1
	305	340	22	7	7	19	44	< 1	6	17	2.2
	355	390	15	10	4	18	53	< 1	3	11	2.5

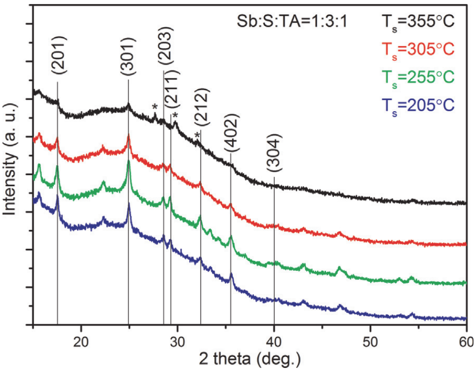

Fig. 3. XRD patterns of Sb_2S_3 films with Sb:S:TA molar ratio of 1:3:1 in spray solution deposited at 205 °C, 255 °C, 305 °C and 355 °C. Unknown phase peaks are marked with *.

Independent of the deposition temperature (T_s=205–355 °C), all the sprayed films with Sb:S:TA molar ratio of 1:3:1 in the spray solution were crystalline according to XRD (Fig. 3), all the identified peaks belong to the orthorhombic stibnite phase (PDF no. 01-075-4015) [22]. Similar to the films with Sb:S:TA ratio of 1:3:10 grown at T_s of 205 °C and annealed at 400 °C in air, an unidentified phase with peaks at 2Θ of 27.7°, 29.8° and 32.1°, not characteristic of stibnite phase, is present in the film grown at T_s=355 °C. Increasing the deposition temperature from 205 °C to 355 °C for spray solution with Sb:S:TA of 1:3:1 decreases the crystallite size from 25 nm to 15 nm (Table 1). From SEM images in Fig. 2 and Fig. 4, it can be seen that the use of Sb:S:TA ratio of 1:3:1 leads to thinner films (ca. 510 nm for film grown at T_s=205 °C) compared to the use of Sb:S:TA ratio of 1:3:10 in the spray solution (ca. 1430 nm for film grown at T_s=205 °C). The work of Gadakh et al. [15] shows that film thickness can be expected to decrease with the increase in the concentration of complexing agent. As expected, an increase in deposition temperature from 205 °C to 355 °C decreases the film thickness from ca. 510 nm to ca. 390 nm, respectively. The approximated mean film thicknesses for films grown at T_s of 205 °C, 255 °C, 305 °C and 355 °C with Sb:S:TA molar ratio of 1:3:1 are presented in Table 1. From Fig. 4a it is visible that the film consists of two detectable layers: the lower part of the film (in contact with glass substrate) has grains while the upper part of the film is covered with an amorphous substance. The SEM images (Fig. 4) indicate that an increase in deposition temperature from 205 °C to 355 °C leads to films where the amount of the substance on top of the grains is decreasing. The substance on top of the grains could be an organic residue from tartaric acid.

The use of lower TA concentration (1:3:1) instead of high tartaric acid concentration in the solution (Sb:S:TA=1:3:10) leads to lower carbon content in the film grown at T_s of 205 °C (Table 1). The Sb:S ratio in the film changes from 4:5 to 5:2 with an increase in T_s meaning that the film compositions are extremely different: the content of S in the film decreases with an increase in the T_s. Furthermore, the amount of oxygen in the film grown at T_s of 355 °C is significantly higher when compared to films deposited at lower temperatures (Table 1). The decreased S and increased O content in the film grown at T_s of 355 °C lead to the conclusion that some of the Sb is oxidized. Itzhaik et al. [1] reported that the Sb_2S_3 layers grown by CBD, annealed in inert atmosphere at 300 °C and cooled in air also contain Sb_2O_3 phase. This relates with the XRD results where the unknown peaks were present for the film grown at T_s of 355 °C and the crystallite size decreased with an increase in deposition temperature (Fig. 3 and Table 1). In addition, an increase in T_s from 205 °C up to 355 °C increases of the optical band gap of the film from 2.3 eV to 2.5 eV (Table 1).

3.3. Residues in the films deposited with tartaric acid as complexing agent

FTIR spectra of the substance of Sb_2S_3 films grown at T_s of 205 °C, 305 °C and 355 °C using the 1:3:1 solution are presented in Fig. 5. The FTIR spectrum of the film deposited at 255 °C was similar to the spectrum of film grown at T_s of 305 °C and is not shown. The films grown at T_s region 205–305 °C have similar spectra. The peaks in the wavenumber range of 1500–1775 cm^{-1} represent the bonding of C=C or C=O bonds [26,27]. The peaks in the range from 1000 cm^{-1} to 1500 cm^{-1} are characteristic of the C–O and C–C bending vibrations [27]. The FTIR spectrum of Sb_2S_3 film grown at T_s of 355 °C is relatively smooth with some weak absorption peaks at 1620 cm^{-1} and 1112 cm^{-1} when compared to the FTIR spectra of films grown at T_s temperatures below 355 °C (Fig. 5). From this we can conclude that independent of the deposition temperature all the films include carbon-containing residues although their amount seems to be significantly lower for the films grown at T_s of 355 °C. EDX shows that the content of C and O is still high in the films grown at T_s of 355 °C (Fig. 5). No residues originated from thiourea are present in the $CuInS_2$ films deposited at ca. 300 °C or higher [23,25,26,28]. Accordingly, tartaric acid that is used as a complexing agent in here should be considered as the main source of the high carbon and oxygen content in the sprayed films.

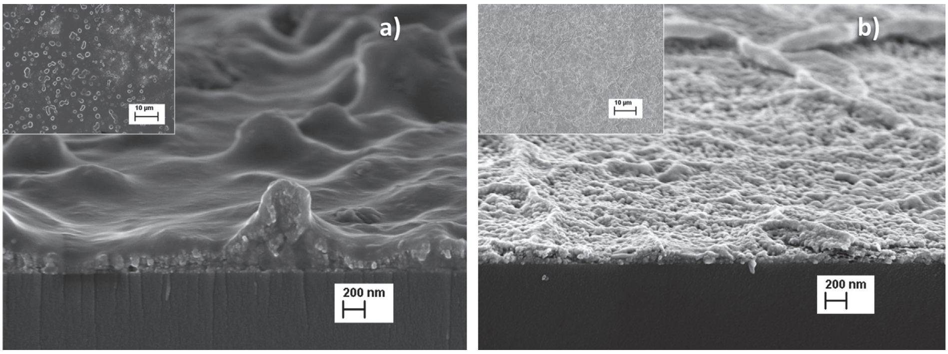

Fig. 4. Cross-sectional SEM images of Sb_2S_3 film with Sb:S:TA molar ratio of 1:3:1 deposited at (a) 205 °C and (b) 355 °C. Plane views of the films are presented as insets on the cross-sectional images.

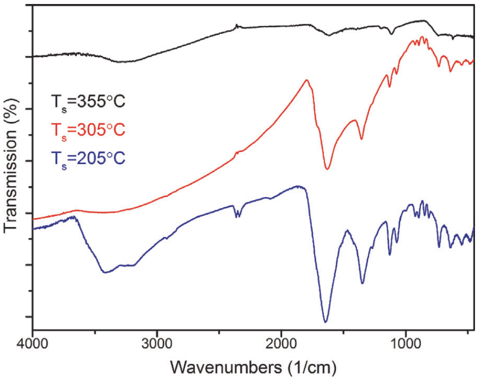

Fig. 5. FTIR spectra of Sb_2S_3 films with Sb:S:TA molar ratio of 1:3:1 in spray solution deposited at 205 °C, 305 °C and 355 °C.

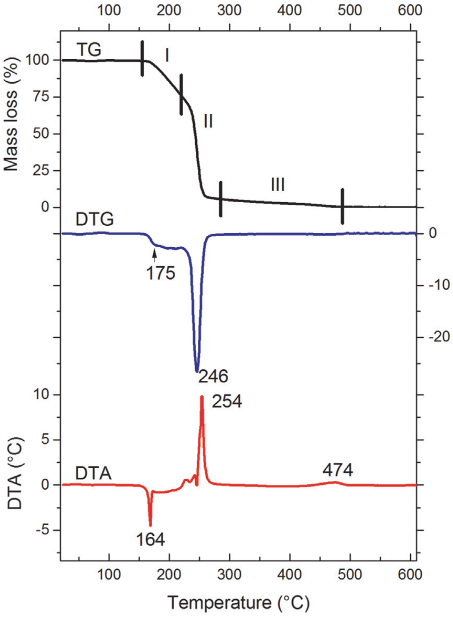

Fig. 6. Simultaneous TG, DTG and DTA curves of tartaric acid. Measurement conditions: Flowing 80% Ar+20% O_2: 60 mL/min; heating rate: 5 °C/min; and initial sample mass: 2.5 mg.

To understand the thermal behavior of tartaric acid, TG/DTA measurements were performed in air. The thermal decomposition of tartaric acid takes place in the range of 160–495 °C with the mass loss of 100% (Fig. 6). The first mass loss step of tartaric acid takes place in the range of 160–220 °C with the DTG minimum at 175 °C and the mass loss of ca. 25%. The DTA curve shows an endothermic process at 164 °C that is melting followed by decomposition as accompanied by the mass loss. The second mass loss step from 220 °C to 280 °C is peaked at 246 °C, according to the DTG curve. The DTA curve shows overlapping endo- and exothermic processes while the most intense exothermic process is peaked at 254 °C. The third mass loss step is an exothermic process peaked at 474 °C and ends at 495 °C with the mass loss of ca. 5% denoting the complete decomposition of tartaric acid. Thermal behavior of tartaric acid in an inert atmosphere has been studied by Yalcin et al. [27]. TG curves in air (Fig. 6) and inert atmosphere [27] are similar in the temperature range of 210–490 °C indicating the main mass loss at temperatures above 200 °C. In both atmospheres a small mass loss occurs at higher temperatures, at around 400 °C in inert atmosphere and close to 470 °C in air.

Thermal analysis results infer that when tartaric acid is used as a complexing agent in spray solution, all films obtained by chemical spray pyrolysis at moderate temperatures (between 200 °C and 400 °C as characteristic of spray process) are expected to contain residues originated from TA. To improve the film quality, post-deposition annealing of the films could be carried out or desisting the use of a complexing agent in the spray solution. Herein, to eliminate the need for complexing agent as the source of residues in the films, the first experiments to grow Sb_2S_3 films from methanol and 2-propanol solutions by chemical spray pyrolysis were carried out. The Sb:S ratio in the spray solution was remained at 1:3 and the deposition temperature of the films was selected to be 255 °C.

3.4. *Sb_2S_3 films sprayed from methanol and 2-propanol solutions*

Independent of the alcohol solvent used, crystalline films with the orthorhombic stibnite phase (PDF no. 01-075-4015) were grown according to XRD (Fig. 7). In addition, the films contained a secondary phase that was attributed to Sb_2O_3 with plane reflections of (222), (400), (331) and (440) at 2Θ of 27.7°, 32.1°, 35.0° and 46.1° (Fig.7), respectively (PDF no. 01-071-0365) [22]. From these results we can speculate that the unknown peaks at 2Θ of 27.7° and 32.1° in Fig. 3 for film deposited at 355 °C might also be from Sb_2O_3 phase due to the coincided 2Θ values in Figs. 7 and 3. Sb_2O_3 could have formed from the partially hydrolyzed $SbCl_3$ that decomposed to an oxide at the Sb_2S_3 deposition temperature. The use of excess thiourea in spray solution can inhibit the formation of the oxide phase as observed in the case of sprayed In_2S_3 [21,29], $CuInS_2$ [23] and SnS [30] films.

The optical band gaps of the Sb_2S_3 films deposited from alcohol solutions were comparable, 1.7 eV (Table 2). The band gaps characteristic of films grown from alcohol solutions are equivalent to the Eg presented by Boughalmi et al. [19] for sprayed Sb_2S_3 films from acetone-aqua mixture (CBD recipe), 1.72 eV. According to EDX, the S/Sb ratio in the film grown from 2-propanol was 1.0 being similar to the S/Sb ratio in the film grown at similar conditions from aqueous solution with Sb:S:TA ratio of 1:3:1 (Table 1). The S/Sb ratio in the film grown from methanol solution was 1.4 (Table 2), being close to the stoichiometry of Sb_2S_3, although the film contained Sb_2O_3 as a secondary phase according

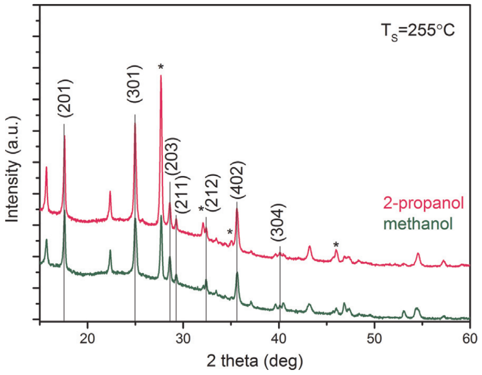

Fig. 7. XRD patterns of Sb_2S_3 films deposited at 255 °C using methanol and 2-propanol solutions. Sb_2O_3 phase peaks are marked with *.

Table 2
S/Sb ratio in the sprayed films according to EDX and Eg of the films (data acquired from Tauc plots) deposited from aqueous, methanol and 2-propanol solutions at 255 °C. Independent of the solvent, the Sb:S molar ratio in the spray solutions is 1:3, a complexing agent (tartaric acid with the molar ratio of Sb:S:TA=1:3:1) is added to aqueous solvent to prevent the hydrolysis of the Sb precursor.

	Aqueous solvent, Sb: S:TA=1:3:1	**Methanol solvent, Sb:S=1:3**	**2-propanol solvent, Sb:S=1:3**
S/Sb	1.0	1.4	1.0
Eg (eV)	2.1	1.7	1.7

to XRD. Further studies are needed to optimize the deposition conditions to grow single phase Sb_2S_3 films from alcohol solutions by chemical spray.

4. Conclusions

Sb_2S_3 films were grown by chemical spray pyrolysis and the effect of tartaric acid concentration and deposition temperatures were studied. The use of high tartaric acid concentrations (Sb:S: TA=1:3:10) as reported in the literature is unnecessary: the lower tartaric acid concentration (1:3:1) leads to stable aqueous spray solution and crystalline orthorhombic stibnite films with lower amount of organic residues.

Independent of the deposition temperature from 205 °C to 355 °C, the use of Sb:S:TA ratio of 1:3:1 in the spray solution leads to crystalline Sb_2S_3 films. Yet, the crystallinity of the Sb_2S_3 films decreased as the temperature was increased from 205 °C to 355 °C: the crystallite size decreased from 25 nm to 15 nm. With an increase in deposition temperature from 205 °C to 355 °C, the Eg increased from 2.3 eV to 2.5 eV. At the deposition temperature of 355 °C, an unknown phase was present in the films besides orthorhombic stibnite, according to XRD. Additionally, the EDX study indicates a decrease in sulfur and an increase in oxygen content in the film when increasing the deposition temperature. Therefore, the unknown crystalline phase in the film could be a byproduct containing antimony and oxide that formed from partially hydrolyzed $SbCl_3$ that decomposed to an oxide at the deposition temperature.

The FTIR spectra of the films grown in the range of 205–305 °C show the presence of C=C, C=O, C–C and C–O vibrations. Therefore, the films contain residues from organic precursors, mainly from tartaric acid. According to thermal analysis study, tartaric acid is completely decomposed only at 495 °C. Although the results of thermal analysis cannot directly be assigned to the growth of thin films due to different experiment conditions, the TG/DTA results show that Sb_2S_3 films sprayed at temperatures below 500 °C contain thermal decomposition product of tartaric acid when TA is used as a complexing agent in spray solution.

Additionally, the first results on spraying Sb_2S_3 films from alcohol solutions are reported. The use of alcohol solvents gives the advantage of avoiding the complexing agent that contaminates the Sb_2S_3 film with organic residues and results in crystalline film with Eg of 1.7 eV. Yet, further studies are needed to optimize the deposition process of Sb_2S_3 films from alcohol solutions by chemical spray pyrolysis.

Acknowledgment

Financing by the Estonian Ministry of Education and Research under project IUT 19-4, by the Estonian Science Foundation (Grant ETF9081) and by the European Union through the European Regional Development Fund, Projects 3.2.1101.12-0023 (Efficient plasmonic absorbers for solar cells) and 3.2.0101.11-0029 (Center of Excellence “Mesosystems: Theory and Applications”) is gratefully acknowledged. This work has been partially supported by graduate school “Functional materials and technologies” receiving funding from the European Social Fund under Project 1.2.0401.09-0079 in Estonia.

References

[1] Y. Itzhaik, O. Niitsoo, M. Page, G. Hodes, J. Phys. Chem. C 113 (2009) 4254.
[2] S.-J. Moon, Y. Itzhaik, J.-H. Yum, S.M. Zakeeruddin, G. Hodes, M. Grätzel, J. Phys. Chem. Lett. 1 (2010) 1524.
[3] S. Nezu, G. Larramona, C. Chone, A. Jacob, B. Delatouche, C. Moisan, J. Phys. Chem. C 114 (2010) 6854.
[4] K. Tsujimoto, D. Nguyen, S. Ito, H. Nishino, H. Matsuyoshi, A. Konno, G.R. A. Kumara, K. Tennakone, J. Phys. Chem. C 116 (2012) 13465.
[5] T. Fukumoto, T. Moehl, Y. Niwa, M.K. Nazeeruddin, M. Grätzel, L. Etgar, Adv. Energy Mater. 3 (2013) 29.
[6] S. Ito, K. Tsujimoto, D.C. Nguyen, K. Manabe, H. Nishino, Int. J. Hydrogen Energy 38 (2013) 16749.
[7] M.Y. Versavel, J.A. Haber, Thin Solid Films 515 (2007) 7171.
[8] P.P. Boix, G. Larramona, A. Jacob, B. Delatouche, J. Bisquert, J. Phys. Chem. C 116 (2012) 1579.
[9] S. Messina, M.T.S. Nair, P.K. Nair, Thin Solid Films 515 (2007) 5777.
[10] H.M. Pathan, C.D. Lokhande, Bull. Mater. Sci. 27 (2004) 85.
[11] M. Haj Lakhdar, B. Ouni, M. Amlouk, Mater. Sci. Semicond. Process. 19 (2014) 32.
[12] N.S. Yesugade, C.D. Lokhande, C.H. Bhosale, Thin Solid Films 263 (1995) 145.
[13] Z.S. El Mandouh, S.N. Salama, J. Mater. Sci. 25 (1990) 1715.
[14] K.Y. Rajpure, C.H. Bhosale, J. Phys. Chem. Solids 61 (2000) 561.
[15] S.R. Gadakh, C.H. Bhosale, Mater. Chem. Phys. 78 (2003) 367.
[16] K.Y. Rajpure, C.H. Bhosale, Mater. Chem. Phys. 73 (2002) 6.
[17] C.H. Bhosale, M.D. Uplane, P.S. Patil, C.D. Lokhande, Thin Solid Films 248 (1994) 137.
[18] K.Y. Rajpure, C.D. Lokhande, C.H. Bhosale, Mater. Chem. Phys. 51 (1997) 252.
[19] R. Boughalmi, A. Boukhachem, M. Kahlaoui, H. Maghraoui, M. Amlouk, Mater. Sci. Semicond. Process. 26 (2014) 593.
[20] K.Y. Rajpure, A.L. Dhebe, C.D. Lokhande, C.H. Bhosale, Mater. Chem. Phys. 56 (1998) 177.
[21] K. Otto, A. Katerski, A. Mere, O. Volobujeva, M. Krunks, Thin Solid Films 519 (2011) 3055.
[22] International Centre for Diffraction Data (ICDD), 2008.
[23] I. Oja Acik, K. Otto, M. Krunks, K. Tõnsuaadu, A. Mere, J. Therm. Anal. Calorim. 113 (2013) 1455.
[24] K. Otto, P. Bombicz, J. Madarász, I. Oja Acik, M. Krunks, G. Pokol, J. Therm. Anal. Calorim. 105 (2011) 83.
[25] J. Madarász, G. Pokol, J. Therm. Anal. Calorim. 88 (2007) 329.
[26] M. Krunks, O. Kijatkina, H. Rebane, I. Oja, V. Mikli, A. Mere, Thin Solid Films 404 (2002) 71.
[27] D. Yalcin, O. Ozcalik, E. Altiok, O. Bayraktar, J. Therm. Anal. Calorim. 94 (2008) 767.
[28] M. Krunks, A. Mere, A. Katerski, V. Mikli, J. Krustok, Thin Solid Films 511–512 (2006) 434.
[29] K. Otto, I. Oja Acik, K. Tõnsuaadu, A. Mere, M. Krunks, J. Therm Anal. Calorim. 105 (2014) 615.
[30] S. Polivtseva, I. Oja Acik, A. Katerski, A. Mere, M. Mikli, M. Krunks, Energy Procedia 60 (2014) 156.

APPENDIX B

APPENDIX B, Table 1. Experimental details and film properties of sprayed and doped ZnO thin films on glass substrates.

Experimental details					Film properties			Ref.
Zinc source, conc. in spray solution	**Solvent,** molar ratio or ml	**Dopant source, conc.**	**Temp.** °C	**XRD** preferred growth	**Transmit.,** %	**Film thickness,** nm	**Resistivity** Ω·cm	
$Zn(C_2H_4O_2)_2\cdot 2H_2O$ 0.7 M	Deionised water, methanol (1:3)	H_3BO_3 1 at.%	450	(002)	90%	n. p.	$2.5\cdot 10^{-3}$	[125]
$Zn(C_2H_4O_2)_2\cdot 2H_2O$ 0.05 M	Deionised water, methanol (1:3)	NH_4F 0.5 at.%	425	(002)	90%	200	10^{-1}	[127]
$Zn(C_2H_4O_2)_2\cdot 2H_2O$ 0.2 M	Water, 2-propanol (2:3)	$InCl_3$ 1 at.%	350	(101)	70%	400	10^{-2}	[15]
$Zn(C_2H_4O_2)_2\cdot 2H_2O$ 0.2 M	Water, 2-propanol (2:3)	$In(NO_3)_3$ 3 at.%	400	(101)	80%	300	10^{-3}	[38]
$Zn(C_2H_4O_2)_2\cdot 2H_2O$ 0.2 M	Methanol	$InCl_3$ 2 at.%	285	(002)	80%	550	$6\cdot 10^{-3}$	[126]
$Zn(C_5H_7O_2)_2\cdot H_2O$ 0.2 M	Deionised water, methanol, acetic acid (300:150:550)	$In(NO_3)_3$ 2.5 at.%	475	(101)	85%	600	$4.8\cdot 10^{-3}$	[128]
	Deionised water, ethanol, acetic acid (300:150:550)			(101)	70%	600	$3.8\cdot 10^{-3}$	
	Deionised water, 2-propanol, acetic acid (300:150:550)			(101)	80%	600	$4.7\cdot 10^{-3}$	

Experimental details					Film properties			Ref.
Zinc source, conc. in spray solution	**Solvent,** molar ratio or ml	**Dopant source, conc.**	**Temp.** °C	**XRD** preferred growth	**Transmit.,** %	**Film thickness,** nm	**Resistivity** Ω·cm	
$Zn(C_5H_7O_2)_2 \cdot H_2O$ 0.1 M	Deionised water, methanol, acetic acid (30:55:15)	$InCl_3$ 2.5 at.%	475	(002)	85%	600	$3.2 \cdot 10^{-3}$	[129]
	Deionised water, ethanol, acetic acid (30:55:15)			(002)	85%	600	$3 \cdot 10^{-3}$	
	Deionised water, 2-propanol, acetic acid (30:55:15)			(002)	85%	600	$2.8 \cdot 10^{-3}$	
$Zn(C_2H_4O_2)_2 \cdot 2H_2O$ 0.2 M	Deionised water, methanol, acetic acid (25:65:10)	$Ga(NO_3)_3$ 3 at.%	475	(002)	80%	2000	$1.5 \cdot 10^{-2}$	[42]
		$Al(C_5H_7O_2)_3$ 3 at.%		(002)	90%	2000	$4 \cdot 10^{-2}$	
		$InCl_3$ 3 at.%		(101)	80%	2000	$8 \cdot 10^{-3}$	
$Zn(C_2H_4O_2)_2 \cdot 2H_2O$ 0.2 M	Deionised water, methanol, acetic acid (300:675:25)	$C_{17}H_{25}AlO_8$ 3 at.%	500	(002)	85%	600	$1.3 \cdot 10^{-2}$	[130]
	Deionised water, ethanol, acetic acid (300:675:25)			(002)	85%	600	n. p.	
	Deionised water, 2-propanol, acetic acid (300:675:25)			(002)	85%	600	n. p.	

Experimental details					**Film properties**			**Ref.**
Zinc source, conc. in spray solution	**Solvent,** molar ratio or ml	**Dopant source, conc.**	**Temp.** °C	**XRD** preferred growth	**Transmit.,** %	**Film thickness,** nm	**Resistivity** Ω·cm	
$Zn(C_2H_4O_2)_2 \cdot 2H_2O$ 0.01 M	Water	$AlCl_3 \cdot 6H_2O$; $Al(NO_3)_3$ 3 at.%	400	(002); (101)	80%	210	0.8	[35]
$ZnCl_2$ 0.01 M						190		
$Zn(C_2H_4O_2)_2 \cdot 2H_2O$ 0.02 M	Water	$AlCl_3$ 3 at.%	350	n. p.	80%	280	10^{-2}	[124]
$ZnCl_2$ 0.02 M								
$Zn(C_2H_4O_2)_2 \cdot 2H_2O$ 0.2 M	Deionised water, methanol, acetic acid (25:65:10)	$Ga(NO_3)_3$ 2 at.%	400	(002)	90%	650	$3 \cdot 10^{-3}$	[132]
$Zn(C_2H_4O_2)_2 \cdot 2H_2O$ 0.2 M	Deionised water, ethanol	$Ga(NO_3)_3$ 3 at.%	400	(002)	90%	200	$7 \cdot 10^{-3}$	[133]
$Zn(C_2H_4O_2)_2 \cdot 2H_2O$ n. p.	Deionised water, methanol, acetic acid (25:65:10)	$Ga(NO_3)_3$ 3 at.%	475	(002)	80%	600	$4 \cdot 10^{-2}$	[134]

n. p. – not presented

APPENDIX B, Table 2. Experimental details and film properties of sprayed Sb_2S_3 *thin films on glass substrates.*

Experimental details						**Film properties**			**Ref.**
Antimony source, conc.	**Sulphur source, conc.**	**Solvent,** ml	**Sb:S precursors ratio in solution**	**Added to the solution**	**Temp.,** °C	**XRD** preferred growth	**Eg, eV**	**Resistivity** Ω·cm	
$Sb(CH_3COO)_3$	$CS(NH_2)_2$	Water-ethanol, n. p.	1:2.22	HCl	260	(220) (130)	1.56	-	[163]
$SbCl_3$ 0.1 M	$CS(NH_2)_2$ 0.1 M	Glacial acetic acid, 20	2:3	-	250	(060)	1.88	10^7–10^8	[180]
$SbCl_3$ 0.1 M	$CS(NH_2)_2$ 0.1 M	Double distilled water, 25	2:3	Tartaric acid, 2 ml, 1M	260	Amorph.	-	10^6–10^7	[181]
		Double distilled water, 25	2:3	Tartaric acid, 4 ml, 1M	260	(221)	1.92	10^6–10^7	
		Double distilled water, 25	2:3	Tartaric acid, 6 ml, 1M	260	(310)	1.98	10^6–10^7	
		Double distilled water, 25	2:3	Tartaric acid, 8 ml, 1M	260	(310)	1.87	10^6–10^7	
		Double distilled water, 25	2:3	Tartaric acid, 10 ml, 1M	260	(310)	2.13	10^6–10^7	
$SbCl_3$ 0.1 M	$CS(NH_2)_2$ 0.1 M	Glacial acetic acid, n. p.	2:3	-	250	(002)	1.80	10^6–10^7	[170]

Experimental details						**Film properties**			**Ref.**
Antimony source, conc.	**Sulphur source, conc.**	**Solvent,** ml	**Sb:S precursors ratio in solution**	**Added to the solution**	**Temp.,** °C	**XRD** preferred growth	**Eg, eV**	**Resistivity** Ω·cm	
$SbCl_3$ 0.1 M	$CS(NH_2)_2$ 0.1 M	Glacial acetic acid, 50	2:3	-	250	(002)	1.80	10^6–10^7	[187]
$SbCl_3$ 0.1 M	C_2H_5NS 0.1 M	Aqua*, 18	2:3	Tartaric acid, 3 ml, 0.5 M	300	Amorph.	1.10	10^6–10^7	[182]
	$CS(NH_2)_2$ 0.1 M	Glacial acetic acid, 20	2:3	-	250	(060)	1.80	10^6–10^7	
$SbCl_3$ 0.1 M	C_2H_5NS 0.1 M	Aqua*, 250	2:3	Oxalic acid, 20 ml, 2 M	300	Amorph.	1.55	10	[183]
$SbCl_3$ 0.1 M	C_2H_5NS 0.1 M	Aqua*, 18	2:3	Tartaric acid, 3 ml, 0.5 M	300	Amorph.	2.70	10^6	[184]
$SbCl_3$ 0.1 M	$Na_2S_2O_3$ 1 M	Acetone+bi-distilled water, 10+90	n. p.	-	250	(130)	1.72	-	[191]

n. p. – not presented,
* – not specified

APPENDIX C

Curriculum vitae

1. Personal data

Name	Merike Kriisa
Date and place of birth	26.09.1986, Tallinn, Estonia
Nationality	Estonian
E-mail address	merike.kriisa@ttu.ee vendike@gmail.com

2. Education

Educational institution	**Graduation year**	**Education (field of study/degree)**
Tallinn University of Technology	2017	Chemical and Materials Technology
Tallinn University of Technology	2012	Materials and Processes for Sustainable Energetics, Master's degree, *Cum Laude*
Tallinn University of Technology	2009	Applied Chemistry and Biotechnology, Bachelor's degree
Keila Secondary School	2005	Secondary education
Keila Primary School	1997	Primary education

3. Language competence/skills (fluent, average, basic skills)

Language	**Level**
Estonian	native
English	fluent
Russian	average
German	basic skills

4. Special courses

2017, February	Performance training, Graduate school of Functional materials and technologies (FMTDK)
2016-2017	UT and TUT graduate school FMTDK, oral presentation at conference

2014, May	Titan and titan alloys, Tallinn University of Technology
2014, May	Nanoparticles in the environment: fate and effects, Estonian Academy of Sciences
2013, May	How to Write a World Class Paper, Tallinn University
2012, April	Publication and Citation, Tallinn University of Technology
2012-2014	UT and TUT graduate school FMTDK, poster presentations at conferences, participations in summer schools
	Participation at international conferences with poster presentations at NANOSMAT (2014), APMAS (2012), SIMC XVI (2011), EMRS Spring Meeting (2011)

5. Professional employment

Period	Organisation	Position
01.10.2015–…	Tallinn University of Technology	Engineer
01.02.2014–30.09.2015	Tallinn University of Technology	Junior Researcher
01.09.2013–31.01.2014	Helmholtz-Zentrum Berlin (HZB)	Visiting Researcher
01.10.2012–31.08.2013	Tallinn University of Technology	Junior Researcher
01.09.2009–30.09.2012	Tallinn University of Technology	Technician

6. Research activity

Projects

01.01.2014−31.12.2019	IUT19-4 "Thin films and nanomaterials by wet-chemical methods for next-generation photovoltaics"
01.09.2013−31.01.2014	Co-operation project between Bosch and HZB
01.01.2013−31.12.2015	B24 "Metal oxide thin films by wet chemical methods for electronic devices"

01.01.2012−31.12.2015	ETF9081 "Absorber layers by chemical spray pyrolysis for nanostructured solar cells"
01.07.2012−31.12.2014	AR12118 "Efficient plasmonic absorbers for solar cells"
01.01.2010−31.12.2013	ETF8509 "Development of ZnO nanorods by chemical spray"
01.01.2008−31.12.2013	SF0140092s08 "Thin film and nanostructured materials by chemical methods"

Recognition

2013 III prize in National contest of students on scientific research in the category of master students, natural sciences and engineering

2010 I prize in Tallinn University of Technology student research competition, Technology area, Bachelor category

Defended dissertations

2012 Deposition of ZnO and ZnO:In thin films by chemical spray on glass and polymeric substrates, Master’s dissertation, supervisor lead research scientist Malle Krunks

2009 ZnO thin films as transparent conductive oxides by chemical spray pyrolysis, Bachelor’s dissertation supervisor lead research scientist Malle Krunks

Elulookirjeldus

1. Isikuandmed

Ees- ja perekonnanimi	Merike Kriisa
Sünniaeg ja –koht	26.09.1986, Tallinn, Eesti
Kodakondsus	eestlane
E-posti aadress	merike.kriisa@ttu.ee vendike@gmail.com

2. Hariduskäik

Õppeasutus (nimetus lõpetamise ajal)	**Lõpetamise aeg**	**Haridus (eriala/kraad)**
Tallinna Tehnikaülikool	2017	Keemia- ja materjalitehnoloogia
Tallinna Tehnikaülikool	2012	Materjalid ja protsessid jätkusuutlikus energeetikas, tehnikateaduste magister, *Cum Laude*
Tallinna Tehnikaülikool	2009	Rakenduskeemia ja biotehnoloogia, loodusteaduse bakalaureus
Keila Gümnaasium	2005	Keskharidus
Keila Algkool	1997	Algharidus

3. Keelteoskus (alg-, kesk- või kõrgtase)

Keel	**Tase**
eesti keel	emakeel
inglise keel	kõrgtase
vene keel	kesktase
saksa keel	algtase

4. Täiendusõpe

2017, veebruar	Esinemiskoolitus, doktorikool “Funktsionaalsed materjalid ja tehnoloogiad” (FMTDK)
2016-2017	TÜ ja TTÜ doktorikool FMTDK, suuline ettekanne konverentsil
2014, mai	Titaan ja titaanisulamid, Tallinna Tehnikaülikool

2014, mai	Nanoparticles in the environment: fate and effects, Eesti Teaduste Akadeemia
2013, mai	How to Write a World Class Paper, Tallinna Ülikool
2012, aprill	Publitseerimine ja viitamine, Tallinna Tehnikaülikool
2012-2014	TÜ ja TTÜ doktorikool FMTDK, poster ettekanded konverentsidel. osalemised suvekoolides
	Osalemine rahvusvahelistel konverentsidel poster ettekannetega: NANOSMAT (2014), APMAS (2012), SIMC XVI (2011), EMRS Spring Meeting (2011)

5. Teenistuskäik

Töötamise aeg	Tööandja nimetus	Ametikoht
01.10.2015–…	Tallinna Tehnikaülikool	Insener
01.02.2014–30.09.2015	Tallinna Tehnikaülikool	Nooremteadur
01.09.2013–31.01.2014	Helmholtz-Zentrum Berlin (HZB)	Külalisteadur
01.10.2012–31.08.2013	Tallinna Tehnikaülikool	Nooremteadur
01.09.2009–30.09.2012	Tallinna Tehnikaülikool	Tehniline töötaja

6. Teadustegevus

Osalemine projektides

01.01.2014−31.12.2019	IUT19-4 "Õhukesed kiled ja nanomaterjalid keemilistel vedeliksadestusmeetoditel uue põlvkonna fotovoltseadistele", täitja
01.09.2013−31.01.2014	Bosch ja HZB koostööprojekt
01.01.2013−31.12.2015	B24 "Keemilistel meetoditel kasvatatud metalli oksiidide õhukesed kiled elektroonikaseadistele", põhitäitja
01.01.2012−31.12.2015	ETF9081 "Absorberkihid keemilise pihustuspürolüüsi meetodil nanostruktuursetele päikesepatareidele", põhitäitja
01.07.2012−31.12.2014	AR12118 "Efektiivsed plasmoonilised absorberid päikesepatareidele", põhitäitja

01.01.2010−31.12.2013	ETF8509 "Keemilise pihustuspürolüüsi meetodil kasvatatud ZnO nanovarraste areng", põhitäitja
01.01.2008−31.12.2013	SF0140092s08 "Õhukesekilelised ja nanostruktuursed materjalid keemilistel meetoditel", täitja

Tunnustused

2013 III preemia Üliõpilaste teadustööde riiklikul konkursil magistriõppe kategoorias, loodusteadused ja tehnika

2010 I koht Tallinna Tehnikaülikooli tudengite teadustööde konkursil, Tehnikateaduste valdkond, Bakalaureuse kategooria

Kaitstud lõputööd

2012 ZnO ja ZnO:In kilede kasvatamine keemilise pihustamise meetodil klaas- ja polümeersetel alustel, magistritöö, juhendaja juhtivteadur Malle Krunks

2009 Elektrit juhtivate ZnO kilede sadestamine keemilise pihustamise meetodil, bakalaureusetöö, juhendaja juhtivteadur Malle Krunks

List of publications

1. **Kriisa, M.;** Krunks, M.; Oja Acik, I.; Kärber, E.; Mikli, V. (2015). The effect of tartaric acid in the deposition of Sb_2S_3 films by chemical spray pyrolysis. Materials Science in Semiconductor Processing, 40, 867−872, 10.1016/j. mssp.2015.07.049.

2. **Kriisa, M.;** Sáez-Araoz, R.; Fischer, C-H.; Köhler, T.; Kärber, E.; Fu, Y.; Hergert, F.; Lux-Steiner, M-Ch.; Krunks, M. (2015). Study of Zn(OS) films grown by aerosol assisted chemical vapour deposition and their application as buffer layers in $Cu(In,Ga)(S,Se)_2$ solar cells. Solar Energy, 115, 562−568, 10.1016/j. solener.2015.02.046.

3. **Kriisa, M.;** Kärber, E.; Krunks, M.; Mikli, V.; Unt, T.; Kukk, M.; Mere, A. (2014). Growth and properties of ZnO films on polymeric substrate by spray pyrolysis method. Thin Solid Films, 555, 87−92, 10.1016/j. tsf.2013.05.150.

4. **Kriisa, M.;** Krunks, M.; Kärber, E.; Kukk, M.; Mikli, V.; Mere, A. (2013). Effect of Solution Spray Rate on the Properties of Chemically Sprayed ZnO:In Thin Films. Journal of Nanomaterials, 2013, Article ID 423632,, 10.1155/2013/423632.

5. Unt, T.; **Kriisa, M.;** Mere, A.; Krunks, M. (2013). Optical properties of sprayed ZnO thin films. In: Proceedings of the 11th International Conference of young scientists on energy issues (VII-482−VII-489). Kaunas, Lithuania: Kaunas Technology University.

6. Krunks, M.; Dedova, T.; Oja Acik, I.; **Kriisa, M.;** Mikli, V.; Katerski, A.; Kärber, E.; Mere, A. (2013). ZnO nanostructures by chemical spray for next generation solar cells. NEXTGEN NANO PV, Book of Abstracts: Nanotechnology for Next Generation High Efficiency Photovoltaics, IES Cargese, Corsica, France, April 1-6, 2013. NanoSciences, Provence-Alpes_Cote d'Azur, 31−32.

7. **Vent, M.;** Kärber, E.; Unt, T.; Mere, A.; Krunks, M. (2012). The effect of growth temperature and spraying rate on properties of ZnO:In films. physica status solidi (c), 9 (7), 1604−1606, 10.1002/pssc.201200008.

8. Annert, K.; **Vent, M.;** Dedova, T.; Kärber, E.; Oja Acik, I.; Volobujeva, O.; Mere, A.; Krunks, M.; Mikli, V. (2010). Impacts of different solvents and substrates on properties of zinc oxide nanorod layers prepared by chemical spray pyrolysis. In: Proceedings of CYSENI 2010. The 7th Annual Conference of Young Scientists on Energy Issues, May 27-28, 2010, Kaunas, Lithuania (301−309). Lithuanian Energy Institute.

9. **Vent, M.;** Annert, K.; Kärber, E.; Krunks , M. (2010). ZnO thin films as transparent conductive oxides by chemical spray pyrolysis. In: Proceedings of CYSENI 2010. The 7th Annual Conference of Young Scientists on Energy Issues, May 27-28, 2010, Kaunas, Lithuania (399−407). Lithuanian Energy Institute.

10. **Vent, M.;** Kärber, E.; Volobujeva, O.; Krunks, M. (2010). Läbipaistvate ja elektrit juhtivate ZnO kilede valmistamine keemilise pihustamise meetodil. Abstracts of Scientific Conference: XXXI Eesti Keemiapäevad, Tallinn, 28.04.2010. Tallinn: Eesti Keemia Selts, 82.

DISSERTATIONS DEFENDED AT TALLINN UNIVERSITY OF TECHNOLOGY ON *NATURAL AND EXACT SCIENCES*

1. **Olav Kongas**. Nonlinear Dynamics in Modeling Cardiac Arrhytmias. 1998.
2. **Kalju Vanatalu**. Optimization of Processes of Microbial Biosynthesis of Isotopically Labeled Biomolecules and Their Complexes. 1999.
3. **Ahto Buldas**. An Algebraic Approach to the Structure of Graphs. 1999.
4. **Monika Drews**. A Metabolic Study of Insect Cells in Batch and Continuous Culture: Application of Chemostat and Turbidostat to the Production of Recombinant Proteins. 1999.
5. **Eola Valdre**. Endothelial-Specific Regulation of Vessel Formation: Role of Receptor Tyrosine Kinases. 2000.
6. **Kalju Lott**. Doping and Defect Thermodynamic Equilibrium in ZnS. 2000.
7. **Reet Koljak**. Novel Fatty Acid Dioxygenases from the Corals *Plexaura homomalla* and *Gersemia fruticosa.* 2001.
8. **Anne Paju**. Asymmetric oxidation of Prochiral and Racemic Ketones by Using Sharpless Catalyst. 2001.
9. **Marko Vendelin**. Cardiac Mechanoenergetics *in silico*. 2001.
10. **Pearu Peterson**. Multi-Soliton Interactions and the Inverse Problem of Wave Crest. 2001.
11. **Anne Menert**. Microcalorimetry of Anaerobic Digestion. 2001.
12. **Toomas Tiivel**. The Role of the Mitochondrial Outer Membrane in *in vivo* Regulation of Respiration in Normal Heart and Skeletal Muscle Cell. 2002.
13. **Olle Hints**. Ordovician Scolecodonts of Estonia and Neighbouring Areas: Taxonomy, Distribution, Palaeoecology, and Application. 2002.
14. **Jaak Nõlvak**. Chitinozoan Biostratigrapy in the Ordovician of Baltoscandia. 2002.
15. **Liivi Kluge**. On Algebraic Structure of Pre-Operad. 2002.
16. **Jaanus Lass**. Biosignal Interpretation: Study of Cardiac Arrhytmias and Electromagnetic Field Effects on Human Nervous System. 2002.
17. **Janek Peterson**. Synthesis, Structural Characterization and Modification of PAMAM Dendrimers. 2002.
18. **Merike Vaher**. Room Temperature Ionic Liquids as Background Electrolyte Additives in Capillary Electrophoresis. 2002.
19. **Valdek Mikli**. Electron Microscopy and Image Analysis Study of Powdered Hardmetal Materials and Optoelectronic Thin Films. 2003.
20. **Mart Viljus**. The Microstructure and Properties of Fine-Grained Cermets. 2003.
21. **Signe Kask**. Identification and Characterization of Dairy-Related *Lactobacillus.* 2003.
22. **Tiiu-Mai Laht**. Influence of Microstructure of the Curd on Enzymatic and Microbiological Processes in Swiss-Type Cheese. 2003.
23. **Anne Kuusksalu**. 2–5A Synthetase in the Marine Sponge *Geodia cydonium.* 2003.
24. **Sergei Bereznev**. Solar Cells Based on Polycristalline Copper-Indium Chalcogenides and Conductive Polymers. 2003.

25. **Kadri Kriis**. Asymmetric Synthesis of C_2-Symmetric Bimorpholines and Their Application as Chiral Ligands in the Transfer Hydrogenation of Aromatic Ketones. 2004.
26. **Jekaterina Reut**. Polypyrrole Coatings on Conducting and Insulating Substracts. 2004.
27. **Sven Nõmm**. Realization and Identification of Discrete-Time Nonlinear Systems. 2004.
28. **Olga Kijatkina**. Deposition of Copper Indium Disulphide Films by Chemical Spray Pyrolysis. 2004.
29. **Gert Tamberg**. On Sampling Operators Defined by Rogosinski, Hann and Blackman Windows. 2004.
30. **Monika Übner**. Interaction of Humic Substances with Metal Cations. 2004.
31. **Kaarel Adamberg**. Growth Characteristics of Non-Starter Lactic Acid Bacteria from Cheese. 2004.
32. **Imre Vallikivi**. Lipase-Catalysed Reactions of Prostaglandins. 2004.
33. **Merike Peld**. Substituted Apatites as Sorbents for Heavy Metals. 2005.
34. **Vitali Syritski**. Study of Synthesis and Redox Switching of Polypyrrole and Poly(3,4-ethylenedioxythiophene) by Using *in-situ* Techniques. 2004.
35. **Lee Põllumaa**. Evaluation of Ecotoxicological Effects Related to Oil Shale Industry. 2004.
36. **Riina Aav**. Synthesis of 9,11-Secosterols Intermediates. 2005.
37. **Andres Braunbrück**. Wave Interaction in Weakly Inhomogeneous Materials. 2005.
38. **Robert Kitt**. Generalised Scale-Invariance in Financial Time Series. 2005.
39. **Juss Pavelson**. Mesoscale Physical Processes and the Related Impact on the Summer Nutrient Fields and Phytoplankton Blooms in the Western Gulf of Finland. 2005.
40. **Olari Ilison**. Solitons and Solitary Waves in Media with Higher Order Dispersive and Nonlinear Effects. 2005.
41. **Maksim Säkki**. Intermittency and Long-Range Structurization of Heart Rate. 2005.
42. **Enli Kiipli**. Modelling Seawater Chemistry of the East Baltic Basin in the Late Ordovician–Early Silurian. 2005.
43. **Igor Golovtsov**. Modification of Conductive Properties and Processability of Polyparaphenylene, Polypyrrole and polyaniline. 2005.
44. **Katrin Laos**. Interaction Between Furcellaran and the Globular Proteins (Bovine Serum Albumin β-Lactoglobulin). 2005.
45. **Arvo Mere**. Structural and Electrical Properties of Spray Deposited Copper Indium Disulphide Films for Solar Cells. 2006.
46. **Sille Ehala**. Development and Application of Various On- and Off-Line Analytical Methods for the Analysis of Bioactive Compounds. 2006.
47. **Maria Kulp**. Capillary Electrophoretic Monitoring of Biochemical Reaction Kinetics. 2006.
48. **Anu Aaspõllu.** Proteinases from *Vipera lebetina* Snake Venom Affecting Hemostasis. 2006.
49. **Lyudmila Chekulayeva**. Photosensitized Inactivation of Tumor Cells by Porphyrins and Chlorins. 2006.

50. **Merle Uudsemaa**. Quantum-Chemical Modeling of Solvated First Row Transition Metal Ions. 2006.
51. **Tagli Pitsi**. Nutrition Situation of Pre-School Children in Estonia from 1995 to 2004. 2006.
52. **Angela Ivask**. Luminescent Recombinant Sensor Bacteria for the Analysis of Bioavailable Heavy Metals. 2006.
53. **Tiina Lõugas**. Study on Physico-Chemical Properties and Some Bioactive Compounds of Sea Buckthorn (*Hippophae rhamnoides* L.). 2006.
54. **Kaja Kasemets**. Effect of Changing Environmental Conditions on the Fermentative Growth of *Saccharomyces cerevisae* S288C: Auxo-accelerostat Study. 2006.
55. **Ildar Nisamedtinov**. Application of ^{13}C and Fluorescence Labeling in Metabolic Studies of *Saccharomyces* spp. 2006.
56. **Alar Leibak**. On Additive Generalisation of Voronoï's Theory of Perfect Forms over Algebraic Number Fields. 2006.
57. **Andri Jagomägi**. Photoluminescence of Chalcopyrite Tellurides. 2006.
58. **Tõnu Martma**. Application of Carbon Isotopes to the Study of the Ordovician and Silurian of the Baltic. 2006.
59. **Marit Kauk**. Chemical Composition of $CuInSe_2$ Monograin Powders for Solar Cell Application. 2006.
60. **Julia Kois**. Electrochemical Deposition of $CuInSe_2$ Thin Films for Photovoltaic Applications. 2006.
61. **Ilona Oja Açik**. Sol-Gel Deposition of Titanium Dioxide Films. 2007.
62. **Tiia Anmann**. Integrated and Organized Cellular Bioenergetic Systems in Heart and Brain. 2007.
63. **Katrin Trummal**. Purification, Characterization and Specificity Studies of Metalloproteinases from *Vipera lebetina* Snake Venom. 2007.
64. **Gennadi Lessin**. Biochemical Definition of Coastal Zone Using Numerical Modeling and Measurement Data. 2007.
65. **Enno Pais**. Inverse problems to determine non-homogeneous degenerate memory kernels in heat flow. 2007.
66. **Maria Borissova**. Capillary Electrophoresis on Alkylimidazolium Salts. 2007.
67. **Karin Valmsen**. Prostaglandin Synthesis in the Coral *Plexaura homomalla*: Control of Prostaglandin Stereochemistry at Carbon 15 by Cyclooxygenases. 2007.
68. **Kristjan Piirimäe**. Long-Term Changes of Nutrient Fluxes in the Drainage Basin of the Gulf of Finland – Application of the PolFlow Model. 2007.
69. **Tatjana Dedova**. Chemical Spray Pyrolysis Deposition of Zinc Sulfide Thin Films and Zinc Oxide Nanostructured Layers. 2007.
70. **Katrin Tomson**. Production of Labelled Recombinant Proteins in Fed-Batch Systems in *Escherichia coli*. 2007.
71. **Cecilia Sarmiento**. Suppressors of RNA Silencing in Plants. 2008.
72. **Vilja Mardla**. Inhibition of Platelet Aggregation with Combination of Antiplatelet Agents. 2008.
73. **Maie Bachmann**. Effect of Modulated Microwave Radiation on Human Resting Electroencephalographic Signal. 2008.
74. **Dan Hüvonen**. Terahertz Spectroscopy of Low-Dimensional Spin Systems. 2008.

75. **Ly Villo**. Stereoselective Chemoenzymatic Synthesis of Deoxy Sugar Esters Involving *Candida antarctica* Lipase B. 2008.
76. **Johan Anton**. Technology of Integrated Photoelasticity for Residual Stress Measurement in Glass Articles of Axisymmetric Shape. 2008.
77. **Olga Volobujeva**. SEM Study of Selenization of Different Thin Metallic Films. 2008.
78. **Artur Jõgi**. Synthesis of 4'-Substituted 2,3'-dideoxynucleoside Analogues. 2008.
79. **Mario Kadastik**. Doubly Charged Higgs Boson Decays and Implications on Neutrino Physics. 2008.
80. **Fernando Pérez-Caballero**. Carbon Aerogels from 5-Methylresorcinol-Formaldehyde Gels. 2008.
81. **Sirje Vaask**. The Comparability, Reproducibility and Validity of Estonian Food Consumption Surveys. 2008.
82. **Anna Menaker**. Electrosynthesized Conducting Polymers, Polypyrrole and Poly(3,4-ethylenedioxythiophene), for Molecular Imprinting. 2009.
83. **Lauri Ilison**. Solitons and Solitary Waves in Hierarchical Korteweg-de Vries Type Systems. 2009.
84. **Kaia Ernits**. Study of In_2S_3 and ZnS Thin Films Deposited by Ultrasonic Spray Pyrolysis and Chemical Deposition. 2009.
85. **Veljo Sinivee**. Portable Spectrometer for Ionizing Radiation "Gammamapper". 2009.
86. **Jüri Virkepu**. On Lagrange Formalism for Lie Theory and Operadic Harmonic Oscillator in Low Dimensions. 2009.
87. **Marko Piirsoo**. Deciphering Molecular Basis of Schwann Cell Development. 2009.
88. **Kati Helmja**. Determination of Phenolic Compounds and Their Antioxidative Capability in Plant Extracts. 2010.
89. **Merike Sõmera**. Sobemoviruses: Genomic Organization, Potential for Recombination and Necessity of P1 in Systemic Infection. 2010.
90. **Kristjan Laes**. Preparation and Impedance Spectroscopy of Hybrid Structures Based on $CuIn_3Se_5$ Photoabsorber. 2010.
91. **Kristin Lippur**. Asymmetric Synthesis of 2,2'-Bimorpholine and its 5,5'-Substituted Derivatives. 2010.
92. **Merike Luman**. Dialysis Dose and Nutrition Assessment by an Optical Method. 2010.
93. **Mihhail Berezovski**. Numerical Simulation of Wave Propagation in Heterogeneous and Microstructured Materials. 2010.
94. **Tamara Aid-Pavlidis**. Structure and Regulation of BDNF Gene. 2010.
95. **Olga Bragina**. The Role of Sonic Hedgehog Pathway in Neuro- and Tumorigenesis. 2010.
96. **Merle Randrüüt**. Wave Propagation in Microstructured Solids: Solitary and Periodic Waves. 2010.
97. **Marju Laars**. Asymmetric Organocatalytic Michael and Aldol Reactions Mediated by Cyclic Amines. 2010.
98. **Maarja Grossberg**. Optical Properties of Multinary Semiconductor Compounds for Photovoltaic Applications. 2010.

99. **Alla Maloverjan**. Vertebrate Homologues of Drosophila Fused Kinase and Their Role in Sonic Hedgehog Signalling Pathway. 2010.
100. **Priit Pruunsild**. Neuronal Activity-Dependent Transcription Factors and Regulation of Human *BDNF* Gene. 2010.
101. **Tatjana Knjazeva**. New Approaches in Capillary Electrophoresis for Separation and Study of Proteins. 2011.
102. **Atanas Katerski**. Chemical Composition of Sprayed Copper Indium Disulfide Films for Nanostructured Solar Cells. 2011.
103. **Kristi Timmo.** Formation of Properties of $CuInSe_2$ and $Cu_2ZnSn(S,Se)_4$ Monograin Powders Synthesized in Molten KI. 2011.
104. **Kert Tamm**. Wave Propagation and Interaction in Mindlin-Type Microstructured Solids: Numerical Simulation. 2011.
105. **Adrian Popp**. Ordovician Proetid Trilobites in Baltoscandia and Germany. 2011.
106. **Ove Pärn**. Sea Ice Deformation Events in the Gulf of Finland and This Impact on Shipping. 2011.
107. **Germo Väli**. Numerical Experiments on Matter Transport in the Baltic Sea. 2011.
108. **Andrus Seiman**. Point-of-Care Analyser Based on Capillary Electrophoresis. 2011.
109. **Olga Katargina**. Tick-Borne Pathogens Circulating in Estonia (Tick-Borne Encephalitis Virus, *Anaplasma phagocytophilum*, *Babesia* Species): Their Prevalence and Genetic Characterization. 2011.
110. **Ingrid Sumeri**. The Study of Probiotic Bacteria in Human Gastrointestinal Tract Simulator. 2011.
111. **Kairit Zovo**. Functional Characterization of Cellular Copper Proteome. 2011.
112. **Natalja Makarytsheva**. Analysis of Organic Species in Sediments and Soil by High Performance Separation Methods. 2011.
113. **Monika Mortimer**. Evaluation of the Biological Effects of Engineered Nanoparticles on Unicellular Pro- and Eukaryotic Organisms. 2011.
114. **Kersti Tepp**. Molecular System Bioenergetics of Cardiac Cells: Quantitative Analysis of Structure-Function Relationship. 2011.
115. **Anna-Liisa Peikolainen**. Organic Aerogels Based on 5-Methylresorcinol. 2011.
116. **Leeli Amon**. Palaeoecological Reconstruction of Late-Glacial Vegetation Dynamics in Eastern Baltic Area: A View Based on Plant Macrofossil Analysis. 2011.
117. **Tanel Peets**. Dispersion Analysis of Wave Motion in Microstructured Solids. 2011.
118. **Liina Kaupmees**. Selenization of Molybdenum as Contact Material in Solar Cells. 2011.
119. **Allan Olspert**. Properties of VPg and Coat Protein of Sobemoviruses. 2011.
120. **Kadri Koppel**. Food Category Appraisal Using Sensory Methods. 2011.
121. **Jelena Gorbatšova**. Development of Methods for CE Analysis of Plant Phenolics and Vitamins. 2011.
122. **Karin Viipsi**. Impact of EDTA and Humic Substances on the Removal of Cd and Zn from Aqueous Solutions by Apatite. 2012.

123. **David Schryer**. Metabolic Flux Analysis of Compartmentalized Systems Using Dynamic Isotopologue Modeling. 2012.
124. **Ardo Illaste**. Analysis of Molecular Movements in Cardiac Myocytes. 2012.
125. **Indrek Reile**. 3-Alkylcyclopentane-1,2-Diones in Asymmetric Oxidation and Alkylation Reactions. 2012.
126. **Tatjana Tamberg**. Some Classes of Finite 2-Groups and Their Endomorphism Semigroups. 2012.
127. **Taavi Liblik**. Variability of Thermohaline Structure in the Gulf of Finland in Summer. 2012.
128. **Priidik Lagemaa**. Operational Forecasting in Estonian Marine Waters. 2012.
129. **Andrei Errapart**. Photoelastic Tomography in Linear and Non-linear Approximation. 2012.
130. **Külliki Krabbi**. Biochemical Diagnosis of Classical Galactosemia and Mucopolysaccharidoses in Estonia. 2012.
131. **Kristel Kaseleht**. Identification of Aroma Compounds in Food using SPME-GC/MS and GC-Olfactometry. 2012.
132. **Kristel Kodar**. Immunoglobulin G Glycosylation Profiling in Patients with Gastric Cancer. 2012.
133. **Kai Rosin**. Solar Radiation and Wind as Agents of the Formation of the Radiation Regime in Water Bodies. 2012.
134. **Ann Tiiman**. Interactions of Alzheimer's Amyloid-Beta Peptides with Zn(II) and Cu(II) Ions. 2012.
135. **Olga Gavrilova**. Application and Elaboration of Accounting Approaches for Sustainable Development. 2012.
136. **Olesja Bondarenko**. Development of Bacterial Biosensors and Human Stem Cell-Based *In Vitro* Assays for the Toxicological Profiling of Synthetic Nanoparticles. 2012.
137. **Katri Muska**. Study of Composition and Thermal Treatments of Quaternary Compounds for Monograin Layer Solar Cells. 2012.
138. **Ranno Nahku**. Validation of Critical Factors for the Quantitative Characterization of Bacterial Physiology in Accelerostat Cultures. 2012.
139. **Petri-Jaan Lahtvee**. Quantitative Omics-level Analysis of Growth Rate Dependent Energy Metabolism in *Lactococcus lactis*. 2012.
140. **Kerti Orumets**. Molecular Mechanisms Controlling Intracellular Glutathione Levels in Baker's Yeast *Saccharomyces cerevisiae* and its Random Mutagenized Glutathione Over-Accumulating Isolate. 2012.
141. **Loreida Timberg**. Spice-Cured Sprats Ripening, Sensory Parameters Development, and Quality Indicators. 2012.
142. **Anna Mihhalevski**. Rye Sourdough Fermentation and Bread Stability. 2012.
143. **Liisa Arike**. Quantitative Proteomics of *Escherichia coli*: From Relative to Absolute Scale. 2012.
144. **Kairi Otto**. Deposition of In_2S_3 Thin Films by Chemical Spray Pyrolysis. 2012.
145. **Mari Sepp**. Functions of the Basic Helix-Loop-Helix Transcription Factor TCF4 in Health and Disease. 2012.
146. **Anna Suhhova**. Detection of the Effect of Weak Stressors on Human Resting Electroencephalographic Signal. 2012.

147. **Aram Kazarjan**. Development and Production of Extruded Food and Feed Products Containing Probiotic Microorganisms. 2012.
148. **Rivo Uiboupin**. Application of Remote Sensing Methods for the Investigation of Spatio-Temporal Variability of Sea Surface Temperature and Chlorophyll Fields in the Gulf of Finland. 2013.
149. **Tiina Kriščiunaite**. A Study of Milk Coagulability. 2013.
150. **Tuuli Levandi**. Comparative Study of Cereal Varieties by Analytical Separation Methods and Chemometrics. 2013.
151. **Natalja Kabanova**. Development of a Microcalorimetric Method for the Study of Fermentation Processes. 2013.
152. **Himani Khanduri**. Magnetic Properties of Functional Oxides. 2013.
153. **Julia Smirnova**. Investigation of Properties and Reaction Mechanisms of Redox-Active Proteins by ESI MS. 2013.
154. **Mervi Sepp**. Estimation of Diffusion Restrictions in Cardiomyocytes Using Kinetic Measurements. 2013.
155. **Kersti Jääger**. Differentiation and Heterogeneity of Mesenchymal Stem Cells. 2013.
156. **Victor Alari**. Multi-Scale Wind Wave Modeling in the Baltic Sea. 2013.
157. **Taavi Päll**. Studies of CD44 Hyaluronan Binding Domain as Novel Angiogenesis Inhibitor. 2013.
158. **Allan Niidu**. Synthesis of Cyclopentane and Tetrahydrofuran Derivatives. 2013.
159. **Julia Geller**. Detection and Genetic Characterization of *Borrelia* Species Circulating in Tick Population in Estonia. 2013.
160. **Irina Stulova**. The Effects of Milk Composition and Treatment on the Growth of Lactic Acid Bacteria. 2013.
161. **Jana Holmar**. Optical Method for Uric Acid Removal Assessment During Dialysis. 2013.
162. **Kerti Ausmees**. Synthesis of Heterobicyclo[3.2.0]heptane Derivatives *via* Multicomponent Cascade Reaction. 2013.
163. **Minna Varikmaa**. Structural and Functional Studies of Mitochondrial Respiration Regulation in Muscle Cells. 2013.
164. **Indrek Koppel**. Transcriptional Mechanisms of BDNF Gene Regulation. 2014.
165. **Kristjan Pilt**. Optical Pulse Wave Signal Analysis for Determination of Early Arterial Ageing in Diabetic Patients. 2014.
166. **Andres Anier**. Estimation of the Complexity of the Electroencephalogram for Brain Monitoring in Intensive Care. 2014.
167. **Toivo Kallaste**. Pyroclastic Sanidine in the Lower Palaeozoic Bentonites – A Tool for Regional Geological Correlations. 2014.
168. **Erki Kärber**. Properties of ZnO-nanorod/In_2S_3/$CuInS_2$ Solar Cell and the Constituent Layers Deposited by Chemical Spray Method. 2014.
169. **Julia Lehner**. Formation of Cu_2ZnSnS_4 and $Cu_2ZnSnSe_4$ by Chalcogenisation of Electrochemically Deposited Precursor Layers. 2014.
170. **Peep Pitk**. Protein- and Lipid-rich Solid Slaughterhouse Waste Anaerobic Co-digestion: Resource Analysis and Process Optimization. 2014.
171. **Kaspar Valgepea**. Absolute Quantitative Multi-omics Characterization of Specific Growth Rate-dependent Metabolism of *Escherichia coli*. 2014.

172. **Artur Noole**. Asymmetric Organocatalytic Synthesis of 3,3’-Disubstituted Oxindoles. 2014.
173. **Robert Tsanev**. Identification and Structure-Functional Characterisation of the Gene Transcriptional Repressor Domain of Human Gli Proteins. 2014.
174. **Dmitri Kartofelev**. Nonlinear Sound Generation Mechanisms in Musical Acoustic. 2014.
175. **Sigrid Hade**. GIS Applications in the Studies of the Palaeozoic Graptolite Argillite and Landscape Change. 2014.
176. **Agne Velthut-Meikas**. Ovarian Follicle as the Environment of Oocyte Maturation: The Role of Granulosa Cells and Follicular Fluid at Pre-Ovulatory Development. 2014.
177. **Kristel Hälvin**. Determination of B-group Vitamins in Food Using an LC-MS Stable Isotope Dilution Assay. 2014.
178. **Mailis Päri**. Characterization of the Oligoadenylate Synthetase Subgroup from Phylum Porifera. 2014.
179. **Jekaterina Kazantseva**. Alternative Splicing of *TAF4*: A Dynamic Switch between Distinct Cell Functions. 2014.
180. **Jaanus Suurväli**. Regulator of G Protein Signalling 16 (RGS16): Functions in Immunity and Genomic Location in an Ancient MHC-Related Evolutionarily Conserved Synteny Group. 2014.
181. **Ene Viiard**. Diversity and Stability of Lactic Acid Bacteria During Rye Sourdough Propagation. 2014.
182. **Kristella Hansen**. Prostaglandin Synthesis in Marine Arthropods and Red Algae. 2014.
183. **Helike Lõhelaid**. Allene Oxide Synthase-lipoxygenase Pathway in Coral Stress Response. 2015.
184. **Normunds Stivrinš**. Postglacial Environmental Conditions, Vegetation Succession and Human Impact in Latvia. 2015.
185. **Mary-Liis Kütt**. Identification and Characterization of Bioactive Peptides with Antimicrobial and Immunoregulating Properties Derived from Bovine Colostrum and Milk. 2015.
186. **Kazbulat Šogenov**. Petrophysical Models of the CO_2 Plume at Prospective Storage Sites in the Baltic Basin. 2015.
187. **Taavi Raadik**. Application of Modulation Spectroscopy Methods in Photovoltaic Materials Research. 2015.
188. **Reio Põder**. Study of Oxygen Vacancy Dynamics in Sc-doped Ceria with NMR Techniques. 2015.
189. **Sven Siir**. Internal Geochemical Stratification of Bentonites (Altered Volcanic Ash Beds) and its Interpretation. 2015.
190. **Kaur Jaanson**. Novel Transgenic Models Based on Bacterial Artificial Chromosomes for Studying BDNF Gene Regulation. 2015.
191. **Niina Karro**. Analysis of ADP Compartmentation in Cardiomyocytes and Its Role in Protection Against Mitochondrial Permeability Transition Pore Opening. 2015.
192. **Piret Laht**. B-plexins Regulate the Maturation of Neurons Through Microtubule Dynamics. 2015.
193. **Sergei Žari**. Organocatalytic Asymmetric Addition to Unsaturated 1,4-Dicarbonyl Compounds. 2015.

194. **Natalja Buhhalko**. Processes Influencing the Spatio-temporal Dynamics of Nutrients and Phytoplankton in Summer in the Gulf of Finland, Baltic Sea. 2015.
195. **Natalia Maticiuc**. Mechanism of Changes in the Properties of Chemically Deposited CdS Thin Films Induced by Thermal Annealing. 2015.
196. **Mario Öeren**. Computational Study of Cyclohexylhemicucurbiturils. 2015.
197. **Mari Kalda**. Mechanoenergetics of a Single Cardiomyocyte. 2015.
198. **Ieva Grudzinska**. Diatom Stratigraphy and Relative Sea Level Changes of the Eastern Baltic Sea over the Holocene. 2015.
199. **Anna Kazantseva**. Alternative Splicing in Health and Disease. 2015.
200. **Jana Kazarjan**. Investigation of Endogenous Antioxidants and Their Synthetic Analogues by Capillary Electrophoresis. 2016.
201. **Maria Safonova**. SnS Thin Films Deposition by Chemical Solution Method and Characterization. 2016.
202. **Jekaterina Mazina**. Detection of Psycho- and Bioactive Drugs in Different Sample Matrices by Fluorescence Spectroscopy and Capillary Electrophoresis. 2016.
203. **Karin Rosenstein**. Genes Regulated by Estrogen and Progesterone in Human Endometrium. 2016.
204. **Aleksei Tretjakov**. A Macromolecular Imprinting Approach to Design Synthetic Receptors for Label-Free Biosensing Applications. 2016.
205. **Mati Danilson**. Temperature Dependent Electrical Properties of Kesterite Monograin Layer Solar Cells. 2016.
206. **Kaspar Kevvai**. Applications of ^{15}N-labeled Yeast Hydrolysates in Metabolic Studies of *Lactococcus lactis* and *Saccharomyces Cerevisiae*. 2016.
207. **Kadri Aller**. Development and Applications of Chemically Defined Media for Lactic Acid Bacteria. 2016.
208. **Gert Preegel**. Cyclopentane-1,2-dione and Cyclopent-2-en-1-one in Asymmetric Organocatalytic Reactions. 2016.
209. **Jekaterina Služenikina**. Applications of Marine Scatterometer Winds and Quality Aspects of their Assimilation into Numerical Weather Prediction Model HIRLAM. 2016.
210. **Erkki Kask**. Study of Kesterite Solar Cell Absorbers by Capacitance Spectroscopy Methods. 2016.
211. **Jürgen Arund**. Major Chromophores and Fluorophores in the Spent Dialysate as Cornerstones for Optical Monitoring of Kidney Replacement Therapy. 2016.
212. **Andrei Šamarin**. Hybrid PET/MR Imaging of Bone Metabolism and Morphology. 2016.
213. **Kairi Kasemets**. Inverse Problems for Parabolic Integro-Differential Equations with Instant and Integral Conditions. 2016.
214. **Edith Soosaar**. An Evolution of Freshwater Bulge in Laboratory Scale Experiments and Natural Conditions. 2016.
215. **Peeter Laas**. Spatiotemporal Niche-Partitioning of Bacterioplankton Community across Environmental Gradients in the Baltic Sea. 2016.
216. **Margus Voolma**. Geochemistry of Organic-Rich Metalliferous Oil Shale/Black Shale of Jordan and Estonia. 2016.
217. **Karin Ojamäe**. The Ecology and Photobiology of Mixotrophic Alveolates in the Baltic Sea. 2016.

218. **Anne Pink**. The Role of CD44 in the Control of Endothelial Cell Proliferation and Angiogenesis. 2016.
219. **Kristiina Kreek**. Metal-Doped Aerogels Based on Resorcinol Derivatives. 2016.
220. **Kaia Kukk**. Expression of Human Prostaglandin H Synthases in the Yeast Pichia pastoris. 2016.
221. **Martin Laasmaa**. Revealing Aspects of Cardiac Function from Fluorescence and Electrophysiological Recordings. 2016.
222. **Eeva-Gerda Kobrin**. Development of Point of Care Applications for Capillary Electrophoresis. 2016.
223. **Villu Kikas**. Physical Processes Controlling the Surface Layer Dynamics in the Stratified Gulf of Finland: An Application of Ferrybox Technology. 2016.
224. **Maris Skudra**. Features of Thermohaline Structure and Circulation in the Gulf of Riga. 2017.
225. **Sirje Sildever**. Influence of Physical-Chemical Factors on Community and Populations of the Baltic Sea Spring Bloom Microalgae. 2017.
226. **Nicolae Spalatu**. Development of CdTe Absorber Layer for Thin-Film Solar Cells. 2017.
227. **Kristi Luberg**. Human Tropomyosin-Related Kinase A and B: from Transcript Diversity to Novel Inhibitors. 2017.
228. **Andrus Kaldma**. Metabolic Remodeling of Human Colorectal Cancer: Alterations in Energy Fluxes. 2017.
229. **Irina Osadchuk**. Structures and Catalytic Properties of Titanium and Iridium Based Complexes. 2017.
230. **Roman Boroznjak**. A Computational Approach for Rational Monomer Selection in Molecularly Imprinted Plolymer Synthesis. 2017.
231. **Sten Erm**. Use of Mother-Daughter Multi-Bioreactor Systems for Studies of Steady State Microbial Growth Space. 2017.